Towards Improving the Quantum Coherence in Ion Microtraps

by

Mariam Akhtar

A thesis submitted in partial fulfilment for the
degree of Doctor of Philosophy

University of Strathclyde
Department of Physics and SUPA
Experimental work conducted at the
National Physical Laboratories

May 2019

Declaration of Authorship

'This thesis is the result of the author's original research. It has been composed by the author and has not been previously submitted for examination which has led to the award of a degree'

Signed: _____

Date: _____

Abstract

Ion traps have a number of applications in optical atomic clocks, quantum metrology and quantum information processing. Quantum coherence is essential in these applications, yet motional decoherence of ions remains a significant limitation. Experiments towards improving the quantum coherence of ions confined in microfabricated traps are presented. Surface contamination, noise on DC sources and instabilities in magnetic field are all potential sources of decoherence that are investigated. Spectroscopy on a single ion as well as a two ion string using $^{88}Sr^{+}$ is then demonstrated.

Hydrocarbon contamination on electrode surfaces is a possible sources of electric-field noise that may result in motional heating of the ion and therefore decoherence. A capacitively-coupled RF microdischarge was generated *in situ* with energies suited to selective removal of surface contamination. The plasma parameters needed for the calculation of the ion bombardment energy, namely the electron density and the gas temperature, were determined using optical emission spectroscopy. For the range of operating parameters tested, the mean ion energies between 0.3 eV and 4.1 eV were calculated. While these energies are below the sputtering threshold for hydrocarbon contamination (12 eV), calculations show that the high energy tail of the ion energy distribution should remove two adsorbate monolayers in as little as 1 min. Furthermore, calculations show that during this time, the distribution is insufficiently energetic to have a significant effect on the Au electrode surface. The results presented here suggest that the microplasma surface processing is suited to *in situ* selective removal of surface adsorbates from ion microtrap electrodes.

If electrical noise present on the electrodes of the trap is resonant with the motion of the ion, ion motional heating can occur and result in a reduced ion coherence time. Therefore it is essential to minimise the electrical noise at the motional frequencies of the ion. A system was created for versatile control of the DC potentials on the ion electrodes. Filtering of the DC signals such that the noise at the motional frequencies of the ion are attenuated, was implemented with a pair of interchangeable filter boards. For heating rate measurements a 2^{nd} order RC filter board was designed with an attenuation of 192 dB at 1 MHz and a cut-off frequency of 6 Hz. A second filter board was made

for ion shuttling; a 3^{rd} order Butterworth filter with 59 dB attenuation at 1 MHz and a cut-off frequency of 100 kHz.

Within this work the $\Delta m_j = -2$ Zeeman component of the optical qubit transition in $^{88}Sr^+$ is used. This transition is beneficial since, given the geometry of the experimental apparatus used here, it allows for a higher coupling strength relative to the other Zeeman components. However this transition also has a higher sensitivity to magnetic field fluctuations. The separation of the energy levels that need to be addressed are dependent on the magnetic field applied. Therefore magnetic field fluctuations lead to dampening of the phase relation between the states; *i.e.* decoherence. A high-precision stabilisation system was implemented for the control of the currents to the coils that generate the magnetic field the ion experiences. A derived stability of the current applied to the coils was expected to result in a magnetic field stability of 3×10^{-7} G over 1000 s. However when measured directly, the magnetic field stability was limited by the drift of the ion pump magnet. The characterisation of this drift and the methods for reducing it are presented.

As atoms are evaporated towards the trap, the atomic flux can adsorb onto the electrode surfaces and, in a similar fashion to the hydrocarbon contamination, form sources of electric field-noise that can cause decoherence. Precise control of the heating of the atomic source enables efficient loading of the ions into the trap, while minimising the flux generated and therefore also maximises the lifetime of the device. An automated system is presented for improved control of the generated Sr atomic flux. This is anticipated to improve the lifetime of the atomic sources and reduce the potential for contamination of the electrode surfaces.

Spectroscopy on a single ion and a two-ion string in the next generation of ion trap design is presented. The motional frequencies are measured in zero magnetic field and in the presence of a bias field. The measured motional frequencies were in-line with expectations. To investigate the effect of pulse-shaping, measurements with square pulses and Blackman shaped pulses were made. The excitation with Blackman-shaped pulses showed the suppression of Fourier components in the wings of the measured spectral line. The temporal control of the spectroscopy pulse is essential for minimising off-resonant excitation. The coherent control of a single ion was then further investigated and Rabi flopping on the carrier transition of the $\Delta m_j = -2$ Zeeman component was observed. The coherent control of the ion was found to be intermittently affected by the presence

of intensity noise on the spectroscopy pump laser. Methods for mitigating the effect of this noise are currently under investigation. The experimental procedures needed to implement a Mølmer-Sørenson entanglement gate have been developed. This remains the next stage in the experimental investigation once stable coherent control of the ion has been established.

Acknowledgements

Firstly, thank you to Alastair Sinclair for his guidance over the course of my PhD. His insight and direction has been invaluable over the years and I was fortunate to have had him as a supervisor. Erling Riis has also been a huge help as a supervisor and I am very grateful for all his support.

Working at NPL has meant that I have been able to work alongside some extremely dedicated and talented scientists. I am indebted to Guido Wilpers for always having the time to share his wealth of expertise. It has been a pleasure to work with Joseph Thom, whose patience in the lab is sincerely appreciated. David Szwer has also been unfailingly helpful as a guru for all things LabVIEW/Matlab related; for which I am enormously grateful.

To the wider community at NPL, my time here has been significantly enhanced by the students and Cake Club members. For all the intriguing discussion and delicious treats, NPL would have felt a lesser place without you. I would also like to say a special thanks to Shaun Geaney for sticking with me through the thesis writing. The long days were made more bearable by having someone to share them with.

Outside of NPL, I have been lucky to have the tremendous support of my friends and family. Ayesha Akhtar, Laura Whitehead, the Waifs and Strays and the extended Basil House gang have all made an amazing difference and I really can't thank them enough. Lastly, and perhaps most importantly, without Reuben Singer this would have been nowhere near as much fun.

Contents

List of Figures

Abbreviations

AC	alternating current
AIN	aluminium nitride
AOM	acoustic-optic modulator
CCD	charge-coupled device
COM	centre of mass
CNOT	controlled-not
CMOS	complementary metal-oxide-semiconductor
DC	direct current
ECDL	extended-cavity diode laser
EED	electron energy distribution
EFG	electric-field generator
EMCCD	electron-multiplying charge-coupled device
FNCS	fibre noise-cancellation system
FWHM	full width at half maximum
GND	ground
GPIB	general purpose interface bus
LCC	leadless-chip carrier
LFS	laser frequency shifter
NPL	National Physical Laboratories
OES	optical emission spectroscopy
PCB	printed circuit board
PBS	polarising beam splitter
PM	polarisation-maintaining
PMT	photo-multiplier tube
RF	radio frequency
SUPA	Scottish Universities Physics Alliance

SMB	SubMinature version B
TTL	transistor-transistor logic
Ti:Sa	titanium-sapphire laser
UHV	ultra-high vacuum
USB	universal serial bus
VCO	voltage-controlled oscillator
QC	quantum computer
QIP	quantum information processing

Chapter 1

Introduction

Technology that takes advantage of quantum effects is of increasing interest. Large-scale technology companies such as Google, Microsoft, IBM and Intel are but a few of the corporations investing in quantum technologies and each of them are developing their own unique devices [1]. Ion traps are one type of device that enables access to a quantum system. Through the use of lasers to manipulate the ion's internal and motional states, ion traps can be used to create cold atomic systems with initialisation, detection and state manipulation fidelities >99.9 % [2, 3] and long coherence times [4, 5]. Ion traps inherently provide access to a well controlled quantum system and have therefore featured in a number of wide-ranging applications.

One key application is in quantum metrology, which is the use of quantum phenomena in setting the standards for measurement [6]. The redefinition of units from mechanical standards to quantum systems has the practical advantages of being more accurate and reproducible - to the extent that they are now internationally accepted [6]. For example, the primary standard for the definition of the second is currently based on the ground state hyperfine transitions of Cs atoms.

There are three key parameters in defining the suitability of a system for an atomic clock. The quality (or Q) factor, the accuracy and the instability.

The Q factor characterises the resonance bandwidth,

$$Q = \frac{\nu_0}{\Delta\nu} \tag{1.1}$$

where ν_0 is unperturbed theoretical frequency of the reference transition and $\Delta\nu$ is

the linewidth of the transition. The accuracy of a clock reference is defined by the fractional uncertainty in the absolute frequency measurement, which is the ratio of the measurement output frequency $\delta\nu$, with ν_0. The instability is defined as the repeatability of the measured clock frequency for a given averaging time; otherwise known as the fractional frequency instability $\sigma_y(\tau)$

$$\sigma_y(\tau) = \frac{1}{Q}\sqrt{\frac{T}{N\tau}} \tag{1.2}$$

where T is the clock cycle duration, τ is the averaging time and the N is the number of atoms.

Generally the primary standard based on hyperfine transitions in Cs atoms has reached fractional frequency instabilities in the range of $2 \times 10^{-16} \leqslant \sigma_y \leqslant 5 \times 10^{-16}$ [7–9]. For example, NPL can reach an accuracy of about 10^{-15} after a day of averaging [10] with an instability of 2.3×10^{-16} [9]. Trapped ion clocks have demonstrated comparable or lower levels of uncertainty. Furthermore, there is the potential to achieve much lower levels of uncertainty using optical transitions due to the higher frequency of the transitions used ($\nu_0 \sim 10^{15}$ Hz) compared to microwave transitions ($\nu_0 \sim 10^{10}$ Hz) [11]. Using optical transitions, i.e. the transitions between a ground state and an optically accessible, metastable excited state, instabilities down to 3×10^{-18} have been published using Yb^+ [12]. Furthermore, recent results have also shown instabilities $< 10^{-18}$ using Al^+ [13].

Trapped ions have also featured in quantum simulation [14, 15]. Richard Feynman initially postulated that an efficient way to model a quantum system would be to use another quantum system as opposed to a classical computer [16]. The process of using trapped ions as a simulator largely consists of three stages; the initialisation of a particular state, the time evolution of the system to be modelled and the read-out of the information of interest [14]. There are two distinct encoding methods for the evolution of the states of the ions. On one hand the evolution could be modelled using an analogue simulator, where the dynamical behaviour of the simulated Hamiltonian is mapped to a physically different but mathematically equivalent system [14]. Therefore the system is purpose built to solve a particular problem, or class of problems [17]. On the other hand, a more general method is to simulate a Hamiltonian as a sum of many local interactions [14]. Given that there is a universal set of quantum operations that can be performed on the many-body quantum system, the simulator could in principle be used to model

any local quantum system. This is effectively a universal approach and is often referred to as a digital quantum simulator [14, 17].

Proposals for the use of trapped ions as quantum simulators have been suggested for a number of applications such as modelling spontaneous symmetry breaking [18], relativistic quantum particles [19, 20], Hawking radiation [21, 22] and particle generation [23]. One example where ions have been used experimentally as both an analogue and digital quantum simulator is for spin systems. Spin systems are used for modelling magnetism in condensed matter physics, however it can be too computationally demanding to classically model systems even with a few tens of spins [14]. In addition it can be very challenging to model long-range interactions and spin frustration [24, 25]. The initial proof-of-principle experiment was done with two $^{25}Mg^{+}$ ions as an analogue simulator in 2008 [26]. Both digital and analogue simulators for a three spin system were developed [27, 28], and though the former offered better accuracy, the latter was simpler to implement and more straightforwardly scalable [29]. Since then the systems have been scaled further to probe the dynamics of a greater number of spins. In analogue simulators a string of 18 modelled spins using hyperfine states in $^{171}Yb^{+}$ ions were used to show how spin frustration can be controlled by tuning the anti-ferromagnetic interaction range [30]. These results have all been shown in radio-frequency traps (known as Paul traps) that confine ions in a linear string (see Section 1.2). However Britton et.al. in their benchmark paper bypassed the limit of a few tens of ions and modelled spin dynamics using hundreds of $^{9}Be^{+}$ ions in a Penning trap (which uses a combination of magnetic and static electric fields) [31]. For a digital simulator the scaling has been more modest and simulations using five [32] and six ions have been shown [17].

Perhaps one of the most salient applications for ion traps is in quantum information processing (QIP), which will be focused on in more detail in Section 1.1.

This thesis aims to highlight some of the developments in improving the performance of ion traps particularly for the application in QIP and quantum metrology with entangled states. This work is arranged as follows:

- *Chapter 1* Introduction to the principles of ion trapping in light of its main applications. In addition it will also cover an introduction into some of the limitations that ion traps face in the form of decoherence.

- *Chapter 2* Details of the ion trapping experimental setup that will form the context of the results presented.
- *Chapter 3* An explanation of the principles developed for surface processing with microplasmas in microfabricated ion traps. It describes how microplasma can be used to potentially remove surface contamination and reduce motional decoherence.
- *Chapter 4* The experimental investigation into the plasma parameters needed to quantify how effective the microdischarges from Chapter 3 might be.
- *Chapter 5* Included are updates to the experimental system (Chapter 2) in order to reduce the effect of decoherence from noise on the DC electrodes, magnetic-field noise and atom flux adsorbates. It will include three main topics, firstly updates to the control of the DC lines to the trap for reduced noise and improved connectivity. Secondly it will have a discussion of the magnetic-field noise present and methods for reducing it. It details a system for stabilising the current sources driving the magnetic field coils. Lastly, an automated procedure for the control of the Sr atom flux generated will be presented.
- *Chapter 6* A preliminary investigation into single and two-ion spectroscopy with a demonstration of single ion coherence.
- *Chapter 7* Conclusion and future work.

1.1 Quantum Computation with Ions

In conventional computers information is encoded in binary systems of 0s and 1s that form classical bits. These are inherently different from quantum mechanical bits (qubits) since qubits can involve superposition and entangled states. These properties enable a quantum computer (QC) to process a number of computational paths simultaneously and result in a final state that is dependent on the interference of these paths [33]. In effect, it allows for large scale parallelism and a speed-up for algorithms that are required to explore a vast number of computational paths simultaneously [1]. One of the foremost motivations for their development is in the implementation of Shor's algorithm; the factorisation of large numbers into primes which is a central problem in data security

[34]. Another potential application is for unstructured searches which leads to more efficient search algorithms than are possible with a classical computer [35]. These are a couple of instances in which a moderately sized QC will outperform even the largest of classical supercomputers [34, 36].

One of the most important considerations when using ions in the implementation of a QC is the choice of qubit. There are several ion species that have been used for QIP such as $^{25}Mg^{+}$, $^{40}Ca^{+}$, $^{43}Ca^{+}$, $^{88}Sr^{+}$, $^{111}Cd^{+}$, $^{137}Ba^{+}$, $^{171}Yb^{+}$ and $^{9}Be^{+}$ [37–44]. There are two distinct methods that have been explored when using an ion to encode a qubit [38]. One method uses optical qubits, where information is encoded in the ground and meta-stable excited state of an optical transition [36, 39]. Here manipulation of the qubit state is via a resonant light field provided by a laser. The other method uses ground state qubits that encode information in the hyperfine or Zeeman levels of the ground state of the ion [38, 45]. It requires either a two-photon stimulated Raman transition or direct microwave excitation in order to perform operations on hyperfine qubits.

DiVincenzo set a criteria to describe the requirements of a system that physically implements a QC [46]:

- *Scalable physical system with well characterised qubits.* For an ion-based QC, scalability implies the potential to incorporate more ions as quantum resources without compromising the gate fidelities. As the number of ions in the trap increases the mode spectrum density also increases. For N ions there are $3N$ modes which makes high fidelity quantum gates progressively more difficult. This is due to mode cross-talk and the distortion of the harmonic potential since the presence of the other ions result in a non-linear spacing of the motional energy levels [34]. To date, the largest number of ions that have been entangled is 20, where the experiment used $^{40}Ca^{+}$ optical qubits [47]. However, a useful QC for the applications of solving Shor's algorithm or for large database searches would require the control of thousands of qubits if not more [48]. A promising solution to this limitation is to use segmented traps that allow for shuttling of the ions between designated zones [48–52]. Section 2.3 will detail the segmented traps used in this work and compare traps with three trapping segments to the next generation with seven trapping segments and a spatially separated loading zone; suggesting the scalability of the design.

- *Ability to initialise the state of the qubit.* State initialisation is the process of preparing the register's input state in a deterministic fashion. Reliable preparation of the ion's state can be achieved using optical pumping. Initialisation of the target state has been demonstrated in trapped atomic ions with an error of 2×10^{-4} [3].

- *Long decoherence times compared to gate operation times.* The coherence time of a qubit refers to the length of time over which the information described by the state is preserved, despite interactions with the environment. More specifically it is the time in which the probability of retaining the state has decayed by $1/e$ [53]. Any physical realisation of a qubit has to have coherence times that are longer than the time needed for the computation. Coherence times with hyperfine qubits of greater than 10 minutes with $^{171}Yb^{+}$ have been measured [4], and around 100 ms for optical qubits [5]. Typically gate times are on the order of a hundred microseconds or less [5, 54, 55].

- *A universal set of quantum gates.* Sleator and Weinfurter showed that single qubit gates (rotations) in combination with the ability to implement a two qubit controlled-NOT (CNOT) gate is sufficient to build a quantum network [56]. A CNOT gate is a conditional correlation of two qubits such that if the control qubit is in the excited state $|e\rangle$ the state of the target qubit is flipped and if the control qubit is in the ground state $|g\rangle$ the target qubit is unchanged. A diagrammatic representation of the gate can be seen in Figure 1.1. A crucial element in the operation of the gate is the ability to correlate the states of the control and target bit; this equates to the ability to conditionally entangle the ions. Cirac and Zoller in their seminal work [33] proposed a method of implementing a CNOT gate using trapped ions and since then the implementation of the gate has shown to be successful [54, 57]. It involves using the Coulomb interaction between ions in a string in order to conditionally affect the state of the target qubit. Similarily, the geometric phase gate also uses the Coulomb repulsion between the ions in order to implement a conditional gate [55]. It applies an external force that is dependent on the electronic state of the ions, such that if they are in different states the stretch mode is excited but if they are in the same state there is no excitation [2]. Another method of entangling ions was proposed by Mølmer and Sørenson [58]. The Mølmer-Sørenson gate correlates the internal states of two ions in a method that is insensitive to their vibrational motion. This method

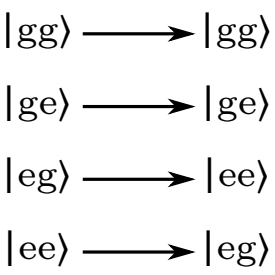

FIGURE 1.1: Diagrammatic representation of the logic for a CNOT gate using two ions that each have a ground $|g\rangle$ and an excited $|e\rangle$ state. If the control qubit (represented by the first letter in the ket) is in an excited state then the state of the target qubit (represented by the second letter in the ket) is inverted.

will be explained in more detail in Section 6.7. In the field of trapped ions, to date the lowest single-qubit gate error was reported to be 1×10^{-6} using hyperfine states in $^{43}Ca^{+}$ [3]. The lowest error for a two qubit gate was $\sim 1\times10^{-3}$ again using hyperfine states with $^{43}Ca^{+}$ and $^{9}Be^{+}$ [44, 59]. For optical qubits single and two-ion gates have be shown with errors of 3×10^{-3} and 7×10^{-3} [36, 60].

- *Qubit-specific measurement capacity.* The read-out of the state of an ion can be achieved by imaging the ion florescence in the implementation of Dehmelt's shelving technique [61]. Using this method ion state detection can be achieved with error rates of $\sim 5 \times 10^{-4}$ for hyperfine qubits [3] and $\sim 2 \times 10^{-4}$ for optical qubits [62]. There are a number of methods which accomplish this for several ions; for example to illuminate the entire string with the read-out laser and to image the fluorescence onto a CCD camera such that each of the ions can be spatially resolved [63, 64]. Other methods include focusing the read-out laser so that each ion can be individually addressed without disturbing their neighbours [39, 65], or shuttling the ions into the beam path of the laser [48].

In addition to the above, DiVincenzo set out two further requirements [46]:

- *The ability to convert between flying and stationary qubits.* This is possible with ions by storing them in high finesse cavities such that the ion's state (the stationary qubit) can be mapped onto a photonic state (the flying qubit) [2, 66, 67].
- *Faithful transmission of the flying qubit between specific locations.* The photon encoded with the qubit information can be transmitted through a fibre where it can then be coupled to an ion stored in another high finesse cavity [66, 67].

For practical applications of a QC not only do all of the DiVincenzo criteria have to be fulfilled but also fidelity and the speed of operations needs to be considered [2].

1.2 Linear Paul Traps

Paul traps are named after Wolfgang Paul who, along with Helmut Steinwedel, developed their first incarnation; a linear mass spectrometer [68]. Initially these devices were used to confine clouds of charged particles and they have since been adapted to isolate single charged particles in what is a good approximation of a harmonic potential.

There are several novel Paul trap geometries that have been developed [40, 48, 51, 52]. However the geometry that will be discussed for the purposes of this work is the quadrupole linear Paul trap, an example of which can be seen in Figure 1.2. This trap geometry uses a minimum of six electrodes. Four electrodes with RF on one diagonal set and the other grounded provide confinement in the radial direction and the last set are DC electrodes, otherwise known as the endcap electrodes, that provide the confinement in the axial direction. In this section all equations and further details can be found in reference [69]. The total potential near the trap centre can be described as

$$\Phi(x,y,z,t) = \frac{U_0}{2}(\alpha_x x^2 + \alpha_y y^2 + \alpha_z z^2) + \frac{U_{RF}}{2}\cos(\Omega_{RF} t)(\beta_x x^2 + \beta_y y^2 + \beta_z z^2) \quad (1.3)$$

where α_i and β_i with subscript $i \in x, y, z$ are constants. The first term in equation 1.3 accounts for the static component to the potential and the second term a time-dependent component that oscillates at the RF frequency Ω_{RF}.

The Laplace equation $\nabla^2\psi = 0$ applies the restriction that $\alpha_x + \alpha_y + \alpha_z = 0$ and $\beta_x + \beta_y + \beta_z = 0$. By using an oscillating electric field the Laplace equation is satisfied for all t, but if the frequency of oscillation is high enough then the ion will experience a time-averaged minimum potential and be trapped. In order to satisfy the Laplace equation the constants α_i and β_i in a linear Paul trap are set as follows

$$-(\alpha_x + \alpha_y) = \alpha_z > 0 \tag{1.4}$$

$$\beta_x = -\beta_y \tag{1.5}$$

$$\beta_z = 0. \tag{1.6}$$

From equation 1.3 the equation of motion in the x direction is

$$\ddot{x} = -\frac{Z|e|}{m}\frac{\partial \Phi}{\partial x} = -\frac{Z|e|}{m}x(U_0\alpha_x + U_{RF}\cos(\Omega_{RF}t)\beta_x), \tag{1.7}$$

where $Z|e|$ is the charge of the ion. This equation can then be expressed in the form of the Mathieu equations as

$$\frac{d^2x}{d\zeta^2} + (a_x - q_x\cos 2\zeta)x = 0, \tag{1.8}$$

by using the following substitutions

$$\zeta = \frac{\Omega_{RF}t}{2}, a_x = \frac{4Z|e|U_0\alpha_x}{m\Omega_{RF}^2}, q_x = \frac{2Z|e|U_{RF}\beta_x}{m\Omega_{RF}^2}. \tag{1.9}$$

The first order solution to this equation is

$$x(t) \approx 2A_xC_0\cos(\omega_x t + \phi_x)\left(1 - \frac{q_x}{2}\cos(\Omega_{RF}t)\right) \tag{1.10}$$

here A_x and ϕ_x are an amplitude and phase that are dependent on the initial conditions of the system and C_0 is a coefficient dependent on a_x and q_x. The parameter ω_x is

$$\omega_x = \frac{\Omega_{RF}}{2}\gamma_x \tag{1.11}$$

which is the frequency of the harmonic oscillations of the ion in the x direction. The parameter γ_x is a function of the stability parameters a_x and q_x and to the lowest order and in the case of $|a_x|, q_x^2 \ll 1$ can be approximated to

$$\gamma_x \simeq \sqrt{a_x + \frac{q_x^2}{2}}. \tag{1.12}$$

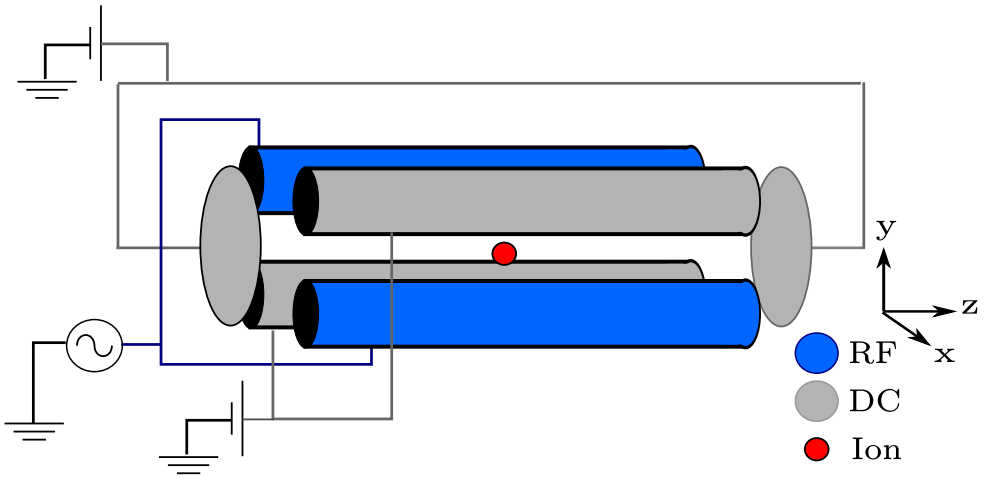

FIGURE 1.2: Example of a Paul trap with a linear quadruple electrode structure for ion trapping.

Equation 1.10 distinguishes between two types of motion. Firstly the harmonic oscillations of the ion referred to as the secular motion, and secondly the driven motion of the ion due to Ω_{RF} which is referred to as micromotion. Micromotion is driven by the applied RF field and is minimised at the RF null. However static fields can cause the ion to be displaced from the RF null causing excess micromotion. The methods employed in this work to correct for this effect will be discussed in Section 2.8.4.

1.3 Laser-Ion Interactions

1.3.1 The Optical Qubit Transition

As described in Section 1.2 the ion is confined in a potential close to the ideal harmonic form. Though there are three modes of motion, here the discussion is restricted to the centre-of-mass (COM) mode along the z-axis. The two levels of the qubit will be described as $|g\rangle$ for the ground state and $|e\rangle$ as the excited state. The laser radiation is described as a monochromatic light wave $\vec{E} = E_0\vec{\epsilon}\cos(k_z z - \omega_L t + \phi)$, with amplitude E_0, polarisation vector ϵ, phase ϕ, k_z as the projection of the wave vector onto the z-axis and the interaction with the ion is at position z and time t.

To describe the interaction of the laser field and the ion, the total Hamiltonian H can be divided in two parts: a stationary part representing the trapped ion without the presence of the light field H_0 and the time-dependent part that describes the interaction H_I [69, 70]

$$H = H_0 + H_I. \tag{1.13}$$

Here H_0 is the ion in the trap system i.e. it represents the two-level internal electronic transitions and the motional energy due to the harmonic potential, and is given by

$$H_0 = \frac{\hbar\omega_0}{2}\sigma_z + \hbar\omega_z\left(a^\dagger a + \frac{1}{2}\right). \tag{1.14}$$

ω_0 and ω_z are frequencies associated with the two-level electronic transition and the axial trap frequency respectively. The Pauli operator is denoted by σ_z and the creation and annihilation operators are a and $a^\dagger$ respectively. The interaction Hamiltonian of the ion with the light field H_I [69] is

$$H_I = \frac{\hbar\Omega}{2}(\sigma^+ + \sigma^-)\left(e^{i(k_z z+\omega_L t+\phi)} + e^{-i(k_z z+\omega_L t+\phi)}\right), \tag{1.15}$$

where Ω is the Rabi frequency that specifies the interaction strength between the light field and the ion, and σ^+ and σ^- are the atomic transition operators. Transformation into the interaction picture can further simplify equation 1.15 by applying the unitary operator $U_0 = exp(-iH_0t/\hbar)$

$$H_{int} = U_0^\dagger H_I U_0 = \frac{\hbar\Omega}{2}\left(\sigma^+ e^{-i(\delta t-\phi)} e^{i\eta(ae^{(-i\omega_z t)}+a^\dagger e^{(i\omega_z t)})} + H.c.\right). \tag{1.16}$$

Note that in equation 1.16 the rotating wave approximation has been applied which neglects the $\omega_L + \omega_0$ terms [69, 70]. In addition, $\delta = \omega_L - \omega_0$, and the Lamb-Dicke parameter η is given by [69, 70]

$$\eta = k_z\sqrt{\frac{\hbar}{2m\omega_z}}, \tag{1.17}$$

which characterises the extent of the ion's ground state wavefunction along the z-axis in relation to the laser wavelength.

When ions are cooled to the extent that their motional quantum number n is low enough so that the condition

$$\eta\sqrt{2n+1} \ll 1 \tag{1.18}$$

holds, the ion is said to be confined in the Lamb-Dicke regime [70]. This is the regime where the spatial extent of the ground state wavefunction is well localised over the laser wavelength. The Hamiltonian in equation 1.14 shows that the internal states are dressed by the harmonic vibrational levels imposed by the trap. The laser-ion coupling strength is dependent on the ion motional quantum number. For a resonant transition between the n' and n motional states the laser-ion coupling on the mth sideband where $m = n' - n$ is [69]

$$\Omega_{n',n} = \Omega e^{-\eta^2/2} \sqrt{\frac{n_<!}{n_>!}} \eta^{|m|} L_{n_<}^{|m|}(\eta^2), \tag{1.19}$$

where the larger (smaller) of n' and n is denoted by $n_>$ ($n_<$) and $L_n^{|m|}$ is the generalised Laguerre polynomial [69].

$$L_n^m(x) = \sum_{k=0}^{n} (-1)^k \frac{(n+m!)}{(n-k)!(m+k)!k!} x^k. \tag{1.20}$$

Within this work three transitions are of particular interest:

- *Carrier Transition*

  The detuning $\delta = 0$ and there is no change in n (black arrow in Figure 1.3) as the ion is excited between states $|g\rangle$ and $|e\rangle$. The Hamiltonian for the carrier transition is

  $$H_{car} = \frac{\hbar\Omega}{2}\left(\sigma^+ e^{i\phi} + \sigma^- e^{-i\phi}\right), \tag{1.21}$$

  where the Rabi frequency that characterises the frequency at which the population is exchanged between the two levels is (to second order) [69, 71]

  $$\Omega_{n,n} = \Omega(1 - \eta^2 n) \tag{1.22}$$

- *Red sideband Transition*

  The case where $\delta = -\omega_z$ and there is a decrease in n by one as the ion transitions to the excited state, therefore $|g\rangle|n\rangle \rightarrow |e\rangle|n-1\rangle$ (represented by the red arrow in Figure 1.3). The red sideband Hamiltonian is

  $$H_{rsb} = \frac{\hbar\Omega}{2}\eta(a\sigma^+ e^{i\phi} + a^\dagger \sigma^- e^{-i\phi}), \tag{1.23}$$

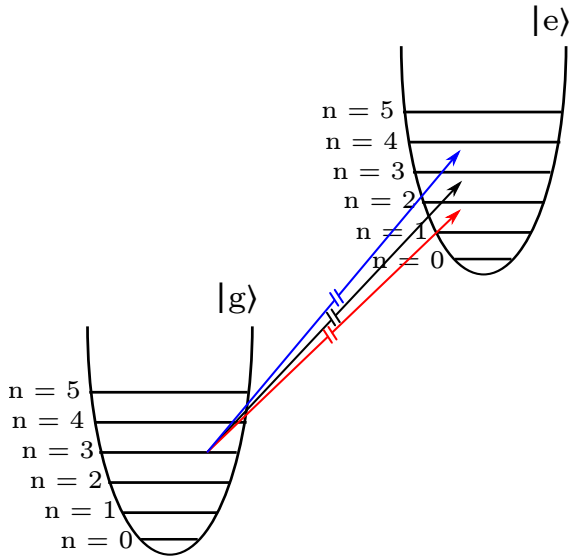

FIGURE 1.3: Optical qubit transition from the ground $|g\rangle$ to the excited $|e\rangle$ state dressed by the harmonic motional levels of the ion in the trap in one dimension. An example of a carrier transition ($|n\rangle|g\rangle \rightarrow |n\rangle|e\rangle$) between these states is denoted by the black arrow and the blue ($|n\rangle|g\rangle \rightarrow |n+1\rangle|e\rangle$) and red sideband ($|n\rangle|g\rangle \rightarrow |n-1\rangle|e\rangle$) transitions are denoted by the blue and red arrows respectively.

with a Rabi frequency that can be written as

$$\Omega_{n,n-1} = \Omega\eta\sqrt{n}. \tag{1.24}$$

- *Blue sideband Transition*

  The detuning $\delta = \omega_z$ and there is a increase in n by one, i.e. $|g\rangle|n\rangle \rightarrow |e\rangle|n+1\rangle$ (represented by the blue arrow in Figure 1.3). The Hamiltonian for this transition is

$$\frac{\hbar\Omega}{2}\eta(a^\dagger\sigma^+ e^{i\phi} + a\sigma^- e^{-i\phi}), \tag{1.25}$$

  with a Rabi frequency that can be written as

$$\Omega_{n,n+1} = \Omega\eta\sqrt{n+1}. \tag{1.26}$$

1.3.2 Laser Cooling

Laser cooling is used to reduce the kinetic energy of the ion in the trap, ideally to the ground state of the harmonic potential. The cooling dynamics are largely controlled by three paramenters: the ion's motional frequency ω_i ($i \in x, y, z$), the linewidth of the

electronic transition Γ and the photon recoil frequency $\omega_R = \hbar k^2/(2m)$. The ratio of Γ/ω_i can be used to define two different regimes

- $\Gamma > \omega_i$ is the weak confinement regime where the sidebands of the electronic transition are not resolvable since the linewidth of the transition is too broad. This is the regime where Doppler cooling is used.
- $\Gamma < \omega_i$ is the strong confinement regime where the cooling transition is sufficiently narrow that the sidebands can be resolved. In this regime the equations 1.21, 1.23 and 1.25 are applicable and resolved sideband cooling can be implemented.

Doppler Cooling

For an ion that is illuminated with monochromatic light that is red-detuned by δ from its electronic transition ω, the Doppler shift from the velocity of the ion travelling towards the laser source can compensate for the detuning. This results in the ion transitioning to an excited state which is then reversed due to spontaneous emission. When the photon is adsorbed the ion receives a momentum impulse that is contrary to its direction of motion. The reduction in the ion's momentum is $\hbar k = \hbar(\omega - \delta)/c$. However since the spontaneous emission is symmetric, the net result of averaging over a number of absorption-emission cycles is deceleration of the ion. The limit of cooling with this method is set by the spontaneous emission, since ion receives a momentum kick of $\hbar k$ in a random direction and therefore can be calculated by considering the ion performing a random walk in momentum space.

The minimum temperature that is achievable T_D is in the case of a laser beam red-detuned to half the linewidth of the transition $\delta = -\Gamma/2$, [72, 73]

$$T_D = \frac{\hbar\Gamma}{2k_B} = \left(\bar{n}_{min} - \frac{1}{2}\right)\frac{\hbar\omega_i}{k_B} \tag{1.27}$$

per motional degree of freedom, where $\bar{n}_{min}$ is the minimum mean motional quantum number of the ion. Equation 1.27 is referred to as the Doppler limit [73].

By way of example, using $^{88}Sr^+$ the most suitable transition for Doppler cooling is the $^2S_{1/2} - ^2P_{1/2}$ which has a linewidth of 20.2 MHz [74]. For a trapped ion with axial and radial frequencies $\omega_z = 2\pi\times0.85$ MHz, $\omega_{r1} = 2\pi\times1.88$ MHz and $\omega_{r2} = 2\pi\times2.16$ MHz the mean vibrational quantum numbers are $\bar{n}_{min,z} = 11.4$, $\bar{n}_{min,r1} = 4.9$ and $\bar{n}_{min,r1} = 4.2$.

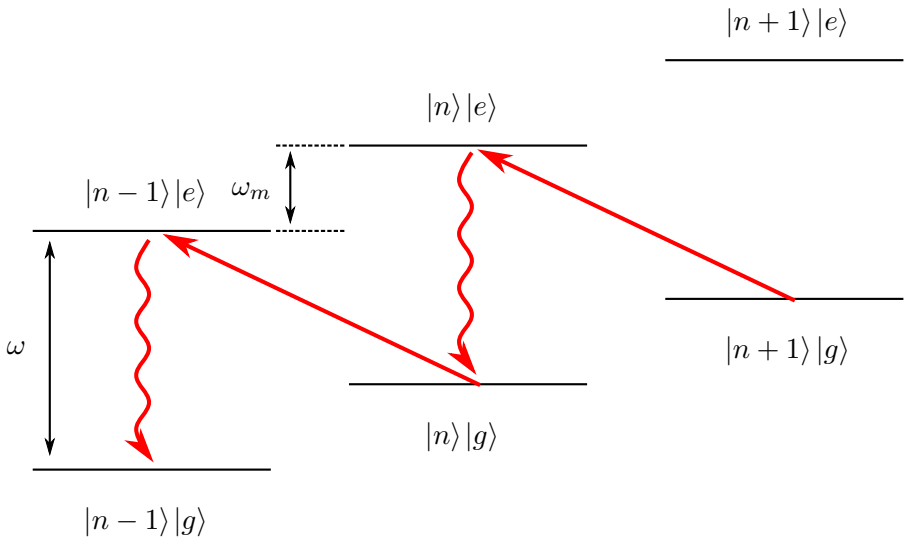

FIGURE 1.4: Schematic of resolved sideband cooling. The excitation to the $|e\rangle$ state on the red sideband reduces the motional quantum number n by one (denoted by the straight red arrow). Spontaneous emission then causes the state to decay to the ground state $|g\rangle$ (denoted by the red wiggly arrow).

Resolved Sideband Cooling

After Doppler cooling the ion into a low motional state, the ion can then be cooled into the ground state using resolved sideband cooling [69]. If the ion is in the Lamb-Dicke regime, a laser can be used to drive the lower sideband of the electronic transition, after which the ion decays to the ground state on the carrier transition with a high probability. On average the ion loses a quantum of vibrational energy on each adsorption-emission cycle. The process is illustrated in Figure 1.4.

For transitions with a long lifetime, the wait for the spontaneous decay can severely affect the cooling of the ion. It can either make cooling the ion a highly inefficient process, or if the heating rate is greater than the cooling rate, an ineffective process. It is necessary to shorten the lifetime of the excited state by coupling it to an auxiliary short-lived state with an additional laser. This is called quenching and it results in the effective linewidth $\widetilde{\Gamma}$ [69]

$$\widetilde{\Gamma} = \frac{\Omega_{aux}^2 \Gamma^2}{(\Gamma + \Gamma_{aux})^2 + 4\delta_{aux}^2} \tag{1.28}$$

where Ω_{aux}, Γ_{aux} and δ_{aux} are the Rabi frequency, the linewidth and the detuning associated with the auxiliary transition respectively.

A robust method for determining $\bar{n}$ after the cooling process is to compare the probabilities of the excitation on the red and blue sideband transitions. As derived in [69] the probability of excitation of the ion on the red sideband $P_e^{rsb}(t)$ is [69]

$$P_e^{rsb}(t) = \frac{\bar{n}}{\bar{n}+1} P_e^{bsb}(t) \tag{1.29}$$

where $P_e^{bsb}(t)$ is the probability of excitation on the blue sideband. The ratio of the two probabilities R is [69]

$$R = \frac{P_e^{bsb}(t)}{P_e^{rsb}(t)} = \frac{\bar{n}}{\bar{n}+1} \tag{1.30}$$

such that the mean vibrational number can be calculated using [69]

$$\bar{n} = \frac{R}{1-R}. \tag{1.31}$$

Therefore $\bar{n}$ can be determined by a frequency scan over the red and blue sidebands and by measuring the amplitude of each.

1.4 Decoherence

An upper bound to the achievable coherence time for a qubit is given by the natural lifetime of the excited state. For optical qubits, the lifetime of the excited state can be about a second as in the case of $^{40}Ca^{+}$ [75] and for hyperfine transitions the time constant for spontaneous emission can be longer than a year [2]. However there are other environmental factors that result in the loss of the information encoded in the state of the ion, i.e. causes decoherence. The sources of decoherence can be divided into three categories [76]:

- Motional decoherence
- Decoherence of the ion's internal electronic levels
- Non-ideal field decoherence

Each of these sources will be briefly reviewed and the reader is referred to [76] for a more detailed description of decoherence mechanisms.

1.4.1 Motional Decoherence

From Section 1.3 it is clear to see that the Rabi oscillations that can be driven coherently depend on the motional quantum number n. As $\bar{n}$ increases it leads to a greater thermal distribution in the ion's vibrational state. If the motional heating rate $\dot{\bar{n}}$ is on a time scale that is relevant to the operation time, for example the gate time in a QIP application, then there is then a dephasing of the coherent transitions between states. For quantum error correction techniques to be effective, the heating rate has to be low enough such that the error of the gate operation is below 10^{-4} [2].

When the ion is trapped there are large electric fields that provide the confinement, however there can also be residual fluctuating electric fields within the environment as well. These smaller fields can resonantly couple to the motion of the ion and cause an increase in its motional state. The subset of noise that directly affects the state of the ion can be quantified by the electric-field noise spectral density $S_E(\omega)$. The rate of increase in the motional quanta of the ion $\dot{\bar{n}}$ is related to $S_E(\omega)$ by [77]

$$S_E(\omega) = \frac{4M\hbar\omega}{q^2}\dot{\bar{n}} \tag{1.32}$$

where q and M is the charge (in C) and mass of the ion (in kg) respectively and ω is the angular motional frequency of the ion (in rads^{-1}). One source of the residual fields that can heat the ion is Johnson noise, which is the noise associated with the thermal motion of the electrons inside the conductors of the system [2, 78]. In order to reduce the injected noise from electronic sources it is desirable to filter the electrodes from the rest of the environment [76, 79–81] or employ an active stabilisation [82]. The exact nature and scaling of the Johnson noise will vary with with each system and be a function of how effective the filtering is at the motional frequencies of the ion. Section 5.2.3 describes the updates to the experimental system to include a set of passive filters to reduce the noise on the DC ion trap electrodes.

Several in-depth studies on the electric-field noise spectral density that the ion sees indicate that the noise scales with the ion-electrode distance d as $\approx 1/d^{3.79}$ [77, 83–86]. Ions in microfabricated traps [83] can have ion-electrode distances typically in the range of 80 μm $\leq d \leq$ 250 μm, which makes them particularly sensitive to the observed noise compared to macro-traps which can be 400 μm $\leq d \leq$ 800 μm [54, 87, 88]. The observed

heating rate dependency is significantly above what would be expected from Johnson noise. For example, in traps at room temperature with $d \leqslant 365$ μm the ion heating rate has been shown to be greater than three orders of magnitude above what would be expected from the electrical characteristics of the system [76, 77]. Since the exact origins of this noise is ambiguous, it has often been dubbed 'anomalous heating' [77]. When trap electrodes are cryogenically cooled (down to 4 K) the heating rate was reduced by over two orders of magnitude [89]. This suggests that the origin of the anomalous heating is a thermally activated process.

One candidate for the source of anomalous heating is surface contamination. Models have shown that the scaling of the heating rate with d can be replicated by randomly distributed fluctuating patch potentials [77, 84]. The patch potentials can be formed by contamination on the electrode surface, which are effectively uncorrelated dipoles that oscillate at a frequency which is resonant with the motion of the ion, causing motional heating. In addition to this theoretical framework, experiments have also indicated that surface contamination may have an adverse affect on ion heating. Through the use of Auger spectroscopy, studies have also determined that hydrocarbon monolayers can form on the electrode surfaces [90, 91]. After fabrication, traps are usually cleaned with some combination of solvents, ozone or plasma processing. However when exposed to the atmosphere several layers of adsorbates will still build up on the surface [92]. To achieve atomically clean electrodes in ultra-high vacuum there are a number of methods that can be used, for instance ion bombardment. Previously, an Ar^+ ion beam has been used to sputter the contamination of the electrodes in a surface trap [90, 91] and the heating rate was reduced by two orders of magnitude [90]. Though this method proved to be effective, it does add a significant engineering complexity to the trapping system and it is also problematic for traps with a 3D structure. Since the ion beam can be highly energetic (500 to 2000 eV) when compared with the sputtering threshold of the electrode material (Au is 15 eV with Ar^+), it is likely that the electrode material will be removed. Redeposition of the electrode material on dielectric surfaces, which are intended as insulating gaps in the electrode structure, risks the formation of an electrical short.

A gentler ion bombardment treatment has also been tested by generating an inductively coupled plasma using a coil located in close proximity to the trap [93]. The ion energy was approximately 20 eV and when compared to the 30 eV sputtering threshold of the

Nb electrodes it suggests that there should be no sputtering of the electrode material. Using this process there was a four-fold reduction in the heating rate. A possible method which does not require the need for a copper coil in the system will be introduced in Chapter 3 and 4; it will investigate the use of a capacitively coupled microdischarge generated *in situ* by the trap electrodes themselves. It will be shown that this method is suited for removal of hydrocarbon contamination and is unlikely to sputter the Au electrode material.

Another technique that has also been used for selective removal of contamination was pulsed laser cleaning [92]. It operates on the similar principle to that of the inductively coupled plasma; it uses the fact that the energy density threshold for the desorption of the surface contaminants is lower than the threshold for ablation of the electrode material [92]. Therefore a pulsed laser could remove the contamination from the surface while in principle keeping the electrodes intact. With laser cleaning of an Al microfabricated surface trap, the heating rate was reduced by a factor of two [92]. However, during the cleaning process the laser can introduce some unwanted effects; local heating of the metal surface, and the differential expansion associated with it, can lead to delamination of the electrode from the substrate.

1.4.2 Decoherence of the Ion's Internal Electronic state

Uncontrolled fluctuation of magnetic fields is a possible source for internal state decoherence [76]. Even when using 'atomic clock' qubits that are insensitive to the magnetic field to first order, the state preparation and readout can still be dependent on the magnetic field [3]. Decoherence arises since the separation of the energy levels to be addressed are dependent on the magnetic field applied. Therefore magnetic-field noise can cause a dampening of the phase relation between the states.

A principal source of magnetic-field noise is at 50 Hz arising from the mains electricity supply. In order to compensate for this, techniques such as a feed-forward circuit to add an additional out of phase signal to the current coil can be used to cancel its effects [2, 94]. Or alternatively, the experimental sequence can be synchronised with the 50 Hz power cycle in order to reduce the influence of the magnetic field variations [2, 36, 95]. A more general method of protecting the system from magnetic field fluctuations is to use magnetic shielding which can attenuate the noise by ∼20-30 dB at room temperature

[96, 97]. Furthermore, for magnetic field fluctuations that are slow on the timescale of the gate operations performed, the system may be made more robust by employing spin echo techniques [98]: the flipping of the qubit state to reverse the precession such that a minimum error state is recoverable.

However, for many experiments, a well-defined magnetic field is still desirable within the shielding in order to lift the degeneracy of the ion's atomic levels. Often, magnetic coils are used to generate a field, however the current sources used to drive these fields can have noise present that is then converted to magnetic field fluctuations. Approaches to reduce this noise include using permanent magnets instead of coils [96] however this results in the loss of flexibility in tuning the size of the magnetic field. Alternatively superconducting coils could be implemented [99], however this would require cryogenic temperatures and therefore substantially increase the system complexity. An alternative stabilisation method will be presented in Section 5.3 that uses a feedback from stable resistors in order to stabilise the current sources to the magnetic field coils.

1.4.3 Non-Ideal Field Decoherence

Imperfections in the laser parameters that address the ion's transitions can also lead to decoherence. Typical candidates for the cause of decoherence are the finite linewidth of the laser and fluctuations in intensity.

Intensity fluctuations arising from laser power instability, or beam pointing instabilities with respect to the ion can alter the Rabi frequency and therefore cause amplitude dampening of the Rabi transitions between states. Stabilising the position of the beam can be done by using mechanically stiff mounts or using a quadrant photodiode in a feedback loop to alter the position of the beam [76, 100].

The finite linewidth or Fourier components within the spectrum of the laser away from the transition of interest can lead to off-resonant excitation. Particularly when attempting to excite a sideband transition, it is essential to minimise the interaction with the stronger carrier transition in order to maximise the coherence of the operation. Pulse-shaping can be used to reduce the amplitude of the Fourier components that are away from the desired transition. For example Blackman-shaped pulses have been used due to the high level of suppression of these unwanted components [36, 101], however there are a number of other functions that could be used for the same purpose [101].

Instabilities in the spectroscopy laser frequency can similarly cause a loss of ion coherence. For hyperfine qubits the frequency sensitivity of the transitions is often dominated by the frequency difference between the two Raman laser beams [76]. Each of the lasers can be derived from the same source with the use of frequency modulators. Therefore, the frequency fluctuations are dominated by those of the oscillators that drive the modulators. Typically these oscillators have high frequency stability and therefore are not a notable source of error [59, 76]. For optical qubits however, the narrow linewidth of the transition requires not only a narrow linewidth laser but also high frequency stability for coherent control of the ion's state. This can be achieved by locking to high-finesse cavities with high temperature and vibration stability, which can lead to relative frequency instabilities of $\sim 10^{-15}$ or less for 1 s averaging times [76, 102, 103].

Chapter 2

Experimental Setup

2.1 Introduction

This section will outline the experimental set up used in this work. The electronic levels of the $^{88}Sr^{+}$ used are highlighted in Section 2.2. The description of the two types of microtraps are in Section 2.3. This includes a three-segment trap and a seven-segment trap with additional purpose specific zones. The latter will be used in the ion trapping experiments relevant to Chapters 5 and 6, whereas both types are used in the microplasma research presented in Chapters 3 and 4. The rest of the sections within this chapter are specific to the ion trapping experiment. A separate test set-up was developed for the microplasma research in Chapter 4 and will be discussed therein. The vacuum system and the optical systems will be described in Sections 2.4 and 2.5. The programmatic control of the ion trapping experiment will be detailed in Section 2.6 and the trap drives in Section 2.7. Finally, some of the general experimental techniques will be discussed in Section 2.8.

2.2 $^{88}Sr^{+}$ Atomic Structure

This work will focus on $^{88}Sr^{+}$ as the ion species which can then be used to encode information in an optical qubit. Using this ion, the important transitions that need to be addressed can be seen in figure 2.1 and thus requires the corresponding lasers. A photoionisation procedure is used to generate the ions. Sr atoms are evaporated towards the trap from a hotplate and the combination of 461 nm and 405 nm lasers are used

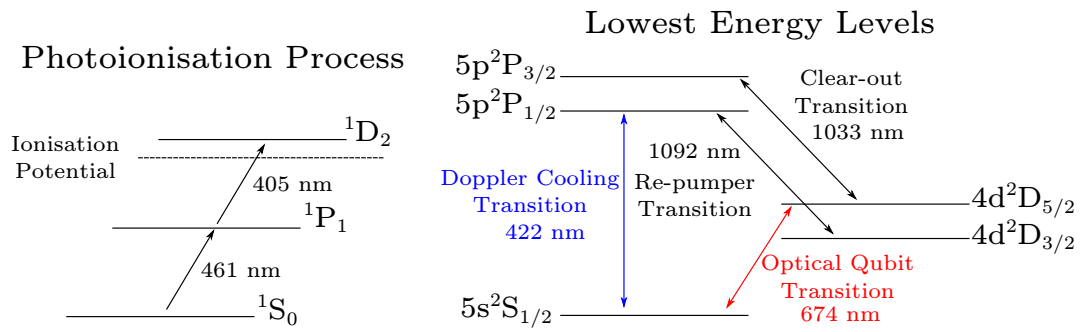

FIGURE 2.1: Internal electronic levels of $^{88}Sr^+$ with no bias magnetic field applied.

to photoionise the atoms which then can be trapped. Laser light at 422 nm is used to Doppler cool the ion to a low motional state on the Doppler cooling transition (see Figure 2.1). More detail on the Doppler cooling process will be provided in Section 1.3.2. Since the ion is initially hot when first trapped, there is inefficient laser cooling on the Doppler cooling transition due to the Doppler shifted-resonance. Therefore an off-resonant beam detuned by -170 MHz is used when initially trapping to more efficiently initiate the cooling process. The 1092 nm laser is also essential for effective Doppler cooling. The ion can decay from the $^2P_{1/2}$ state to the $^2D_{3/2}$ state which has a lifetime of 435 ms [104]. The 1092 nm re-pumper laser cycles the ion back in to the $^2P_{1/2}$ so that it can transition down to the $^2S_{1/2}$ state.

The quadrupole transition from the $^2S_{1/2}$ to the $^2D_{5/2}$ state which is driven using a 674 nm laser, is called the optical qubit or 'clock' transition. This transition effectively provides a two-level system for coherent operations and has a coherence time of 391 ms [105]. In order to remove the ion from the $^2D_{5/2}$ state, a 1033 nm laser is used excite the ion into the $^2P_{3/2}$ state on the clear-out transition.

The diagram in Figure 2.1 shows the energy levels in the presence of no magnetic field. However when a bias magnetic field is applied there is a spitting of the energy levels due to the Zeeman effect. The $^2S_{1/2}$ and the $^2D_{5/2}$ energy levels are split according to

$$\Delta E = \mu_B B m_j g_j, \tag{2.1}$$

where μ_B is the Bohr magneton, B is the magnitude of the applied magnetic field, m_j is the total magnetic quantum number and g_j is the Landé g-factor

$$g_j = \frac{3}{2} + \frac{S(S+1) - L(L-1)}{2J(J+1)}. \tag{2.2}$$

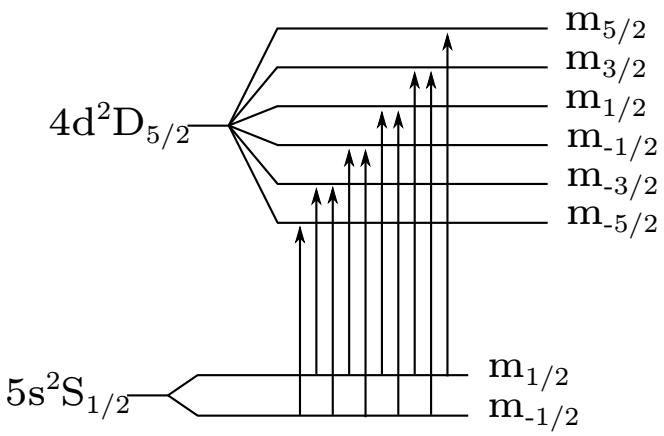

FIGURE 2.2: Schematic of the splitting of the $^2S_{1/2}$ and the $^2D_{5/2}$ energy levels into 10 Zeeman components due to the presence of an external magnetic field.

Here S, L and J are the spin, orbital and total angular momentum quantum numbers respectively. For the $^2S_{1/2}$ transition $g_{1/2} = 2$ and for $^2D_{5/2}$ $g_{5/2} = 26/5$. Equation 2.1 can then be rewritten as

$$E_{S-D} = \mu_B B(m_{1/2}g_{1/2} - m_{5/2}g_{5/2}). \tag{2.3}$$

Figure 2.2 shows a schematic of these energy levels in an external magnetic field.

2.3 Microfabricated Linear Ion Traps

The ion traps used in this work are microfabricated, monolithic and symmetric in design [106]. To create the device, a 350 μm SiO_2-on-Si wafer is processed with metallisation and micro-machining in order to generate the aperture and electrode structure. More details on the microfabrication techniques used can be found in [107]. Figure 2.3a shows the cross-sectional view of the ion trap aperture with its electrode microstructure and its material system. The 3D trapping geometry has a unit aspect ratio which leads to a highly efficient trapping potential.

In this work two geometries of trap will be used, both of which share the same cross-sectional structure to the trapping aperture. The first design, denoted as trap type A, can be seen in Figures 2.3b and d. The device has a linear array of three trapping segments. The second ion trap geometry, hereafter trap type B, can be seen in Figures 2.3c and e. This design is a scaled version of trap type A with a more sophisticated structure. It includes seven trapping zones and a spatially separated ion loading zone. Figure 2.4 is

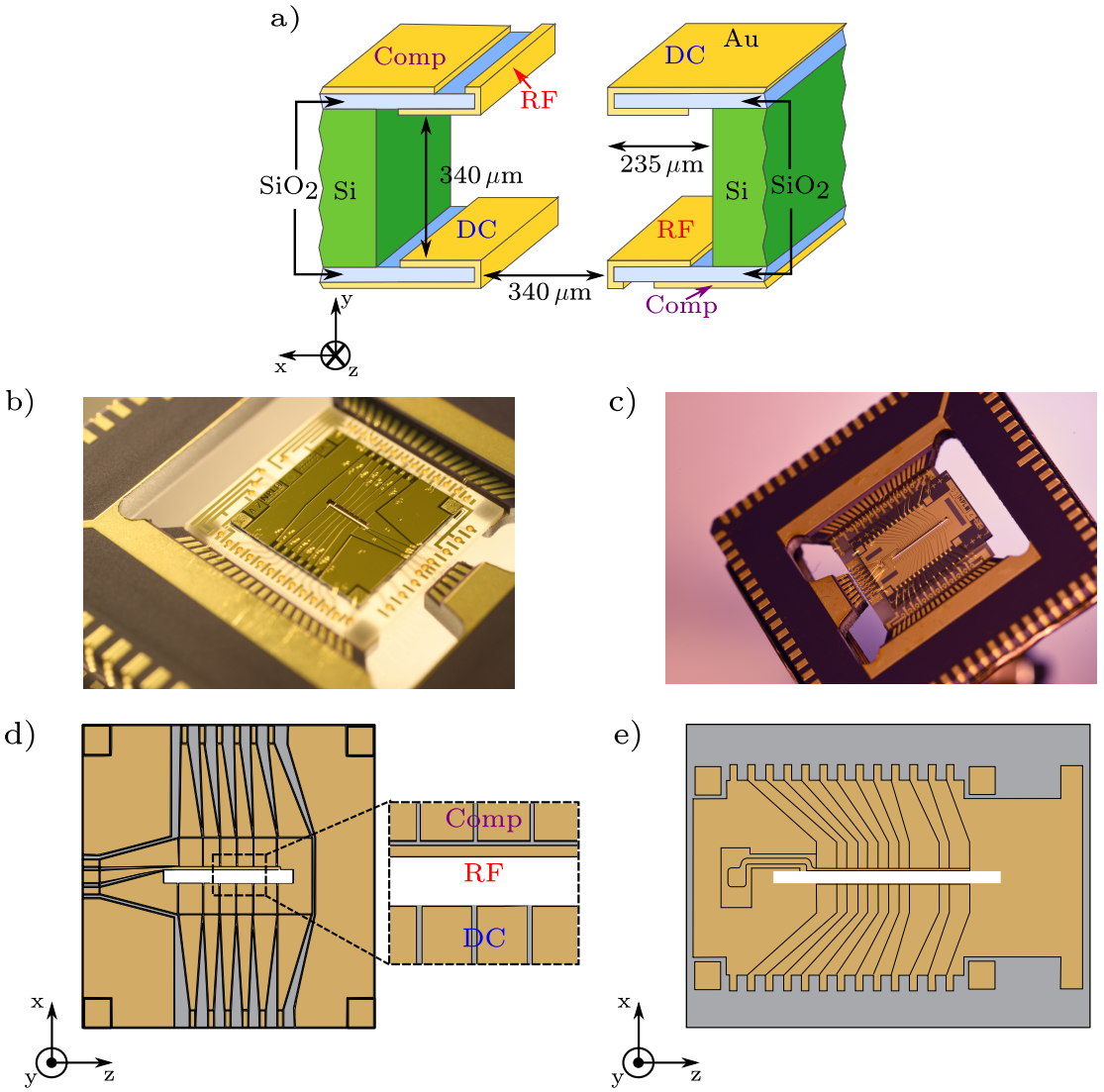

FIGURE 2.3: a) Schematic diagram of ion trap cross-sectional structure and material system. The cross-section is common to both ion trap types A and B. b) Example of ion trap type A in an electronic package. c) Example of ion trap type B in an electronic package. d) Front-side electrode layout for trap type A. The magnified inset shows the detail for the RF and DC electrodes surrounding the trapping aperture. Rotating the image by 180° would result in the layout for the back-side of the trap. e) Front-side electrode layout for trap type B, as in d) the layout on the back-side is identical.

a schematic of the electrode structure of trap type B. The diagram highlights how the loading zone 'L' is separated by an elongated electrode 'T', which is the transfer zone, from the zones '1-7' which are experimental zones. Mounted to the trap package is an atomic flux shield that restricts the flux of Sr atoms to the loading zone only. Pictures of the implemented shielding can be seen in Figure 2.5. The flux of Sr atoms can build up on the electrode surfaces of the ion trap over time and increase the ion's motional heating rate. Therefore as Z1 to Z7 are shielded from the flux they provide a low-noise environment for the atom and will be the segments that are used for coherent control of

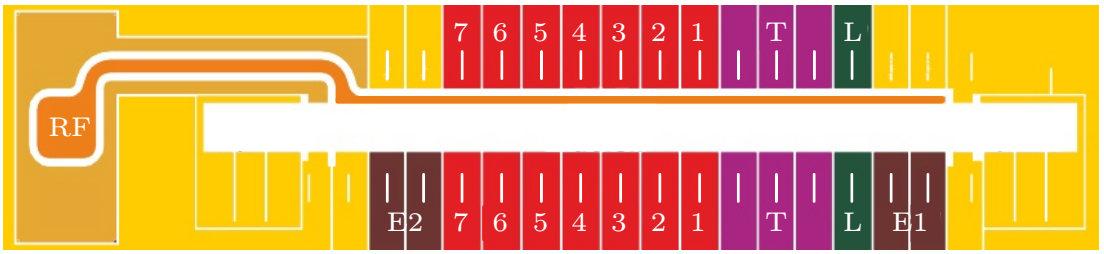

FIGURE 2.4: Schematic of trapping segments in trap type B. The endcap electrodes are denoted by 'E1' and 'E2', loading zone by 'L' the transfer zone by 'T'. The transfer zone spatially separates the experimental zones '1-7' from the loading zone.

a) b)

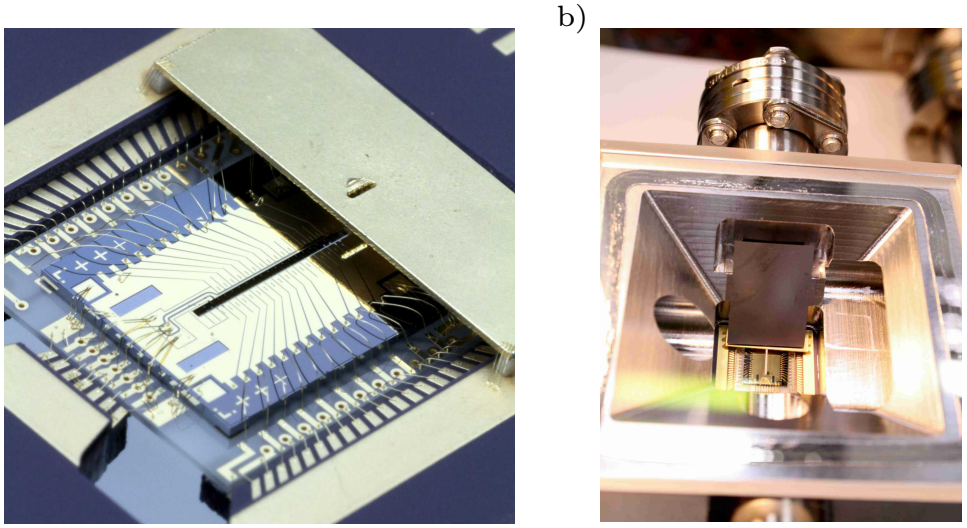

FIGURE 2.5: a) Picture of the ion microtrap with the on-chip atomic flux shield in place. b) Picture of the an ion microtrap within the vacuum system. An added shield to the vacuum system restricts the atomic flux from the electrodes that the on-chip shield does not cover.

the ions.

The fabricated traps are glued and wirebonded into robust electronic packages that standardise connectivity and enable them to be easily handled. The traps are mounted on a commercial leadless-chip carrier (LCC) via an aluminium-nitride (AIN) intermediate substrate. Wirebonds connect the electrodes of the trap on the front and the back side of the chip to the AIN substrate and again from the substrate to the LCC. The LCC then provides the air-side electrical connectivity (see Section 2.4 for more details).

2.4 Vacuum System

In order to seal the trap in ultra-high vacuum (UHV), cold welded indium seals are used. One seal is used from the LCC to the stainless steel vacuum, another from the LCC to a

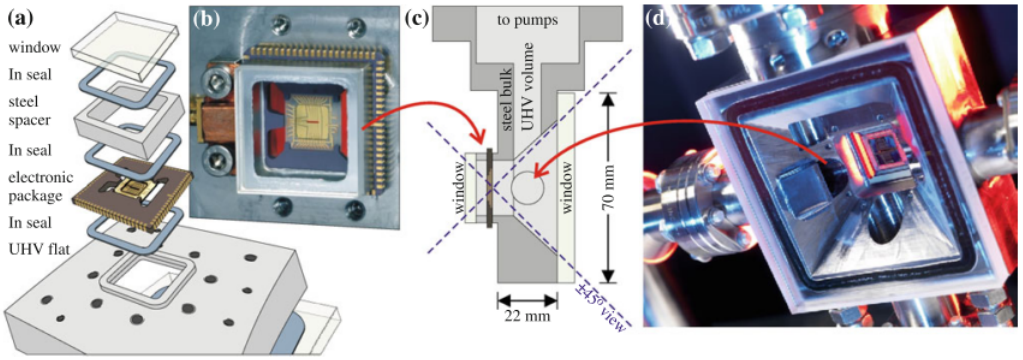

FIGURE 2.6: UHV packaging of ion microtrap. a) Detail pf the layers that form the bonding of the trap package to the vacuum chamber and to a window. b) View of the trap from the small window once welded to the chamber. c) Cross-section of the optical access provided by the windows either side of the trap aperture. d) View of the trap from the large window. Image taken from: [106]

steel spacer and again from the spacer to an anti-reflection coated window. An exploded view of the stack can be seen in Figure 2.6a. Figures 2.6b-d show how the windows that are at both faces of the trap provide the optical access. This sealing method, in conjunction with a non-evaporable getter and ion pump, allows for pressures of about 1×10^{-11} mbar. Another benefit of this method is that there is direct and efficient air-side access to the trap electrodes on contacts which are approximately 20 mm from the trap centre. Therefore all the electronic filtering can be done close to the trap electrodes but outside of the vacuum itself; see Chapter 5 for more details.

2.5 Optical systems

2.5.1 461 nm & 405 nm Photoionisation Laser

The first photoionisation step from the $^1S_0$-$^1P_1$ transition is achieved using 461 nm light. The laser light is formed by a frequency-doubling cavity in conjunction with an extended -cavity diode laser (ECDL) at 922 nm [108]. The ECDL emits up to 35 mW of light, some of which is picked off to go to the wavemeter and the rest is converted into 461 nm by a doubling cavity containing a potassium niobate crystal ($KNbO_3$). One of the cavity mirrors is on a piezoelectric mount that is used to fine tune the cavity length. The cavity length is maintained on resonance with the laser fundamental frequency by using a Hänch-Couillaud polarisation lock [109]. The cavity emits up to 2 mW of laser light which is coupled into a polarisation maintaining (PM) fibre that goes to the trap.

The fibre emits 600 μW of power and has a spot size of $2\omega_0 = 200$ μm at the trap centre. The laser frequency has sufficient passive stability and therefore no to active feedback is required. The wavemeter monitors the wavelength and a mechanical shutter at the PM fibre input is used to control the switching on and off of the beam in the trap aperture.

The second ionisation step involves exciting the atom from the $^1P_1 -^1 D_2$ state where a valence electron is then excited past the ionisation threshold to produce $^{88}Sr^+$. Due to the broad linewidth of the transition (0.9 nm) no stabilisation of the laser frequency is necessary. The laser emission propagates through the same fibre as the 461 nm light and also subject to the same switching via the mechanical shutter.

2.5.2 422 nm Cooling Laser

The Doppler cooling is derived from a Toptica diode laser (DL-pro) which emits 54 mW of light at 843 nm. Some light is picked off from the main beam and sent to a tunable etalon (finesse = 115) and the wavemeter. The etalon reduces the drift in the frequency of the laser via a side fringe lock. The light in the main beam (34 mW) is then focused into a doubling cavity in a similar fashion to the 461 nm laser, see Section 2.5.1, which produces up to 8 mW of light at 422 nm. From the doubling cavity the 422 nm light is split into three branches. One branch is double passed through an AOM (270 MHz) the down shifted light is locked to an Rb atomic vapour cell using a saturated absorption lock. The error signal from this lock is used to adjust the tuneable etalon. The Rb cell provides an atomic reference that provides the long-term laser stability [110].

At the 422 nm output another branch is used for the Doppler cooling light which goes through two douple-pass AOMs and is coupled into one of the inputs to a PM 2 x 4 fibre splitter. After the first pass of the first AOM some of the light is picked off and used for the second input to the fibre splitter; this light is used for the off-resonant Doppler cooling beams. The third branch of the 422 nm light is similarly passed through two AOMs and into another PM fibre and is used for the optical pumping beam. More details about the system can be found in [111].

To summarise, there are three main uses for the 422 nm light generated by this system;

- 3 Off-resonant beams for efficient Doppler cooling of hot ions. Each with $\sim$8 μW and waist $2\omega_0 = 70$ μm at the ion.

- 3 Near-resonant beams for Doppler cooling. Each with $\sim$2 μW and waist $2\omega_0 = 70$ μm at the ion.
- An optical pumping beam with 0.6 μW and waist $2\omega_0 = 70$ μm at the ion.

2.5.3 1092 nm Repumper Laser

The 1092 nm laser is used to excite the atom from the $^2D_{3/2}$–$^2P_{1/2}$ state to ensure efficient Doppler cooling. A neodymium doped fibre is used as a gain medium and is pumped with a 825 nm diode laser. A diffraction grating is used to reflect the light back into the fibre such that it forms a laser cavity. A paddle polarisation controller is used to adjust the polarisation of the light to the angle at which the grating is maximally reflective. The output of the laser has a large number of modes with 1 MHz separation under a $\sim$1.5 GHz wide envelope. The wavelength of the laser is not actively stabilised, since when one mode drifts out of resonance with the atomic transition the adjacent mode drifts into resonance. Very coarse adjustment of the wavelength is achieved by altering the angle of the grating by hand. Finer adjustment is implemented by changing the angle of the intra-cavity etalon and the finest adjustment by altering the angle of the diffraction grating via a piezo mount. The 1092 nm light is then split such that a small amount is picked off for a photodiode and the wavemeter. The photodiode is used to monitor the laser power. The main beam is coupled into a 1x2 fibre splitter with both fibre outputs focused on the trap aperture with a $2\omega_0 = 580$ μm. One 1092 nm beam passes through a polariser and a $\lambda/2$ waveplate. This beam is used to coarsely minimise the ambient magnetic field. The $D_{3/2}$ - $P_{1/2}$ transition splits into 6 Zeeman components in the presence of a magnetic field: two π components with $\Delta m_j = 0$ and four σ components with $\Delta m_j = \pm 1$. In the instance where the linear polarisation of the 1092 nm beam is parallel to the magnetic field direction, only the $\Delta m_j = 0$ transitions of the Doppler cooled ion are driven and the ion is optically pumped into a dark state. By altering the magnetic field such that the ion fluorescence is minimised for the vertical and horizontal polarisations of the 1092 nm beam, a coarse nulling of the magnetic field is attained.

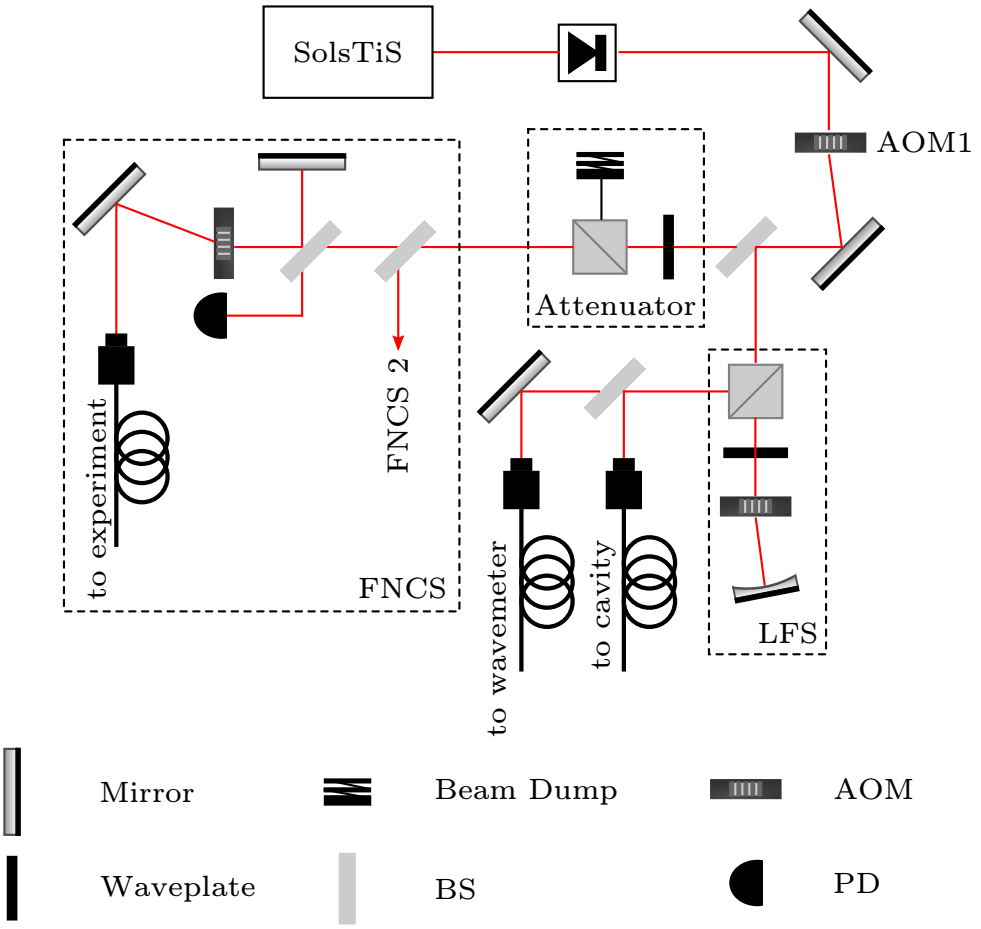

FIGURE 2.7: Schematic of the 674 nm spectroscopy laser. Note that here only one of the two fibre noise cancellation systems (FNCS) are depicted.

2.5.4 674 nm Spectroscopy Laser

An M Squared SolsTiS laser in conjunction with a Stable Laser Systems control system (SLS-674-300-1) is used to supply the 674 nm light to probe the optical qubit transition. The laser system is arranged in three levels. On the top breadboard level, there is an M-Squared SolsTiS laser, pumped by a Lighthouse Photonics Sprout laser. A small portion of the light is coupled into a high-finesse, optical reference cavity on the middle level. The middle level rests on a vibration isolation platform enclosed by sound isolation panels. The lower level, containing the control units, is floating off the main rack in order to provide a further level of isolation from potential vibrations.

The top breadboard level optics can be seen in Figure 2.7. The Sprout laser pumps the SolsTiS laser with 14 W of 532 nm light. The SolsTiS emits 1 W of 674 nm light to an optical isolator and a feedback AOM (AOM1). At this point 5 mW of light is then split off to the laser frequency shifter (LFS) and subsequently into fibres to the cavity and the

wavemeter. The main beam continues to an attentuator; formed from a $\lambda/2$ waveplate and a laser polariser and a beam dump. By adjusting the waveplate the laser power can be attenuated downstream. Once the beam is attenuated to the required levels the light is coupled into two fibre inputs. The reflections from each of the output of these fibres are used for the fibre noise cancellation system.

The LFS system is used to provide a fixed-frequency offset such that the light can be coupled to the cavity. The system comprises of a $\lambda/4$ waveplate, a focusing lens and a double pass AOM, and a curved mirror, as shown in Figure 2.7. The waveplate circularly polarises the incoming light which is then focused onto the AOM crystal. The curved mirror reflects the generated +1 order of frequency shifted light back through the AOM. The waveplate then vertically polarises the light and the PBS directs the frequency shifted beam to the cavity and wavemeter.

The laser is stabilised to to the cavity using a Pound-Drever-Hall lock [112]. The light from the top level passes through an electro-optical modulator and output from the fibre towards the cavity with horizontal polarisation. The beam is then coupled into the cavity through a PBS and a $\lambda/4$ waveplate. After the light has been reflected twice through the $\lambda/4$ waveplate the polarisation of the light is shifted by 90°. The now vertically polarised light passes through the PBS cube and is directed on to the Stable Laser Systems PDH detector. A Vescent Laser Servo (D2-125) stabilises the laser frequency by either feeding back to AOM1 in Figure 2.7 for high frequency corrections, or to two piezos within the SolsTiS to remove slower drifts in frequency. The cavity is kept under vacuum (10^{-7} mbar) and the temperature of the cavity and the vacuum housing are both stabilised. Two Wavelength Electronics (LFI-3751) temperature controllers are used to keep the temperature of the cavity at a measured zero crossing of the spacer's coefficient of thermal expansion and to hold the vacuum housing at 37.1°C.

The fibre noise cancellation system consists of using the light reflected from each of the fibre outputs to the main experimental system in order to reduce the perturbations in the phase [113]. The forward propagating light is sampled by a beam splitter and overlapped with the light reflected from the fibre output. A photodiode is used to generate a signal from the beat-note of the overlapping beams and to provide a feedback to an AOM. The AOM pre-modulates the input light with the opposite phase to the fibre noise such that the light from the fibre output emerges with reduced noise.

The fibre-noise cancelled light is modulated using a double pass AOM referred to as the

tuner AOM as it provides the frequency tuning of the 674 nm light to the ion. Some of the frequency shifted light from the tuner AOM is sampled and sent to a photodiode. The signal from the photodiode provides the feedback to amplitude of the RF supplied to the tuner AOM which stabilises the output optical power. The power stabilised light from the tuner AOM is then modulated with another double-pass AOM, referred to as the agile AOM, which does the temporal shaping of the light in order to have defined pulse shapes [100, 110]. From the agile AOM the light is further modulated with a single-pass AOM that is connected to two RF synthesizers and a series of RF switches. The RF switches enable the single-pass AOM to be driven by either one or both of the synthesizers. The operation in the dual frequency mode, results in bichromatic light that is important for the implementation of entanglement with a Mølmer-Sørensen gate [58]. The Mølmer-Sørensen gate is discussed in more detail in Section 6.7.

2.5.5 1033 nm Quencher/Clear Out Laser

After probing on the optical qubit transition, the 1033 nm laser is used to excite the atom from the $^2D_{5/2}$ state to the $^2P_{3/2}$ state where it can then decay back to the ground state. The laser light is generated in an ECDL that is of a similar design to the 461 nm laser in Section 2.5.1. The light is coupled, separately, into two fibres [110].

In one fibre the light is transmitted to a 2x2 fibre splitter with one output leading to the wavemeter and the other to a tunable low-drift cavity. A side-of-fringe lock is used to stabilise the laser to the cavity. To form the cavity, a mirror at one end is fixed to a spacer and mirror at the opposite end is attached to a back-plate by a set of actuators. A second set of actuators attaches the back-plate to a spacer. The back-plate and spacers are formed of ultra-low expansion glass. In order to tune the cavity a voltage is applied to the first set of actuators, while the second are grounded. This system forms a tunable cavity with finesse =125 that is approximately insensitive to the thermal fluctuations in the actuators. The cavity is mounted in a vacuum chamber (at 10^{-6} mbar and stabilised to ∼1 mK) which is in a thermal enclosure (stabilised to ∼5 mK). Two photodiodes are used to generate an intensity-independent error signal.

The laser light coupled into the other fibre is split into two paths that both go to two double-pass AOMs. One path is detuned by 600 MHz from the other and is used as the ‘quench’ for efficient sideband cooling. The other path is the resonant ‘clear-out’

Card	Description	Quantity
NI PXI-6608	high precision timer	1
NI PXIe-6537	digital I/O	1
NI PXI-6733	analogue output	2
NI PXI-6254	analogue input	1
NI PXIe-4139	source measure units	4
NI PXI-4071	digital multimeters	4

TABLE 2.1: Table of National Instruments PXI chassis cards used to control the experiment.

light for spectroscopy routines. Both these paths are then recombined into a 2x2 fibre splitter where one output is to a photodiode, which monitors the generation of the laser pulses, and the other goes to the trap. The output to the trap focuses a $2\omega_0 = 180$ μm waist beam in the centre of the aperture with the clear out and quencher light of up to 700 μW and 100 μW respectively. The set-up allows each of the beams to be switched independently and with high extinction.

2.5.6 Imaging Systems

In order to detect the state of the ion after probing on the optical qubit transition, the fluorescence from the $S_{1/2} - P_{1/2}$ transition needs to be collected. A photomultiplier tube (PMT) and electron multiplying CCD camera are both used with high numerical aperture lenses (NA = 0.43) to image each side of the trapping aperture (with a magnification of 10). Both detection devices are fitted with filters that block out 674 nm, 1033 nm and 1092 nm wavelengths. Though the devices are sensitive to light from the 405 nm and the 461 nm lasers, they are only used during the loading of the ion and therefore they do not interfere with the state detection. The dark count on the PMT is approximately $\sim$10 s^{-1}.

2.6 Experimental Control

The control of the experimental system is handled by a single National Instruments PXI chassis containing 13 PXI cards which are detailed in Table 2.1.

The high precision timer card is used to gate the photon signals from the PMT in order to determine the count rate and to generate the clock signal for the digital I/O card. The digital I/O card is capable of providing 32 independent TTL signals to the experiment. The card is used to control mechanical shutters, to provide RF switches and to trigger the RF sources for the AOMs in order to generate pulse sequences. In addition, it is also used for switch on and off the hotplate and oven DC sources (see Section 5.4). The analogue output card is used as a input to the VCO for controlling the 422 nm laser frequency. The analogue input card is primarily used for monitoring photodiode signals, however it also is used to monitor the thermocouple signals from the hotplate and the oven. Each of the cards is linked to high precision trigger lines, enabling the synchronisation of the timing between cards. The RF sources are all phase locked to a stable 10 MHz reference signal that is provided by a local hydrogen maser.

The control of magnetic field for nulling the ambient magnetic field and applying a bias field is also through the PXI chassis using four source measure units (NI PXIe-4139) and four digital multimeters (NI PXI-4071) this will be discussed in more detail in Section 5.3.

2.7 Trap Drives

The RF potential is coupled to the ion trap through a tank circuit. An RF source (HP 8647A) used in conjunction with an amplifier provides 1-4 W of power. A bidirectional coupler samples the forward-going and reflected signals. The RF is fed into a helical resonator [114] and then to trap itself via a short (7 cm) coaxial cable. Briefly, the resonator comprises of two coils in a shield. The output of the RF from the bi-directional coupler is coupled to a seed coil, which in turn is coupled to an antenna coil. The antenna coil then drives the RF electrodes on the trap. The seed coil in the resonator is mounted on an adjustable lever so that the distance between it and the antenna coil can be altered; this enables fine tuning of the impedance matching to the trap. Two helical resonators are primarily used in this work; one with a loaded resonance of 23 MHz for the microplasma testing in ion traps in Section 4.4 and another for the rest of the chapters with a loaded resonance of 18 MHz. Typically, the voltage amplitude used for ion trapping in this work is 150 V.

The control of the DC and compensation electrode potentials is outlined in Chapter 5.

2.8 Experimental Techniques

Within this section some of the standard techniques used in trapping and manipulating the state of the ion will be outlined.

2.8.1 Generating Ions

To generate the Sr vapour a tantalum hotplate containing a previously deposited Sr reservoir is heated to 190 - 230°C, evaporating atoms towards the trap [108]. The process is outlined in more detail in Section 5.4. A shield is attached to the trap such that the flux of the Sr atoms is restricted to passing through an aperture which results in atoms in the loading zone (see Figure 2.4). The two photoionisation lasers are used to ionise atoms such that they can be trapped by the electric field.

2.8.2 Optical Pumping

Optical Pumping is a standard technique used to prepare the ion in a given state [76]. Here the ion needed to be prepared in the $m_j = -1/2$ sublevel of the $S_{1/2}$ manifold that occurs in an applied magnetic field. By using circularly polarised light at 422 nm, where the $\hat{k}$ vector for the beam is aligned in parallel to the applied magnetic field only the $\Delta m_j = \pm 1$ transitions can be driven. The sign of the driven transition depends on the handedness of the polarisation. With σ^- light, only the $\Delta m_j = -1$ transition is driven and can spontaneously decay into either the $S_{1/2}(m_j = -1/2)$ or the $S_{1/2}(m_j = 1/2)$ state, see Figure 2.8. If the ion decays into the $S_{1/2}(m_j = 1/2)$ state it is excited again if it decays into the $S_{1/2}(m_j = -1/2)$ state no further excitation is possible. After 40 μs of optical pumping the ion is prepared in the $S_{1/2}(m_j = -1/2)$ state with a probability measured to be 99.4(7) %.

2.8.3 State Read out

Dehmelt's electron shelving technique [61] is used to measure the state of the ion. The ion's fluorescence, as measured by the PMT, has a count rate of $2{\times}10^4$ s^{-1} when cycling on the Doppler cooling transition. However, if the ion is manipulated such that it is in the $D_{5/2}$ state, then illumination with the cooling light no longer causes the ion to

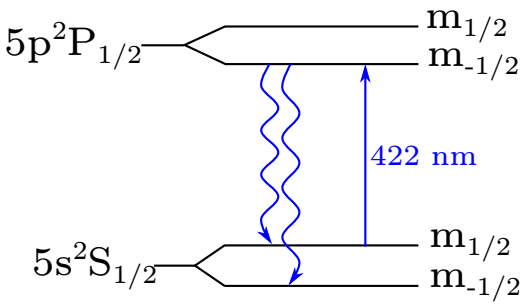

FIGURE 2.8: Schematic of polarisation resolved optical pumping to prepare the ion in the $S_{1/2}(m_j = -1/2)$ state. 422 nm light with σ^- polarisation is used to excite the $S_{1/2}(m_j = 1/2)$ to $P_{1/2}(m_j = -1/2)$ transition only. If the ion decays into the $S_{1/2}(m_j = -1/2)$ state no further excitations are possible.

fluorescence and the detected counts drops to the background level of 300 s^{-1}. Therefore the ion fluorescence can be used as to discriminate between the states of the ion.

2.8.4 Minimising Micromotion

Due to stray fields from the electrodes, the vacuum windows etc., DC fields can build up and displace the ion from the RF null in the centre of the harmonic potential. This causes excess micromotion: the ion oscillates at the applied Rf frequency with a greater amplitude. DC potentials applied to the compensation electrodes are used shift the ion back to the centre of the trapping potential and thus to minimise the ion's micromotion.

Firstly, and most coarsely, the compensation voltages can be adjusted to alter the position of the ion (as seen on the CCD camera) in order to determine where it is least sensitive to changes in the RF amplitude. Secondly, the RF correlation technique [111] is used to minimise the micromotion in three dimensions. The 422 nm laser is detuned from the Doppler cooling transition by $\sim \Gamma_{atom}/2$, where Γ_{atom} is the atomic transition linewidth. This results in half the ion fluorescence rate observed when compared with the peak signal at the transition centre. Due to the Doppler effect the micromotion results in a modulation of the observed fluorescence and with an amplitude that increases with the magnitude of the micromotion. The compensation voltages can be adjusted to minimise the oscillation in the ion fluorescence. The process can then be repeated for each of the cooling beams in turn. The minimisation of the ion vibration in one beam direction can have the effect of projecting the vibrational component into another beam direction, therefore the micromotion minimisation is repeated for each of the beams to ensure that it converges to to a minimum for all three directions.

Chapter 3

Microplasma Surface Processing - Theoretical Proposal

For ion traps to achieve the high fidelity operation that many quantum technologies require, the ion motional decoherence needs to be minimised (see Section 1.4.1). One likely source of noise has been shown to be fluctuating patch potentials [77, 84] or thin dielectric layers (*i.e.* native oxide or hydrocarbons) on electrode surfaces [115]. Within a few minutes, a clean Au surface can acquire a 0.4 monolayer of hydrocarbon coverage when exposed to ambient air, and during a vacuum-bakeout process the coverage can increase to a few monolayers [115]. Ion beam milling of electrode surfaces, for the purpose of removing surface contamination, has shown a two hundred fold reduction in the ion motional heating rate [90, 91]. This method, however, uses an energetic ion beam with Ar^+ energies of 300 - 2000 eV [90, 91]. The Au electrode material sputtering threshold with Ar^+ ions is 15 eV [116]. Therefore the ion beam would not only remove the surface adsorbates but also the Au. While this effect is not fundamentally an obstacle in traps with a planar electrode geometry, in a 3D electrode structure this method becomes inappropriate. Re-deposited material from the electrode surface on the dielectric material intended as insulating gaps risks forming an electrical short and failing the device.

A more selective approach to surface cleaning has been adopted by [93]. By introducing a conductive coil in close proximity to the surface on an ion trap, an inductively coupled Ar plasma is generated. The ion bombardment energies generated are 20 eV in comparison to the 30 eV sputtering threshold of the Nb electrodes with Ar^+. Therefore, this

method is likely to be more selective in the sputtering of hydrocarbon material from the surface. Using this approach, a four-fold reduction in ion heating rate was observed. An alternative procedure will be adopted in this work that negates the need for an inductive coil. Instead, the electrodes of the ion trap themselves are used to generate a capacitively coupled, RF microdischarge. The analysis suggests that the generated microdischarge results in an *in situ*, low energy and selective method for removal of hydrocarbon contamination.

This chapter presents a method to assess the suitability of a microplasma for selective surface processing of ion trap electrodes. Section 3.1 defines the sputtering thresholds necessary for this work. The treatment of collisions between gaseous particles, or gaseous particles and a surface are considered in Sections 3.2 and 3.3 respectively. Section 3.4 shows how the plasma regime can be determined and therefore how a number of model assumptions can be justified. Section 3.5 details the calculation of the ion and neutral atom flux distributions at the electrode surface and the processing time needed to remove contaminants. Finally, section 3.6 contains a selection of equation flow charts that will be referenced throughout this chapter. These will hopefully add some clarity to the system of equations being implemented. It should be noted that the following calculations rely on two fundamental plasma parameters that are determined experimentally; the electron density (n_e) and the gas temperature (T). The process of determining theses parameters and the results from applying the calculations contained in this chapter can be found in Chapter 4.

Within this chapter all units will be in SI unless stated otherwise. However, specific values for energies may be quoted in eV to be consistent with the literature on this topic.

3.1 Sputtering Thresholds

During the microplasma processing, it is essential that the damage to the electrode surface is minimised. The sputtering threshold for gold is about 57 eV [116]. In addition, the sputtering threshold E_{th} for amorphous hydrocarbons sputtered by He can be found using the following equation [117, 118].

TABLE 3.1: Sample table of microplasma gas choices. Shown is the plasma gas type, the type of sputtering the gas is capable of, the Au sputtering threshold $\epsilon_{th,Au}$ (all values taken from [116] and the amorphous hydrocarbon threshold $\epsilon_{th,a}$ (all values calculated using equation 3.1)

Gas	**Sputtering Type**	$\epsilon_{th,Au}$	$\epsilon_{th,a}$
Ne	Physical	19	26
He	Physical	57	12
Ar	Physical	15	38
O_2	Physical & Chemical	21	23
N_2	Physical & Chemical	22	22
H_2	Physical & Chemical	206	11

$$E_{th} = \left[7.0\left(\frac{M_C}{M_{He}}\right)^{-0.54} + 0.15\left(\frac{M_C}{M_{He}}\right)^{1.12}\right]E_{sb}, \tag{3.1}$$

where M_{He} and M_C are the masses of He and C respectively and E_{sb} is the surface binding energy which is 2.8 eV for amorphous hydrocarbons [119]. Therefore, using equation 3.1, the threshold energy of amorphous hydrocarbon sputtering with He is approximately 12 eV. Table 3.1 shows some of the sputtering thresholds associated with potential gases. From the table it is clear to see that He, N_2 and H are preferable choices since the amorphous hydrocarbon threshold is lower than that of Au. They minimise the risk of sputtering the Au material while maximising the possibility of removing the contaminants. However H has the added complication that it is highly reactive and could potentially chemically interact with ion trap itself. Therefore He and N_2 provide the most promising gases for hydrocarbon contamination removal off a gold substrate.

3.2 Characterisation of Gaseous Particle Collisions

The collisional dynamics of interacting particles can be defined using the hard sphere model, where particles are modelled as hard spheres with a collisional cross-sectional area that defines the type of interaction. In its simplest form of the collisional cross-section σ_{HS} is to be defined as two interacting spheres with constant radii [120, 121]

$$\sigma_{HS} = \pi a_{12}^2, \tag{3.2}$$

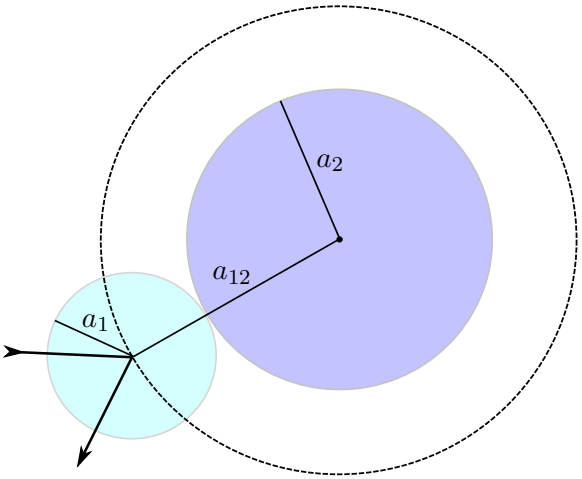

FIGURE 3.1: Hard sphere model representation of colliding particles with radii a_1 and a_2. The dashed line of radius a_{12} is often called the mutual sphere of influence [122].

where a_{12} is the distance of closest approach. Figure 3.1 shows a depiction of two particles with radii a_1 and a_2 colliding where the distance between the centres at the point of collision is a_{12}. Therefore using $a_{12} = 2.30 \times 10^{-10}$ m, for a He^+-He interaction [121] $\sigma_{HS} = 1.66 \times 10^{-19}$ m^2. However, this assumes that the collisional cross-section is independent of the ion energy. For a more realistic estimate the ion energy needs to be taken into account.

An alternative method describes the total collisional cross-sectional area of He ions colliding with He gaseous atoms as the sum of two energy dependent contributions

$$\sigma_{He^+-He} = \sigma_L + \sigma_{ct} \tag{3.3}$$

where σ_L is the contribution from polarisation scattering and σ_{ct} is the contribution from charge transfer scattering. The polarisation cross-section, also known as the Langevin cross-section, σ_L (in m^2) is [120]

$$\sigma_L = \left(\frac{\pi \alpha_P q^2}{\epsilon_0 \mu} \frac{M}{2\epsilon} \right)^{1/2} \tag{3.4}$$

where ϵ_0 is the permittivity of free space, α_P is the polarisability (for He α_P =1.8×10^{-31} m^3 [121]), q is the ion charge, M is the ion mass, ϵ is the ion energy and μ is the reduced mass.

The charge transfer collisional cross-section σ_{ct} (in m^2) for He is [123]

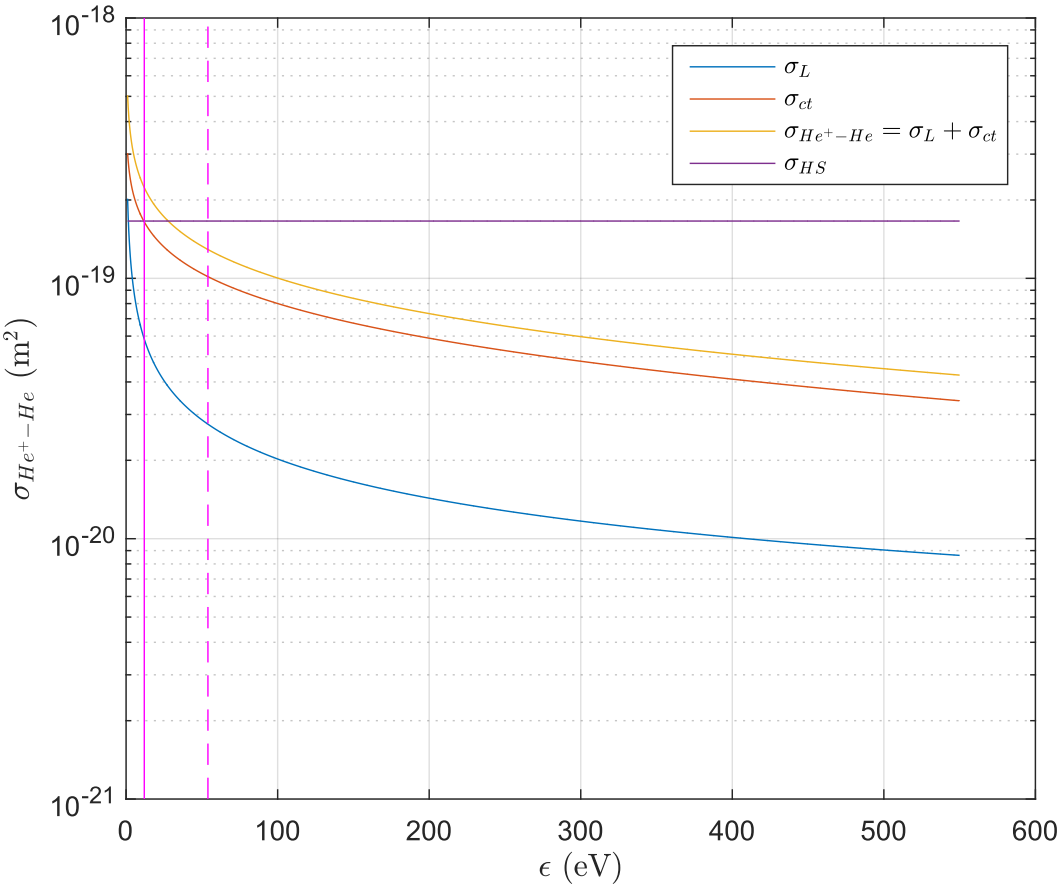

FIGURE 3.2: Calculated collision cross-sectional area for He ions with He gaseous atoms σ_{He^+-He} as a function of ion energy ϵ. The vertical lines represent the sputtering thresholds for Au (dashed) and amorphous hydrocarbons (solid).

$$\sigma_{ct} = \left(5.5 - \left[0.58 \times ln\left(\frac{\epsilon}{e}\right)\right]\right) \times 10^{-20}. \tag{3.5}$$

where e is the electron charge. Using equations 3.4 and 3.5, the total cross-sectional area can be calculated for He^+ with He atoms using equation 3.3. The results of the calculation for the total collision cross-section, as a function of ϵ, can be seen in Figure 3.2. The figure also shows the each of the contributions σ_L and σ_{ct}, in addition to the comparison with the constant ion velocity case σ_{HS}.

Four main regions of interest can be defined for σ_{He^+-He};

- Within the plasma bulk.
- Associated with the mean ion energy in the sheath.
- Associated with ion energy above the sputtering threshold for Au.
- Associated with ion energy above the sputtering threshold of hydrocarbons.

In the analysis that follows, for ion energies ϵ where $\epsilon \gtrsim 1$ eV, equations 3.4 and 3.5 will be used. However, for energies lower than this limit, as in the case of the plasma bulk dynamics, the equation for σ_{ct} in equation 3.5 is replaced with the following equation for the charge transfer cross-section [124]

$$\sigma_{ct<} = \frac{1.2 \times 10^{-9}}{\mu^{1/2}} \left(\frac{M}{2\epsilon} \right)^{1/2} \tag{3.6}$$

which is valid in the energy range of 0.02 eV$\lesssim \epsilon \lesssim$ 1 eV. Figure 3.3 shows the difference between the intermediate energy, the low energy and the constant energy case. The constant energy case clearly underestimates the collision cross-section in the range of interest and the energy dependent cases show similar results. Due to the highly collisional nature of the plasma generated in this work (see: Section 3.4) the ion energy in the bulk of the plasma can be calculated by assuming the ions are in equilibrium with the neutrals. The results from the plasma spectroscopy (see Chapter 4) show that the gas temperature is in the region of room temperature up to 460 K. The corresponds to an ion energy of 0.3 eV$\lesssim \epsilon \lesssim$ 0.5 eV. Within this energy region the cross-section is approximated to a constant $\sigma_{He^+-He} = 5{\times}10^{-19}$ m^{-2}.

The mean ion bombardment energies, for either pure He or He:N_2 gas mixtures for a few percent of N_2 can be assumed to be in the region of 1 to 10 eV. Over this range the collision cross-section is only weakly dependent on ion energy (see Figure 3.4) therefore σ_{He^+He} can be approximated with a mean value; $\sigma_{He^+He} = 3.10 \times 10^{-19}$ m^{-2}.

The calculation of the neutral flux that is energetic enough to sputter contaminants of the electrode surface requires σ_{He^+-He} valid over a wide energy range (see Section 3.5.5). Figure 3.2 shows the ranges of interest; from the threshold of Au (57 eV [116]) and from the threshold of sputtering amorphous hydrocarbons (12 eV, see Section 3.1) up to 500 eV. The upper limit of 500 eV was calculated to be the maximum ion bombardment energy at peak sheath voltage given that the ion undergoes no collisions; see Section 3.5.5 for more details. Over these ranges a weighted mean value for the cross-section was calculated, where the weighting was with respect to the neutral flux energy distribution (equation 3.57). Using this method $\sigma_{He^+-He} = 1.2 \times 10^{-19}$ m^2 for calculations above the Au sputtering threshold and $\sigma_{He^+-He} = 2.1 \times 10^{-19}$ m^2 for calculations above the amorphous hydrocarbon sputtering threshold.

A summary of the σ_{He^+-He} values used in this work can be seen in table 3.2. It contains

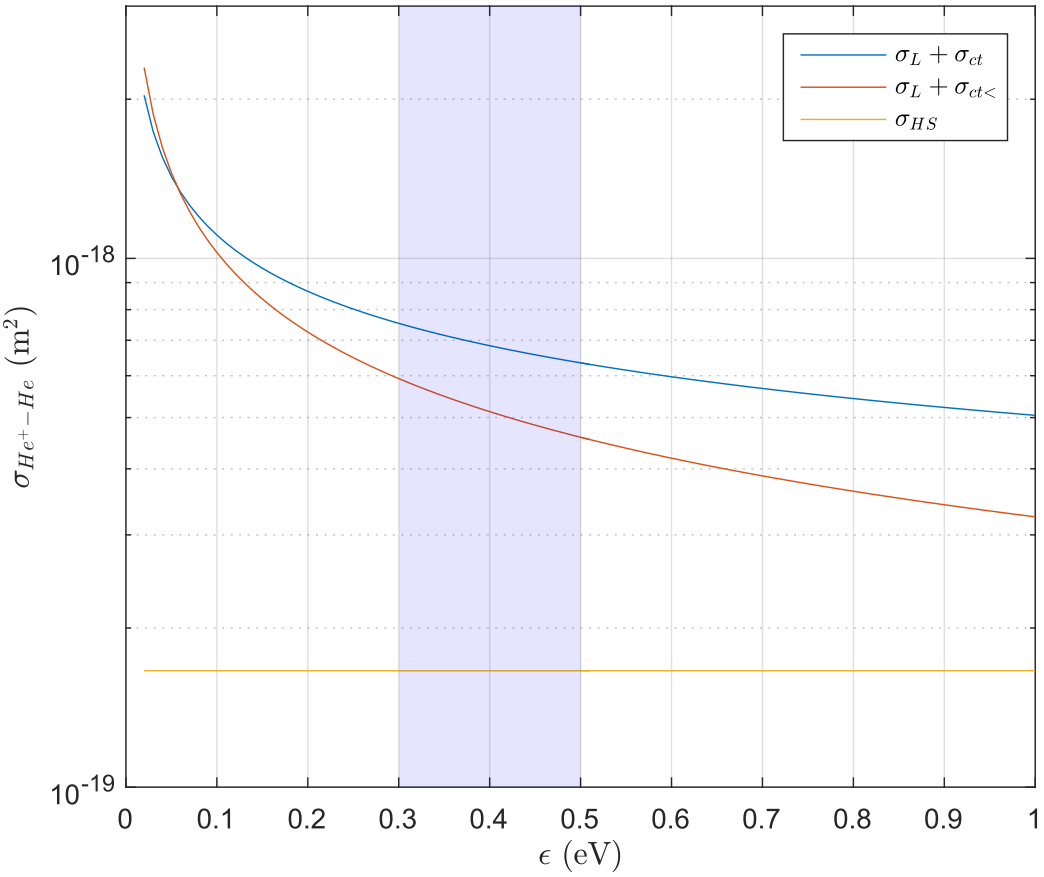

FIGURE 3.3: Calculated total collision cross-sectional area for He ions with He gaseous atoms σ_{He^+-He} as a function of ion energy ϵ. The shaded region corresponds to the relevant plasma bulk ion energy range for this work. The total cross-section for the intermediate ion energy regime $\sigma_{He^+-He} = \sigma_L + \sigma_{ct}$ is calculated using equations 3.4 and 3.5. The total collision cross-section for the low energy regime $\sigma_{He^+-He} = \sigma_L + \sigma_{ct<}$ is calculated using equations 3.4 and 3.6.

TABLE 3.2: Summary of calculated He^+-He collision cross-sections.

σ_{He^+-He} (m^2)	Ion Energy Region (eV)	Relevant Calculation Region
5×10^{-19}	$0.3 \leqslant \epsilon \leqslant 0.5$	$T_i = T$
3.1×10^{-19}	$1 \leqslant \epsilon \leqslant 10$	ϵ_{bom}
1.2×10^{-19}	$57 \leqslant \epsilon \leqslant 500$	$\epsilon_{th,Au} \leqslant \epsilon \leqslant \epsilon_{up}$
2.1×10^{-19}	$12 \leqslant \epsilon \leqslant 500$	$\epsilon_{th,a} \leqslant \epsilon \leqslant \epsilon_{up}$

the values used in four ion energy regions of interest as listed earlier in the section. Firstly in the bulk region of the plasma where the ion temperature $T_i = T$. Secondly in the calculation of the mean ion bombardment energy ϵ_{bom}. Thirdly in the calculation of the neutral flux for ion energies between the sputtering threshold of Au $\epsilon_{th,Au}$ and the upper bound of the ion energy ϵ_{up}, and lastly σ_{He^+-He} for ion energies between the sputtering threshold of hydrocarbons $\epsilon_{th,a}$ and ϵ_{up}.

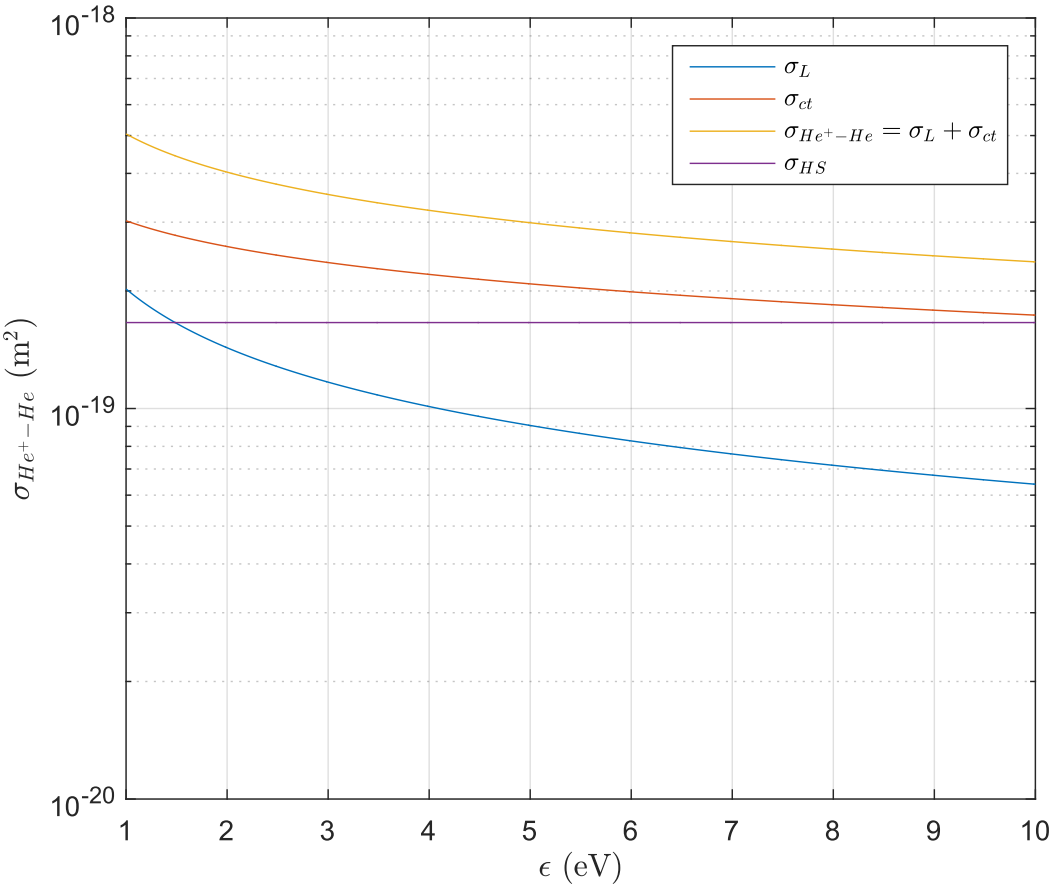

FIGURE 3.4: Calculated total collision cross-sectional area for He ions with He gaseous atoms σ_{He^+-He} as a function of ion energy ϵ in the plasma sheath region.

3.3 Characterisation of Collisions between Gaseous Particles with a Surface

The collisions of energetic projectiles on a surface can be characterised by a sputtering cross-sectional area. This work is principally concerned with calculating the sputtering cross-sectional area for He projectiles on a Au surface for the removal of hydrocarbon adsorbates σ_a and Au surface atoms σ_{He^+-Au}. These values can then be used to calculate the rate of removal of the contaminants and also to assess the potential to damage the electrodes.

For low energy ions (when ϵ is below the keV region) the sputtering cross-sectional area for binary collisions of bombarding atoms on a surface can be calculated following the theory proposed by [125]. The total cross-sectional area σ is composed of three partial cross-sections that represent different sputtering mechanisms

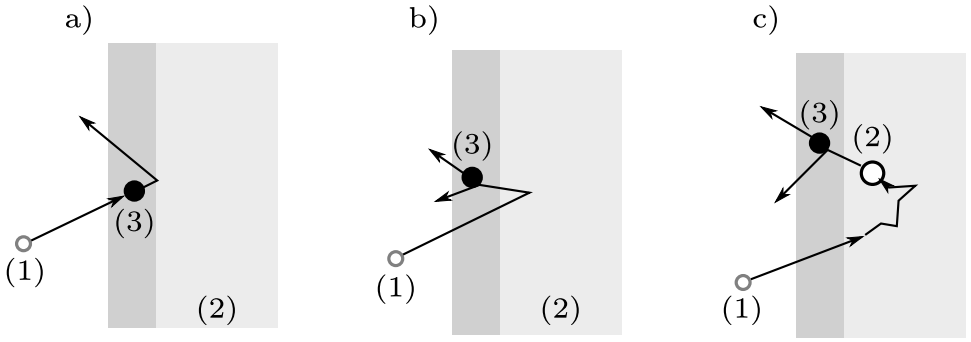

FIGURE 3.5: Schematic of sputtering cross-section contributions. a) Direct knock off contribution. b) Ion reflection contribution. c) Cascade sputtering contribution. The number (1) refers to the projectile, (2) the substrate and (3) the adsorbate layer.

$$\sigma = \sigma_D + \sigma_R + \sigma_C. \tag{3.7}$$

Each contribution is defined as one of the following:

- Direct knock off contribution σ_D; incoming ion collides with an adsorbate or substrate surface atom which results in its direct removal.
- Reflection removal contribution σ_R; the incoming ion is reflected at a particular substrate depth and sputters atoms on the way out.
- Cascade sputtering contribution σ_C; the incoming ion transfers energy to the substrate atoms which, through a cascade process, generates an outward flux of sputtered atoms.

This framework is suited to the study of chemisorbed gases from metals (*i.e.* for adsorbates or surface atoms with binding energies in the eV range) as opposed to physisorbed gases (those particles with binding energies in the meV range) This is appropriate since the binding energy of amorphous hydrocarbons on Au is 2.8 eV [119] and the heat of sublimation for Au is 3.65 eV [126].

Figure 3.5 shows a schematic of each of the sputtering mechanisms. In the following section, the subscripts 1, 2 and 3 will denote the atomic properties associated with the projectile, the substrate and the adsorbate atoms respectively. However for ion bombardment energies ($\epsilon < 500$ eV), σ_D and σ_R dominate the total sputtering cross-section and this effect becomes more pronounced with light projectiles such as H and He [125, 127]. Therefore only the contributions from σ_D and σ_R will be taken into account.

The direct knock off contribution σ_D (in m^2) for an ion with energy ϵ (in J) is defined as [127]

$$\sigma_D = \frac{C_{13}}{cos(\theta)m}\left(\epsilon U_3\right)^{-m}\left(1 - X^{-m}\right) \tag{3.8}$$

where θ is the angle between the surface normal and the incoming ion, for the following calculations it is assumed that $\theta = 0$. In addition, m is an inverse power parameter (for light ions such as He $m = 0.4$ [128]), U is the surface binding energy (in J) and $X = \gamma_{13}(\epsilon/U_3)$, which can be found using the energy transfer factor γ_{ij} [127, 128]

$$\gamma_{ij} = \frac{2M_iM_j}{\left(M_i + M_j\right)^2}. \tag{3.9}$$

The coefficient C_{ij} is [127, 128]

$$C_{ij} = \frac{\pi a_{ij}^2}{2}\left(\frac{M_i}{M_j}\right)^m\left(\frac{Z_2Z_3e^2}{4\pi\epsilon_0 a_{ij}}\right)^{2m} \tag{3.10}$$

here Z denotes atomic number, ϵ_0 is the permittivity of free space, e is the electron charge and a_{ij} is the screening length (in m) given by [127]

$$a_{ij} = \frac{0.4683 \times 10^{-10}}{\left(Z_1^{3/2} + Z_2^{3/2}\right)^{1/2}}. \tag{3.11}$$

The reflected contribution σ_R (in m^2) is defined as [127, 128]

$$\sigma_R = \sigma_D R_N\left(4 - \frac{4ln(X)}{3\left(X^{1/3} - 1\right)}\right) \tag{3.12}$$

The reflection coefficient R_N has to be either determined experimentally or, as in the case of this work, taken from numerical calculations.

The reflection coefficient R_N at normal ion bombarding incidence to the surface can be defined as [129]

$$R_N = \left(1 + \frac{a_1}{\nu^{1/2}} + \frac{a_2}{\nu} + \frac{a_3}{\nu^{3/2}} + \frac{a_4}{\nu^2}\right)^{-1/2} \tag{3.13}$$

with

$$
\begin{aligned}
a_1 &= \frac{6}{\pi^{1/2}} && = 3.39 \\
a_2 &= \frac{27}{\pi} && = 8.59 \\
a_3 &= \frac{27}{\pi^{1/2}}\left(\frac{4}{\pi} - 1\right) && = 4.16 \\
a_4 &= \left(\frac{3}{2} - 2^{1/2}\right)^{-2} && = 135.9
\end{aligned}
$$

and ν is the ratio of the range the ion can penetrate in the substrate R to the transport mean free path λ_{tr}. Therefore ν is [129]

$$\nu = \frac{R}{\lambda_{tr}} \tag{3.14}$$

which can be intuitively understood as the mean number of wide-angle collisions the ion undergoes before slowing down to rest [129]. The range R is a function of the maximum ion bombardment energy ϵ_{up},

$$R(\epsilon_{up}) = \frac{\epsilon_{up} \times 1.66 \times 10^{-27}}{2NM_1S(\epsilon_{up})} \tag{3.15}$$

where N is the substrate density and S is the total stopping cross-section per scattering centre. The latter parameter is a summation of contributions from the electronic stopping cross-section S_e and the nuclear stopping cross-section of the ion S_n. Therefore

$$S = S_n + S_e, \tag{3.16}$$

where the nuclear stopping cross-section S_n can be defined in terms of the reduced energy ϵ_r. The reduced energy is the ratio of the incident projectile energy with the Coulomb energy of the ion and the target at the screening distance in the ion centre of mass frame ϵ_c; *i.e.* $\epsilon_r = \epsilon/\epsilon_c$. More explicitly, ϵ_c is [130]

$$\epsilon_c = \frac{Z_1 Z_2 e^2}{4\pi\epsilon_0 a_{ij}} \frac{M_1 + M_2}{M_2}. \tag{3.17}$$

Using ϵ_r, S_n for low energy sputtering (in the region of $\epsilon \leq 1$ keV) is [130, 131]

$$S_n = \frac{0.5ln(1+\epsilon_r)}{\epsilon_r + 0.14\epsilon_r^{0.42}} \tag{3.18}$$

On the other hand, S_e is

$$S_e = Z_1^{1/6} 8\pi e^2 a_0 \frac{Z_1 Z_2}{\left(Z_1^{2/3} + Z_2^{2/3}\right)^{3/2}} \left(\frac{2\epsilon}{M_1}\right)^{1/2} \frac{1}{v_0} \tag{3.19}$$

where $v_0 = e^2/\hbar$.

Using equations 3.18 and 3.19, equation 3.16 can then be solved for S which then determines the range R from equation 3.15. However to find the mean free path λ_{tr} the following equation can be used

$$\lambda_{tr}(\epsilon) = \frac{1}{N\sigma_{tr}(\epsilon)} \tag{3.20}$$

where σ_{tr} is the transport collision cross-section,

$$\sigma_{tr} = \frac{M_2}{2M_1\epsilon} S_n(\epsilon), \tag{3.21}$$

which describes the deflection of the ion as it slows down in a medium. Both R and λ_{tr} are inversely proportional to the substrate density, however note that the dependency is removed when the ratio is taken, resulting in ν in equation 3.14 being independent of N.

The total sputtering cross-sectional area for He ions on a Au substrate with amorphous hydrocarbons on the surface σ_a can be seen in figure 3.6. The range plotted is from the hydrocarbon sputtering threshold (12 eV, see Section 3.1) up to the maximum ion energy that is likely to occur within the experimental parameters of this work (500 eV). A similar calculation for the removal of surface Au atoms can also be done to find the sputtering collision cross-sectional of He ions on a Au surface. In this instance, for the equations listed in this section, the subscript 1 will still denote the He ions, however the subscripts 2 and 3 will both be represented by Au properties. Figure 3.7 shows the total collision cross-sectional area for He ions sputtering Au atoms from an Au substrate plotted from the threshold energy of 57 eV [116] up to 500 eV. The calculated sputtering cross-sections for both σ_a and σ_{He^+-Au} are weakly dependent on the ion energy over the

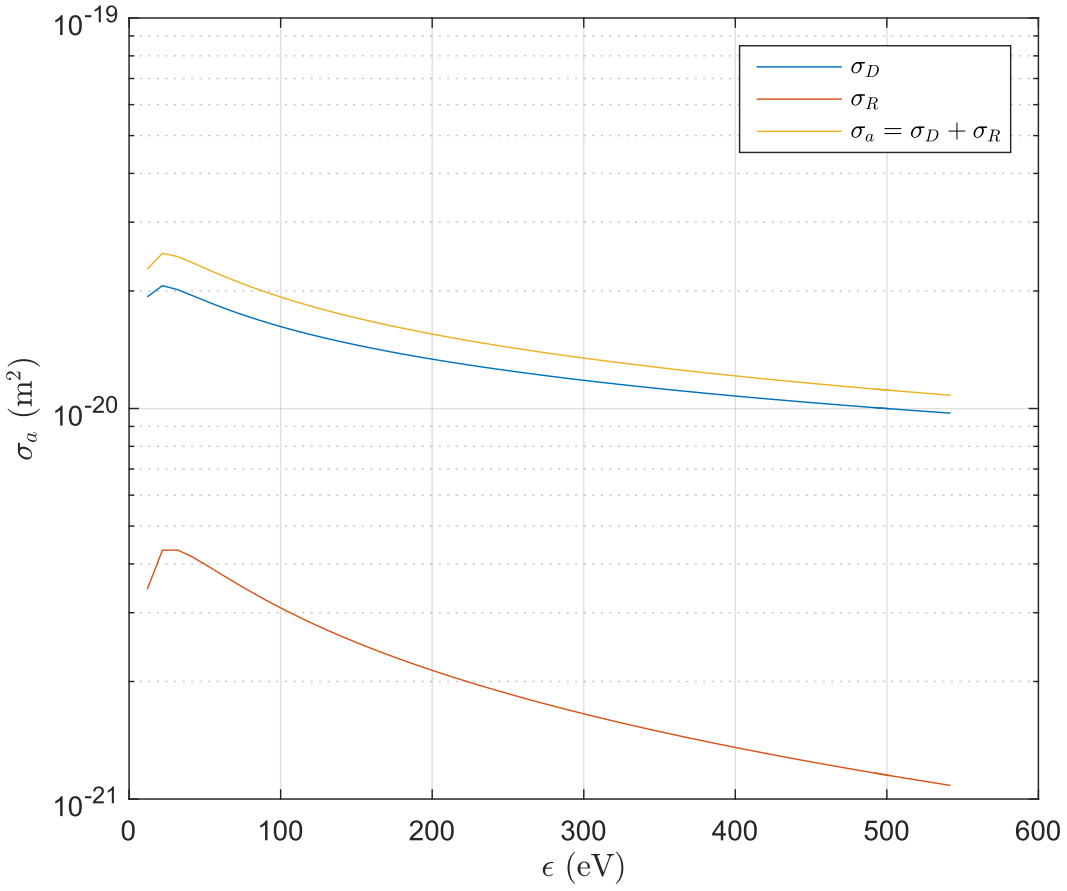

FIGURE 3.6: Collision cross-section for He^+ with a Au surface containing hydrocarbon adsorbates σ_a as a function of ion energy ϵ. Plotted is the total cross-sectional area σ_a and its two calculated contributions σ_D and σ_R from equations 3.8 and 3.12 respectively.

range of interest, therefore in the following calculations an average value will be used; $\sigma_a = 1.52 \times 10^{-20}$ m^{-2} and $\sigma_{He^+-Au} = 1.42 \times 10^{-20}$ m^{-2}.

3.4 Defining a Plasma Regime

There are a number approximations that can be made depending on the plasma operating regime, this section outlines the general discharge classifications that are relevant to this work. The microdischarge generated in the microtraps using He are low frequency, high pressure discharges with collisional, high voltage sheaths.

3.4.1 High vs Low Voltage Sheaths

A sheath can be described as high or low voltage, where the defining criteria for a high voltage sheath is; $eV_s >> k_B T_e$ [120, 132], where V_s is the sheath voltage (in V) and T_e

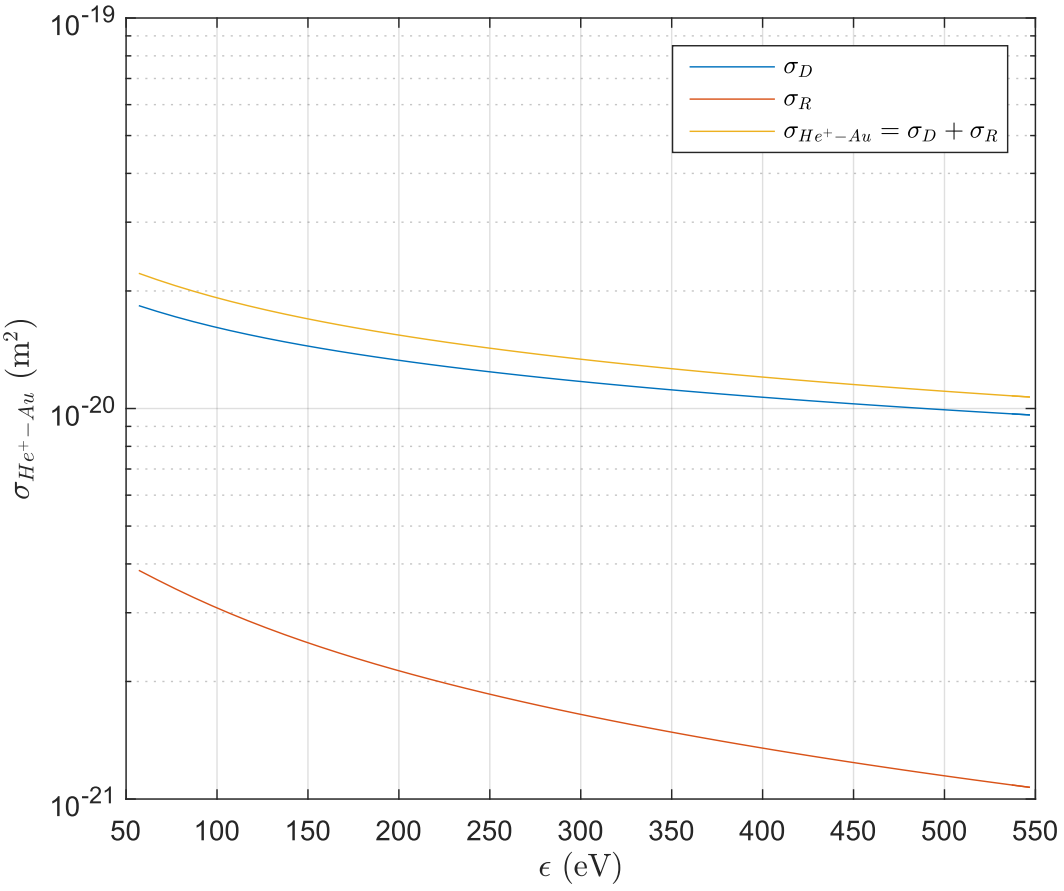

FIGURE 3.7: Collision cross-section for He^+ with a Au surface σ_{He^+-Au} as a function of ion energy ϵ. Plotted is the total cross-sectional area σ_{He^+-Au} and its two calculated contributions σ_D and σ_R from equations 3.8 and 3.12 respectively.

is the electron temperature.

The average T_e is expected to be in the range of 0.1-4 eV = 1161 - 46435 K [133–136], therefore

$$2 \times 10^{-20}\text{J} \leq k_B T_e \leq 6 \times 10^{-19}\text{J}. \tag{3.22}$$

The sheath voltage V_s for an RF discharge is roughly equivalent to the RF voltage amplitude U_{RF} at low frequencies and to $0.4U_{RF}$ at high frequencies [120]. The voltage range used in the experimental testing of the discharge was 140 V $\leqslant U_{RF} \leqslant$ 220 V. Without assuming a particular frequency regime, the maximum possible range for V_s is then; 0.4×140 V $\leqslant V_s \leqslant 220$ V, which leads to

$$1 \times 10^{-17}\text{J} \leq eV_s \leq 4 \times 10^{-17}\text{J} \tag{3.23}$$

and the $eV_s >> k_B T_e$ criterion is satisfied for a high voltage sheath.

3.4.2 High vs Low Frequency within the Sheath

A low plasma frequency satisfies the condition that angular RF drive frequency $\Omega_{RF} \leq \Omega_i$, where Ω_i is the ion plasma frequency [120]

$$\Omega_i = \pi \left(\frac{e^2 n_s}{\epsilon_0 M} \right)^{1/2} \left(\frac{2T_e}{V_0} \right)^{1/4}. \tag{3.24}$$

Here n_s is the ion density at sheath edge (in m^{-3}) (see Section 3.5.2), ϵ_0 is the permittivity of free space, M is ion mass (in kg) and V_0 is the sheath voltage amplitude. At low RF frequencies compared to Ω_i the ion responds to the instantaneous field. At high frequencies the ion takes a number of oscillations in order to traverse the sheath and therefore sees a time-averaged electric field. The discharges generated here are characteristically low frequency. For example, at 23 MHz $\Omega_{RF} = 1.4 \times 10^8$ rads^{-1} with gas pressure $P = 790$ mbar, $T_e = 2$ eV $= 23209$ K, $V_0 = 191$ V and $n_s = 4 \times 10^{19}$ then $\Omega_i = 3 \times 10^9$ rads^{-1}. Therefore $\Omega_{RF} < \Omega_i$ and the discharge is in a low frequency regime.

3.4.3 Collisional vs Collisionless Sheaths

The frequency of the collisions between particle species in a plasma determines the transport properties and therefore is a central feature in describing the plasma system. Ion bombardment energies are strongly affected by the atomic interactions in the sheath. If there are no collisions, the ions are accelerated the length of the sheath to the electrode surface. However if the sheath is collisional, some of the ion energy is dissipated in collisions with neutral atoms. In addition, these collisions will generate fast neutrals in the sheath that can also effect the electrode surface. A plasma is said to be collisional if it satisfies the requirement that $\lambda_i < s_m$, where λ_i is the mean free path of the ion and s_m is the sheath thickness. Using this model the mean free path of a particle λ can be calculated using [120]:

$$\lambda = \frac{1}{\sigma n_g} \tag{3.25}$$

where σ as the collision cross-section area which characterises the particular collisional process, more details can be found in Sections 3.2.

In order to calculate the sheath thickness s_m the following equation from [120] can be used to compare the mean free path with a high voltage, DC, collisional sheath

$$s_m = \left[\frac{2}{3}\left(\frac{5}{3}\right)^{3/2}\epsilon_0\left(\frac{2e\lambda_i}{\pi M}\right)^{1/2}\frac{V_0^{3/2}}{en_s u_s}\right]^{2/5}. \tag{3.26}$$

where V_0 is the sheath voltage amplitude (in V) and u_s is the ion velocity at sheath edge (see Section 3.43).

Equation 3.26 assumes that there is a maximum voltage across the sheath and therefore finds the maximum sheath thickness. The use of a DC model here is appropriate due to the low ion plasma frequency (see Section 3.4.2) and fast electron relaxation times (see Section 3.4.5).

Typically the ion mean free path is calculated to be in the sub-micron range and the sheath thickness (calculated using equation 3.26) is tens of microns. Therefore the condition $\lambda_i < s_m$ for a collisional sheath is satisfied.

Furthermore, in order to verify that the collisional condition was not satisfied as a result of using a collisional model, λ_i was also compared to the sheath thickness calculated from a DC, high-voltage, non-collisional model $s_{m_{non-col}}$

$$s_{m_{non-col}} = \left[\frac{4}{9}\frac{\epsilon_0 V_0^{3/2}}{en_e u_s}\left(\frac{2e}{M}\right)^{1/2}\right]^{1/2}. \tag{3.27}$$

Note that when comparing equations 3.26 and 3.27 for a collisional and collisionless sheath, that the former scales with the mean free path whereas the latter does not. For both the collisional and collisionless models $\lambda_i < s_m$.

3.4.4 High vs Low Pressure Plasma

Within the particle dynamics of the bulk of the plasma, a high pressure plasma satisfies the condition that

$$\lambda_i \leq \frac{T_i}{T_e} l. \tag{3.28}$$

where T_i is the ion temperature and l is the inter-electrode distance. In a high pressure plasma the particle transport in the bulk of the plasma is diffusive and ambipolar. Here it is assumed that the ions in the bulk are in equilibrium with the surrounding neutral atoms due to their high collision frequency. For 300 K $\leqslant T \leqslant$ 450 K, $T = T_i$, 0.1 eV $\leqslant T_e \leqslant$ 4 eV (1161 K $\leqslant T_e \leqslant$ 46435 K) and $l = 340$ μm the condition in equation 3.28 is satisfied since

$$2.6 \ \mu\text{m} < \frac{T_i}{T_e} l < 104 \ \mu\text{m} \tag{3.29}$$

whereas λ_i, for this work, is in the sub-micron range. The high pressure regime is highly collisional and will be used when calculating the ion distribution at the sheath edge.

3.4.5 Electron Relaxation Time

Another quantity that characterises the dynamics in a discharge is the electron energy relaxation time τ_e. In high pressure discharges τ_e can be shorter that the RF period τ_{RF} which leads to the electron energy distribution being strongly modulated by the RF drive frequency. Due to this fast relaxation time the discharge can then be seen as a succession of DC discharges at different voltages [133]. For a discharge being driven at 23 MHz ($\tau_{RF} = 43$ ns) τ_e is determined by

$$\tau_e = \frac{\lambda_e}{u_e} \tag{3.30}$$

where λ_e is the electron mean free path. The average electron velocity u_e is

$$u_e = \left(\frac{2 k_B T_e}{m} \right)^{1/2} \tag{3.31}$$

where m electron mass. The electron mean free path λ_e is calculated using

$$\lambda_e = \frac{1}{n_g \sigma_{e-He}} \tag{3.32}$$

where $\sigma_{e-He} = \pi a_{e-He}^2$ and the mutual sphere of influence between the electron and the He atom is defined as $a_{e-He} = 1.15 \times 10^{-10}$ [121], therefore $\sigma_{e-He} = 4.15 \times 10^{-20}$.

For a discharge at 350 mbar $\leqslant P \leqslant$ 950 mbar, 300 K $\leqslant T \leqslant$ 450 K and 0.1 eV $\leqslant T_e \leqslant$ 4 eV; 4 ps $\leqslant \tau_e \leqslant$ 23 ps. From these calculations, $\tau_e < \tau_{RF}$ and the microdischarge can be seen as a sequence of DC discharges with varying sheath voltages.

3.5 Quantifying Surface Effects

Using the conditions in Section 3.4, the plasma generated in an ion microtrap is likely to be termed as high pressure with sheaths that are low frequency, high voltage and collisional. The following section details how to quantify the effect of the particles bombarding the electrode surface by calculating the average bombardment energy (Section 3.5.4), the particle flux and thus the cleaning time to remove two hydrocarbon monolayers (Section 3.5.5). The calculation of these quantities however all depend on three calculated parameters that are functions of the electron density n_e and the gas temperature T. These quantities are: 1) the ion velocity at the sheath edge $u_s(n_e, T)$, 2) the ion density at the sheath edge $n_s(n_e, T)$, and 3) the electron temperature $T_e(T)$ in the bulk of the plasma, which allows the calculation of the former two quantities. The methodology for determining these values is laid out in Sections 3.5.1 - 3.5.3. The plasma parameters depend on n_e and T, which are determined from the plasma spectroscopy in Section 4.2.

3.5.1 Electron Temperature in High Pressure Discharges

The electron temperature is a necessary for calculating the ion dynamics. In the bulk of the plasma at high pressures, T_e can be found by numerically solving the following equation

$$\frac{\left[K_{mi}(T)K_{iz}(T_e)\right]^{1/2}}{u_B(T_e)} = \frac{\pi}{n_g(T)l} \tag{3.33}$$

where K_{mi} is ion-neutral momentum transfer rate constant, K_{iz} is ionisation rate constant, u_B is the Bohm velocity, n_g is the gas density and l is the distance between the electrodes. The Bohm velocity u_B is defined as

$$u_B = \left(\frac{k_B T_e}{M}\right)^{1/2}, \tag{3.34}$$

where the mass of the ion is denoted by M and e is the charge of the electron. Similarly, K_{iz} is also a function of T_e, and is given by

$$K_{iz} = \sigma_0 u_e \left(1 + \frac{2k_B T_e}{\epsilon_{iz}}\right) \exp\left(\frac{-\epsilon_{iz}}{k_B T_e}\right). \tag{3.35}$$

Here σ_0 is a constant associated with the ionisation cross-sectional area, given by

$$\sigma_0 = \pi \left(\frac{e}{4\pi\epsilon_0 \epsilon_{iz}}\right)^2, \tag{3.36}$$

and ϵ_{iz} is the atom ionisation energy. For a He discharge $\epsilon_{iz} = 24.6$ eV. The electron velocity in the bulk of the plasma u_e in Equation 3.35 is derived from assuming a Maxwellian distribution of electron energies, therefore

$$u_e = \left(\frac{8k_B T_e}{\pi m}\right)^{1/2}. \tag{3.37}$$

Equations 3.34, 3.35 and 3.37 contain the T_e dependence that features in equation 3.33. The components of that equation that contain the gas temperature dependence are n_g and K_{mi}; the latter is given by

$$K_{mi} = \sigma_{He^+ - He} u_0, \tag{3.38}$$

where u_0 is the average velocity of ions in the bulk of the plasma. Due to the highly collisional nature of the discharge, the ions in the bulk of the plasma are assumed to be in thermal equilibrium with the neutral atoms. Therefore, assuming a Maxwellian distribution associated with the ions,

$$u_0 = \left(\frac{8k_B T}{\pi M}\right)^{1/2}. \tag{3.39}$$

The assumption of a Maxwellian distribution of the electron energy, however, is not strictly true. In fact, the microplasma generated should have an electron energy distribution (EED) that contains three groups [133, 137]: 1) the low energy electrons that are confined by the ambipolar potential in the bulk of the plasma, 2) the mid-energy electrons capable of escaping from the bulk of the discharge, and 3) the high energy electrons which are due to accelerated secondary electrons in the sheath. Here the high energy

tail of the distribution within the bulk of the plasma can be neglected due to the short penetration depth (a few μm) when compared to the inter-electrode distance (340 μm) [133]. The EED is therefore more accurately described by a bi-Maxwellian distribution. However the density of the mid-energy electrons are several orders of magnitude smaller than that of the of the low energy electrons. It was found that the error associated with neglecting the mid-energy electrons is small in comparison to the statistical error in the fitting of the spectral lines.

3.5.2 Ion density at Sheath Edge in High Pressure Discharges

The ion density at the sheath edge n_s for a high pressure discharge can be found using the equation [120]

$$\frac{n_s}{n_0} = \left[1 + \left(\frac{l u_B}{\pi D_a}\right)^2\right]^{-1/2}, \tag{3.40}$$

where n_0 is the ion density in the bulk of the plasma and D_a is the ambipolar diffusion coefficient. At high pressures D_a is calculated using [120]

$$D_a = \frac{k_B T_e}{M n_g K_{mi}}. \tag{3.41}$$

Furthermore the quasi-neutrality condition in the bulk region of the plasma entails that $n_0 \simeq n_e$. Therefore equation 3.40 can be rewritten as

$$n_s(n_e, T) \simeq n_e \left[1 + \left(\frac{l u_B(T)}{\pi D_a(T)}\right)^2\right]^{-1/2} \tag{3.42}$$

where the T dependence is indicated in parentheses. Both T and n_e are determined by spectroscopic measurements.

3.5.3 Ion Velocity at Sheath Edge

The ion velocity at a collisional sheath edge is calculated using [120]

$$u_s(n_e, T) = \frac{u_B(T)}{\left(1 + \frac{\pi \lambda_{Ds}(n_e, T)}{2\lambda_i(T)}\right)^{1/2}}. \tag{3.43}$$

The Debye length at sheath edge is given by λ_{Ds}

$$\lambda_{Ds} = \left(\frac{\epsilon_0 k_B T_e}{e^2 n_s}\right)^{1/2} \tag{3.44}$$

3.5.4 Calculating Ion Bombardment Energy

The sheath of the microdischarge is low frequency and with fast electron relaxation times, as stated previously, this shows that the discharge can be seen as a sequential set of DC discharges with varying sheath voltages [133]. Using a simple theoretical DC model proposed by [138] the mean ion bombardment energy at the surface γ can be calculated as

$$\gamma = \frac{eE}{n_g \sigma_{He^+-He}}. \tag{3.45}$$

The electric field in the sheath E is [120]

$$E = \left(\frac{3en_s u_s}{2\epsilon_0 (2e\lambda_i/\pi M)^{1/2}}\right)^{2/3} s^{2/3}, \tag{3.46}$$

where s is the time-varying sheath thickness

$$s(t) = \left[1.43\epsilon_0 \left(\frac{2e\lambda_i}{\pi M}\right)^{1/2} \frac{V_s(t)^{3/2}}{en_s u_s}\right]^{2/5}, \tag{3.47}$$

Here $V_s(t)$ is the sheath voltage and when $V_s = V_0$, the peak sheath voltage, then $s = s_m$ from Equation 3.26. The functional form of V, assuming electrodes with equal areas, is strongly non-sinusoidal. When the electrodes are negative the sheath forms and the ions are accelerated towards the surface, however when the electrode potential increases to positive values the sheath collapses. Due to the high electron mobility the sheath voltage at the positively driven electrode is self-rectifying and is effectively held at zero [120]. Therefore, for an RF period, $V_s(t)$ has the form

$$V_s = \begin{cases} U_{RF}\sin(\Omega_{RF}t), & 2n\pi < \Omega_{RF}t < \pi(2n+1), \\ 0, & (2n-1)\pi \leqslant \Omega_{RF}t \leqslant 2n\pi. \end{cases} \tag{3.48}$$

Equations 3.46, 3.47 and 3.48 show that Equation 3.45 for the mean bombardment energy γ is a time varying quantity. The time-averaged mean bombardment energy ϵ_{bom} is then

$$\epsilon_{bom} = \frac{1}{t}\int_0^t \gamma dt \tag{3.49}$$

However since the sheath voltage accelerates the ion towards the surface of a given electrode for only half the RF cycle Equation 3.49 becomes

$$\epsilon_{bom} = \frac{eE_0}{\pi n_g \sigma}\int_0^\pi (\sin\theta)^{2/5} d\theta \tag{3.50}$$

where $\theta = \Omega_{RF} t$ and E_0 is the electric field when $V_s = U_{RF}$.

3.5.5 Estimating Adsorbate Removal Time

As the ions are accelerated across the sheath, they collide with neutral atoms. The momentum transfer between the particles allows for a flux of fast moving neutrals in addition to the accelerated ions to bombard the electrode surface. The time taken for these energetic particles to remove surface adsorbates requires knowledge of the time-averaged particle flux Φ_x with energies above the sputtering threshold, given by

$$\Phi_x = \frac{1}{2\pi}\int_0^\pi \int_{\epsilon_{th}}^\infty \Gamma_x(\epsilon) d\epsilon d\theta, \tag{3.51}$$

where $x \in \{i, n\}$ (denoting the quantity associated the ions and neutrals respectively), Γ_x is the time-varying particle flux and ϵ_{th} is the sputtering threshold.

Taking into account the current continuity equation [120] it was found that

$$\int_0^\infty \Gamma_i d\epsilon = n_s u_s \tag{3.52}$$

and therefore that the time-varying ion flux energy distribution is then [138]

$$\Gamma_i(\epsilon) d\epsilon = \frac{n_s u_s}{\gamma} \exp\left(-\frac{\epsilon}{\gamma}\right) d\epsilon. \tag{3.53}$$

Equation 3.51 can then be re-written to calculate Φ_i as

$$\Phi_i = \frac{1}{2\pi}\int_{\epsilon_{th}}^{\epsilon_{up}}\int_0^{\pi}\frac{n_s u_s}{\gamma_0(\sin\theta)^{2/5}} \times \exp\left(\frac{-\epsilon}{\gamma_0(\sin\theta)^{2/5}}\right)d\theta d\epsilon. \tag{3.54}$$

The instantaneous mean ion bombardment energy γ_0 occurs when $E = E_0$ and ϵ_{up} is the absolute upper limit of the ion energy. Here ϵ_{up} is defined as the energy of an ion crossing the sheath at maximum potential without any collisions, which is given by

$$\epsilon_{up} = \frac{M}{2}\left(\frac{2s_m e E_0}{M} + u_s^2\right). \tag{3.55}$$

Typically, 350 eV $\leqslant \epsilon_{up} \leqslant$ 500 eV.

The bounds of the neutral flux energy distribution $\Gamma_n(\epsilon)d\epsilon$ for an instantaneous sheath voltage can be found in [138]. The upper limit is given by

$$\Gamma_n(\epsilon)d\epsilon < \frac{\sigma_{He^+-He}}{\sigma_{He-He}}\left(1 + \frac{2\gamma}{\epsilon} + \frac{2\gamma^2}{\epsilon^2}\right)\Gamma_i(\epsilon)d\epsilon \tag{3.56}$$

and the lower limit of the neutral flux is

$$\Gamma_n(\epsilon)d\epsilon > \frac{\sigma_{He^+-He}}{\sigma_{He-He}}\Gamma_i(\epsilon)d\epsilon. \tag{3.57}$$

The calculation for Φ_n is done in a similar fashion to Φ_i, for both the upper and lower bound limits of $\Gamma_n(\epsilon)d\epsilon$. Using these limits an average value for Φ_n is then calculated. Figure 3.8 shows two examples of the ion and neutral flux distributions calculated at different pressures and voltages.

The removal of an adsorbate layer is described by the rate equation [127]

$$\frac{dN_a}{dt} = -\Phi_x \sigma_a N_a(t), \tag{3.58}$$

where N_a is the adsorbate surface density and σ_a is the sputtering cross-section (see Section 3.3 for more details). Solving equation (3.58) gives

$$N_a = N_0 \exp(-t/\tau_a), \tag{3.59}$$

where N_0 is the initial adsorbate surface density and $\tau_a = (\Phi_x \sigma_a)^{-1}$ is the time constant for the process. The time taken to reach a target surface density for the adsorbate, N_t,

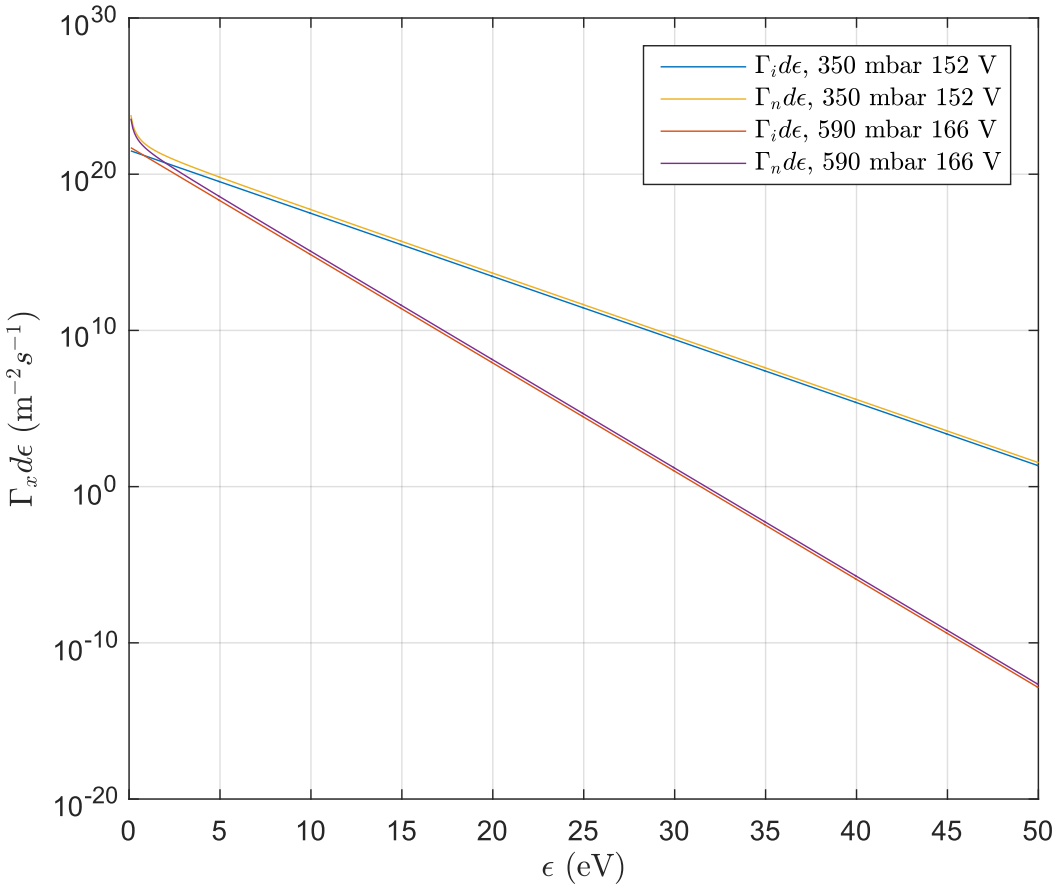

FIGURE 3.8: Ion and neutral flux energy densities combined for He discharge generated in Type B microtrap at $\Omega_{RF}/2\pi = 23$ MHz. This calculation is for maximum sheath voltage and does not take into account the voltage time dependence.

is then given by

$$t_{clean} = \left(\ln \frac{N_0}{N_t} \right) \tau_a. \tag{3.60}$$

Studies have shown that atmospheric hydrocarbon contamination that can build up on the surface of gold, is roughly two C atoms thick [139]. An estimate for $N_a(t = 0) = N_0$ was made on the basis that the H-C bond length is, on average, 110 pm [140]. Assuming a grid of these bonds in two monolayers, the pre-processing surface adsorbate density can be estimated as

$$N_0 = \frac{1}{2 \times 110 \times 10^{-12} \times 110 \times 10^{-12}} = 4.1 \times 10^{19} \text{ m}^{-2}. \tag{3.61}$$

In reality, the hydrocarbon density will depend on the structure of the hydrocarbons themselves and the adsorption sites that exist on the electrode surface.

3.6 Equation Flow Charts

This section contains equation flow charts that are intended as an aid to the reader; they summarise the equations used (from Section 3.5) alongside the assumptions made (see Section 3.4) at each stage of the calculation. Within the flow charts in this section, the calculated parameters are in green, the experimental parameters are in blue and the assumptions or approximations made are detailed in red. Figure 3.9 shows the equations used to calculate the ion density at the sheath edge n_s, the ion velocity at the sheath edge u_s and the electron temperature T_e. The calculation of these plasma parameters depend on the gas temperature T and the electron density n_e which is determined by using optical emission spectroscopy (see Section 4.2). Figure 3.10 shows the equations used to calculate both the ion and neutral flux to the electrode surface and subsequently the cleaning time. The calculations in this chart require n_s, u_s and T_e from Figure 3.9.

3.7 Summary

A theoretical frame work has been established to justify the treatment of a microplasma generated in the ion microtraps as a low frequency, high-pressure discharge with collisional and high-voltage sheaths. Furthermore, key assumptions and approximations made have also been outlined including the treatment of the electron energy distribution as Maxwellian. To assess effectiveness of a generated microplasma the calculations needed for estimating the adsorbate removal time were also presented. From the system of equations developed, it is clear that there are two experimental parameters that need to be identified; namely the electron density n_e and the gas temperature T. These parameters will be determined with optical emission spectroscopy (OES), the detail of which can be found in the next chapter.

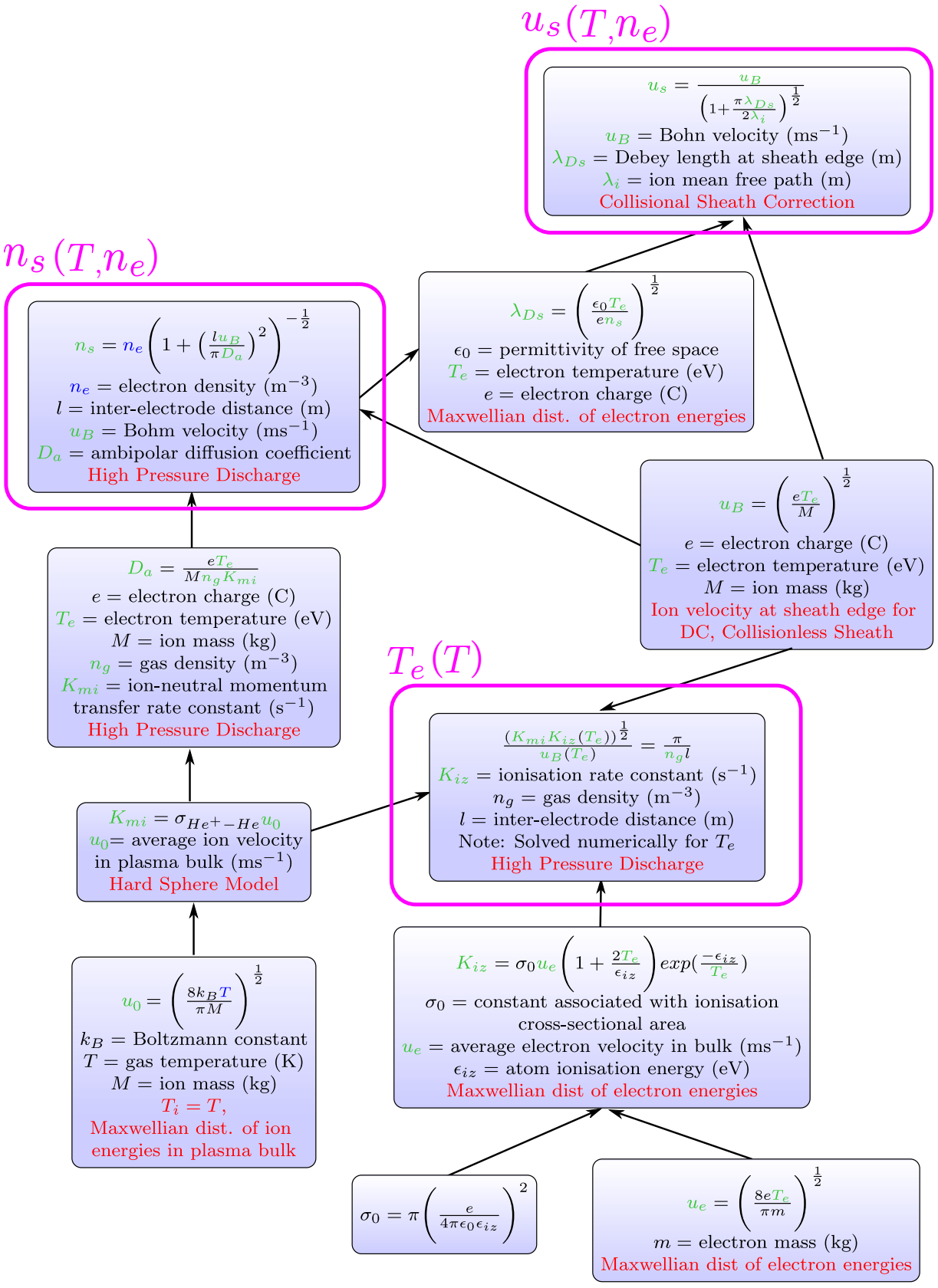

FIGURE 3.9: Equation flow-chart for the calculation of n_s, u_s and T_e.

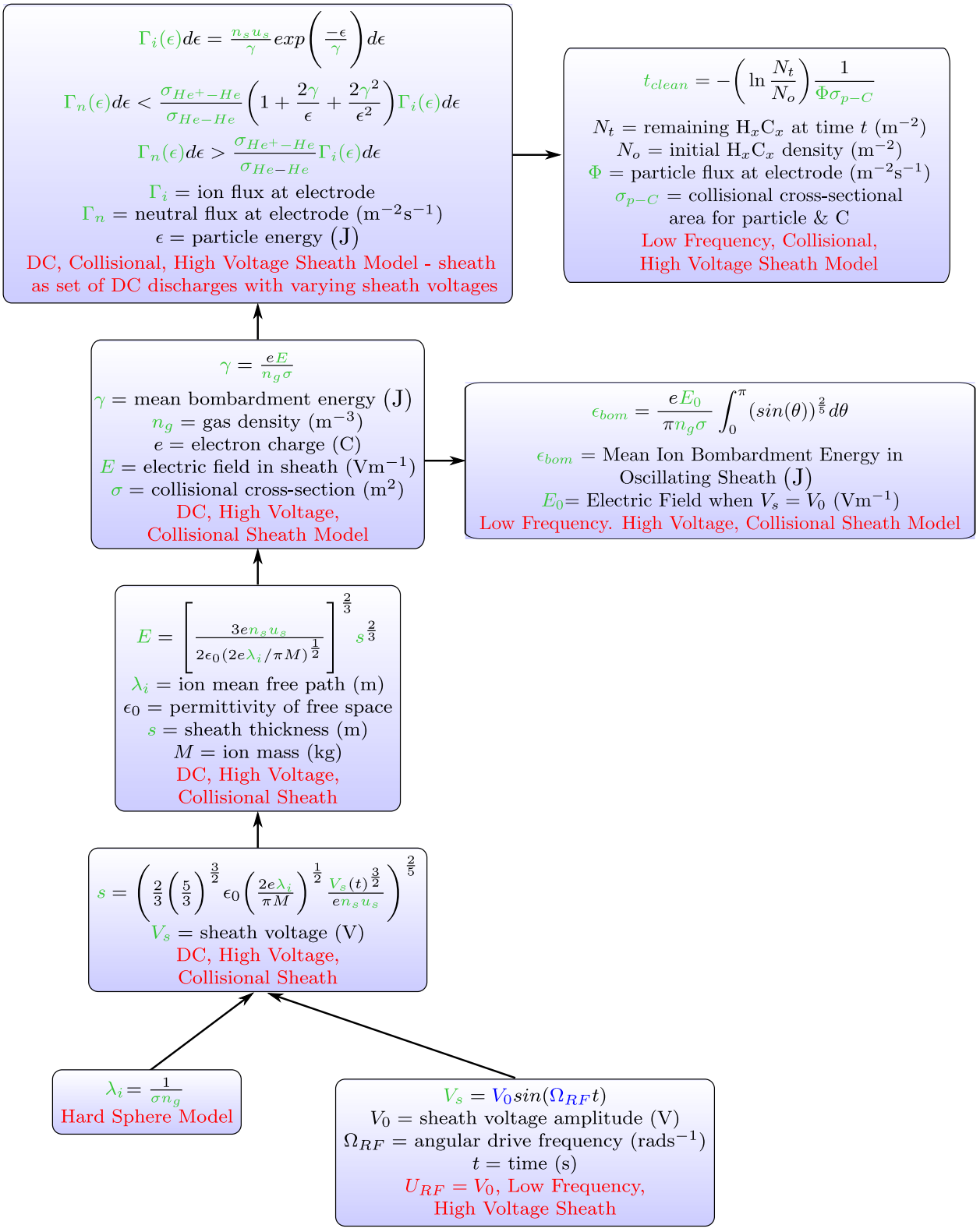

FIGURE 3.10: Equation flow-chart for the calculation of the particle flux and cleaning time.

Chapter 4

Microplasma Experimental Implementation

This chapter contains the experimental implementation of the theoretical framework that was presented in Chapter 3. The calculations in Chapter 3 rely on being able to measure the electron density n_e and the gas temperature T. These parameters will be determined by optical emission spectroscopy (OES). With these values an estimation of the time needed to remove amorphous hydrocarbon contamination can then be made.

Ultimately the microdischages would be generated using the system outlined in Chapter 2, however for the purposes of testing a separate analogous system was used which will be detailed in Section 4.1. The necessary calculations for OES and its application in the lineshape fitting procedure will be highlighted in Section 4.2. Before the microplasma was trialled in the ion traps themselves, the plasma was generated in test wire structures that were made with a similar electrode spacing to that of the traps. These wire structures were used as a means of initially exploring the experimental parameter space needed for microplasma generation; the results are shown in Section 4.3. Section 4.4 shows the results associated with generating the microplasma in the ion microtraps themselves using He and He:N_2 gas mixtures.

4.1 Experimental Setup

For the microplasma testing a similar vacuum set-up was used to the one described in Chapter 2.4 and in [106]. The main differences are that the microplasma set-up

offers straight-forward interchanging of trap chips and the ability to test gas mixtures; a schematic of the system can be seen in Figure 4.1. The trap is attached to the vacuum system in a stack consisting of a butyl rubber seal between either side of the ceramic chip carrier and the vacuum chamber. The stack is than clamped together and the butyl rubber under pressure forms a seal that allows for pressures down to 10^{-7} mbar. The use of the butyl seals allows for a trap to be easily removed and therefore a number of traps to be tested in a more efficient fashion when compared to the use of indium seals. An active strain gauge (Edwards D35736000, 1 mbar $\leqslant P \leqslant$ 1000 mbar) and a Pirani gauge (Edwards D02602000, 10^{-3} mbar $\leqslant P \leqslant$ 1000 mbar) in conjunction with a gauge controller (Edwards D39591500), were used to monitor the pressure in the chamber. The system had the capability of using two gases that were introduced into the chamber using a leak valve; this allowed for plasma testing of gas mixtures.

Similar to the system described in Section 2.4, the vacuum seal that is formed on the chip carrier still allows for air-side access to the LCC gold plated feed-throughs. Connectors are then mounted onto these feed-throughs in order to control the potential on the Si bulk and the DC electrodes. The RF signal used to create the capacitively-coupled discharge was controlled by a National Instruments frequency generator (PXI 5404) in line with a variable attenuator (Minicircuits ZX73-2500-S+) which provided the required amplitude range. The signal was then amplified (Minicircuits ZHL-5W-1) and connected to a bi-directional coupler and a tank circuit which is the combination of a helical resonator [114, 141] and the trap. The bi-directional coupler samples the forward-going and reflected RF signal from the trap, and each of these signals is measured by a power meter (Minicircuits PWR-4GHS). Three different helical resonators were used in the testing of the microplasmas; they resulted in resonant frequencies of 8 MHz, 18 MHz, and 23 MHz when combined with a microtrap. The resonance is measured by scanning the frequency and sampling the transmitted and reflected signals from the bi-directional coupler; the minimum in reflectivity determines the resonance of the system. An example of a measured resonance with a microtrap type A can be seen in Figure 4.2.

To record the optical emission spectrum, the light from the plasma is imaged onto a multi-mode fibre (50 μm core diameter, 0.22 NA). The positions of the lenses and the fibre are fixed in relation to each other, however this assembly can be translated in three dimensions which allows for some spacial resolution. The overall profile of the plasma generated in the aperture is also recorded by a CMOS camera (Thorlabs DCC3240M)

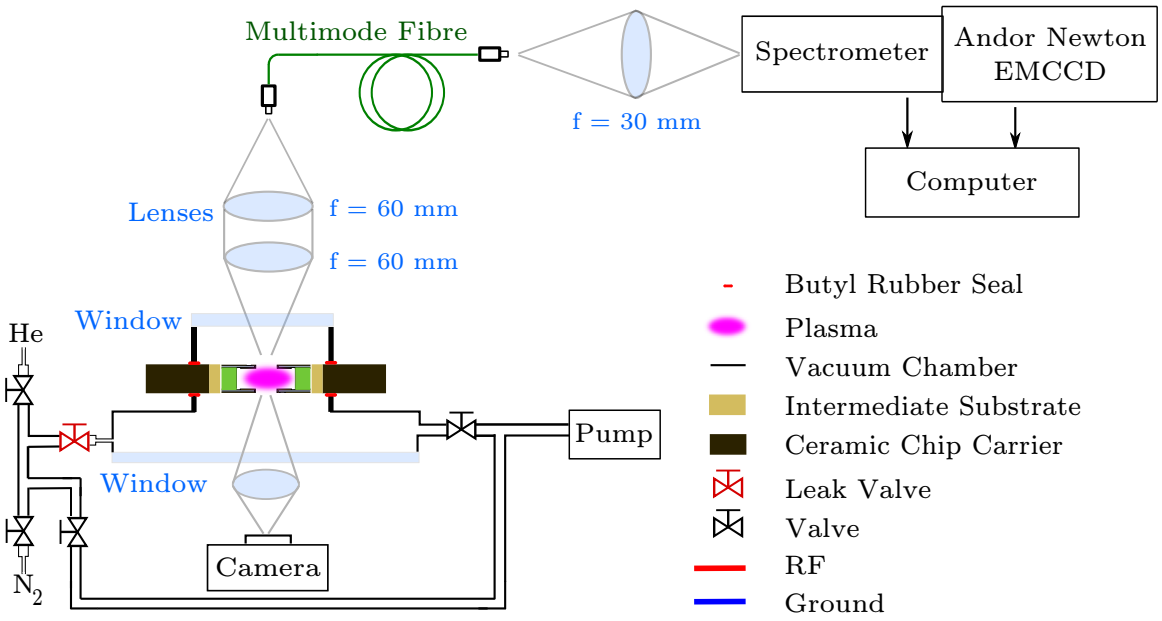

FIGURE 4.1: Experimental set-up to record the optical emission generated by a microplasma in the trapping aperture.

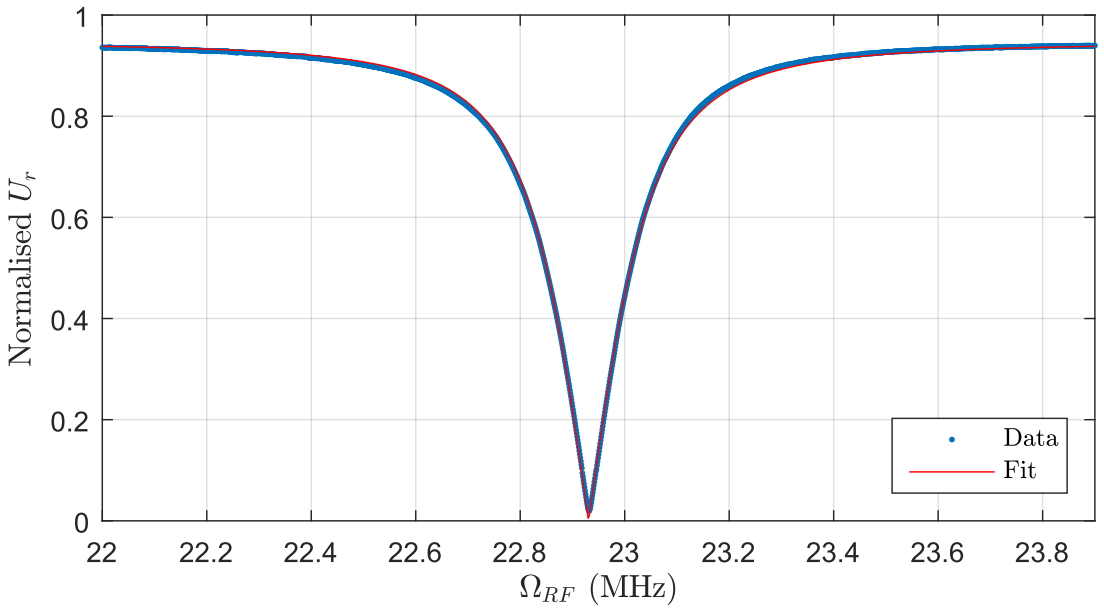

FIGURE 4.2: Example of an RF frequency scan using microtrap type A in conjunction with the 23 MHz helical resonator.

and, as the fibre and the camera are on the same optical axis, it can be used to adjust the imaging spot of the fibre. At the other end of the fibre, another achromatic lens is used to couple the light into an imaging spectrometer (Horiba iHR550) with magnification of 0.7. The spectrum is then recorded by an electron multiplying CCD camera (Andor Newton DU971N-FI) which has a 16 μm pixel size. During standard operation the entrance slit width of the spectrometer was set to 34 μm, and a 1200 lines/mm grating was used to achieve a measured resolution of 0.029(4) nm.

Due to the operating parameters of the plasma studied, the microplasma emission was relatively weak. To record a spectral lineshape, 10 sequential EMCCD images where captured at exposure times of 10 seconds each, and then averaged in order to achieve sufficient signal-to-noise. The measurements were made sequentially in order to detect any time varying plasma instability. A background measurement was also made using the same detection parameters but without the plasma being generated. The lineshape with the background subtracted was used for analysis and determination of n_e and T.

4.2 Optical Emission Spectroscopy

The essential plasma parameters needed to determine to the effect of the plasma at the electrode surface are the electrode density n_e and the gas temperature T. Many of traditional techniques for measuring these quantities involve intrusive methods, such as Langmuir probes, which can have a large perturbative effect on plasmas with small length scales [133]. Conversely, optical emission spectroscopy (OES) is a non-intrusive method of finding the relevant plasma parameters which is suited to microdischarge operation [133, 135, 142]. OES measures the broadening of the spectral lines emitted from the plasma. By decomposing the broadening into its constituent contributions n_e and T can be found.

4.2.1 Broadening Mechanisms

The spectral spread of optical emission from the plasma consists of Lorenztian and Gaussian components which convolve to yield a Voigt profile. An example of each of these lineshapes can be seen in Figure 4.3. The linewidth of the Gaussian component, $\Delta\lambda_G$, is defined as

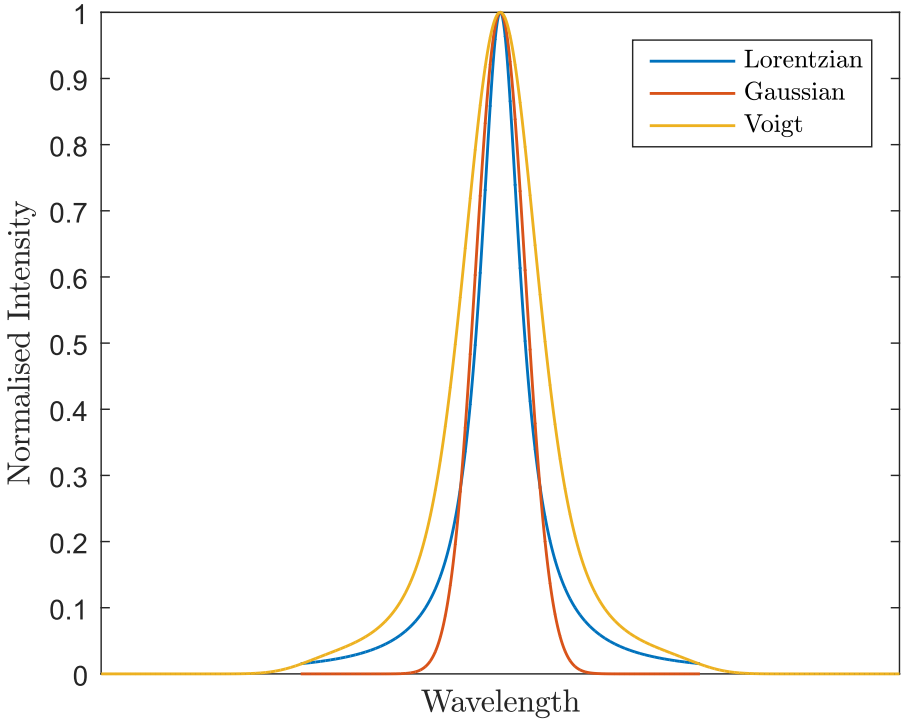

FIGURE 4.3: Example of a Gaussian, Lorentzian and their convolution which is a Voigt profile.

$$\Delta\lambda_G = (\Delta\lambda_I^2 + \Delta\lambda_D^2)^{1/2}, \tag{4.1}$$

where $\Delta\lambda_I$ and $\Delta\lambda_D$ are the contributions arising from instrument and Doppler broadening respectively. The spectrometer property $\Delta\lambda_I$ was measured to be on average 0.029(4) nm via a Gaussian fit (using a Levenberg-Marqardt algorithm) to the spectral line arising from a He-Ne laser. For each spectral data set obtained the spectrometer was re-calibrated and the $\Delta\lambda_I$ remeasured. An example of the measured lineshape for the instrument broadening can be seen in Figure 4.4.

The linewidth of the Lorentzian component, $\Delta\lambda_L$, is a combination of the van der Waals, resonance and Stark broadening, which are quantified by linewidth contributions $\Delta\lambda_{VW}$, $\Delta\lambda_R$ and $\Delta\lambda_S$ respectively:

$$\Delta\lambda_L = \Delta\lambda_{VW} + \Delta\lambda_R + \Delta\lambda_S \ . \tag{4.2}$$

Within this section, the wavelengths and linewidths are in units of nm in all equations. In addition, many of the units are not SI for ease of use, however in those instances it

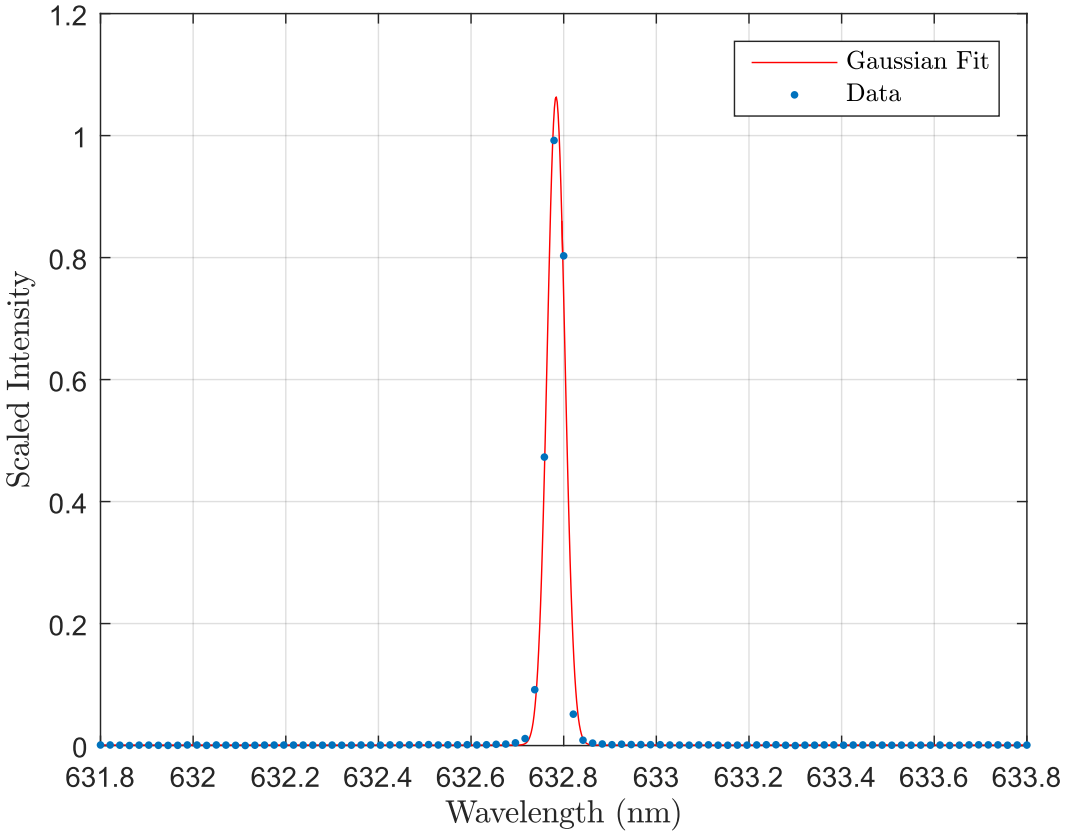

FIGURE 4.4: Example of instrument broadening profile of the spectroscopy set-up measured using a He-Ne laser. In this instance the linewidth was measured to be 0.0271(4) nm.

will be clearly stated. Otherwise, the units can be assumed to be in SI.

Doppler Broadening

The distribution of velocities of the ions and atoms in the plasma leads a range of Doppler shifts associated with a spectral line; which consequently broadens the spectrum. The Doppler Broadening $\Delta\lambda_D$ is defined by the following equation [142–145]:

$$\Delta\lambda_D = 2.919 \times 10^{-17} \lambda_0 \left(\frac{T}{M}\right)^{1/2} \tag{4.3}$$

where λ_0 is the centre transition wavelength, T is the temperature of the emitters and M is atomic mass of the emitter. Here T is assumed to be equal to the gas temperature in the microplasma due to the high collisional frequency between the emitters and neutral atoms.

Van der Waals Broadening

Van der Waals broadening is the result of the dipole of the excited emitter particle interacting with the induced dipole of the surrounding ground state atoms during a collisional process. The following equations associated with the van der Waals broadening are found in [143]. The spectral linewidth, $\Delta\lambda_{VW}$ is

$$\Delta\lambda_{VW} = 8.18 \times 10^{-19}\lambda_0^2(R^2\alpha)^{2/5}\left(\frac{T}{\mu}\right)^{3/10} n_g \tag{4.4}$$

where R^2 is a transition-dependent constant (in units of the Bohr radius a_0), α is the average polarisability (in cm^3), μ is the emitter-perturber reduced mass (in amu) and n_g is the neutral gas density (in cm^{-3}). Here R^2 can be calculated as $R^2 = R_U^2 - R_L^2$, where L(U) is the lower (upper) energy level of the transition,

$$R^2_{L(U)} = \frac{n^{*2}_{L(U)}}{2}(5n^{*2}_{L(U)} + 1 - 3l_{L(U)}(l_{L(U)} + 1)). \tag{4.5}$$

The orbital momentum quantum number of the transition level is denoted by $l_{L(U)}$ and the square of the effective quantum number $n^{*2}_{L(U)}$ is

$$n^{*2}_{L(U)} = \frac{I_H}{I_{IP} - E_{L(U)}} \tag{4.6}$$

where I_H is the ionisation potential of hydrogen, I_{IP} is the ionisation potential of the emitter atoms (both in cm^{-1}) and $E_{U(L)}$ is the energy of the upper or lower levels of interest (in cm^{-1}). The average polarisability of the emitter atoms can be estimated using

$$\alpha = \frac{9}{2}a_0^3\left(\frac{3I_H}{4E_{ex}}\right)^2 \tag{4.7}$$

where a_0 is in units of cm, E_{ex} (in cm^{-1}) is the energy of the first excited level of the perturber particles.

Resonance Broadening

Resonance (or self) broadening [146] occurs due to collisions with neighbouring identical species, where the transition giving rise to the spectral emission has an upper or lower

energy level with an electric dipole coupling to the ground state [143]. The associated contribution to linewidth, $\Delta\lambda_R$, can be calculated using [135, 145, 146]

$$\Delta\lambda_R = 8.61 \times 10^{-28} \left(\frac{g_L}{g_U}\right)^{1/2} \lambda_r f_r \lambda_0^2 n_{emit} \tag{4.8}$$

where $g_{L(U)}$ is the statistical weight of the lower (upper) level of the transition, λ_r and f_r are the resonance wavelength and the oscillator strength respectively of the transition coupling to the ground state, and n_{emit} is the ground state density of the emitter atoms (in cm^{-3}).

Stark Broadening

Due to the presence of charged perturbers in the microplasma such as ions and electrons, the Stark effect can broaden the spectral emission. The magnitude of the effect varies across different species. The Stark broadening contribution to the linewidth, $\Delta\lambda_S$ for H lines in a non-equilibrium discharge is calculated as [147]

$$\Delta\lambda_S = 2.05 \times 10^{-11} n_e^{0.63}, \tag{4.9}$$

where n_e is in cm^{-3}. For the Stark broadening of the He 667 nm transition $\Delta\lambda_{S,He}$, the analysis in [148] defines the contribution as

$$\Delta\lambda_{S,He} = 2\omega_0 \left(\frac{n_e}{n_{e,0}}\right) \left[1 + 1.75\alpha_0 \left(\frac{n_e}{n_{e,0}}\right)^{1/4} \times \left(1 - 0.068 n_e^{1/6} T_e^{-1/2}\right)\right] \tag{4.10}$$

where $2\omega_0$ is the electron-impact half width parameter, α_0 is the ion broadening parameter, T_e is the electron temperature and $n_{e,0}$ is the reference electron density. Both $\omega_0(T_e)$ and $\alpha_0(T_e)$ are functions of the electron temperature and values for both of these parameters can be found for a wide range of elements in [148, 149]. A linear extrapolation between tabulated values was used order to estimate the parameters for values of T_e not listed. Examples of the values used here can be seen in Table 4.1.

The use of Equation 4.10 however is limited to the instances where the following inequalities are satisfied [143]

$$8.99 T_e^{-1/2} n_e^{1/6} \times 10^{-2} \leq 0.8 \tag{4.11}$$

TABLE 4.1: Examples He 667 nm Stark broadening parameters for the relevant range of T_e. The values at $T_e = 20000$ K and $T_e = 40000$ K are taken from [149], the others are calculated linearly.

$\mathbf{T_e}$	$\omega_\mathbf{e}/\mathbf{2}$	**A**
20000	36.6	0.52
25000	35.7	0.53
30000	34.8	0.54
35000	33.8	0.55
40000	32.9	0.56

$$0.05 \leq \alpha_0 n_e^{1/4} \times 10^{-4} \leq 0.5. \tag{4.12}$$

For the following investigation both of these conditions are met.

4.2.2 Lineshape Fitting Procedure

For a specific combination of P and U_{RF}, the following analysis details how the plasma parameters T, n_e were determined. Both the He and the Hα lines depend on both parameters, therefore both lines were fit to simultaneously, as part of the same spectrum, in order to determine both parameters. The spectral linewidths were measured by fitting a Voigt profile of the form [142]

$$f_V = \frac{2ln2}{\pi^{3/2}} \frac{\Delta\lambda_L}{\Delta\lambda_G^2} \times \int_{-\infty}^{+\infty} \frac{e^{-t^2}}{[2\sqrt{ln2}\frac{\lambda-\lambda_0}{\Delta\lambda_G} - t]^2 + [\sqrt{ln2}\frac{\Delta\lambda_L}{\Delta\lambda_G}]^2} dt \tag{4.13}$$

to each of the lines. Therefore the total fitted function was

$$f_{V,H,He} = f_{V,He} + f_{V,H}, \tag{4.14}$$

where the contributions $f_{V,He}$ and $f_{V,H}$ are derived from Equation 4.13 with appropriate $\Delta\lambda_L$ and $\Delta\lambda_G$ for the He and Hα spectral lines. Equation 4.14 is fit to both the measured spectral lines using the Levenberg-Marquardt method, which is a non-linear least squares fitting procedure.

Due to the low Hα gas concentration the $f_{V,H}$ profile has has negligible resonance broadening. Therefore Equation 4.2 is reduced to

$$\Delta\lambda_L = \Delta\lambda_{VW} + \Delta\lambda_S. \tag{4.15}$$

Using Equations 4.3, 4.4, and 4.9 the Gaussian and the Lorentzian components to the Hα line broadening can be written as

$$\Delta\lambda_G = (\Delta\lambda_I^2 + 5.129 \times 10^{-13}\lambda_0^2 T)^{1/2}, \tag{4.16}$$

and

$$\Delta\lambda_L = \left(4.652 \times 10^{-9}\frac{P\lambda_0^2}{T^{7/10}}\right) + (2.05 \times 10^{-11} n_e^{0.63}), \tag{4.17}$$

where P is in mbar and n_e in cm^{-3}. For the $f_{V,He}$ profile on the other hand, using Equations 4.3, 4.4, 4.8 and 4.10 the $\Delta\lambda_G$ and $\Delta\lambda_L$ contributions are

$$\Delta\lambda_G = (\Delta\lambda_I^2 + 1.282 \times 10^{-13}\lambda_0^2 T)^{1/2}, \tag{4.18}$$

and

$$\Delta\lambda_L = \left(3.537 \times 10^{-9}\frac{P\lambda_0^2}{T^{7/10}}\right) + \left(5.811 \times 10^{-8}\frac{P_{emit}\lambda_0^2}{T}\right) + \frac{2\omega_0 n_e}{10^{18}}\left(1 + \alpha_0 n_e^{1/4} 1.75 \times 10^{-4.5}\left(1 - 0.068 n_e^{1/6} T_e^{-1/2}\right)\right). \tag{4.19}$$

Equation 4.19 has a T_e dependence which in turn is a function of T. The process for solving for T_e is outlined in Section 3.5.1. Due to the complexity of the function, it is difficult to solve for T_e in terms of T analytically, therefore for each value of T in the fitting procedure T_e is numerically solved using a Newton-Raphson method.

Constants associated with the fitting of a Voigt lineshape to either the He I 667 nm or the Hα 656 nm lines can be seen in Table 4.2. An example of the fit to the He I and Hα line can be seen in Figure 4.5.

Transition	Symbol	Value	Reference
He	g_L	1	[146]
He	g_U	3	[146]
He	λ_r	58.4334 nm	[146]
He	f_r	0.2762	[146]
He	I_{IP}	198311 cm^{-1}	[146]
He	E_L	171135 cm^{-1}	[146]
He	E_U	186105 cm^{-1}	[146]
He	E_{ex}	171135 cm^{-1}	[146]
He, Hα	I_H	109737 cm^{-1}	[143]
Hα	E_L	82259 cm^{-1}	[150]
Hα	E_U	97492 cm^{-1}	[150]

TABLE 4.2: Constants used in fitting procedure outlined in Section 4.2.2. He and Hα denote values associated with the He I 667 nm transition and Hα 656 nm transition respectively.

In order to determine that the fits were functioning as expected, another chi-squared minimisation routine was made which calculated the chi-squared values for a matrix of T and n_e values. This was then used to map out the chi-squared functional space and to determine if there were likely to be any additional local minima that could disrupt the Levenberg-Marqardt fitting algorithm. An example of the chi squared mapping can be seen in Figure 4.6. The fit cycled through a coarse matrix of n_e and T and, after determining the minimum, each of the adjacent points around the minimum in the matrix is then used to form the bounds of another finer matrix. This step was then repeated a further two times to achieve a resolution in T of 1 K and 1×10^{12} cm^{-3} in n_e. The manual fitting method showed that the chi-squared functional space was a smoothly varying curve and that the two fitting methods only showed a small deviation in the fit parameters of 1 % and 4 % in T and n_e respectively.

4.3 Microplasma in Wire Structures

The initial stages of microplasma testing were conducted not with the ion traps themselves but with wire micro-structures that had a similar spacing to the electrodes of the trap. This was done so that the plasma parameters could be mapped out and the system

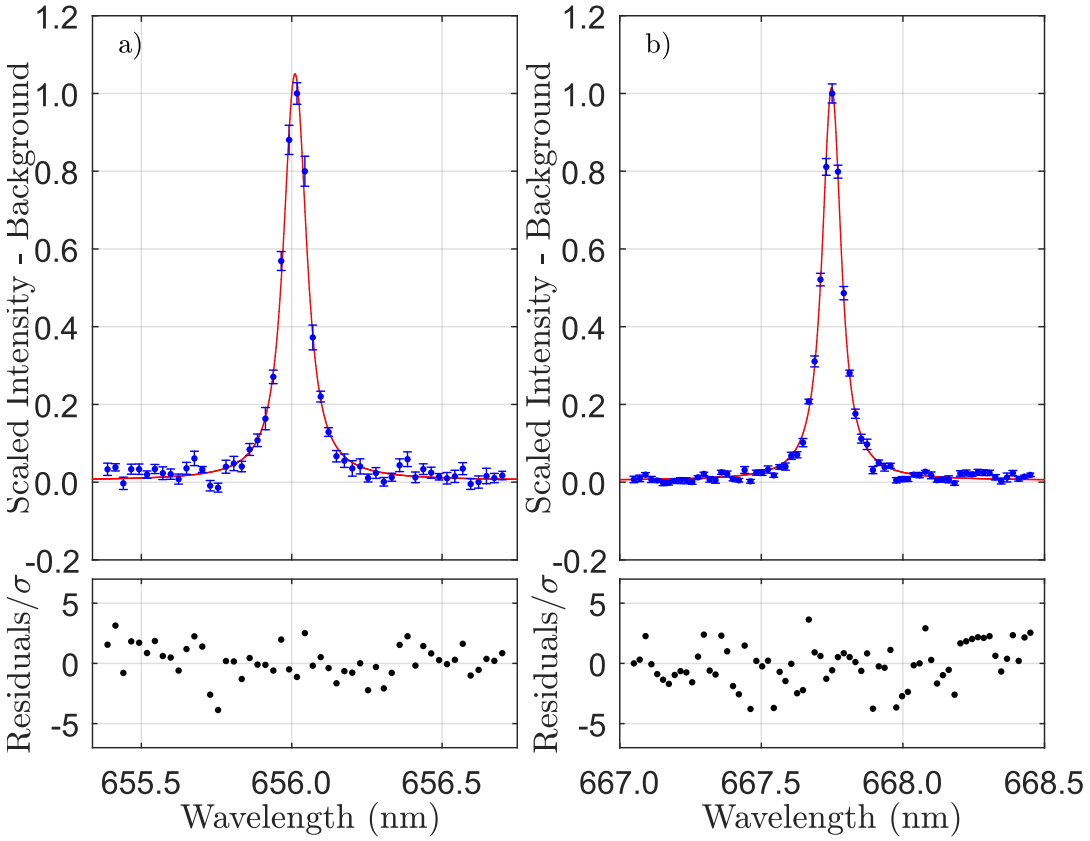

FIGURE 4.5: Examples of He I 667 nm and Hα 656 nm spectral line data observed at plasma parameters of $P = 590$ mbar, $\Omega_{RF}/2\pi = 23$ MHz and $U_{RF} = 182$ V. From the fit to both lineshapes, $T = 323(12)$ K and $n_e = 5.8(7)\times10^{14}$ cm^{-3}, where the errors are 1σ statistical from the fit only. The errorbars reflect the 1σ error from averaging over 10 recorded data sets. a) Hα 656 nm line data (blue points) and Voigt lineshape fitted using equations 4.14, 4.16 and 4.17. Broadening contributions: $\Delta\lambda_I$=0.0261 nm, $\Delta\lambda_D$= 0.0085 nm, $\Delta\lambda_{VW}$=0.0207 nm, $\Delta\lambda_S$=0.0408 nm. The studentised residuals are shown below the lineshape. b) He I 667 nm line data (blue points) and Voigt lineshape (red line) fitted using equations 4.14, 4.18 and 4.19. Broadening contributions: $\Delta\lambda_I$=0.0261 nm, $\Delta\lambda_D$= 0.0043 nm, $\Delta\lambda_{VW}$=0.0183 nm, $\Delta\lambda_R$=0.0473 nm, $\Delta\lambda_S$=0.0046 nm. The studentised residuals are shown below the lineshape.

tested in a fashion that minimised the risk of damaging the traps while still establishing the principles of operation.

The wire micro-structure was made by gluing (using Torr Seal adhesive) two 250 μm diameter gold-plated copper wires onto an empty chip carrier with a 350 μm wire spacing. One wire was then wirebonded to the RF supply and another to ground. Examples of these structures generating a discharge can be seen in Figure 4.7. A number of these structures were made to test the generation of a microdischarge with varying frequency, voltage, pressure and gas type. There were three gases tested; He, N_2 and O_2, the results can be seen in Figures 4.8, 4.9 and 4.10 respectively. The graphs reflect when the plasma had the greatest coverage in the aperture, good stability and with no other

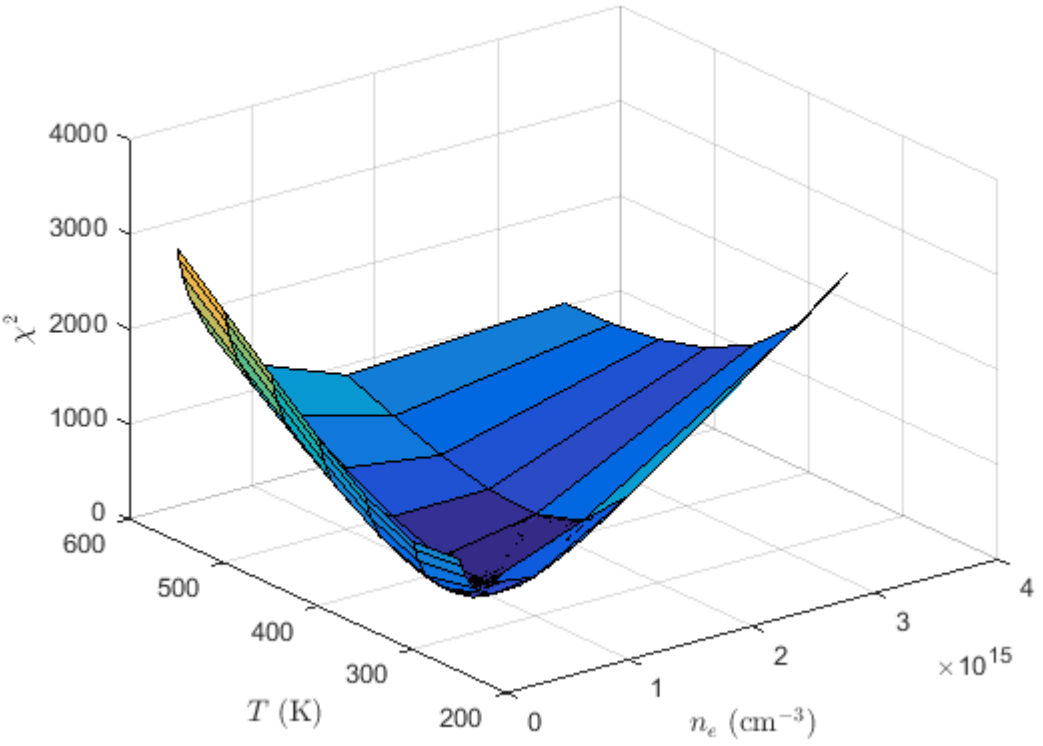

FIGURE 4.6: An example of a chi-squared map for a matrix of T and n_e values, at $U_{RF} = 172$ V and $P = 510$ mbar.

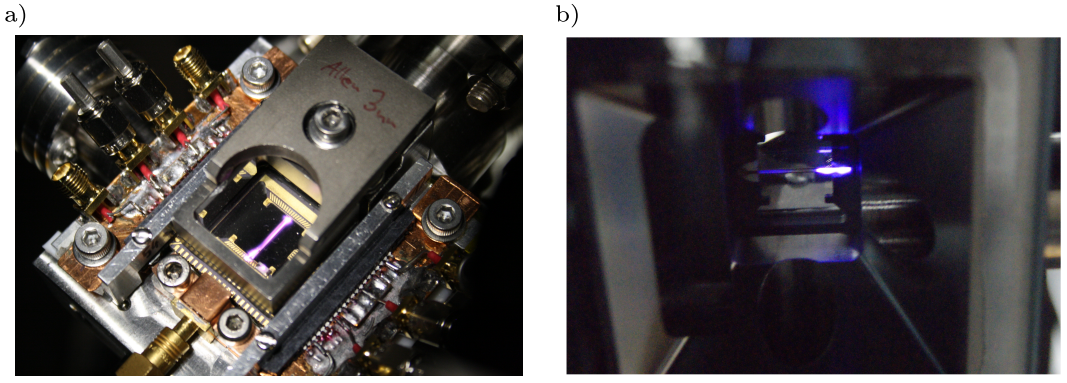

FIGURE 4.7: Examples of wire structures generating a microplasma, a) shows a He discharge and b) shows an N_2 discharge.

plasma generated outside the aperture. The exceptions to this is the O_2 plasma data, where there was no stability and the coverage was localised into spots between the two wires, and the N_2 data at $\Omega_{RF}/2\pi = 9$ MHz which was was also unstable.

The He discharge was maintained over the greatest pressure range and also at the lowest voltage, 140 V $\leq U_{RF} \leq$ 330 V. Many of the test traps that will be discussed in Section 4.4 have risk forming an electrical short at around 300 V. The N_2 and the O_2

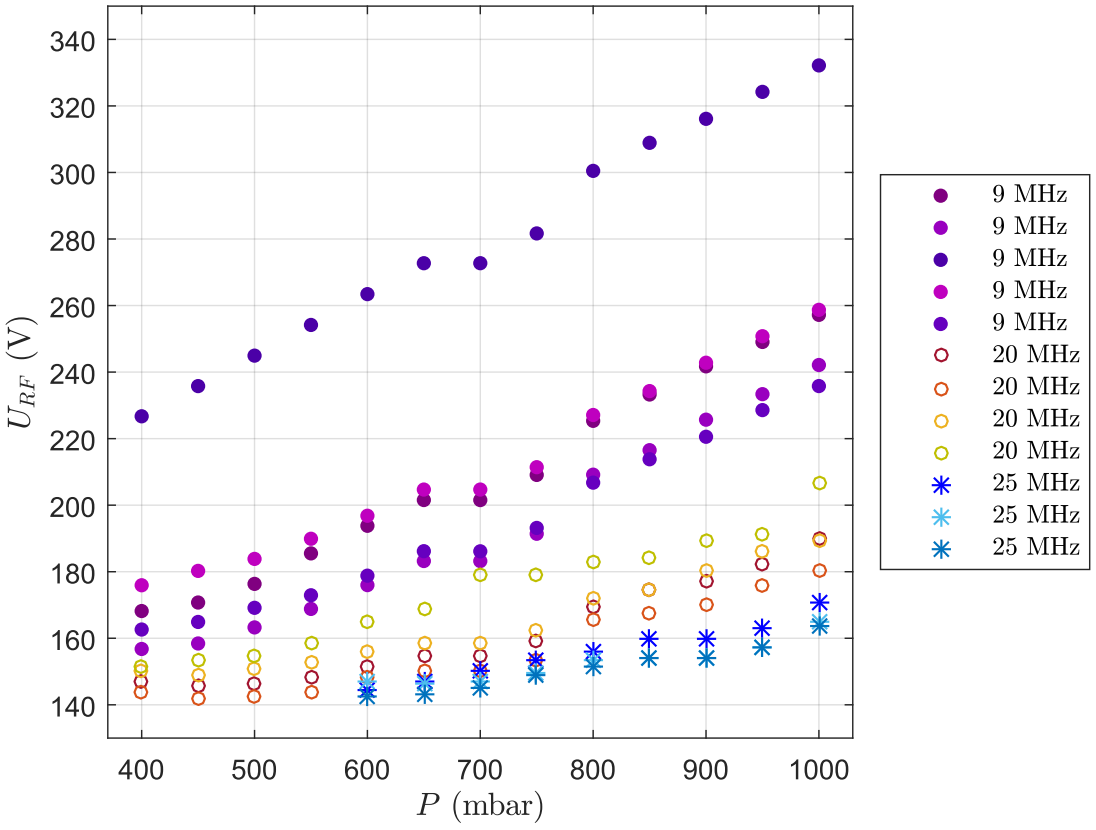

FIGURE 4.8: Plasma operation parameters for a He microdischarge in a wire microstructure. The data describes the most optimum point to generate the discharge to achieve a stable homogeneous plasma solely in region between the wires.

plasmas both had to be operated above 300 V; at 340 V $\leq U_{RF} \leq$ 520 V and 400 V $\leq U_{RF} \leq$ 640 V respectively. This is to be expected since the breakdown voltage for He is lower than that of the other gasses [144, 151–153]. It should be noted that there is an anomalous data set in Figure 4.8 at 9 MHz which was approximately 50 V higher than the other data sets at the same frequency. The exact cause of this is unknown. The He plasma operated at higher pressures and over a greater pressure range (400 mbar $\leqslant P \leqslant$ 1000 mbar) than N_2 (25 mbar $\leqslant P \leqslant$ 100 mbar) and O_2 (2 mbar $\leqslant P \leqslant$ 18 mbar).

With increasing frequency there is a decrease in the voltage needed to sustain a plasma in the aperture. Additionally, at higher frequencies the plasma tended to be more homogeneous in the aperture and with better coverage. Therefore a He plasma at 23 MHz, in a range of 400 mbar $\leqslant P \leqslant$ 1000 mabar with = 100 V $\leqslant U_{RF} \leqslant$ 200 V was estimated to be the operating range for ion traps.

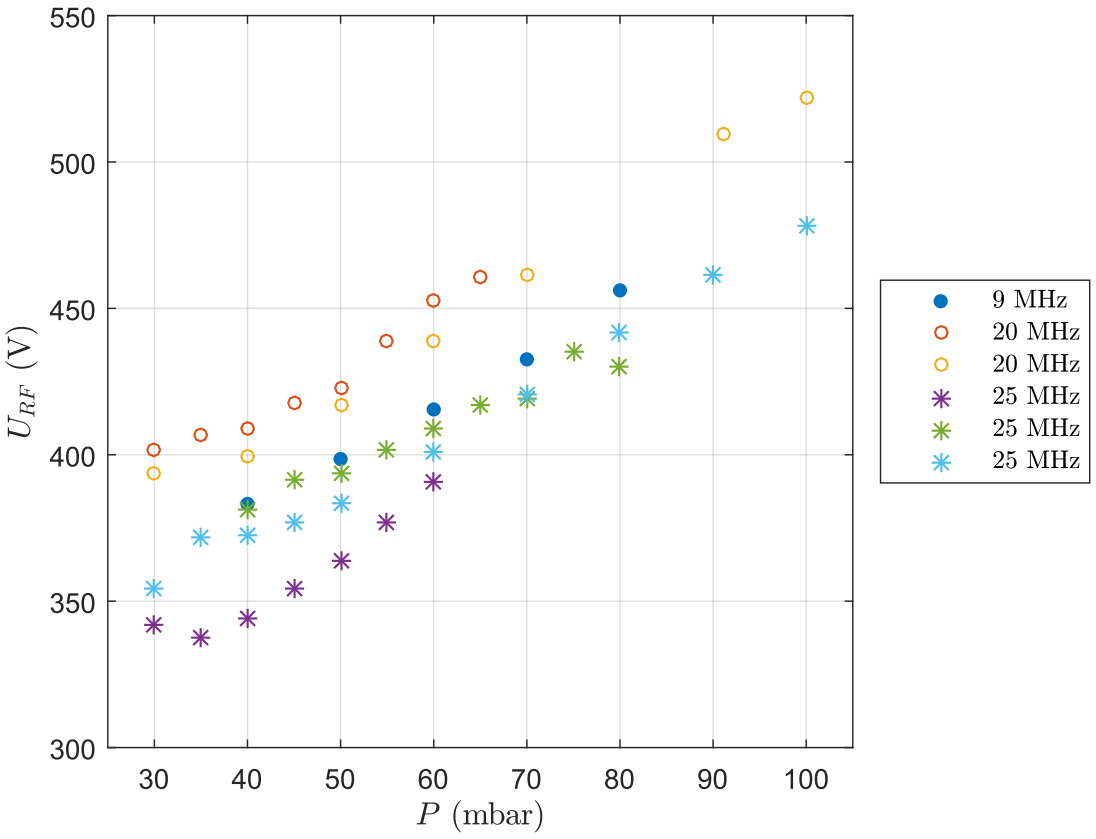

FIGURE 4.9: Plasma operation parameters for a N_2 microdischarge in a wire microstructure. The data describes the most optimum point to generate the discharge to achieve a stable homogeneous plasma solely in region between the wires. The data at 9 MHz was not stable, however it has been included for reference.

4.4 Microplasma in Ion Traps

This section describes the results obtained from generating a microdischarge within the ion microtraps.

4.4.1 Microplasma Aperture Coverage

When generating a microdischarge it is advantageous to maximise the plasma coverage of the ion aperture in order to minimise redeposition of sputtered material [154]. As sputtered particles enter the plasma and after several collisions, they can then leave and diffuse in all directions. Therefore if the plasma only partially covers the electrodes, then an increase of the contamination on the uncovered areas is possible. In particular, redepostition in the ion trapping zones should be minimised, since these are the regions where the condition of the surface is most likely to effect the motional heating rate of the ion. Figure 4.11a and b presents example images of trap types A and B respectively

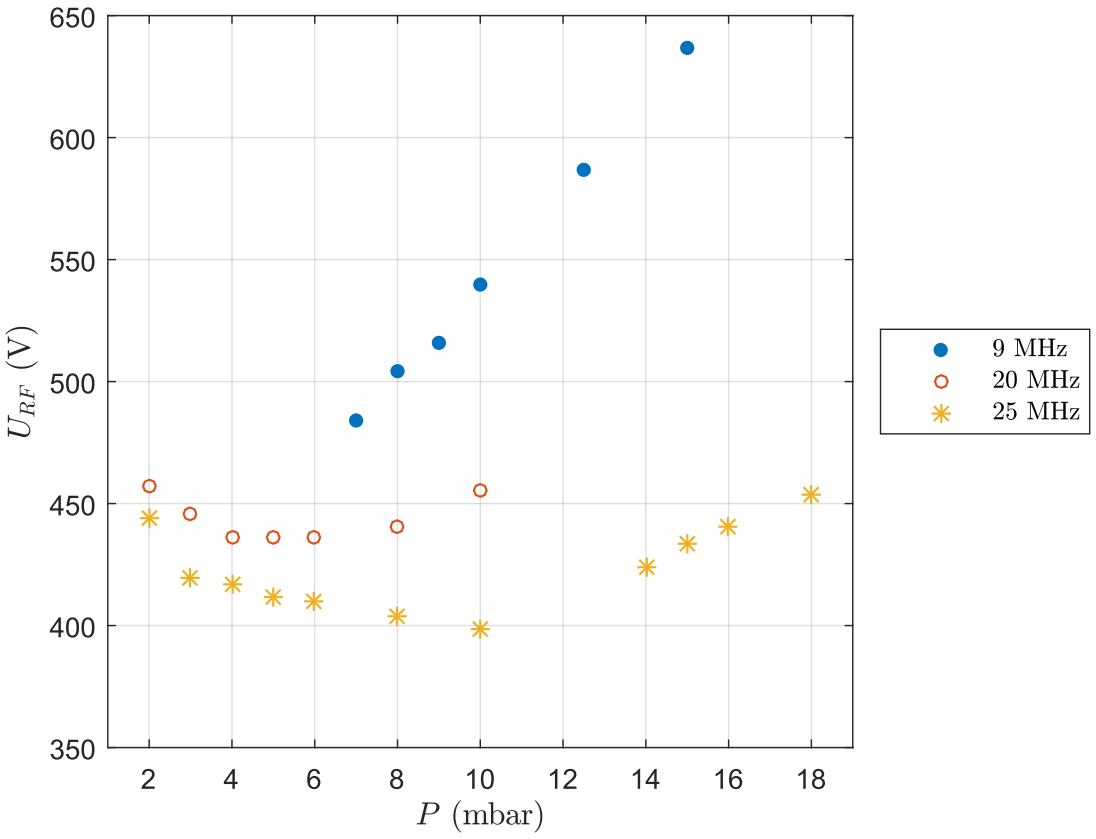

FIGURE 4.10: Plasma operation parameters for an O_2 microdischarge in a wire microstructure. The plasma generated was not stable and constricted to bright spots.

generating a He discharge and illustrate the coverage that can be attained. More quantitative data on the aperture coverage for a particular device of each type can be seen in Figure 4.12. This shows that for trap type B, adequate coverage of the trapping zones can be achieved at 330 mbar $\leqslant P \leqslant$ 440 mbar. For trap type A the microplasma covers each side of the aperture less symmetrically, which results in incomplete coverage of the trapping zones. However at $P = \{390,450,490\}$ mbar coverage is almost complete. The coverage could be improved by increasing U_{RF}, however that was not possible with the test devices that were used here.

4.4.2 Microplasma Parameters

Repeated measurements of a He and He:N_2 microdischarge were made in order to calculate what would be optimal parameters for hydrocarbon contamination removal. The results for pure He can be seen in Figure 4.14. Here, similar to the wire structure testing, the results are based on the plasma being maximally distributed in the trap aperture and with good plasma stability. Compared to the wire micro-structures, the pressure

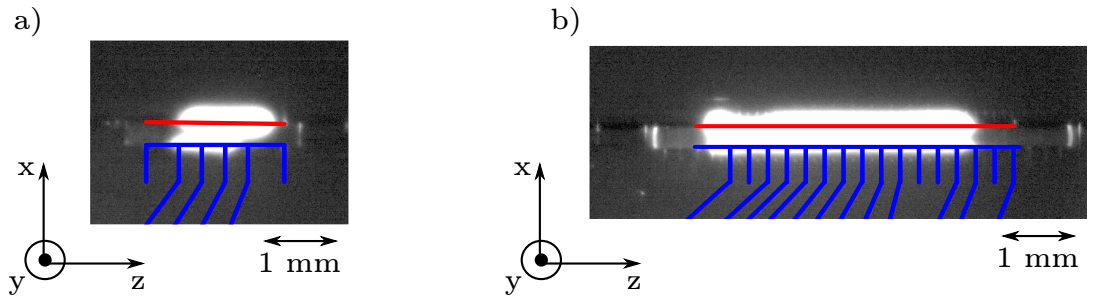

FIGURE 4.11: a) Example of trap type A generating a He microplasma at $P = 390$ mbar, $\Omega_{RF}/2\pi = 23$ MHz and $U_{RF} = 154$ V. b) Example of trap type B generating a He microplasma at $P = 400$ mbar, $\Omega_{RF}/2\pi = 23$ MHz and $U_{RF} = 160$ V. The electrode boundaries are overlaid on the images in a) and b). Exposure time was 93 ms for both images.

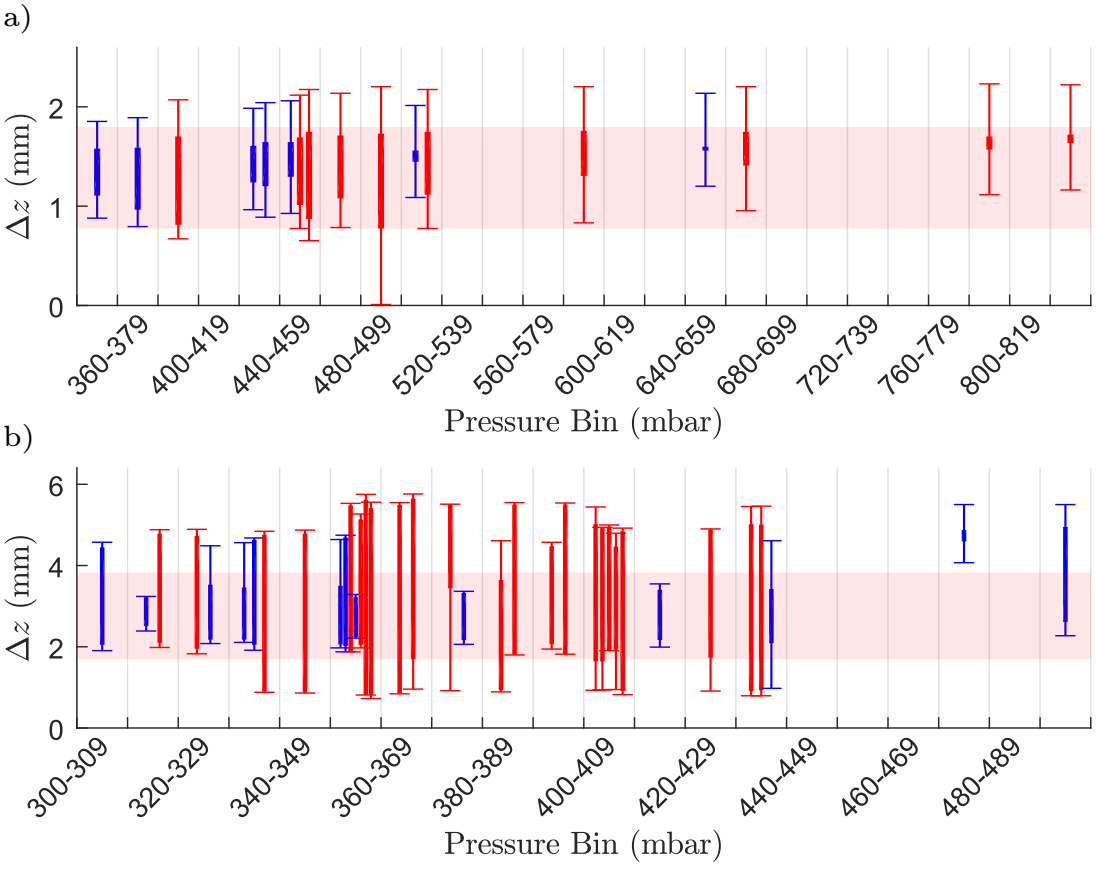

FIGURE 4.12: Example of aperture coverage in the axial direction (Δz) attained for a) trap type A and b) trap type B, using a He microplasma at $\Omega/2\pi = 23$ MHz. The data is binned into consecutive pressure ranges (20 mbar in type A and 10 mbar in type B). For each data point, the error bars denote the plasma extremes and the boxed region indicates where the plasma symmetrically covers both sides of the aperture in the axial direction. The shaded region in each figure corresponds to the trapping zones of each device, which are the principal electrodes requiring surface processing. a) Trap type A aperture coverage data taken at $U_{RF} \leqslant 150$ V is in blue and $U_{RF} > 150$ V is in red. b) Trap type B aperture coverage data taken at $U_{RF} \leqslant 190$ V is in blue and $U_{RF} > 190$ V is in red.

a) b)

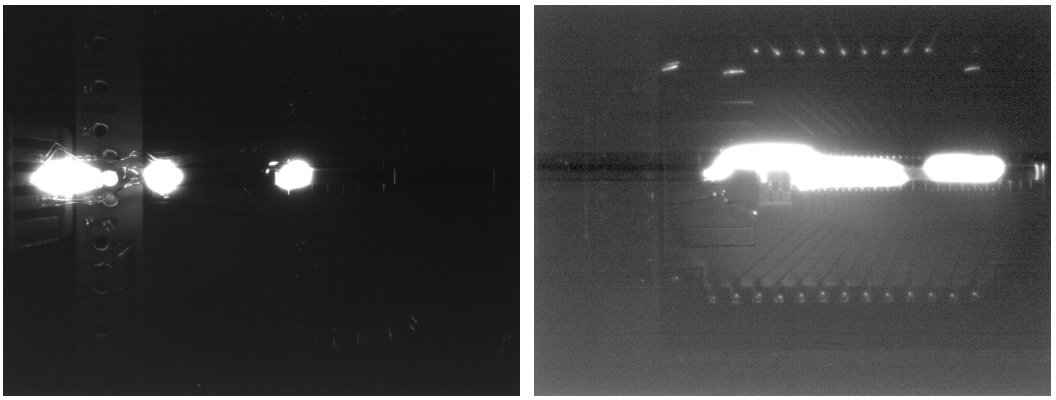

FIGURE 4.13: Two examples of plasma formations that are avoided in the ion microtraps. a) A plasma being generated at the wirebonds from the trap chip to the intermediate substrate and again from the intermediate substrate to the LCC in a trap type B. b) The plasma arches out of the aperture and along the surface of the RF electrode in a trap type A.

and voltage range of the plasma operation was restricted; $U_{RF} \leq 230$ V and a pressure range of 290 mbar $\leqslant P \leqslant$ 490 mbar in trap type A and to 350 mbar $\leqslant P \leqslant$ 910 mbar for trap type B. This was due to a number of factors. Firstly, the traps used for micoplasma testing had defects that made them unsuitable for ion trapping. A symptom of these defects was a low electrical breakdown voltage ($U_{RF} \leq 230$ V). Secondly, the plasma can become delocalised; the plasma was observed to spread beyond the trapping aperture and along the RF electrodes. Thirdly, there was the risk of generating a plasma at the wirebonds that form the electrical connection from the LCC to the intermediate substrate and again from the substrate to the trap itself. Examples of these last two issues can be seen in Figure 4.13. In both instances damage to the gold surface is possible, which could result in an electrical short. In order to reduce the occurrence of these plasma formations the grounded planes that run parallel to the RF electrodes were left floating when generating the discharge. In addition, the plasma stability was also improved by floating the Si bulk and the compensation electrodes. During normal plasma operation the plasma was confined to the trap aperture.

OES was used to determine the gas temperature T and the electron density n_e (see Section 4.2). The results for T are in Figure 4.14b. There is a positive correlation of T with P, which is to be expected, however note that for some results there is an increase in voltage U_{RF} as well as P (see Figure 4.14a) which is also expected to increase T [137, 144, 147, 155]. Similar temperatures for T, in the range of 300 K $\leq T \leq$ 600 K, have been reported for microplasmas under similar conditions [137, 144, 147, 155]. The

calculated T ranges from room temperature up to ∼460 K and this low gas temperature is beneficial since it minimises the possibility of thermally damaging the trap. The errors in the Figure 4.14b are based on a 1σ error from the statistical fit. In addition there are three further systematic errors that are included; the error from the 1) Stark and 2) instrument broadening contributions and 3) the error from deviations to the ideal Voigt fit. Firstly in the fit to the He I line, previous work has shown that the semi-classical calculations used to determine the Stark broadened linewidth agree with experiment to within ±20 %. By varying the He I Stark contribution by a factor of 0.8 to 1.2, an additional uncertainly was estimated to be ±2 % for T and ±1 % for n_e. Secondly, the Gaussian fit to He-Ne laser linewidth to determine the instrument broadening had an associated error, that when propagated, resulted in a 1 % error in T and a 2 % error in n_e. Thirdly, a few data points in Figure 4.14b suggest that the estimated gas temperature is below room temperature. In these instances, the ideal fitted Voigt noticeably deviates from the He I line data in the wings of the profile. This leads to an overestimation of the Lorentzian component of the fit and subsequently an underestimation of T. An estimation of the change in the FWHM was made from the deviation in the wings. This was then added as a correction factor in the fit to the lineshape, which, from the analysis of several fits lead to an associated systematic underestimation of 45 K in T and correspondingly 4×10^{13} cm^{-3} in n_e. For those points, the systematic uncertainty has been reflected in the upper error bar for both T and n_e.

Due to the small length scales of a microdischarge, they operate at higher pressures and therefore have a correspondingly higher electron density than plasmas with a larger length scale. The result of the measured n_e is shown in Figure 4.14c. A weighted linear least squares fit to the to the data shows that there is a weak positive correlation of the increasing P and U_{RF} range tested. This trend is consistent with literature [136, 137].

From the graphs in Figure 4.14a-c and Equation 3.45 the mean average bombardment energy ϵ_{bom} can be calculated. The results are displayed in Figure 4.14d and show that the mean ion energy is 0.3 eV $\leq \epsilon_{bom}$(He) $\leq$ 2.1 eV. The ion energy is very low simply because of the highly collisional nature of the plasma. In addition, the energy is well below the 54 eV threshold for sputter Au. However the average energy is also substantially below the threshold for sputtering hydrocarbons. Therefore it is the tail of the energy distribution that will contribute to the removal to the contamination.

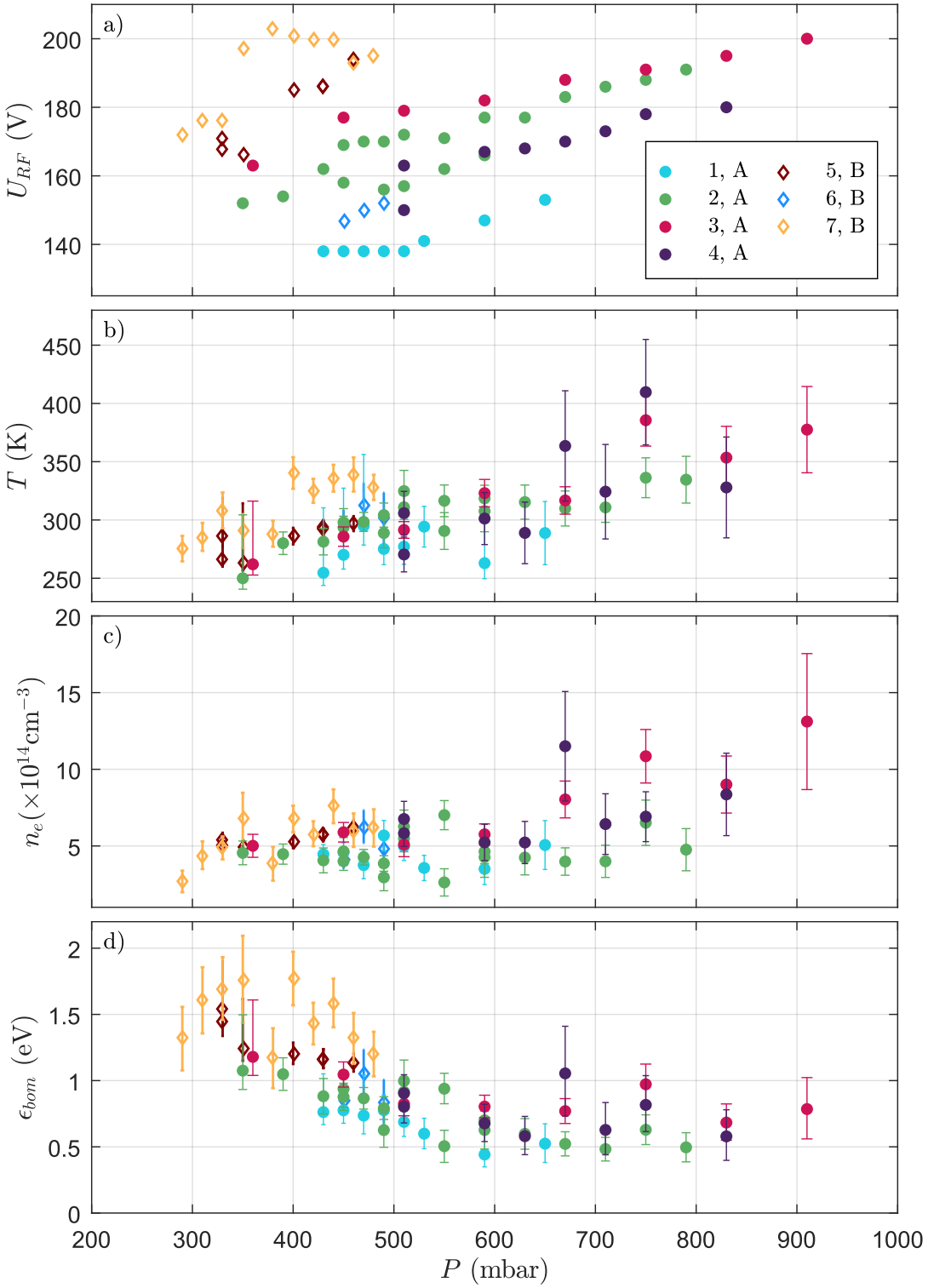

FIGURE 4.14: Measurements to determine the average ion bombardment energy with He at $\Omega_{RF}/2\pi = 23$ MHz. a) Operating U_{RF} values for a microplasma confined to the aperture with maximum coverage, for trials 1 to 3 in trap type A (diamonds) and trials 4 to 7 in trap type B (circles). b) T and c) n_e measured from lineshapes fitted to the He I 667 nm and Hα 656 nm lines, using the method in Section 4.2.2 and the voltages U_{RF} from (a). d) ϵ_{bom} deduced from measured results in (a-c) using Equation 3.50. The uncertainties in ϵ_{bom} values are propagated from those in T and n_e, which are described in the text.

4.4.3 Calculation of Cleaning Times

Using Section 3.5.4 the number of energetic He ions and neutral atoms which occur beyond the sputtering threshold of amorphously adsorbed hydrocarbons can be calculated. Using Equation 3.60 the estimated sputtering time constant $\tau = (\Phi_x \sigma_a)^{-1}$ is plotted in Figure 4.15, in addition to estimates for processing times to reach a target adsorbate density of 1 mm^{-2}. This density is relevant in our instance, since the area of the electrodes within the microtrap aperture are 4.5 mm^2. Over the pressure and voltage ranges tested the processing times vary from ~60 s upwards. The figure shows that energetic neutrals can have a significant sputtering effect that is equal to, if not greater, than that of the ions. This is due to the energetic neutral atom flux to the electrode surface being larger than the He ion flux (see Section 3.5.4). Both simulations and experiments have shown that fast neutrals can significantly contribute to the sputtering at electrode surfaces [156–159]. For example in an O_2 plasma sputtering a Cr surface at $P = 0.01$ mbar, 30 % of the total sputtering was attributed to fast neutrals [158].

The optimal parameters for a homogeneous plasma that was well-distributed in the aperture, with good stability and a reasonable time scale for surface processing is likely to occur for trap type A at $P = 360$ mbar, $U_{RF} = 160$V and with $t_{clean} = 40$ minutes. On the other hand, the range for trap type B is likely to be $P = 350$ mbar with $U_{RF} = 200$ V resulting in $t_{clean} = 1$ min.

The effect of the microplasma on the Au electrode surface can be quantified by estimating the time constant for the removal of surface Au layers

$$\tau_{Au} = \frac{1}{\Phi_{He,max}\sigma_{He-Au}} \tag{4.20}$$

where $\Phi_{He,max}$ is the maximum neutral He flux density in the range $\epsilon > \epsilon_{th,Au}$ which is calculated using $\sigma_{He^+-He} = 1.2 \times 10^{-19}$ m^2 (see Section 3.2) and $\sigma_{He-Au} = 1.42 \times 10^{-20}$ as calculated in Section 3.3. For the optimum parameters above, $\Phi_{He,max} = 9.2 \times 10^4$ $m^{-2}s^{-1}$ for trap type A and $\Phi_{He,max} = 7.1 \times 10^{10}$ $m^{-2}s^{-1}$ for trap type B. Therefore using equation 4.20, $\tau_{Au,A} \simeq 7.8 \times 10^{14}$ s and $\tau_{Au,B} \simeq 1 \times 10^9$ s (where subscripts A and B denote trap type). A comparison of time constants to those in Figure 4.15 show that $\tau_{Au} >> \tau_a$ and therefore the sputtering of Au from the surface can be considered to be negligible. This is beneficial since the sputtering of electrode material can result

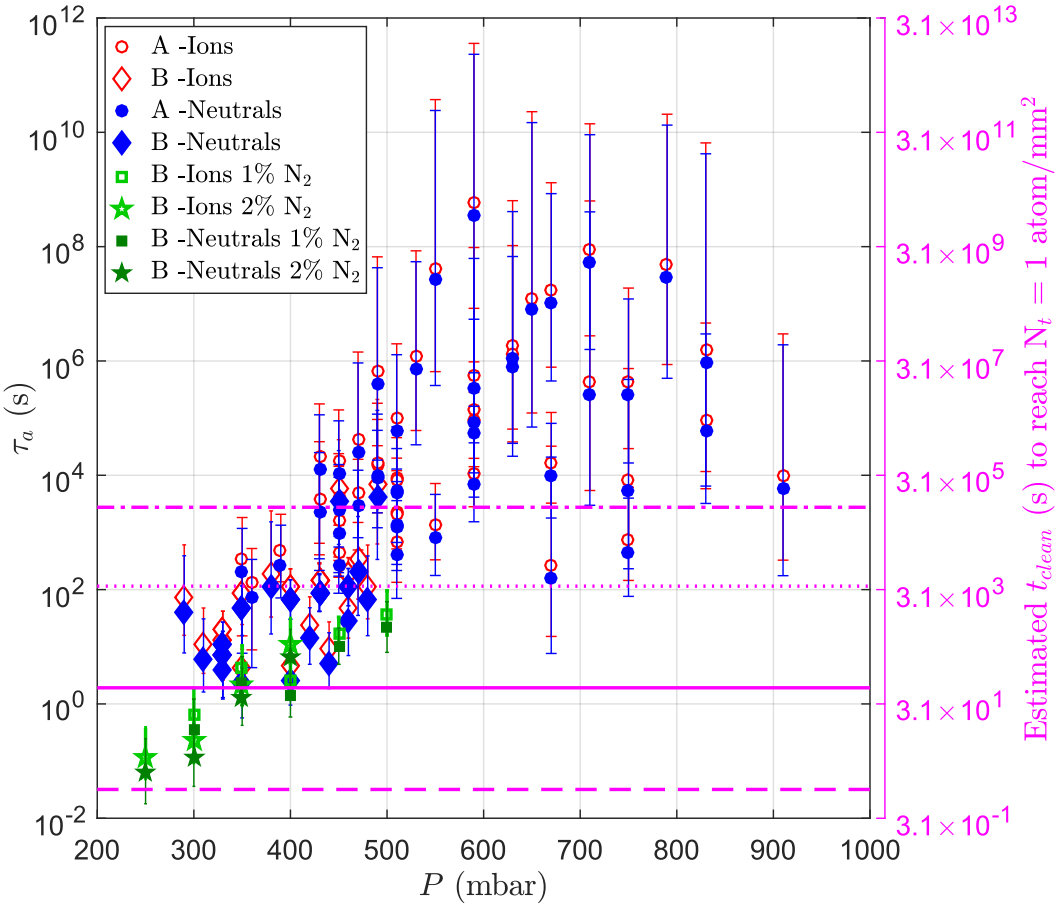

FIGURE 4.15: Calculated time constant (τ_a) and plasma processing times (t_{clean}) to remove two hydrocarbon monolayers from the electrode surface in trap types A (empty diamonds) and B (filled circles). The processing times using only He ions (in red) and only He neutral atoms (in blue) are plotted separately. Processing times for He:N_2 mixtures in a trap type A are plotted in the green for comparison. The plasma parameters used in this calculation can be found in Figure 4.14 a-c and 4.19 a-c. In addition, indicators of cleaning times for 1 s (dashed), 1 minute (solid), 1 hour (dotted) and 1 day (dot-dashed) are plotted in purple.

in re-deposition of conductive material in the insulating spaces between electrodes and the grounded Si wafer bulk leading to an electrical short.

In order to verify that the electrode surfaces were undamaged, images of the internal Au surface were taken for a trap type B before and after plasma treatment. To record the state of the surface, an RF and a DC electrode were imaged at five different points, Figure 4.16 shows a schematic of where the trap was imaged. Due to the insufficient depth of focus, the images were taken at three different focal depths. A schematic highlighting the viewing angle and different focal lengths can be seen in Figure 2.4. The focal depths correspond to the edge of the electrode closest to the Si bulk, the centre of the electrode and the edge of the electrode furthest from the Si Bulk. The pictures of the internal electrodes were taken, the trap was then exposed to a plasma generated at

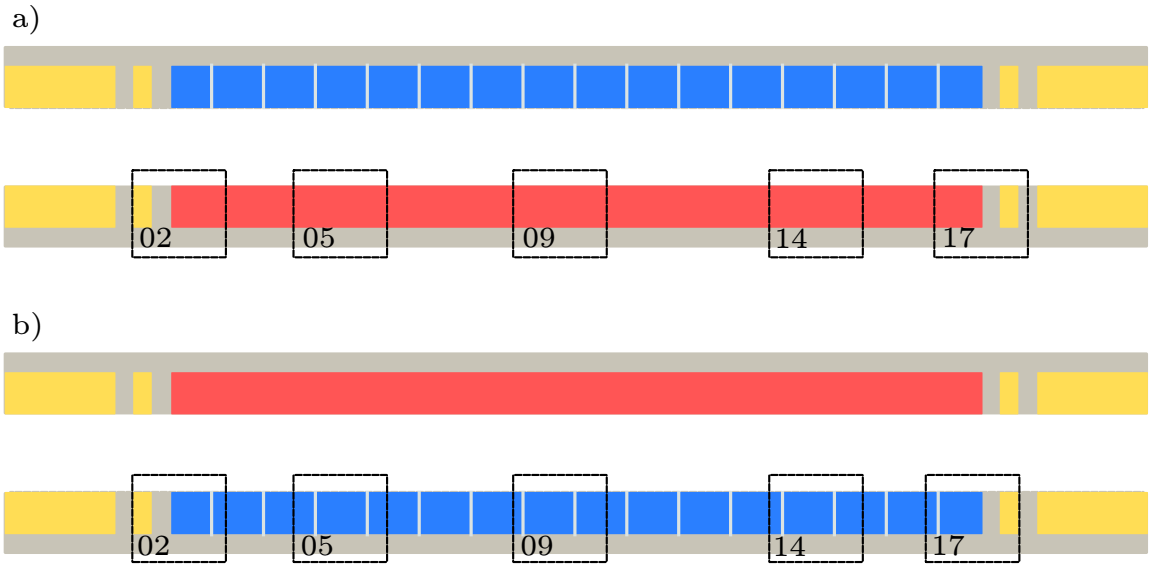

FIGURE 4.16: Spatial locations of recorded images (denoted by a series of numbers {02,05,09,14,17}). Both diagrams depict the internal electrode surfaces, in a direction normal to the plane of the chip. The grey area shows the extent of the silicon substrate. Red = RF, blue = DC and yellow = other metallised surfaces at ends of aperture (grounded/floating). The top (bottom) image illustrates the internal view of the back-side RF electrode (front-side DC electrode).

$P = 360$ mbar at $U_{RF} = 160$ V for 15 min ($\sim 27\tau_a$ where $\tau_a = 33$ s for these operating parameters), and the electrodes imaged again. The trap was then used for further two further tests at 1) $P = 350$ mbar $U_{RF} = 140$ V for 20 min and at 2) $P = 360$ mbar at $U_{RF} = 160$ V for 10 min following which the trap was then imaged again. Figure 4.18a shows example pictures for each of these imaging stages, at the three different focal depths, for the centre of a DC electrode (imaging point '09' in Figure 4.16). This set of images shows that there was no observable damage to the Au surface. The rest of the images similarly showed there to be no difference between the before and after images, with one exception. The only difference was found to be at the tip of the corner of the RF electrode (corresponding to imaging point '17' in Figure 4.16) where a slight tarnishing of the Au is seen, these images are displayed in Figure 4.18b. This effect is likely due to the localised high field emission that arises due to the electrode geometry. Since the effect is at a spatial location that is removed from the trapping zones, the effect is considered to be negligible.

4.4.4 He:N_2 Gas Mixtures

In addition the trials with pure He, gas mixtures of He:N_2 were also investigated. Due to the high breakdown voltage of N_2, (see Figure 4.9) and the limited voltage range of the

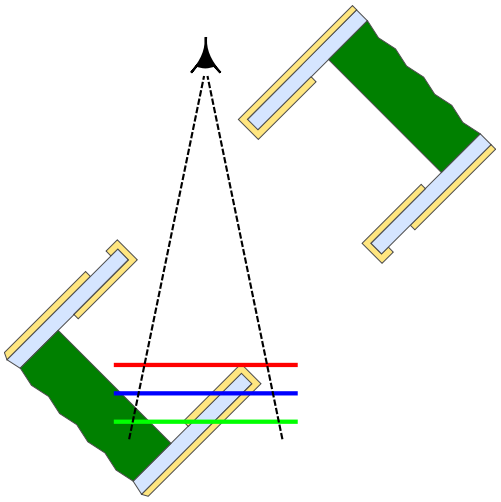

FIGURE 4.17: Cross-section of microtrap electrode structure showing the viewing angle needed to image the electrode surfaces. Three depth of foci were required to record the surfaces in sufficient detail, these are denoted by the red, blue and green solid lines.

test ion traps used for microplasma generation, testing with pure N_2 was not possible. However, where comparing the N_2 and He plasma generated, the former showed superior confinement in the aperture, where as the latter showed a lower breakdown voltage and better stability. By testing the mixture of the two it presented the possibility of combining these traits in conjunction with the use of both physical and chemical sputtering (see Table 3.1). Figure 4.19 shows the results from using a He:N_2 gas mixture in a trap type B. As seen in Section 4.3, the voltages needed to generate a N_2 plasma are greater than that of a He plasma. Due to the limited voltage range of the test ion trap, the N_2 concentrations were restricted to 1 % and 2 %. The plasma parameters shown in Figure 4.19 show a deviation towards higher ϵ_{bom}. It is also worth noting that for the data shown in Figure 4.19, at 400 mbar $\leqslant P \leqslant$ 500 mbar, the U_{RF} limit of the device was less than the required voltage for a plasma that extended the full length of the aperture. for both the concentrations of N_2 1.2 eV $\leqslant \epsilon_{bom} \leqslant$ 4.1 eV. In comparison to pure He the ϵ_{bom} values for He:N_2 are roughly double. Consequently, this results in lower surface processing times, which can be found alongside the data for pure He in Figure 4.15. To reach a target density of $N_t = 1$ mm^{-2}, the time taken is 2 s $\leqslant t_{clean} \leqslant$ 650 s. The results with the He:N_2 mixture show that the surface processing times can be reduced by seeding the with N_2. However, a more stringent comparison is to consider the data in which the maximum coverage of the trapping zones was achieved. This occurred at 1 % N_2 at $P = 350$ mbar and 400 mbar, $t_{clean} = 74$ s and 43 s respectively. This is comparable to $t_{clean} = 60$ s in pure He for the same trap type at the optimum conditions

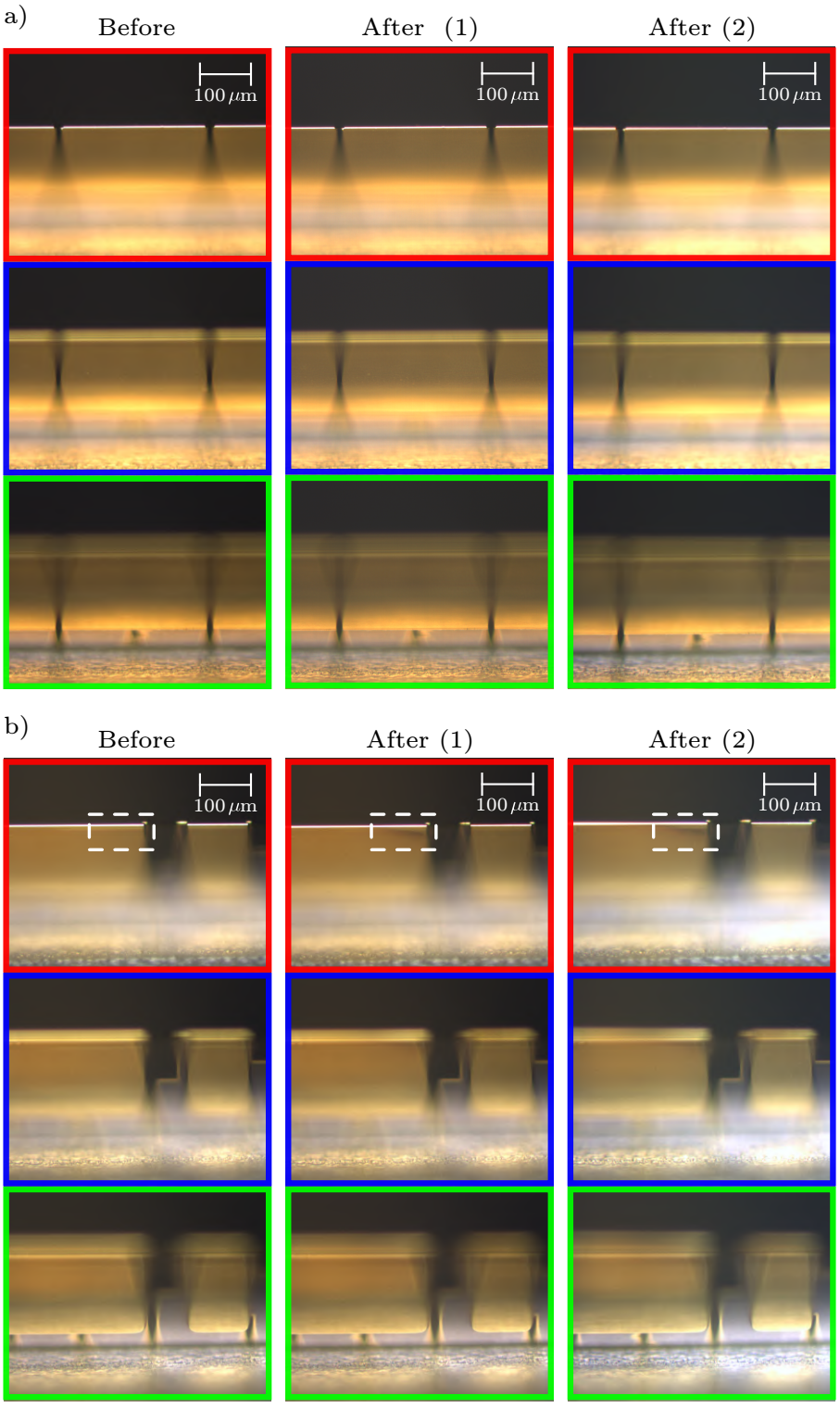

FIGURE 4.18: Sample images of the internal electrode surfaces before and after two stages of microplasma processing. The first stage of processing ('After (1)') was at $P = 360$ mbar, $\Omega/2\pi = 23$ MHz and $U_{RF} = 160$ V for 15 min ($\sim 27\tau_a$, where $\tau_a = 33$ s). The second , 'After (2)', was at the same setting as (1) but for 10 min and at $P = 350$ mbar $U_{RF} = 140$ V for 20 min. The coloured frames correspond to the different focal depths in Figure 4.17. a) Imaging of centre of DC electrode (imaging point '09' Figure 4.16). b) Imaging of end of RF electrode (imaging point '17' Figure 4.16). A dashed white box is superimposed onto the top set of images to indicate the position of slight discolouration of the Au electrode.

stated in the previous section.

4.5 Summary

A capacitively coupled RF microplasma was successfully generated within the trapping aperture of two different ion trap types. The plasma parameters (namely the electron density n_e and the gas temperature T) needed for the theretical framework set out in Chapter 3 was successfully determined using OES of the He I 667 nm and Hα 656 nm lines. Using n_e and T the mean ion bombardment energies were calculated along with estimates for the adsorbate removal time.

Due to the highly collisional nature of the plasma the mean ion bombardment energies with pure He (0.3 eV $\leqslant \epsilon_{bom}$(He) $\leqslant$ 2.1 eV) were found to be much lower than the threshold for sputtering hydrocarbons (12 eV). The sputtering of the surface adsorbates is reliant on the high energy tail of the ion energy distribution. The surface processing time for removal of two hydrocarbon monolayers was estimated as down to $\sim$ 40 minutes for type A microtraps. For trap type B on the other hand, corresponding times were calculated to be 60 s. At these operating parameters the plasma coverage was almost complete for trap type A and complete for trap type B. With a He:N_2 gas mixtures higher ion bombardment energies were achieved. For plasma coverage that was almost complete the ion bombardment energies were in the range of 1.2 eV $\leqslant \epsilon_{bom}$(He) $\leqslant$ 4.1 eV, with cleaning times in the range of 43 s $\leqslant t_{clean} \leqslant$ 74 s. During the surface processing with He and He:N_2, the sputtering of the electrode material is expected to be negligible, which was confirmed with microscopy. The results suggest that the microplasma surface processing technique presented is suited to *in situ* selective removal of surface adsorbates from ion microtrap electrodes.

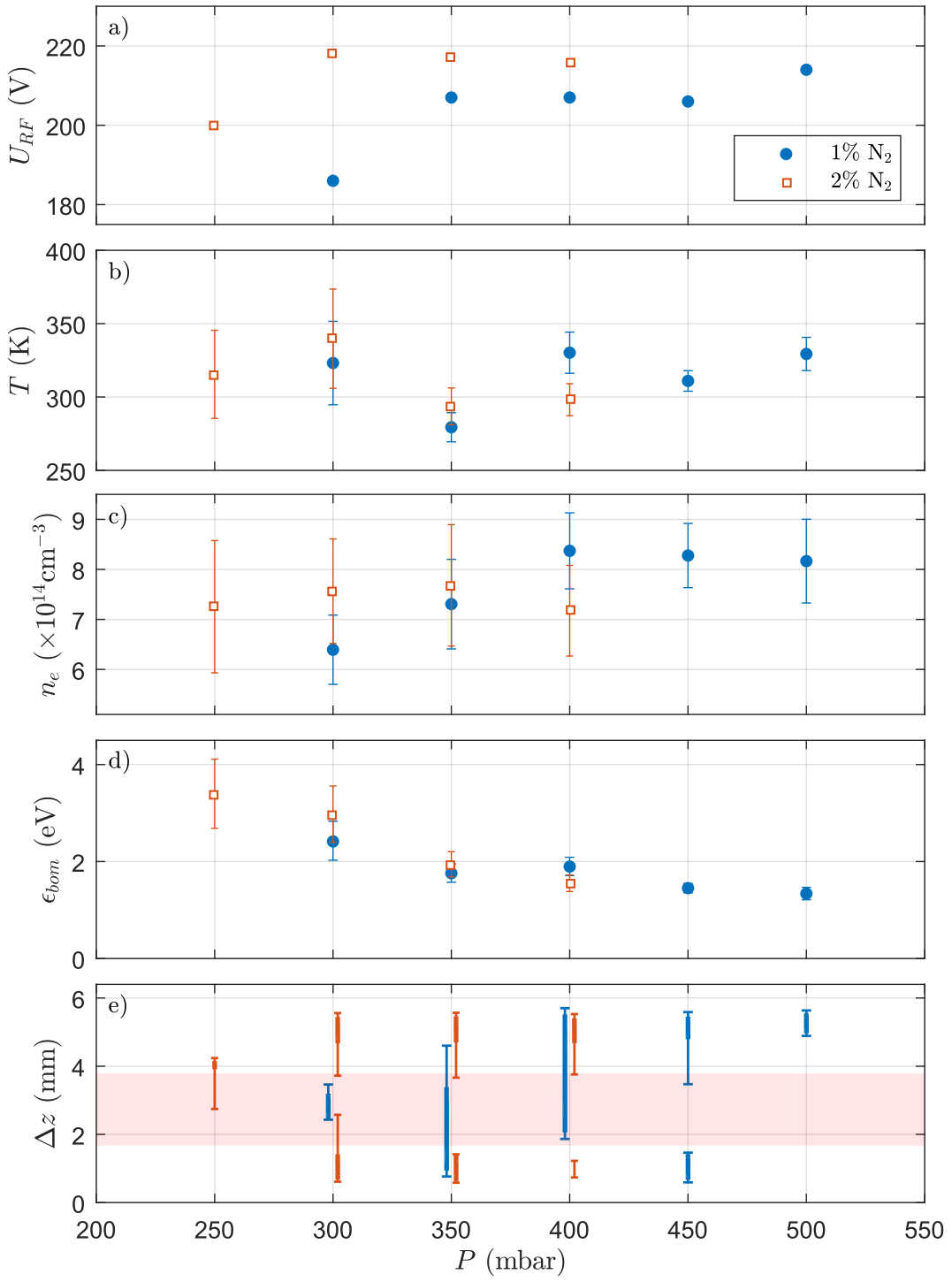

FIGURE 4.19: Measurements to determine the average ion bombardment energy with a He:N_2 microplasma at $\Omega_{RF}/2\pi = 23$ MHz. a) Operating U_{RF} values for a microplasma confined to the aperture of trap type B, for N_2 concentrations of 1 % (filled circles) and 2 % (empty squares). b) and c) show T and n_e as measured from lineshapes fitted to the He I 667 nm line and Hα 656 nm line simultaneously, using the method in Section 4.2.2 and the voltages U_{RF} from (a). d) ϵ_{bom} deduced from measured results in (a-c) via time-averaging of Equation 3.50. The uncertainties in ϵ_{bom} values are propagated from those in T and n_e, which are based on a 1σ confidence interval. e) Axial spatial extent Δz of the microplasma in this data set, at $P = \{300,350,400\}$ mbar the range bars are offset from the exact P for clarity.

Chapter 5

Reducing Decoherence from Electric, Magnetic and Atomic Sources

5.1 Introduction

Chapters 3 and 4 focused on one potential source of decoherence; hydrocarbon surface contamination giving rise to increased electric-field noise in the ion microtrap. This chapter includes the upgrades to the experimental system described in Chapter 2 with the aim of reducing the effects of other decoherence sources. In Section 1.4 various sources of decoherence were outlined, including the potential for noise on the electrodes and that arising from magnetic fields. Both of these can can cause dephasing of the coherent control of the ion's state. Section 5.2 details the improvements to the control of the voltages to the DC electrodes in order to improve the versatility of the system and also minimise any noise present at the motional frequencies of the ion. Section 5.3 focuses on the implementation of an active stabilisation method for the currents to the magnetic field coils. Deviations in the magnetic field as a result of electrical noise or drifts in the current source are potential sources of decoherence. Therefore a feedback system is implemented for precise control of the currents to the magnetic field coils in order to establish long-term stability of the magnetic field generated. The final section in this chapter focuses on the automated control of the ion loading procedure. As Sr atoms are evaporated towards the trap some of the atomic flux inevitably adsorbs onto the

electrode surfaces. This could generate stray fields of increased motional heating [160], in a similar fashion to hydrocarbon contamination discussed in Section 1.4. With the design of the trap package the shield limits ion flux to zone L (see Section 2.3). However, while the shield decreases the probability of electrode contamination, it also restricts the flux of atoms available for trapping to a narrow range that passes unobstructed through the aperture. Therefore the loading rate decreases and the lifetime of the oven and hotplate also decreases. Section 5.4 describes automated procedures for 1) loading the hotplate with Sr and, 2) loading ions into the trap. In each of the procedures the temperature of the hotplate and oven are well controlled in order to prolong their lifetime and for more efficient loading.

5.2 Control of DC Electrodes

This section describes the control of the DC electrodes which are used as the compensation and endcaps when controlling the position of an ion in the trap. It includes the development of a system of re-routable signals for versatile control of each of the 42 DC electrodes. In addition, the development of interchangeable filters for each of the signal lines will also be presented. Electrical noise coupling to the ion at the motional frequencies risks ion heating and subsequent decoherence. Electrical filters can be used to modify the frequency spectrum of the electrical signal for a specific outcome. Here, passive filter designs are discussed with the aim of modifying the DC signals such that the noise at the motional frequency of the ion is attenuated. Section 5.2.1 will describe the experimental set-up and software control. The details on the re-configurable termination board that provides the routing of the DC voltages is in Section 5.2.2. The filtering of the DC lines will be discussed in Section 5.2.3.

5.2.1 System Overview

The system that controls the DC potentials supplied to the trap is comprised of three main elements; an electric field generator (EFG) which is the voltage source, a routing board and a filter board. The EFG was developed by the Wunderlich group, Siegen [161] and is a 24 channel arbitrary waveform generator with a range of ± 9 V. The supplied voltages are routed through a re-configurable termination board which allow each of the channels to be connected to 1) a single electrode, 2) several electrodes or 3) grounded.

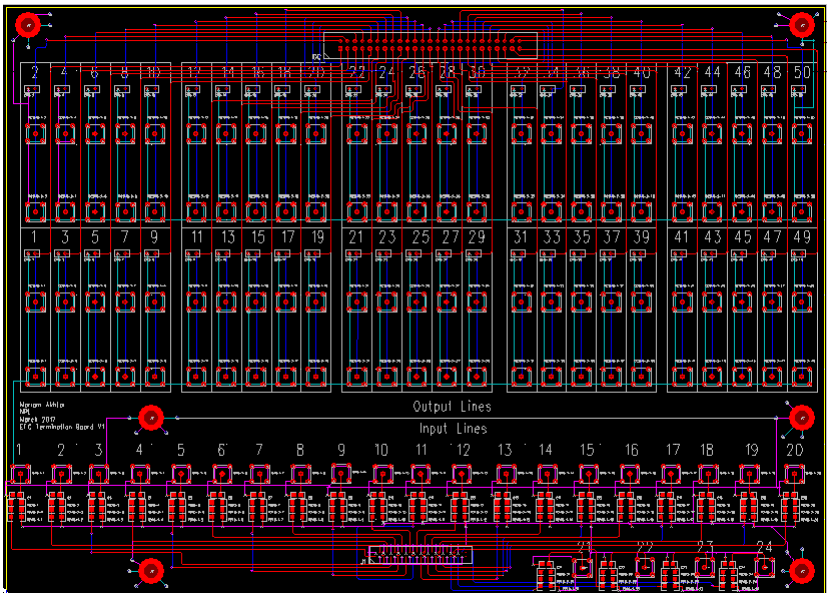

FIGURE 5.1: PADs Layout design of re-configureable termination board interfacing between the EFG and filter boards.

After the routing, a 50 line ribbon cable interfaces the termination board to a PCB where each of the 42 signal lines to the microtrap electrodes are filtered.

The EFG is programatically controlled via USB to set the voltages on the trap electrodes. A LabVIEW control system was developed to ramp the voltages to the required level at a user-specified rate. The voltages were ramped using sine waveforms. The program allows the user to not only manually set the required voltages but also to use predefined shuttling routines which include procedures such as merging ion strings, splitting ion strings and oscillating ions between segments.

5.2.2 Re-configurable Termination Board

A PCB was created to interface the EFG to the filter boards. This termination board was designed to allow several of the DC electrodes to be connected to the same EFG channel and for each channel to be able to be connected to any DC electrode. The board was designed using PADS Logic and Layout software and the layout of the design can be seen in Figure 5.1. The implementation of the design can be seen in Figure 5.2, which shows a picture of the board within its metal enclosure.

A schematic of the electrical connectivity of the termination board can be seen in Figure 5.3. The input section connects the EFG signal to two 240 Ω resistors in parallel which provides the impedance matching to the EFG which is a 120 Ω impedance source. This

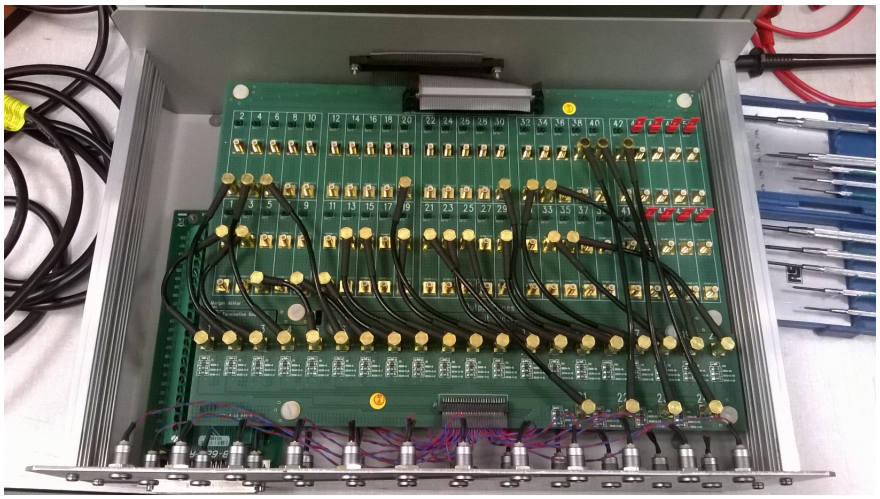

FIGURE 5.2: Picture of the re-configurable termination board within its enclosure.

is then followed by a 820 Ω resistor in series and a 10 pF capacitor in parallel which provides a first order RC filter for some initial attenuation of any noise. SMB coaxial cables then make the connection from the input section of the termination board to the output section which allows each of the 24 EFG channels to be connected to any of the 50 lines on the ribbon cable that connects to the filter board. The output section has two SMB ports so that each EFG channel can be connected directly to a DC electrode or indirectly via the second SMB port. This allows each of the 24 EFG channels to control more than one electrode on the ion trap. In addition a jumper was installed in line with the two SMB ports on the output section. This enables the possible grounding of the electrical lines to the trap.

5.2.3 DC Line Filtering

Filter Characterisation

The following section detials some of the methods needed to characterise the electronic filters, such at the transfer function and the step response. It also describes some of the generally used passive analogue filter types and compares the different responses.

Transfer Function

For the particular application of electronic filters to the DC source, the filters in question need to respond to a continuous-time signal. That is a signal which is represented by

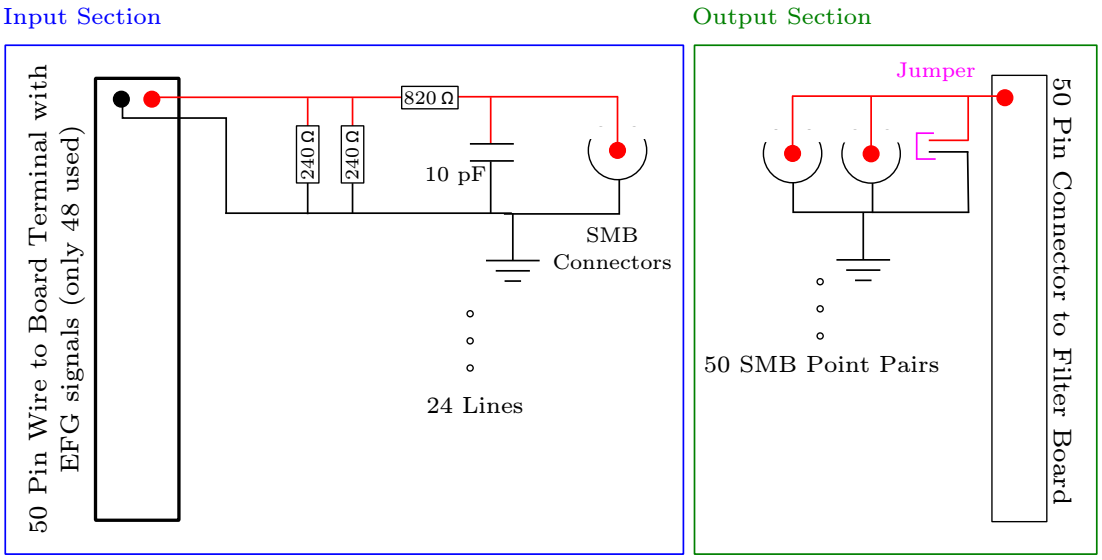

FIGURE 5.3: Schematic of a single signal line for the input and output section of the re-configurable termination board. Each of the 24 lines in the input section corresponds to one of the 24 voltage channels from the EFG.

$x(t)$ in a range of (t_1, t_2) where $-\infty \leq t_1$ and $t_2 \geq \infty$ to enable an output of $y(t)$. For linear analogue passive RLC filters, their response can be characterised by the following equation [162]:

$$b_n \frac{d^n y(t)}{dt^n} + b_{n-1} \frac{d^{n-1} y(t)}{dt^{n-1}} + ... + b_0 y(t) = a_n \frac{d^n x(t)}{dt^n} + a_{n-1} \frac{d^{n-1} x(t)}{dt^{n-1}} + ... + a_0 x(t), \quad (5.1)$$

where the coefficients $a_0, ..., a_n$ and $b_0, ..., b_n$ are functions of the filter component values and both $x(t)$ and $y(t)$ can be in terms of either voltage or current. The order of the differential equation that represents a particular filter is known as the order of the filter.

One of the principal ways to characterise the response of a filter is its transfer function, which is the ratio of the Laplace transformation of $y(t)$ with the Laplace transformation of $x(t)$. The Laplace transformation $\mathcal{L}$ of $x(t)$ is defined as [162]

$$X(s) = \mathcal{L}x(t) = \int_{-\infty}^{\infty} x(t) exp(-st) dt, \quad (5.2)$$

where s is a complex variable, and the reverse process is

$$x(t) = \mathcal{L}^{-1} X(s) = \frac{1}{2\pi i} \int_{C-i\infty}^{C+\infty} X(s) exp(st) ds. \quad (5.3)$$

Here C is a positive constant. The Laplace transformation is particularly useful since it transforms a differential equation into an algebraic equation which is easier to manipulate.

For a time-invariant, continuous-time filter, the response is given by the convolution integral [162]

$$y(t) = (h * x)(t) = \int_{-\infty}^{\infty} h(t-\tau)x(\tau)d\tau = \int_{-\infty}^{\infty} h(\tau)x(t-\tau)d\tau, \tag{5.4}$$

where $h(t)$ is the impulse response of the filter. Taking the Laplace transform of equation 5.4 gives

$$Y(s) = \int_{-\infty}^{\infty} \left[\int_{-\infty}^{\infty} h(t-\tau)x(\tau)d\tau \right] exp(-st)dt. \tag{5.5}$$

Rearranging this equation and letting $t = t' + \tau$ yields

$$Y(s) = \int_{-\infty}^{\infty} h(t')exp(-st')dt' \int_{-\infty}^{\infty} x(\tau)exp(-s\tau)dt' = H(s)X(s). \tag{5.6}$$

Therefore the transfer function $H(s)$ is

$$H(s) = \frac{Y(s)}{X(s)} = \mathcal{L}h(t), \tag{5.7}$$

and is defined as the ratio of the Laplace transform of $x(t)$ and $y(t)$. Equally, it could be defined as the Laplace transform of the impulse response of the filter.

Step Response

Another means of analysing the response of a filter is to use its step response, i.e. the response of the filter to the input signal $u(t)$ where

$$u(t) = \begin{cases} 1 & \text{for } t \geq 0 \\ 0 & \text{for } t < 0. \end{cases} \tag{5.8}$$

Taking the Laplace transform of $u(t)$

$$\mathcal{L}u(t) = U(s) = \int_{-\infty}^{\infty} u(t)exp(-st)dt = \frac{1}{s}, \tag{5.9}$$

therefore the response of the filter is

$$y_u(t) = \mathcal{L}^{-1}\left[\frac{H(s)}{s}\right]. \tag{5.10}$$

There are three parameters that are typically associated with the step response:

- The overshoot: difference (in %) of the peak value with the step target value as $t \to \infty$.
- The time delay: time taken to reach 50 % of the target value.
- The rise time: time required to go from 10 % to 90 % of the target value.

Passive Filter Types

There are a number of passive low pass filter types that can be characterised by the form of their frequency response. Common types include the Butterworth, RC, Chebyshev and elliptic filters. The Chebyshev filter has the sharpest attenuation gradient after the cutoff frequency, therefore resulting in the maximum attenuation at the motional frequencies of the ion, compared to the other filter types with the same cut-off frequency. However, the filter also has the largest ripples in the pass-band, which leads to modifications in the phase. Similarly, the elliptic filter type also suffers from pass-band ripples.

The RC filter retains a flat pass-band, however it would result in the least attenuation at the motional frequency. The Butterworth filter on the other hand, equally has maximal flatness in the pass-band and a greater attenuation gradient than the RC filter. The filter boards designed here are primarily for two measurement scenarios; one being heating rate measurements and the other to be used during ion shuttling. Both require maximal attenuation of noise at the motional frequencies of the ion. However in the case of the ion shuttling measurements there is an additional consideration; the cut-off frequency needs to be high enough such that the desired shuttling speeds are not compromised. Therefore, for our purposes, the RC filter and particularly the Butterworth filter are most appropriate for the DC electrode filtering.

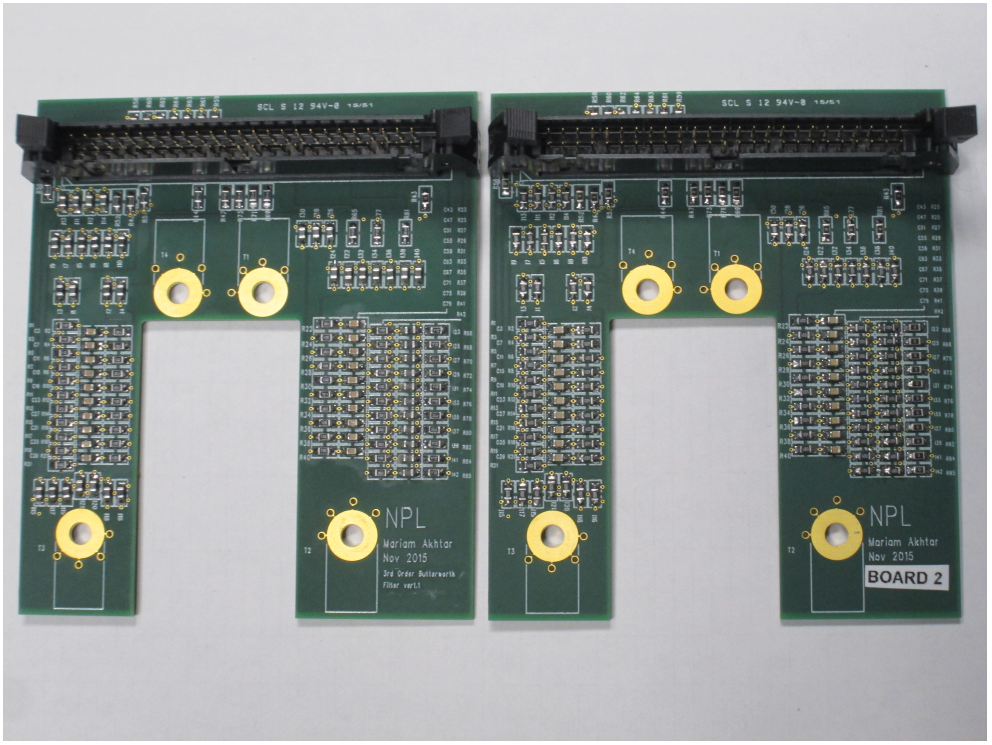

FIGURE 5.4: Picture of the populated heating rate and ion shuttling filter boards. Each board comprises of 8-layers in a s-g-s-g-g-s-g-s configuration (where s is a signal plane and g is a ground plane) in order to reduce crosstalk between tracks on each signal layer. Components are mounted to both sides of the board.

5.2.4 Results

Two filter boards were designed with the aim of reducing the noise on the DC electrodes of the trap. For practical purposes the same design was used for both boards, but populated with different components to achieve the desired frequency response. Similar to the re-configurable termination board, the filter boards were designed using PADS Logic and Layout software. A picture of the populated boards can be seen in Figure 5.4. One board was designed for heating rate measurements and the other for ion shuttling between the different segments of the trap. The board layout was designed to be screwed down onto the vacuum chamber such that pins pushed down onto the air-side electrical contacts of the chip carrier, which then connect to the electrodes of the trap in vacuum (see Section 2.3 and 2.4 for more details). This configuration ensures most relevant filter for the desired measurement can be straight-forwardly interchanged without the need for breaking vacuum.

For the purposes of heating rate measurements, the desired filter would have maximum attenuation at the motional frequencies of the ion. A 2^{nd} order RC filter was used since

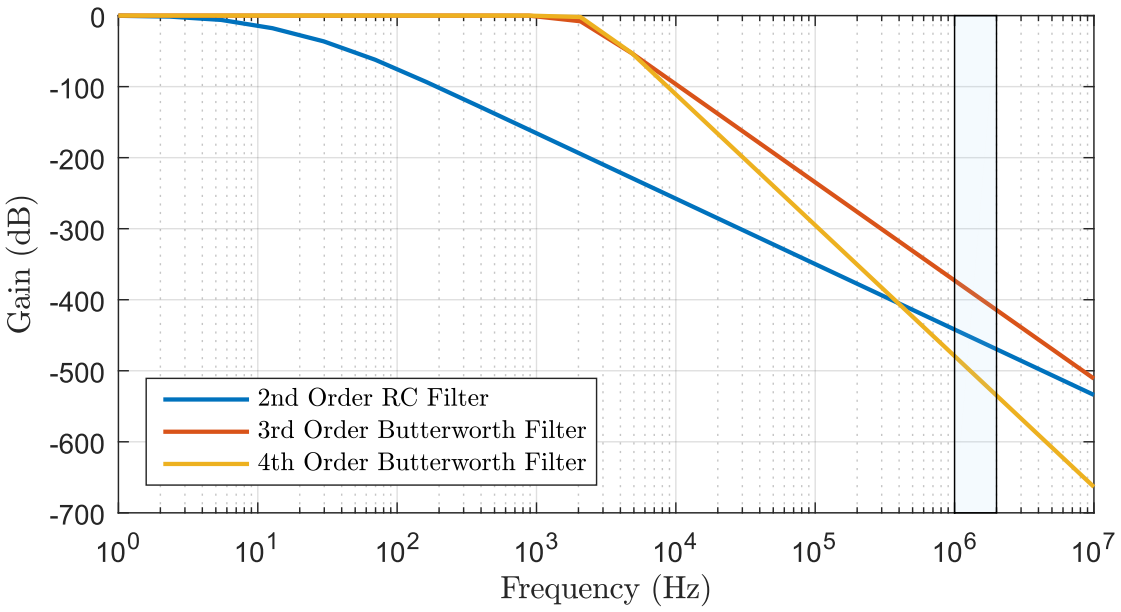

FIGURE 5.5: Calculation of a 2^{nd} order RC filter board with a 15 Hz cut-off frequency with a 3^{rd} order and 4^{th} order Butterworth filter with a 2 kHz and 2.5 kHz frequency cut-off respectively. The shaded region is used to indicate the range of the motional frequencies of the ion.

the available components restricted the cut-off frequency of the potential Butterworth filters. A 2^{nd} order RC filter was used instead of a Butterworth filter type since cut-off frequency was limited by the available components. Figure 5.5 shows a calculation of the frequency response of a 2^{nd} order RC filter with a 3^{rd} and 4^{th} order Butterworth filter. The motional frequencies of the ion in the trap occur at approximately 1-2 MHz as indicated by the shaded region. Figure 5.5 shows that despite the 3^{rd} order Butterworth filter having a steeper attenuation gradient past the cut-off frequency, the 2^{nd} order RC filter, has greater attenuation at the motional frequencies. This is due to the low cut-off frequency that can be achieved with the RC filter. The 4^{th} order Butterworth filter has a greater attenuation than either of the other two filter types. However it is difficult to implement without any ringing in the transfer function, and the space constrictions on the board footprint made it difficult to include the extra set of components in the design. Therefore the 2^{nd} order RC filter was deemed the most appropriate.

Testing of the frequency response of the filter can be seen in Figure 5.6. The filter board was connected to a blank CLCC and a dynamic signal analyser (Stanford Research SR785) was used to measure the response. The response was found to be in good agreement with a simulation of the testing set up that was done in NIMultisim 14.1. The simulated response of the filter board when used within the context of the main

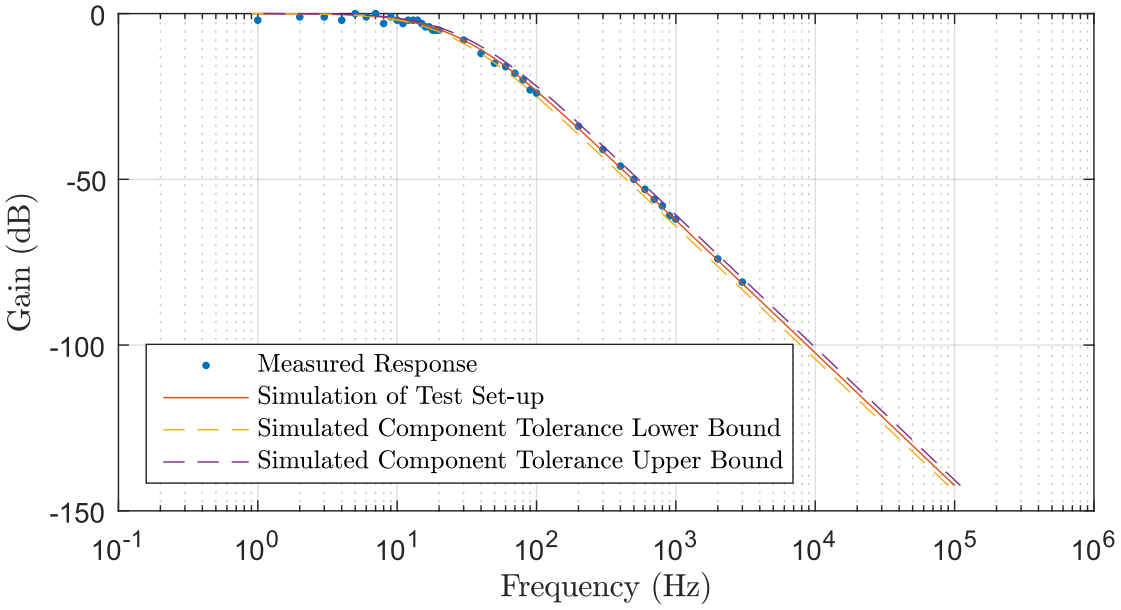

FIGURE 5.6: Measured 2^{nd} order RC filter response with a test set-up.

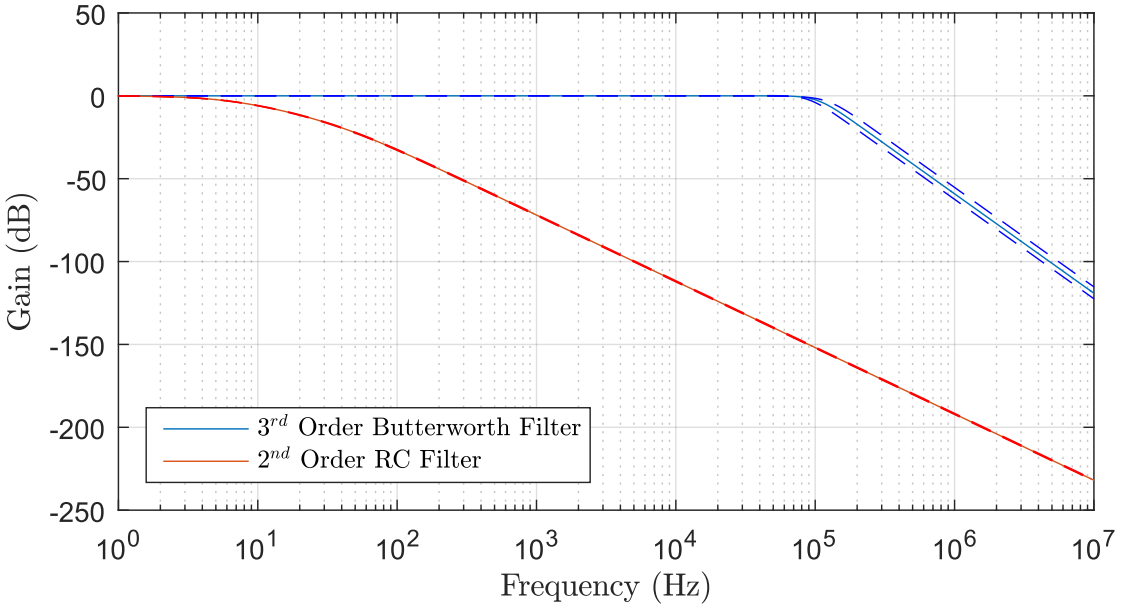

FIGURE 5.7: Simulation of the Butterworth filter and RC filter designs when used in the conjunction with the ion trapping system. The dashed lines indicate the error derived from the component tolerances.

trapping apparatus can be seen in Figure 5.7. The simulations show that the cut-off frequency is 6 Hz and the gain at 1 MHz is -192 dB.

The design for the filter board used for ion shuttling had two primary considerations. Firstly, as with the RC filter, that there is a steep gradient after the cut-off frequency in order to attain the maximum attenuation at the motional frequencies of the ion. Secondly, that there is a reasonable cut-off frequency such that the bandwidth allows

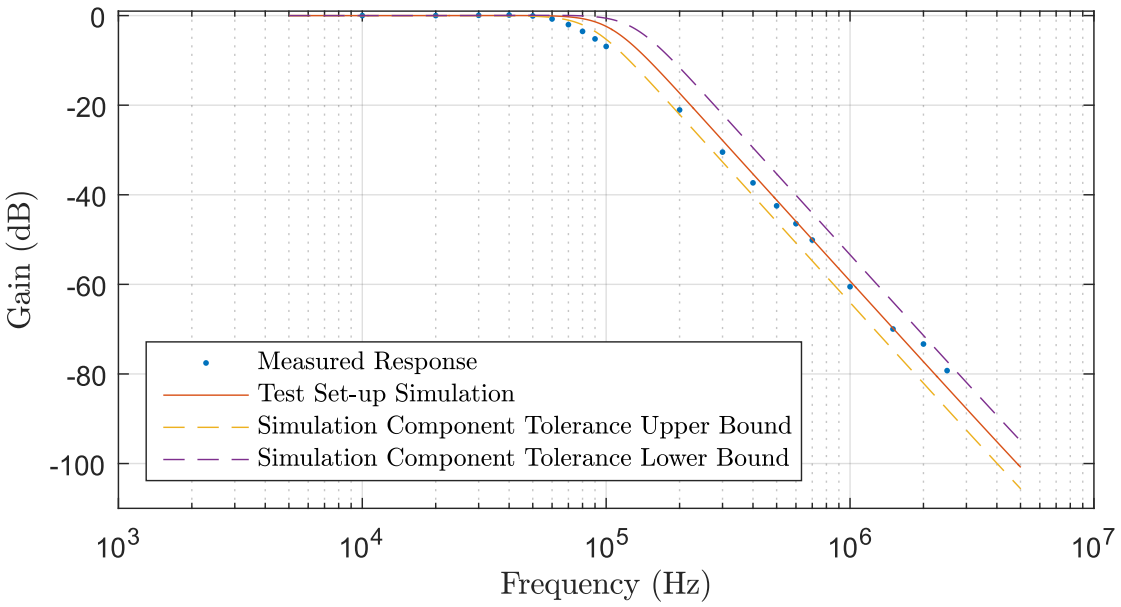

FIGURE 5.8: Measured 3^{rd} Order Butterworth filter response with a test set-up.

for the desired shuttling speed. Here the target cut-off frequency was chosen to be 100 kHz in a similar fashion to [163], where a 300 kHz cut-off frequency of a π-filter was used and an ion was shuttled 280 μm in 3.6 μs with an increase of the ion motional quantum number of 0.1 quanta. Using the same test set-up that was used for the RC filter board the frequency response of the Butterworth filter board was measured and can be seen in Figure 5.8. The filter operates as expected given the quoted component tolerances.

The simulated response for the Butterworth filter with the ion microtrap can be seen in Figure 5.7 alongside the simulation of the 2^{nd} order RC filter response. The graph shows that at the Butterworth filter has a cut-off frequency of 105 kHz and a gain of -59 dB at 1 MHz as opposed to the -192 dB of the RC filter.

The step response of the RC filter can be seen in Figure 5.9 the delay time is 22 ms and the rise time is 58 ms. In contrast, the Butterworth filter (Figure 5.10) has a delay time of 38 μs and a rise time of 115 μs.

5.3 Magnetic Field Control

As detailed in Section 1.4.1 the application of a stable static magnetic field is used to lift the degeneracy of the optical qubit transition through the Zeeman effect. However, since the energies of these transitions are now field dependent, they become susceptible to

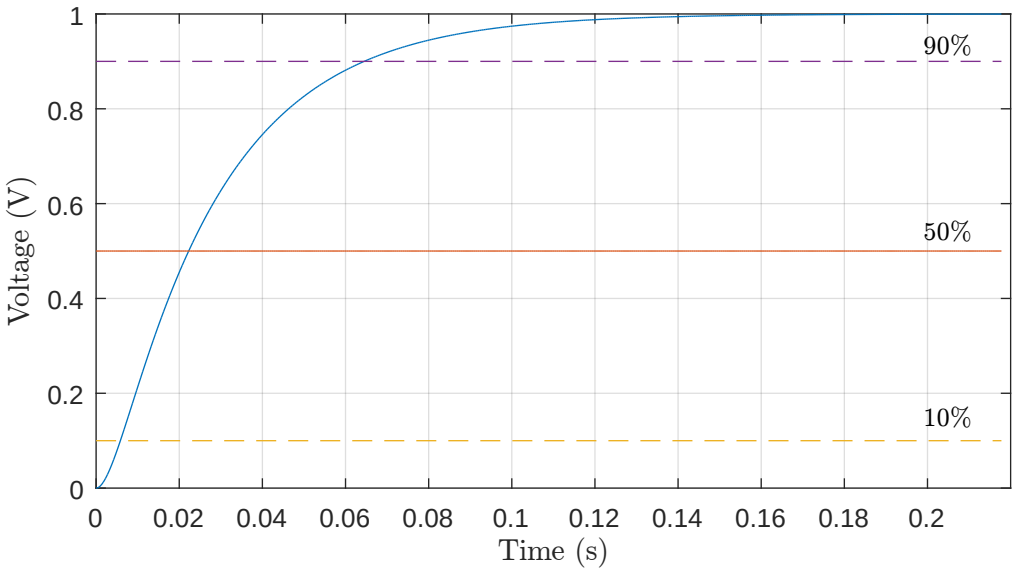

FIGURE 5.9: 2^{nd} order RC filter simulated step response when in the ion microtrap experimental system. The step voltage was 1 V, the delay time is shown at 50 % of the amplitude (solid red line). The 10 % and 90 % levels needed to calculate the rise time are also indicated with dashed lines (yellow and purple respectively).

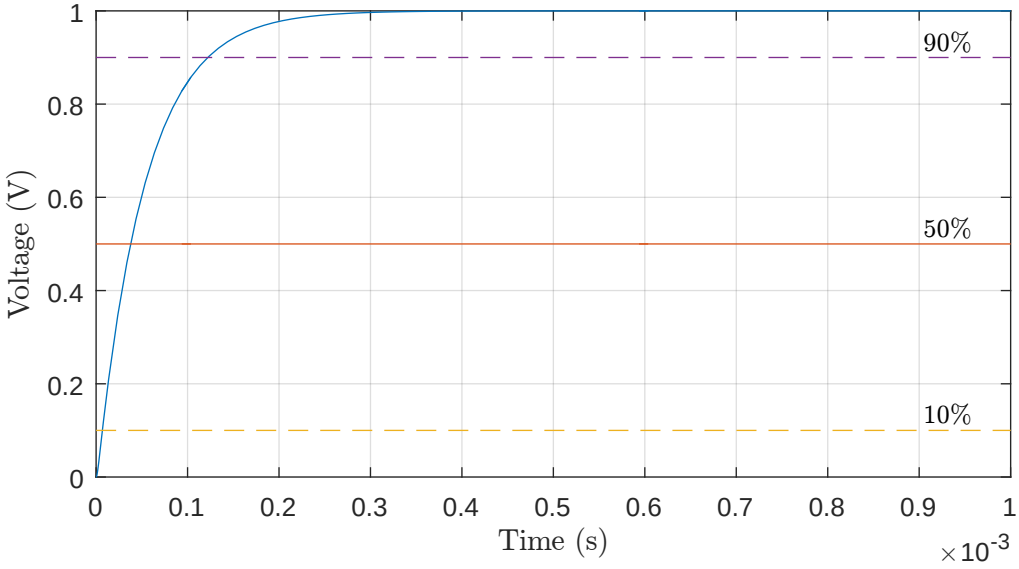

FIGURE 5.10: Butterworth filter simulated step response. The step voltage was 1 V, the delay time is shown at 50 % of the amplitude (solid red line). The 10 % and 90 % levels needed to calculate the rise time are also indicated with dashed lines (yellow and purple respectively).

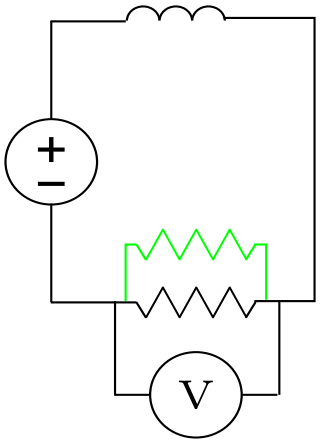

FIGURE 5.11: Circuit diagram of the control system for a magnetic field coil pair (in black). For the bias field coil there is an extra resistor connected in parallel (shown in green).

magnetic field noise which is therefore a source of decoherence. This section describes the development of a control system for the generation of the magnetic field. The system is comprised of three pairs of orthogonal field coils to compensate for the ambient magnetic field and an additional pair to apply a magnetic bias field. Each coil is connected in series to a precision resistor. The voltage is measured across the resistor with a high resolution voltmeter. From the knowledge of the voltage and the resistance a current is then calculated which is used to feedback to the current source. For the bias field coils, due to the high current being applied, the coil has two of the resistors in parallel, over which the voltage is measured. Figure 5.11 shows a circuit diagram that is applicable to each coil pair.

The current supply used here is a high precision source measure unit (NI PXIe-4139) with a maximum power output of 20 W (DC) and seven digit resolution. The resistors (Wika Instruments CER6000A) were chosen due to their insensitivity to temperature fluctuations. These resistor exhibit long-term stability ($\leq \pm 5$ ppm per year) and have a low temperature coefficient ($\leq$ 1 ppm per °C). Furthermore each of the resistors were heat-sunk in a large Al block to further improve their temperature stability. To measure the voltage over the resistors a digital multimeter (NI PXI-4071) with a 7.5 digit resolution was used for each coil pair.

By monitoring the voltage over the resistor for each of the coil pairs the current stability was obtained with and without the feedback mechanism engaged. Table 5.1 shows the currents supplied to each of the coils. The Allan deviation can be used to quantify the noise that is present in the measured current. The Allen deviation σ_y for a discrete set

Coil	**Current (A)**
X	$I_x = 0.077$
Y	$I_y = 0.8$
Z	$I_z = 0.022$
Bias	$I_b = 2$

TABLE 5.1: Table of currents typically applied to coil pairs in order to minimise the magnetic field (coils X-Z) and to apply a bias field (bias coil).

of measurements y_k ($k = 1$ to N), with a sample time τ_0 is calculated using the following equation [164]

$$\sigma_y^2(\tau) = \frac{1}{2(N-2n+1)} \sum_{k=1}^{N-2n+1} \left(\frac{1}{n} \sum_{j=k+n}^{k+2n-1} y_j - \frac{1}{n} \sum_{j=k}^{k+n-1} y_j \right)^2, \tag{5.11}$$

where $\tau = n\tau_0$ is the averaging time. Figure 5.12 shows the Allen deviation measured for each of the current coils. These measurements however constitute the in-loop stability. In order to calculate the out-of-loop stability an additional voltmeter was connected in parallel to the voltmeter that provided the feedback to the current source. Figure 5.13 shows a comparison of the in and out-of-loop data for a supply current of 1 A and 22 mA. These measurements show that the current can be stabilised to approximately $2{\times}10^{-7}$ A for a 20 s averaging time when the feedback is engaged. This corresponds to a magnetic field instability of $3{\times}10^{-7}$ G. The effect of the magnetic field instability of this level on a trapped ion can be quantified by the contribution of the noise to the shift of the ion atomic transitions. For the $^2S_{1/2}$ ($m_j = -1/2$) to $^2D_{5/2}$ ($m_j = -5/2$) transition, equation 2.3 can be used show that there is 2.8 MHz/G variation of transition frequency with magnetic field. Therefore for a $3{\times}10^{-7}$ G instability there is a corresponding error of 0.8 Hz shift in the atomic transition for the 20 s averaging time. At longer times of 1000 s the current instability is 3×10^{-7} A, corresponding to 4×10^{-7} G which is equivalent to a transition frequency change of 1.1 Hz.

The stability of the current sources contributes to the stability of the magnetic field as generated by the coils, however other sources of ambient magnetic field instability can be present, such as from nearby equipment in the lab. The 3-layer magnetic shield enclosure is used to attenuate these additional sources and contains the vacuum system with the ion trap as well as the field coils. The attenuation of the magnetic shielding

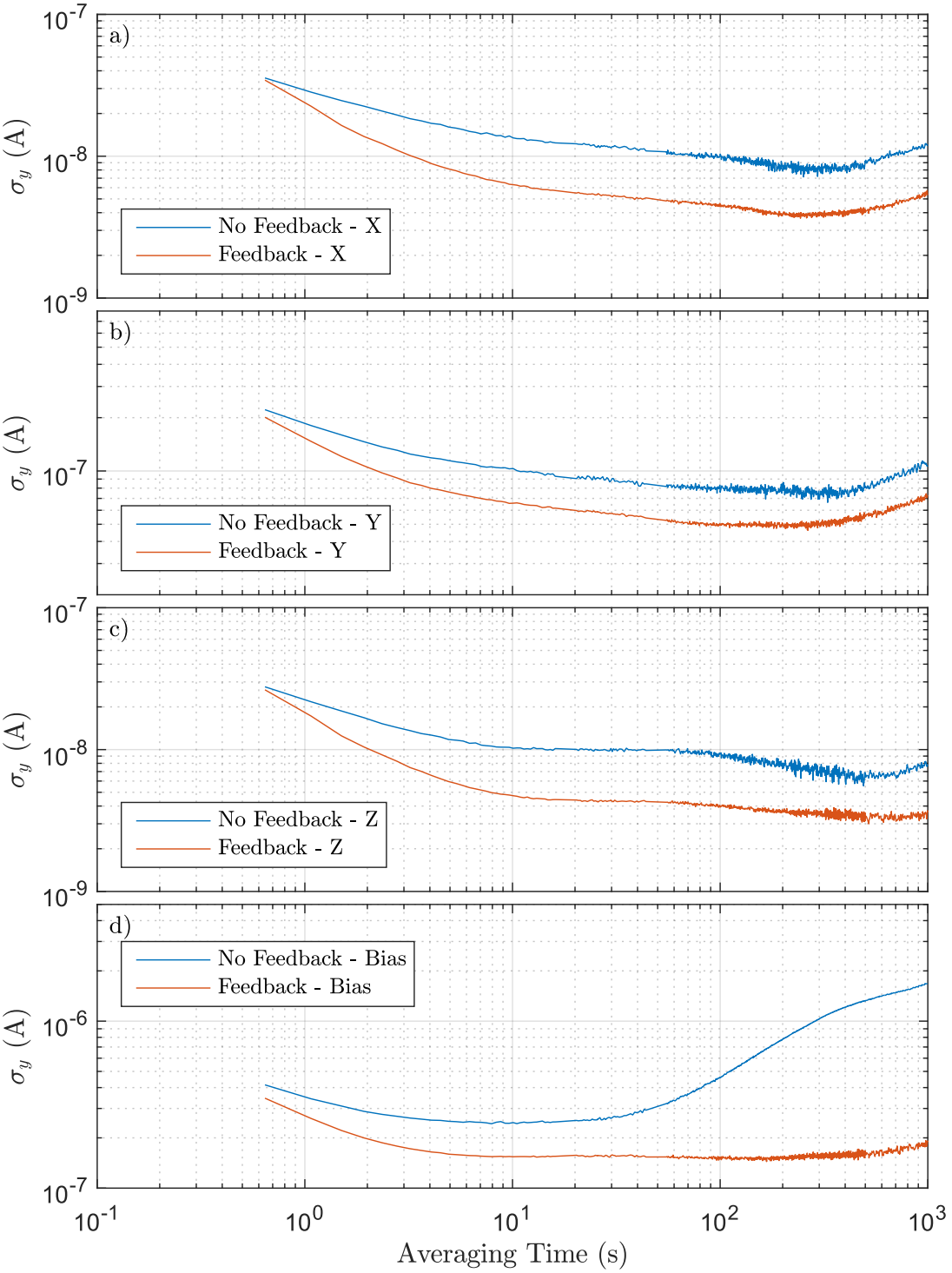

FIGURE 5.12: Allen deviation σ_y in each of the coil pairs: the X, Y, Z and bias. The current is derived from voltage measurements over the precision resistors. The current driving each of these coils can be seen in table 5.1

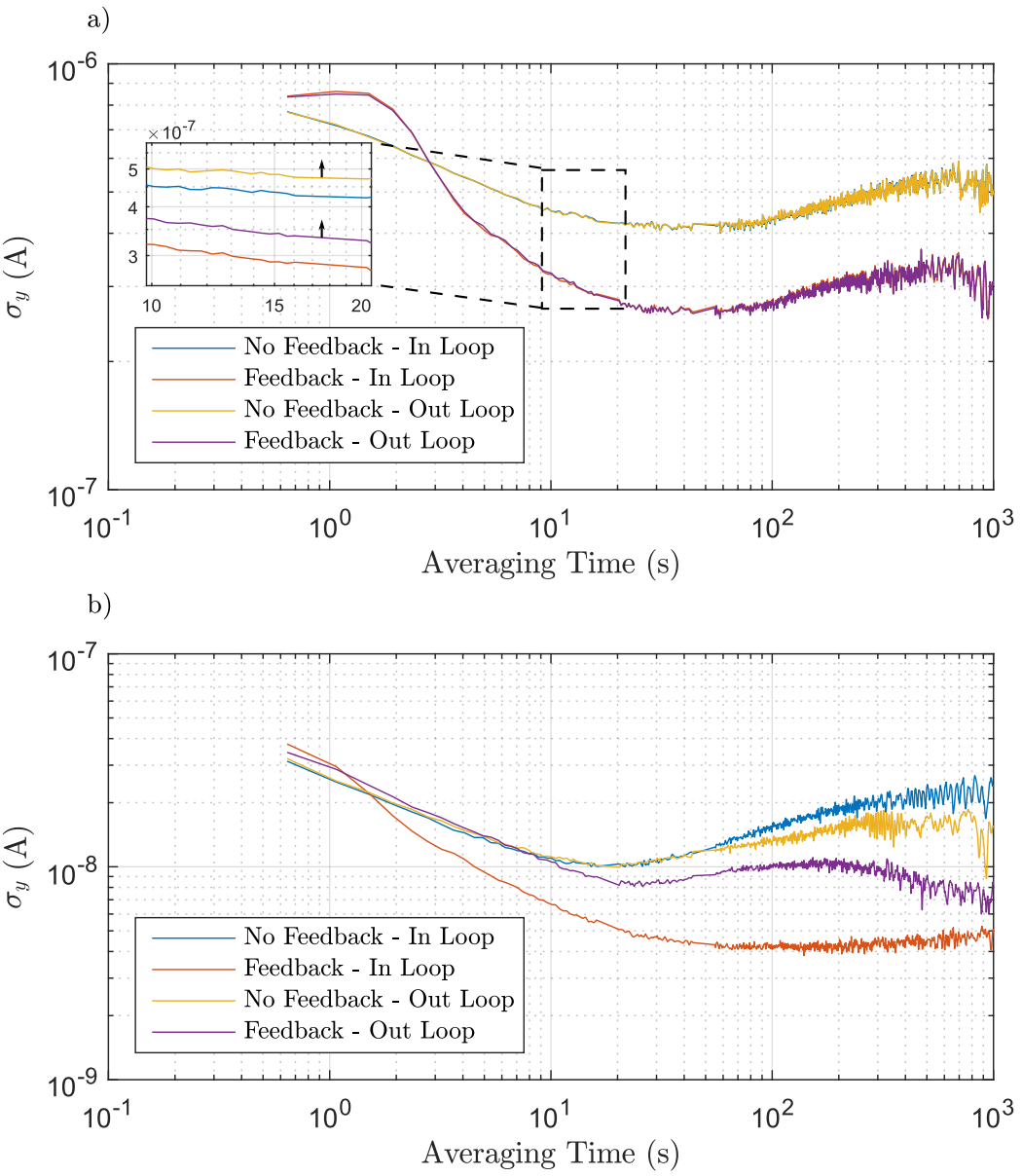

FIGURE 5.13: Allen deviation (σ_y) of the current supplied to the Z-axis magnetic field coils with the in-loop data corresponding to the current used to provide the feedback and the out-of-loop measurement is used as a passive measure the current. Two different currents were used; a) shows the stability for $I_z = 1$ A and b) for $I_z = 22$ mA. The inset in a) shows a zoomed in portion of the graph with an offset of 0.5×10^{-7} A applied to the 'Out Loop' data to highlight the overlap of the 'In Loop' and 'Out Loop' plots.

was measured by Guido Wilpers to be a factor of 10^3 at 50 Hz. The effect of the shielding measured over a 6 hour timescale can be be seen in Figure 5.14. Six Bartington sensors with a sensitivity of 0.5 G/V were arranged such that three of them were inside the shield and orientated along each of the trap axis and the other three arranged in the same configuration but outside the shield. The graphs a-c show that there is a 1-2 orders of magnitude improvement in the magnetic field stability when compared to the sensors outside of the shield. At 50 Hz the attenuation ranged from a factor of 170 in the x-direction to 40 in the z-direction. The reduction in the attenuation factor indicates that there is a possible source of magnetic field noise present inside the shielding. Furthermore, the stability of the current sources suggest the magnetic field stability should be a factor of ∼1-2 orders of magnitude better than what was observed within the shield.

To monitor this effect more closely a magnetic field sensor (Bartington mag-03 with sensitivity of 0.1 G/V) was set up near the trap, within the shield and in the direction of the bias field. It was found that the magnetic field variation was on the order of 10^{-4} G over the 15 hour measurement (see Figure 5.15a. The Allen deviation associated with the measurement is shown in Figure 5.15b. For an averaging time of 7 s the magnetic field instability is 1.3×10^{-6} G. A likely cause for this was found to be the temperature drift of the ion pump magnet. Figure 5.15c shows the resistance of a thermistor taped to the ion pump magnet that was measured alongside the flux gate sensor measurement in Figure 5.15a. An estimate of the temperature variation in Figure 5.15a was done by linearly extrapolating between the stated values for the resistance of the thermistor at 15°C (7855 Ω) and 20°C (6245 Ω) which corresponds to 0.03°C/10 Ω in the region of interest. Therefore for the temperature drift was estimated to be 0.016°C over the 15 hour measurement time with a 0.04°C spike at 40160 s.

The ion pump magnet is made of ferrite material and has a magnetic field variation with temperature that is expected to be ∼0.2 %/°C [165]. Therefore for a mean magnetic field of -0.0748 G (as in Figure 5.15) and a temperature variation of 0.016°C, the expected variation in the magnetic field is $\sim 2 \times 10^{-4}$ G. This is in reasonable agreement with our observation of a variation in the magnetic field of 1×10^{-4} G. One option to improve the system performance is to use Sm-Co magnets which have a magnetic field variation ∼0.04 %/°C [165]; approximately a factor 5 improvement over the use of the current ferrite magnets. Another possibility is to use temperature compensated Sm-Co magnets

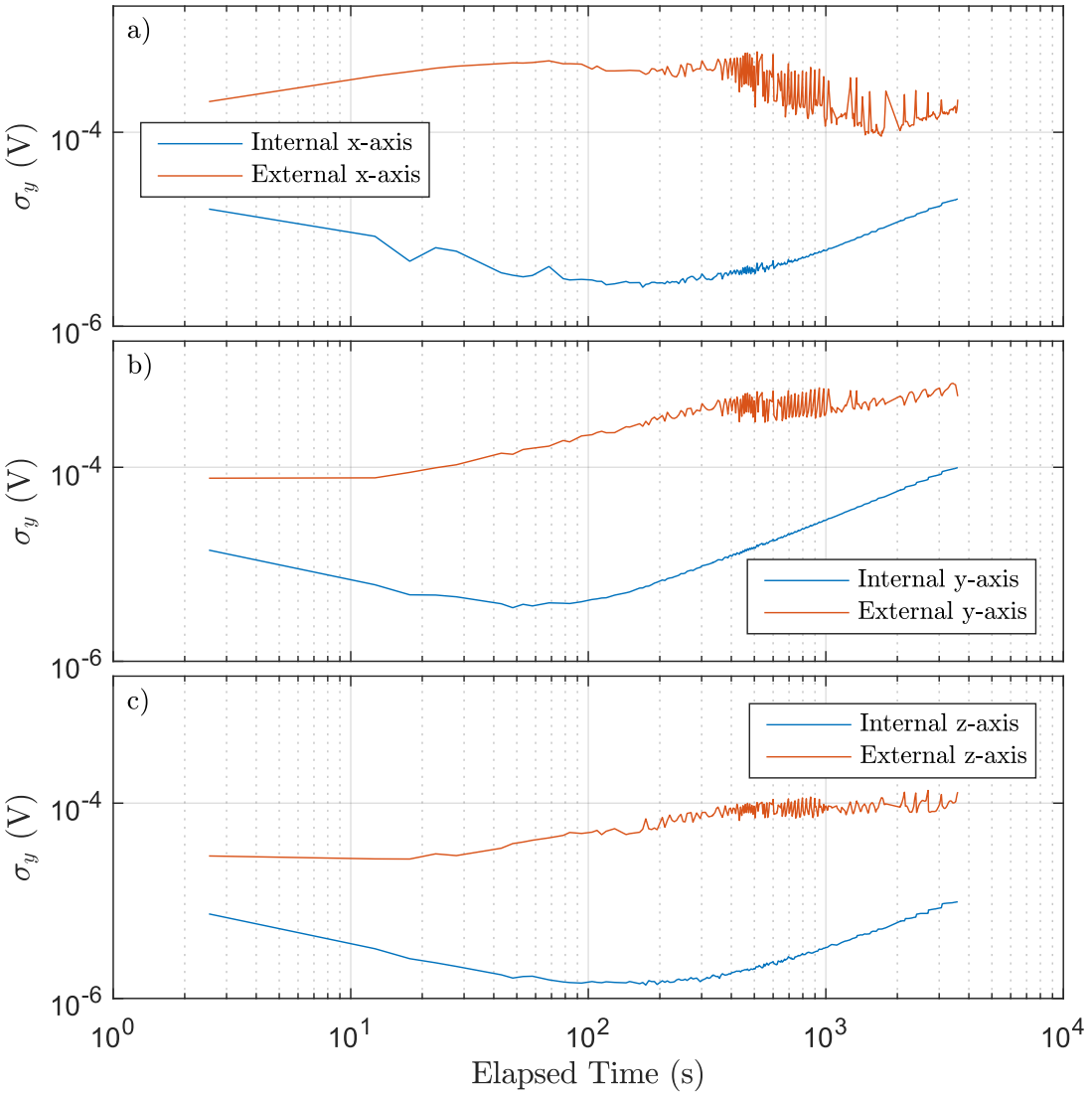

FIGURE 5.14: Allen deviation (σ_y) of magnetic field flux gate sensor measurements made inside (labelled 'Internal') and outside (labelled 'External') of the magnetic shielding over a 6 hour period. Note that the sensitivity of the sensors used here are 0.5 G/V. Here the currents used were $I_x = 71$ mA , $I_y = 804$ mA, $I_z = 21$ mA and $I_b = 2.0032$ A. The current stability feedback was engaged.

that can have a 0.001 %/°C magnetic field variation in a temperature range of -50°C to 150°C [166]. This would improve the magnetic field stability of the ion pump by two orders of magnitude. The incorporation of such a magnet into the experimental system instead of the ferrite magnet is currently under investigation.

5.4 Automated Loading of Ions and Hotplate

A two stage process is used to generate the Sr atoms in the trapping aperture. First an oven containing a reservoir of SrO:Ta is heated to $\sim$ 800°C, evaporating Sr onto

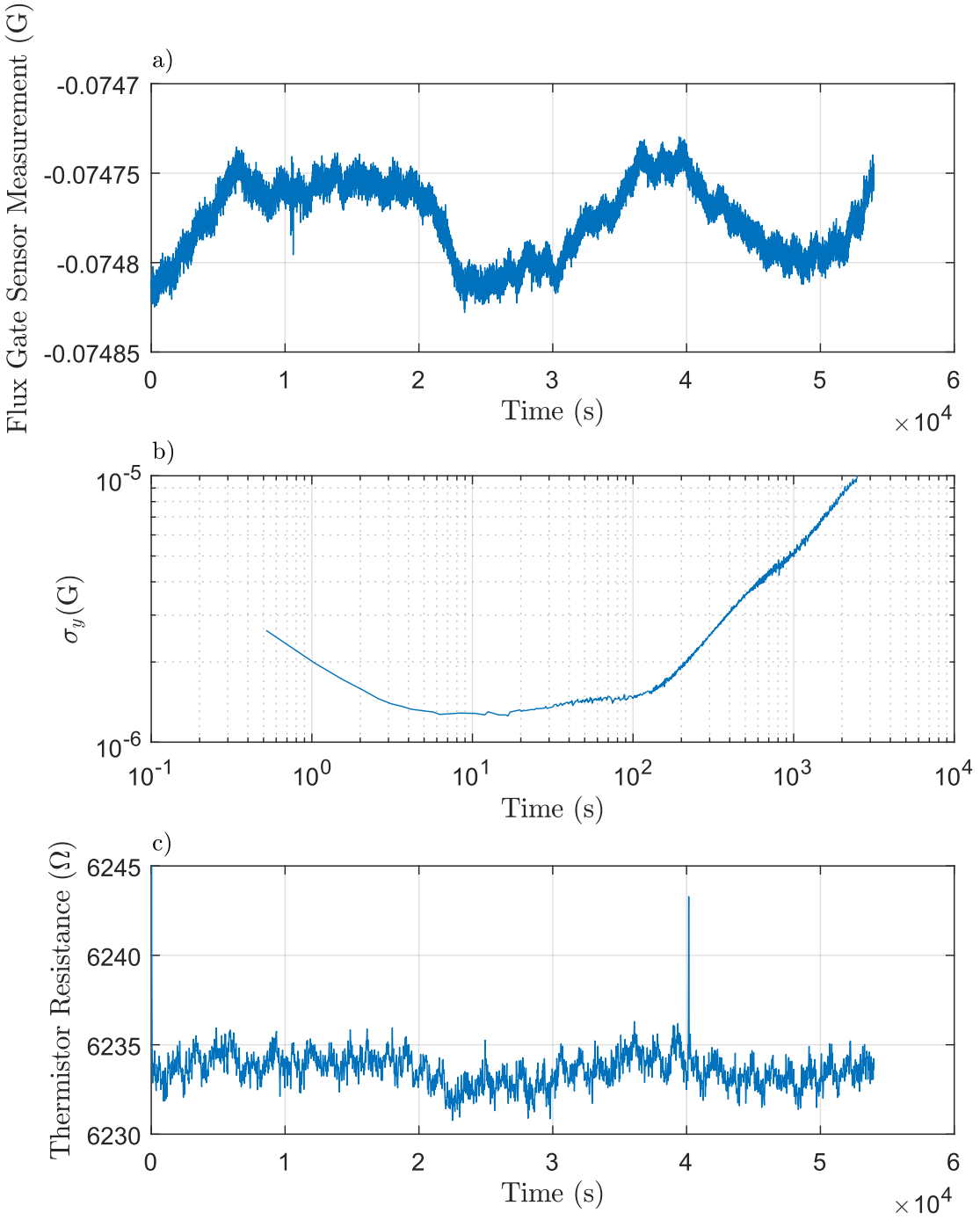

FIGURE 5.15: Graphs to show a 15 hour measurement of the magnetic field and the ion pump temperature. a) Measurement of the magnetic field derived from voltage measurements of a Bartington flux gate sensor. b) Allen deviation σ_y of the magnetic field in a). c) Resistance measurements of a 5 kΩ thermistor taped to the ion pump. The data displayed as a ten point rolling average which corresponds to a 5 s averaging time to mitigate the effect of short term noise.

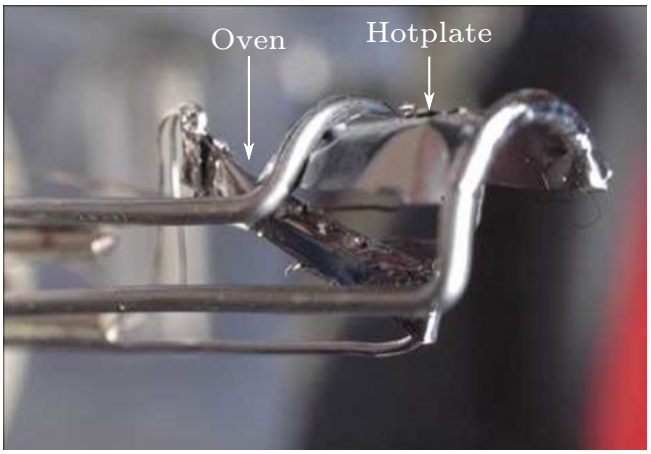

FIGURE 5.16: Picture of oven an hotplate assembly removed from vacuum. Both the oven and the hotplate are made from thin sheets of tantalum foil.

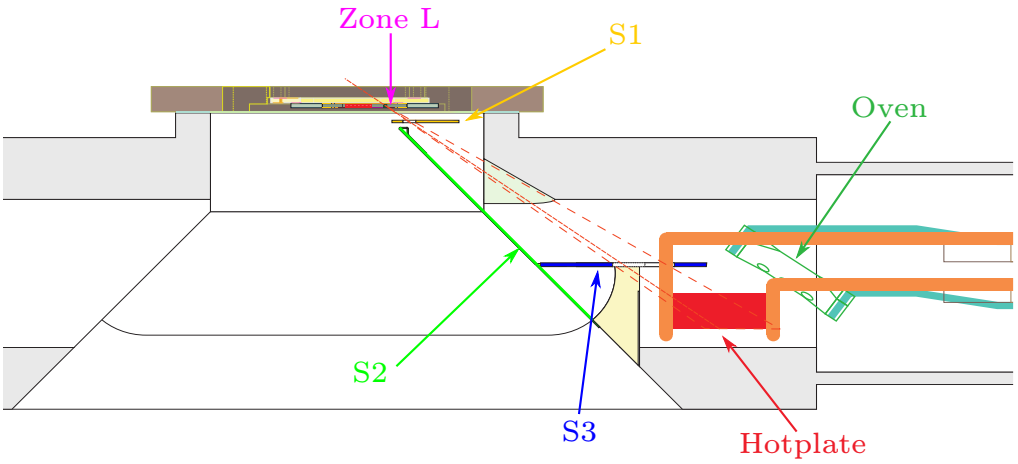

FIGURE 5.17: Schematic diagram of the oven and hotplate within the vacuum system. Three shields (S1, S2 and S3) are used to ensure the atom flux it targeted towards the loading zone (zone L) only. S1 is the atomic flux shield that is on-chip (see Figure 2.5a), S2 protects the rest of the trap electrodes not covered by S1 (see Figure 2.5b). S1 and S3 contain apertures that are used to define the beam direction of the Sr atoms towards zone L.

and tantalum hotplate. There is no line of sight between the oven and the trapping aperture. Once the hotplate is loaded with Sr, the hotplate can be repeatedly heated to ~200°C in order to generate a flux of high purity Sr atoms towards the trapping aperture. Thermocouples that are spot welded to the hotplate and the oven are used to monitor the temperature. A picture of the hotplate and oven can be seen in Figure 5.16. A schematic of the oven and hotplate within the vacuum system can be seen in Figure 5.17. It details how the three shields (S1, S2 and S3) restrict the flux from the hotplate to zone L and shows how there is no line of sight between the oven and the trap electrodes.

An automated process was created to load Sr atoms into the trap and also to load the hotplate with Sr. The oven and the hotplate were each heated by a DC source (Thandar TSX1820P) that was controlled programmatically through USB to GPIB converters. The DC signals were routed through a transistor relay switch which was controlled by a digital I/O card (NI PXIe-6537) contained in a National Instruments chassis. The signals from the thermocouples were monitored by an analogue input card (NI PXI-6254) contained in the same chassis.

An example of hotplate loading with a 12 A source can be seen in Figures 5.18. The oven was heated to 33 mV which corresponds to 800°C after which the source turns off, and the minimum threshold after which the oven has cooled down enough to turn on again was set to 10 mV. Due to the close proximity of the hotplate to the oven, there is a thermal coupling between the two. However as the hotplate heats while it is being loaded, there is a greater loss of Sr as atoms; instead of largely accumulating atoms on its surface it also starts to evaporate atoms towards the trap. Therefore the hotplate thermocouple temperature is monitored and the heating of the oven is limited such that the hotplate thermocouple does not exceed 4.1 mV (120°C). Note that in Figure 5.18c the hotplate thermocouple maximum threshold was set to 2.3 mV to account for the overshoot. The hotplate thermocouple minimum value needed to turn on again was set to 0.3 mV. Only when both the hotplate and the oven have passed the thermocouple minimum thresholds can the next loading cycle commence. In the 2 hours of loading the hotplate, there were 43 heating cycles. During each cycle, the portion of time the oven thermocouple voltage was greater than 33 mV was ∼1 s. The mean peak oven thermocouple reading was 35.6(5) mV and the mean peak hotplate thermocouple reading was 4.0(1) mV.

Once the hotplate is loaded, it can then be heated repeatedly in order to generate a flux of Sr atoms towards the trapping zone. An example of this process can be seen in Figure 5.19 with a set current of 6 A and a voltage limit of 4 V. The maximum hotplate threshold limit was 7.5 mV (205°C) after which the source was turned off until it cooled to the minimum threshold set at 7 mV (190°C). Using these settings the hotplate took 53 s to reach the maximum threshold and a ion was loaded within 50 s thereafter.

During the process of loading an ion, the Sr atoms are evaporated towards the trap and restricted to entering the loading zone (L). Two photoionisation beams (the 461 nm and 405 nm) and a 422 nm resonant and off-resonant cooling beam (see Section 2.5.2)

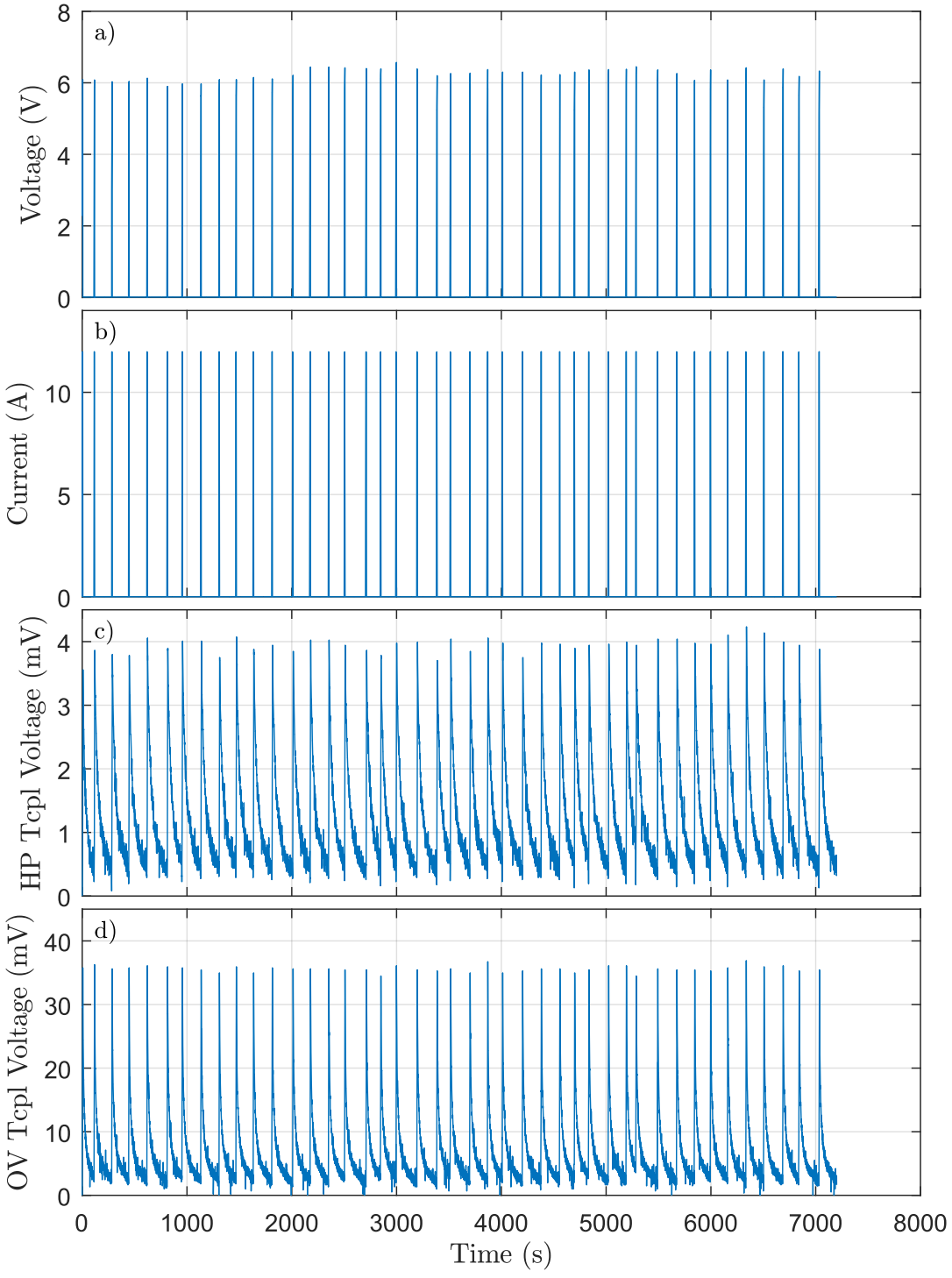

FIGURE 5.18: Automated oven operation for Sr loading of the hotplate. The oven thermocouple voltage thresholds were set at 33 mV and 10 mV. The hotplate thermocouple setpoints were 2.3 mV and 0.3 mV. The total loading time was 2 hours. a) The DC supply voltage. b) The DC supply current. c) Measured hotplate thermocouple voltage (HP Tcpl Voltage). d) Measured oven thermocouple voltage (OV Tcpl Voltage).

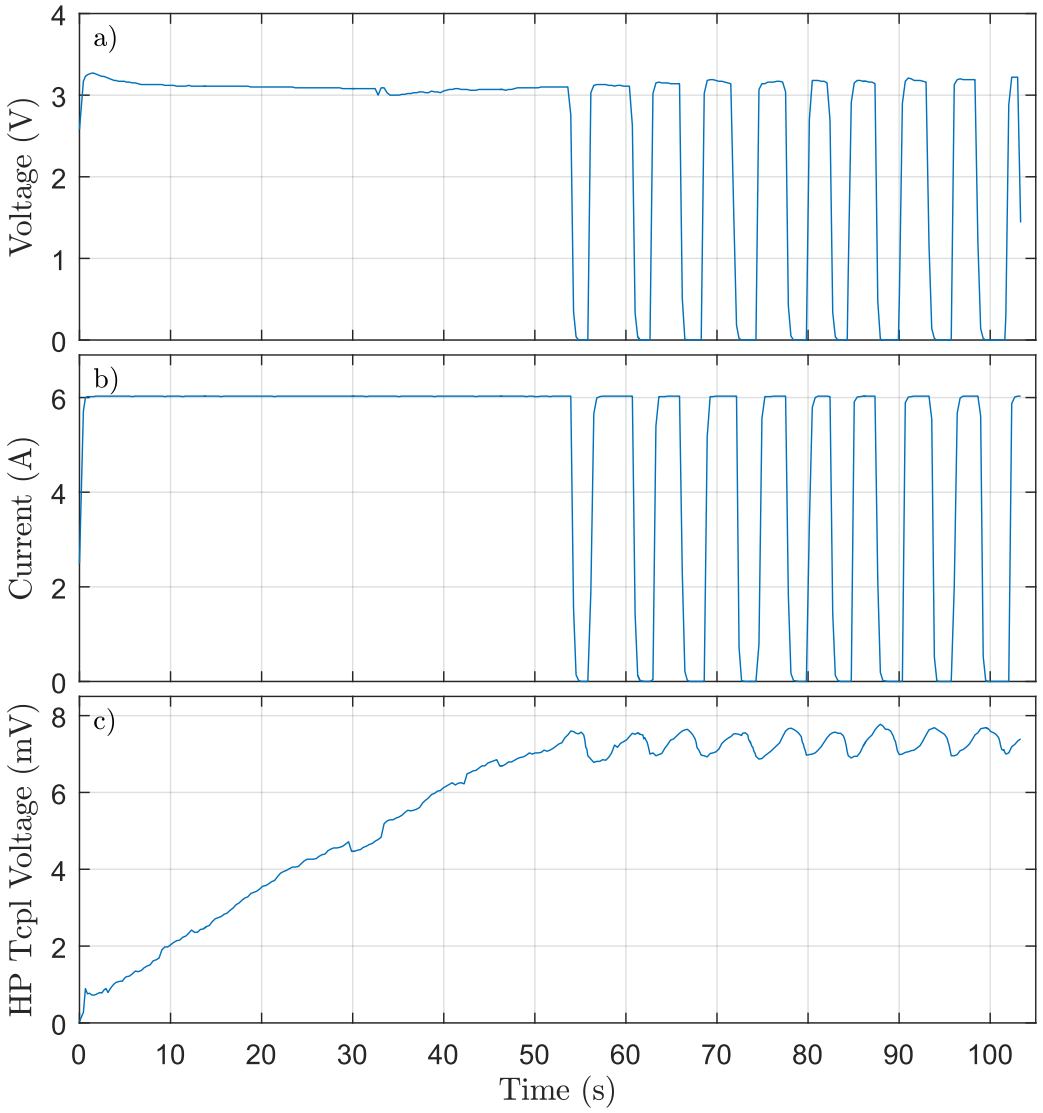

FIGURE 5.19: An example of the automated hotplate operation to generate Sr atoms in zone L of the ion microtrap.The hotplate thermocouple voltage thresholds were set at 7 mV and 7.5 mV. a) The DC supply voltage. b) The DC supply current. c) Measured hotplate thermocouple voltage (HP Tcpl Voltage) with 10-point averaging applied.

illuminate L in order to generate and cool the ion. A shuttling routine uses a sequence of DC voltages to move the trapping potential back and forth between L and experimental zone 2 (Z2) where the PMT and CCD camera can be used to detect the presence of a trapped ion. Two cooling beams are on Z2 during the process. In order to load a second ion the remaining ion is shuttled between the zones until two ions are detected. A more sophisticated approach was initially attempted; the first cold ion was stored in zone 4 (Z4) and once another ion was loaded, the two could then be merged into a single string. This would then be a more scalable approach to loading larger strings since it minimises the probability of ion loss due to a hot ion collision. However, it was found

that although a cold ion could be stored in Z4 without cooling for over 15 mins and then retrieved, the ion could not be kept while the shuttling between L and Z2 was occurring. This was attributed to the oscillating voltages in proximity to the stored ion perhaps causing heating. Therefore, successful implementation of this shuttling routine will need careful consideration of the potentials that each ion sees during transport and storage [163, 167, 168].

Another aspect to consider when loading ions is the effect of the hotplate operation on the magnetic field. Figure 5.20 shows an example of the magnetic field when loading an ion as recorded by three Bartington sensors (mag-03 with a sensitivity of 0.5 G/V) placed in orthogonal directions in close proximity to the trap. The notation of the directions used here correspond to the notation used in the ion trap; see Figure 2.3, where the z-axis is in the axial direction. The step changes at at times 340 s and 661 s correspond to when the source is enabled and disabled respectively. Furthermore the figure shows there is a settling time of approximately 1000 s for the magnetic field to get within 1.8×10^{-4} G of its final steady state value, which would correspond to ∼0.5 kHz shift in the Δm_j = -2 Zeeman transition. Note that the final steady state value is not the same at the initial value; an offset in each of the directions is observed. The effect is most prominent in the x-direction, which was in this instance would correspond to a 5.4×10^{-4} G offset, whereas the offsets for the y and z directions were less than 1.8×10^{-4} G. Larger offsets in the magnetic field however have been observed. The largest would correspond to a 3.6×10^{-3} G offset, which was for a hotplate operation time of 131 s as opposed to the 98 s in Figure 5.20. Therefore if an ion is reloaded, or more ions are loaded into the trap the frequency of the transition of interest will need approximately ∼1000 s to settle to a steady state value, and be subject to frequency shifts compared to previously made measurements.

The exact cause for the remaining offset is unknown however one potential source could be the presence of the magnetic materials within the system. For example, part of the thermocouples used are made of Alumel which is a ferromagnetic material [169] and as a result of the relatively large magnetic field perturbations, as seen in Figure 5.20, there could be remanent magnetisation that generates an offset.

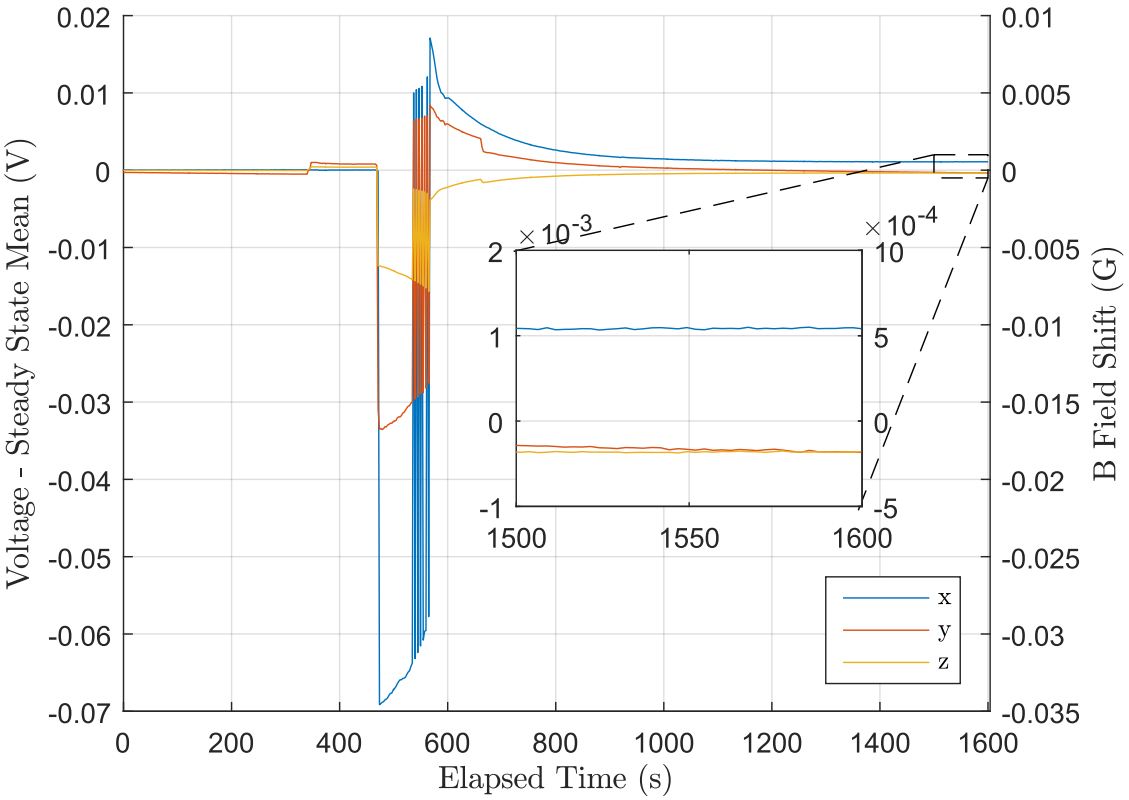

FIGURE 5.20: Example of the magnetic field measured in three orthogonal directions, denoted by x, y and z, when operating the hotplate in order to load ions. The source was enabled at 340 s and disabled at 661 s. The current was first turned on at 469 s and finally turned off at 567 s. The right-hand axis shows variation in the magnetic field compared to time 0 s. Inset shows the offset of the steady state values after hotplate operation in more detail.

5.5 Summary

Sources of decoherence from electrical noise on the DC source, instability in the magnetic field and adsorption of the atom flux are discussed. The development of a re-configurable termination board and process-specific filter boards enabled versatile control of the potentials to the trap electrodes. Two filter boards were designed; one for the purpose of heating rate measurements and another for ion shuttling. For the former, the filters were made to have maximum attenuation at the motional frequencies of the ion. A 2^{nd} order RC filter was used with 192 dB at 1 MHz. For the latter there was the added consideration of the shuttling speeds; a 100 kHz cut-off was chosen and a 3rd order Butterworth filter type which resulted in a 59 dB attenuation at 1 MHz.

A stabilised current system was presented for the coil pairs that generate the magnetic field that the ion sees. From the current stability a magnetic field stability of 3×10^{-7} G over 1000 s was anticipated. However other sources of magnetic field instability within

the mu shielding were discovered; principally from the temperature dependence of the ion pump magnet. Therefore, with this limitation, the magnetic field stability was found to be 5×10^{-6} G over 1000 s. However, by changing ion pump magnet from ferrite material to temperature compensated Sm-Co the magnetic field drift from the ion pump magnet is expected to be reduced by a factor of 10^2.

Due to the atom flux shield on the trap the evaporated Sr atoms is limited to zone L. On one hand this minimises the risk of atoms adsorbing onto the electrodes surface and generating stray fields or ion heating. However on the other hand the restricted atomic flux could also limit the lifetime of the oven and hotplate if not well-controlled. Automated control of the oven and hotplate was established such that thermocouple of each of the devices could be used to feedback to the DC source. This process can be used to apply well-defined limits on the temperatures that the hotplate and oven reach for efficient Sr atom generation and maximising the life span for both the devices. In addition, the fluctuations in the magnetic field as a result of operating the hotplate was measured. It was found that a settling time of ∼1000 s was needed for the magnetic field to get within 1.8×10^4 G of its final steady state; corresponding to ∼0.5 kHz shift in the $\Delta m_j = -2$ Zeeman component of the $^2S_{1/2}$ - $^2D_{5/2}$ transition.

Chapter 6

Single and Two Ion Spectroscopy

6.1 Introduction

Coherent control of one and two ions form the benchmarks of ion trap performance. For example, in QIP it can be shown that single qubit operations in combination with a specific two-qubit operation, such as a CNOT-gate, is sufficient to build a quantum network [56]. The single- and two-qubit coherence times and gate fidelities are key indicators for how a QC will perform [4]. The coherence time of a qubit will limit the number of sequential gates that can be implemented. Furthermore, the fidelity of each single- and two-qubit gate will dictate the level of error correction, and therefore the amount of additional resources, that will be needed [46]. In quantum metrology the ion coherence time is a limiting factor on the interrogation time which directly affects the fractional frequency instability (see equation 1.2). Two-ion entanglement has also been shown to be of significant interest. The use of entangled states can improve the sensitivity of the spectroscopic measurements beyond what is attainable with non-entangled particles [170, 171]. However, the exploitation of this extra sensitivity is only possible if the measured signal is not degraded or lost due to decoherence.

This chapter details an investigation into the control of single and two ion states in the new generation of ion trap design (trap type B in Section 2.3). Section 6.2 will show the single ion motional spectrum. It highlights the dependency of the axial frequency on the endcap voltages and the range of the motional frequencies in zero magnetic field as well as when a bias field is applied. Section 6.3 investigates the motional spectrum for two ions with and without the presence of a magnetic field in a similar fashion to

the single ion. The effect of pulse shaping the amplitude of the 674 nm qubit excitation pulse in order to reduce off-resonant excitation will then be detailed in Section 6.4. The measurements in these sections use frequency-resolved spectroscopy. Section 6.5 will be an investigation into time-resolved spectroscopy. This section will demonstrate Rabi flopping on the optical qubit carrier transition, which is used as a measure of the average motional quantum number of a Doppler cooled ion. However, in the process of this work certain technical limitations in the apparatus were observed and these will also be explained in more detail.

The data displayed in this chapter was taken using the experimental setup described in Chapter 2 with the experimental upgrades detailed in Chapter 5. Furthermore, all measurements were made with the ions located in experimental zone 2 of the ion microtrap (see Section 2.3); a low-noise region suited to maximising the coherence of the measurements made. The experimental sequence used for each of the ion spectroscopy measurements in this section involves the following stages;

1. Doppler cooling.
2. Optical pumping into the m_j = -1/2 sublevel of the $^2S_{1/2}$ transition.
3. Application of a spectroscopy pulse.
4. Ion state read-out.
5. If the ion state has been determined to be in the $^2D_{5/2}$ state a clear-out 1033 nm pulse is applied.
6. Stages 1 to 5 are repeated for a set number of interrogations and an average of the measured data is taken.

For frequency-resolved spectroscopy (Sections 6.2 to 6.4) stages 1 to 6 are repeated where the frequency of the spectroscopy pulse is incremented at each iteration. For time-resolved spectroscopy (as in Section 6.5) the spectroscopy pulse duration is incremented and the laser frequency is fixed. A discussion into the current system limitations will be contained in Section 6.6. It will detail the noise that is observed and the timescales involved as well as the potential solutions. The final section, Section 6.7, highlights some of the work towards the implementation of a Mølmer-Sørenson gate. The aim is to

apply the developed experimental procedures once the noise limitations in Section 6.6 have been resolved.

6.2 Single Ion Motional Spectrum

For 3D geometries the analytical and numerical modelling of the ion trap potentials and the resultant motional frequencies of the ion has been done by [172]. The axial ω_z frequency can be calculated as [172]

$$\omega_z = \sqrt{\frac{2\kappa e U_{DC}}{M d_{DC}^2}}, \tag{6.1}$$

where κ is the static potential geometric efficiency factor, e is the charge of the electron, M is the ion mass and d_{DC} is the distance between the ion and the nearest point on the endcap electrodes. The two radial frequencies ω_{r1} and ω_{r2} can also be calculated as [172]

$$\omega_{r1} = \sqrt{\frac{e^2 U_{RF}^2 \eta^2}{2M^2 \Omega_{RF}^2 d^4} - \frac{2\epsilon\kappa e U_{DC}}{M d_{DC}^2}} \tag{6.2}$$

and

$$\omega_{r2} = \sqrt{\frac{e^2 U_{RF}^2 \eta^2}{2M^2 \Omega_{RF}^2 d^4} - \frac{2(1-\epsilon)\kappa e U_{DC}}{M d_{DC}^2}}. \tag{6.3}$$

Here U_{RF} is the RF potential, η is the geometric efficiency factor in the radial plane, Ω_{RF} is the trap drive angular frequency, d is the ion-electrode distance and ϵ is the geometric anisotropy factor. The appearance of the second radial frequency arises due to the geometry of the endcap potentials; *i.e.* when $\epsilon \neq 0.5$. If the endcap voltages were applied symmetrically along the axis of the ion in radial plane, the two radial frequencies would be degenerate. In the microtraps used in this work the endcaps are applied by using the DC electrodes of neighbouring segments. Therefore the field the ions experiences from the static potential does not have a circular symmetry in the radial plane which results in the appearance of a second radial frequency.

The motional spectrum for a single ion in zero magnetic field can be seen in Figure 6.1 for a spectroscopy pulse tuned to the $^2S_{1/2}$ to $^2D_{5/2}$ transition with a duration of

40 μs and an endcap voltage of 6.8 V. Each of the notable spectral lines is labelled with its frequency detuning and the motional sideband it corresponds to. Here the axial frequency occurs at $\omega_z/2\pi = 0.85$ MHz and the radial frequencies at $\omega_{r1}/2\pi = 1.86$ MHz and $\omega_{r2}/2\pi = 2.15$ MHz. Using equations 6.1 and 6.2 with the measured motional frequencies; $\kappa = 0.14$ and $\epsilon = 2.06$. However by re-inserting the values κ and ϵ into equation 6.3, the calculated $\omega_{r2}/2\pi = 2.39$ MHz, which shows a 10% difference from the measured value. This discrepancy is likely due to finite length of the trap electrodes. Implicit in equations 6.1 to 6.3 is the assumption that the electrodes are infinitely long in the axial direction [172]. The finite electrode lengths and the small gaps between the electrodes will lead to a potential offset. Therefore for the purposes of the calculation made here, the measured motional frequencies are in reasonable agreement with the expected values.

Figure 6.2 shows the detuning from the carrier transition of the axial motional frequencies as a function of applied endcap voltage. The fit used a Levenberg Marquardt fitting algorithm and in line with equation 6.1 is of the form

$$\omega_z = a\sqrt{U_{DC} + b}, \tag{6.4}$$

where a and b were fit parameters. The parameter b accounts for the drift in the calibration of the EFG (~0.04 V) and also for a offset that occurs in the axial direction due to the finite length of the electrodes. From the fit, it was found that b = -0.1. In addition, the fit also resulted in $a = 2.06 \times 10^6$ which can be used to calculate $\kappa = 0.14$ (see equation 6.1).

Once the spectrum has been determined in zero B-field, a bias field can then be applied to separate out the Zeeman components for each of the transitions (see Section 2.2). Figure 6.3 shows a measurement of the $^2S_{1/2}$ ($m_j = -1/2$) to $^2D_{5/2}$ ($m_j = -5/2$) Zeeman component when a 2.9 G bias field is applied and the ion has been optically pumped into the $^2S_{1/2}$ $m_j = -1/2$ state. The figure shows not only the axial and radial frequencies but also the presence of second and third order motional sidebands.

For both spectra in Figures 6.1 and 6.3, the power in the spectroscopy beam was high enough that for the pulse duration τ, $\Omega\tau > \pi$, where Ω is the Rabi Frequency. This is so that the motional sidebands can be more easily detected. A spectrum where $\Omega\tau < \pi$ can be seen in Figure 6.4

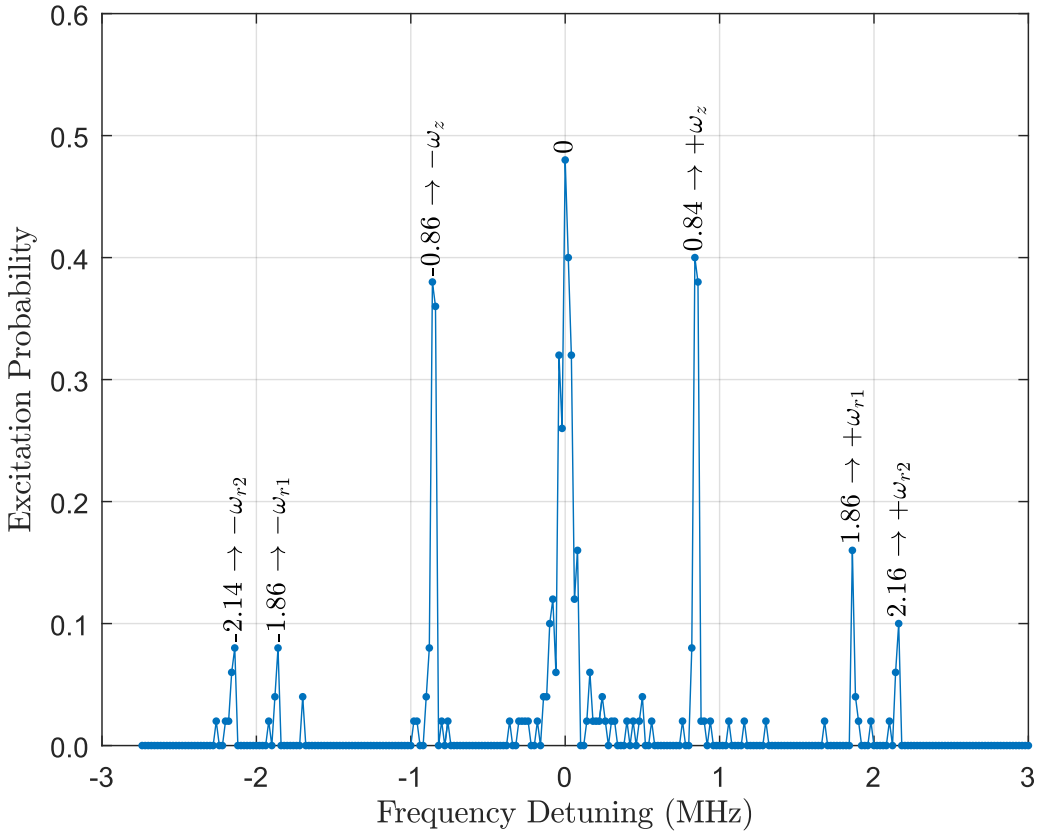

FIGURE 6.1: Frequency spectrum at zero magnetic field with 6.8 V endcap voltages and 20 kHz frequency steps. Each data point is the result of 50 interrogations. The pulse power and duration was 40 μs and 177 μW respectively. Each of the spectral lines are labelled with the frequency detuning at which they occur and what transition they correspond to.

6.3 Two Ion Motional Spectrum

A similar process of scanning the 647 nm spectroscopy laser frequency can be applied to two ions. For N number of ions there are $3N$ normal modes of vibration. Therefore there are 6 motional modes for a two ion crystal. There are 3 center-of-mass (COM) modes as in the single ion case, and in addition there are one stretch mode and two rocking modes. The frequency detuning of the stretch mode ω_s can be calculated in relation to the axial mode ω_z using [173]

$$\omega_s = \omega_z\sqrt{3}. \tag{6.5}$$

The rocking mode ω_{roc} can be calculated by using both the axial and radial motional frequencies [173]

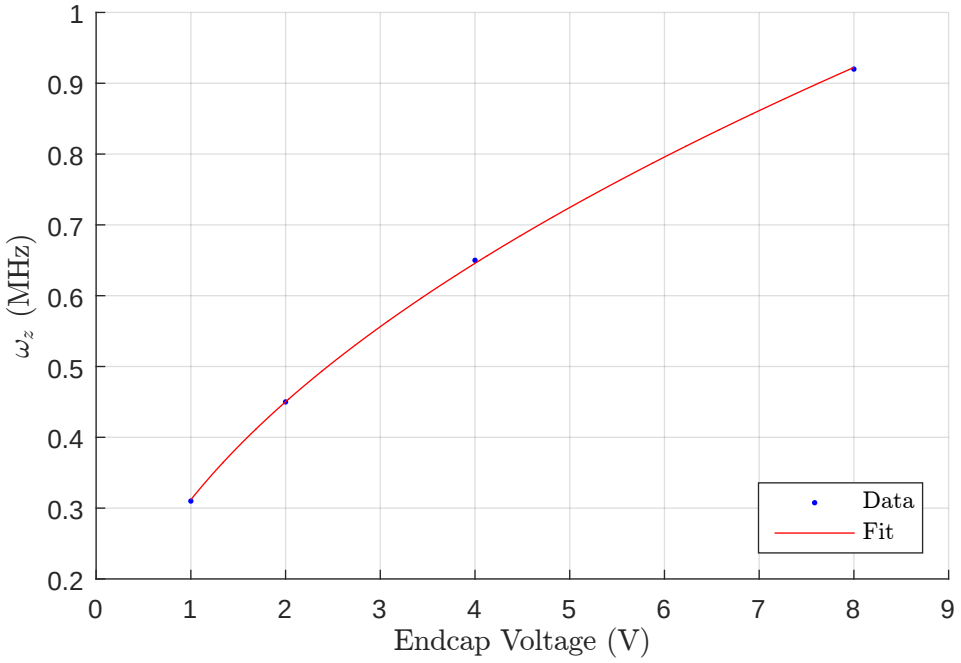

FIGURE 6.2: Single ion motional frequency in the axial direction ω_z as a function of endcap voltage. A 40 μs probe pulse duration with power 177 μW was used in these measurements. A fit to the data was made using equation 6.4.

$$\omega_{roci} = \sqrt{\omega_{ri}^2 - \omega_z^2}, \tag{6.6}$$

where $i \in \{1, 2\}$.

A measured motional spectrum for two ions in zero magnetic field with 6.8 V endcaps can be seen in Figure 6.5. From the motional spectrum of two ions, the measured axial and radial frequencies should be the same as in the case of a single. The axial and radial frequencies can then be used to calculate the position of the stretch and rocking modes and compared to the measured values. A summary of the calculated and expected motional frequencies can be seen in Table 6.1. The expected and observed motional frequencies show good agreement.

Once the spectrum in zero B-field has been established for a two-ion string a bias field can be applied and the Zeeman components resolved. An example of the $\Delta m_j = -2$ transition spectrum for two ion and with optical pumping into the $^2S_{1/2}$ (m_j= -1/2) state can be seen in Figure 6.6. The measured detuning of the motional frequencies from the carrier transition are summarised alongside the expected values and the frequencies measured in zero magnetic field in Table 6.1. The results show good agreement with the

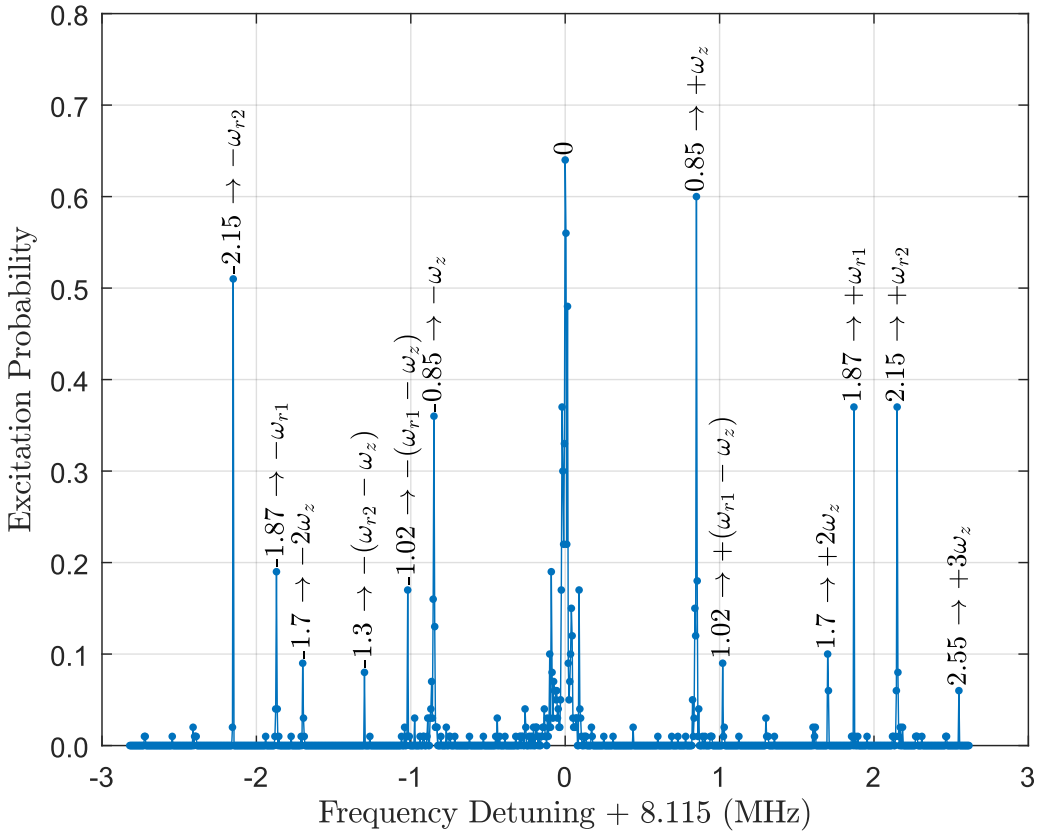

FIGURE 6.3: Example of a single ion frequency spectrum in a 2.9 G bias magnetic field with 6.8 V applied to the endcaps and 5 kHz frequency steps. For ease of comparison with Figure 6.1, the spectral lines are plotted with a 8.115 MHz offset such that motional frequencies relative to the carrier transition are apparent. Each data point is the result of 100 interrogations. The pulse duration and power was 200 μs and 55 μW respectively. Each of the spectral lines are labelled with the frequency detuning at which they occur and what transition they correspond to.

expected values.

6.4 Pulse Shaping

The spectra presented in this chapter have thus far been measured using square-shaped spectroscopy pulses. However by controlling the temporal profile of the amplitude of the probe pulse, the power spectral density remote from the carrier can be greatly suppressed. There are several pulse shapes that can be used [101]. Commonly the Blackman-shaped pulse is favoured since it provides high sidelobe suppression under Fourier transform [36, 101]. The consequence of this suppression for coherent interactions with the ion is the reduction in off-resonant excitation. This can be essential when addressing a motional sideband since it minimises the interaction with the much stronger carrier transition.

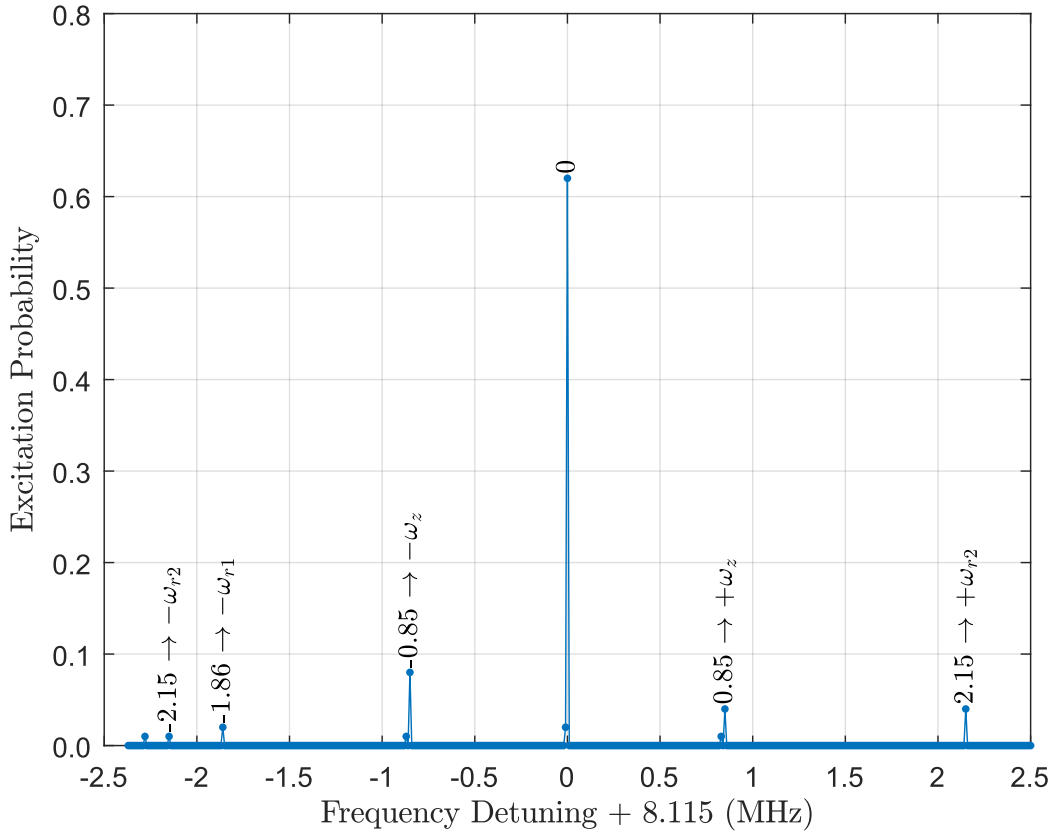

FIGURE 6.4: Example of a single ion frequency spectrum in a 2.9 G bias magnetic field with low laser probe power (1.4 μW). The pulse duration was 100 μs with 6.8 V applied to the endcaps and 10 kHz frequency steps. For ease of comparison with Figure 6.1, the spectral lines are plotted with a 8.115 MHz offset such that motional frequencies relative to the carrier transition are apparent. Each data point is the result of 100 interrogations. The pulse duration and power was 100 μs and 1.4 μW respectively. Each of the spectral lines are labelled with the frequency detuning at which they occur and what transition they correspond to.

Figure 6.7 shows two frequency scans across the carrier of the Δm_j = -2 transition in 2.9 G bias field. In Figure 6.7a square-shaped pulses were used and Blackman-shaped pulses in Figure 6.7b. To generate temporally-shaped optical pulses, the non-linear response of the double pass-AOM in the agility set-up (see Section 2.5.4) needs to be taken into account [100]. An automated calibration routine correlates the RF input to the AOM with the measured optical power output. A 9th order polynomial fit to the calibration curve is then used to linearise the response of the modulator. This calibration then allows of the production of pulses with arbitrary temporal shape. The set-up used to generate the spectroscopy pulses was developed by Joseph Thom and the full details can be found in [100, 110]. It is clear to see from comparing the two figures that the spectral density in the wings of the spectral lineshape is reduced in Figure 6.7b.

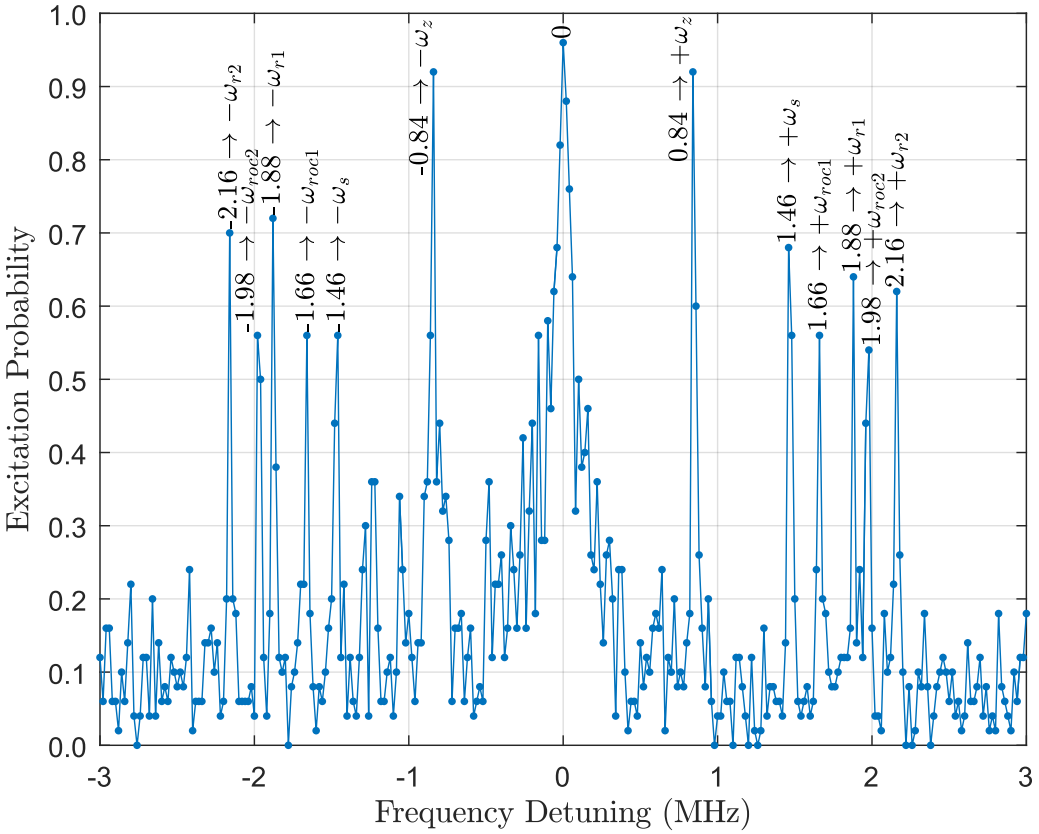

FIGURE 6.5: Two Ion frequency spectrum in zero magnetic field with 6.8 V applied to the endcaps and 20 kHz frequency steps. Each data point is the result of 50 interrogations. The pulse duration and power was 40 μs and 177 μW respectively. Each of the spectral lines are labelled with the frequency detuning at which they occur and what transition they correspond to.

TABLE 6.1: Motional frequencies for a two-ion string in zero and 2.93 G magnetic field with 6.8 V endcap voltages. The observed frequencies can be seen in Figures 6.5 and 6.6. The expected values for ω_z, ω_{r1} and ω_{r2} are from the measurement using 1 ion and with the same experimental parameters (see Figure 6.1). The expected values for ω_s, ω_{roc1} and ω_{roc2} are calculated using equations 6.5 and 6.6. For the observed motional frequencies in the presence of a bias field (2.93 G), values stated are relative detunings from the carrier transition. Note that the detuning shown corresponds to $\omega_\alpha/2\pi$ where $\alpha \in \{z, r1, r2, s, roc1, roc2\}$ and the stated errors are from the frequency step size in each of the measurement.

	Detuning		
Motional Mode	**Expected**	**Observed (0 G)**	**Observed (2.93 G)**
ω_z	0.85(1)	0.84(1)	0.86(1)
ω_{r1}	1.86(1)	1.88(1)	1.86(1)
ω_{r2}	2.15(1)	2.16(1)	2.15(1)
ω_s	1.45	1.46(1)	1.48(1)
ω_{roc1}	1.68	1.66(1)	1.65(1)
ω_{roc2}	1.99	1.98(1)	1.97(1)

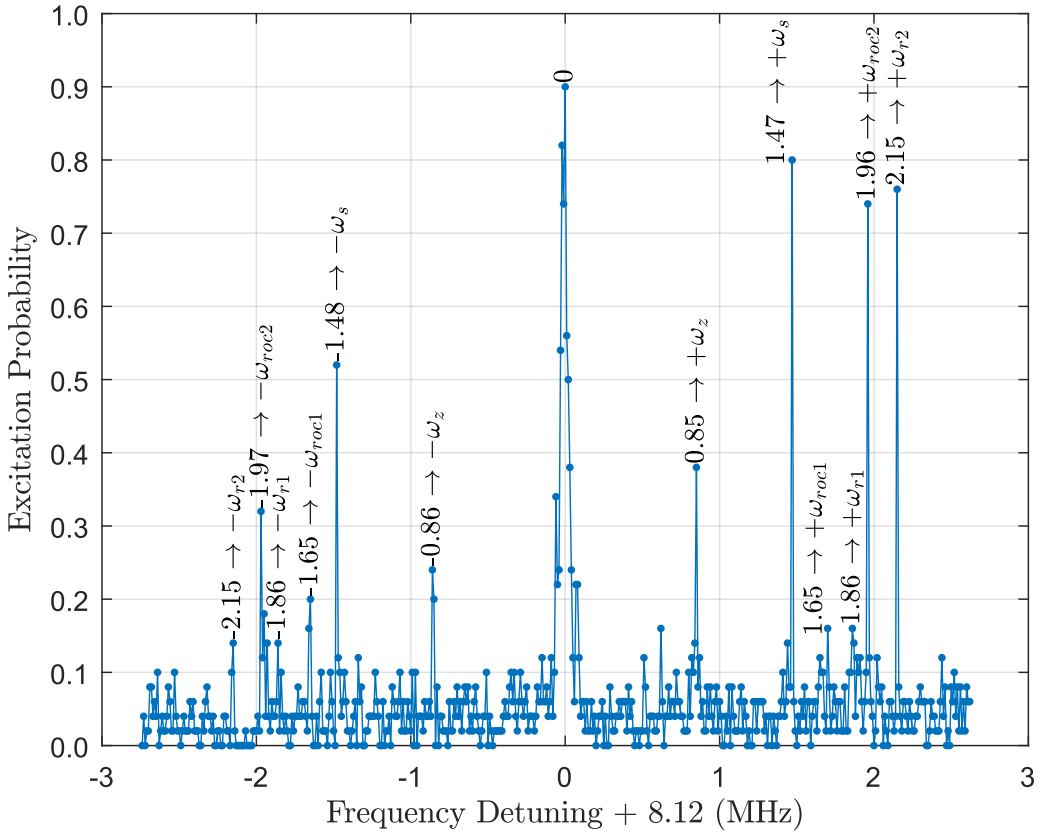

FIGURE 6.6: Frequency spectrum in a 2.93 G magnetic field with 6.8 V endcap voltages and 10 kHz frequency steps. For ease of comparison with Figure 6.5, the spectral lines are plotted with a 8.12 MHz offset such that motional frequencies relative to the carrier transition are apparent Each data point is the result of 50 interrogations. The pulse power and duration was 200 μs and 97 μW respectively. Each of the spectral lines are labelled with the frequency at which they occur and what transition they correspond to.

6.5 Time-Resolved Spectroscopy

The demonstration of coherent oscillations of the ion's state on a given transition (otherwise known as Rabi flopping) is an unambiguous indicator of coherent control. Driving the ion on the quadrupole transition can coherently manipulate the ion into a superposition of the $^2S_{1/2}$ and $^2D_{5/2}$ states. By using a fixed intensity and increasing the pulse duration Rabi oscillations are observed. In the ideal case of an atom that is prepared in the ground state the oscillations would have full contrast from 0 to 1 excitation probability and exhibit no decay over time. However in this work the ion is only Doppler cooled. Therefore, the non-zero vibrational quantum number of the ion causes dephasing due to the thermal distribution of the ion's occupation probability across the motional states in the trap. In this instance the rate of dephasing will be reliant on the particular transition since the Rabi frequency on the carrier transition has a weaker dependence

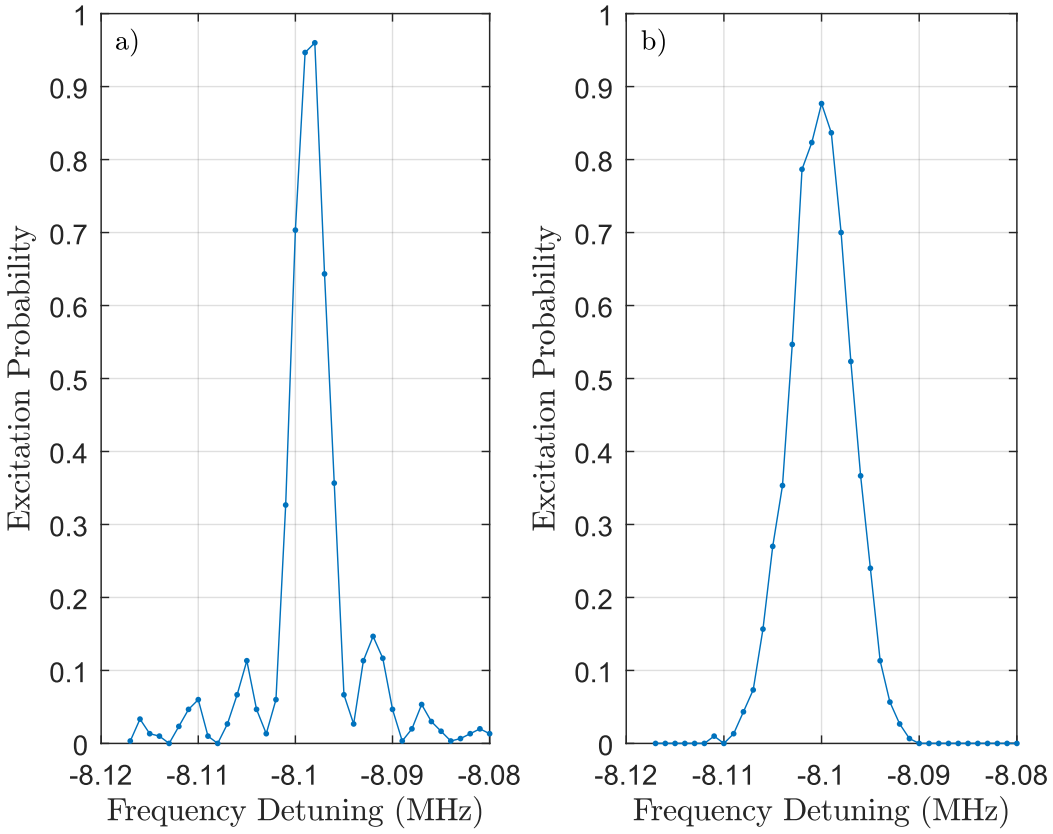

FIGURE 6.7: Comparison of effect of a) square-shaped pulses (with 200 μs duration and 1.1 μW power) with b) Blackman-shaped probe pulses (with 400 μs duration and 1.8 μW power) on carrier of the Δm_j = -2 transition. Each data point is the result of 300 interrogations and the frequency was scanned in 1 kHz steps.

on the motional quantum number than the motional sidebands (see equations 1.22, 1.26 and 1.24). Other effects that degrade the Rabi flopping contrast include decoherence from the finite laser linewidth, and drifts in the magnetic field, which are discussed in more detail in Section 1.4.

To demonstrate Rabi flopping with a single ion, a magnetic field of 2.9 G was applied, the ion was Doppler cooled and then optically pumped into the $^2S_{1/2}$ (m_j= -1/2) state. The spectroscopy laser, tuned to the centre of the $^2S_{1/2}$ (m_j= -1/2) to $^2D_{5/2}$ (m_j= -5/2) transition, was then used to excite the ion with increasing pulse duration.

An example of the this measurement can be seen in Figure 6.8 for pulse duration τ, where 0 μs $\leqslant \tau \leqslant$ 10 μs in steps of 100 ns. The probability of the ion occupying a particular vibrational state is given by a thermal distribution

$$P(\bar{n}) = \frac{\bar{n}^n}{(1+\bar{n})^{1+n}} \tag{6.7}$$

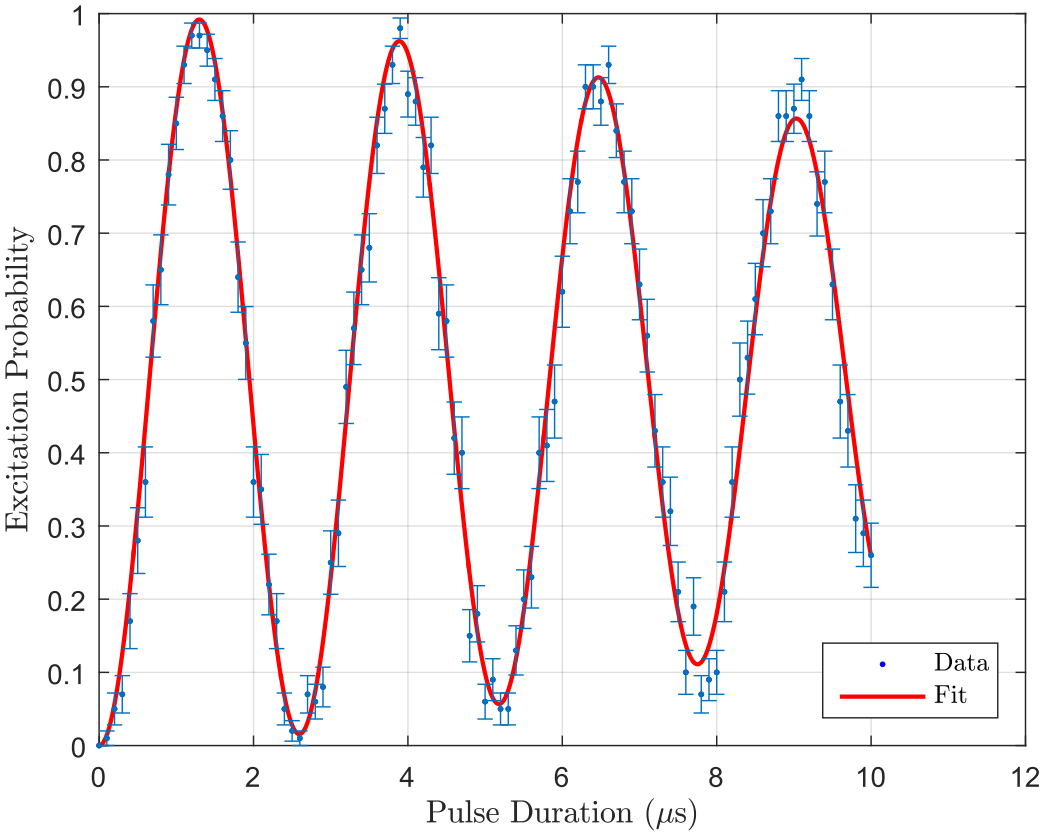

FIGURE 6.8: Rabi flopping on the carrier of the Δm_j= -2 transition in a 2.9 G bias field. The pulse duration was incremented in steps of 100 ns and the pulse power was 8.26 mW. Each data point is the result of 100 interrogations.

where $\bar{n}$ is the average vibrational quantum number. In order to extract the average motional quantum number in the axial and radial directions ($\bar{n}_z$ and $\bar{n}_r$ respectively) a fit to the data using a series of sinusoidal curves is made in a manner similar described in Valliappan Letchumanan's PhD thesis [71]. Using this method the excitation probability P_D is approximated by fitting sinusoidal solutions of the Rabi Frequency $\Omega_{(n_r,n_z),(n_r,n_z)}$ for each of the motional state assuming a constant decoherence rate for each state γ

$$P_D = \frac{A}{2}\left(1 - e^{\gamma t}\sum_{n_r,n_z} P_{n_r}(\bar{n}_r)P_{n_z}(\bar{n}_z)\cos(\Omega_{(n_r,n_z),(n_r,n_z)}t)\right). \tag{6.8}$$

The optical pumping efficiency into the $^2S_{1/2}$ $m_j = -1/2$ state is given by A (where $A = 99.4(7)$ see Section 2.8.2) and a Levenberg-Marqardt fitting algorithm was used. The errorbars represent the statistical noise for each of the data points measured as the 1σ quantum projection noise, $QPN(1\sigma)$, given by [174]

$$QPN(1\sigma) = \sqrt{\frac{\rho_{DD}(1-\rho_{DD})}{N}}, \tag{6.9}$$

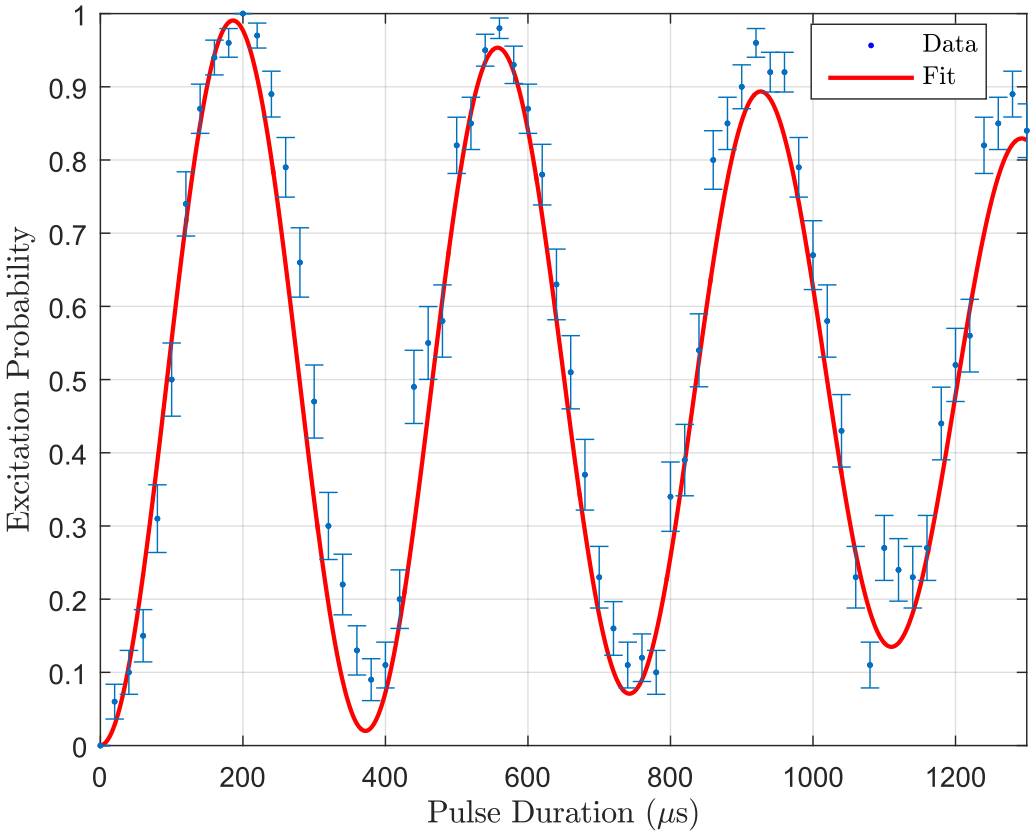

FIGURE 6.9: Rabi flopping on the carrier of the Δm_j= -2 transition in a 2.9 G bias field. The pulse duration was incremented in steps of 20 μs and the pulse power was set at 6.2 μW. Each data point is the result of 100 interrogations.

where ρ_{DD} is the excitation probability at each measured pulse duration and N is the number of interrogations used. The errors here are statistical errors associated with rotations around the Bloch sphere, where there is minimum uncertainty at the poles and a maximum at the equator.

There are two radial frequencies present in the trap (ω_{r1} and ω_{r2}). The fit used an average of ω_{r1} and ω_{r2} to generate $\bar{n}_r$. Given that the axial and radial frequencies are $\omega_z/2\pi = 0.85$ MHz, $\omega_{r1}/2\pi = 1.88$ MHz and $\omega_{r2}/2\pi = 2.16$ MHz, the fit in Figure 6.8 resulted in mean axial and radial quantum numbers $\bar{n}_r = 10(2)$ and $\bar{n}_z = 24(4)$, a decoherence rate $\gamma/2\pi = 0.01$ Hz and a Rabi frequency $\Omega/2\pi = 40.65$ kHz. At the Doppler limit associated with the cooling transition (see Section 1.3.2) the lowest achievable average motional quantum numbers are; $\bar{n}_{min,z} = 11$, $\bar{n}_{min,r1} = 5$ and $\bar{n}_{min,r2} = 4$; roughly a factor of two below those measured in Figure 6.8.

Rabi flopping on the carrier of the $^2S_{1/2}$ (m_j= -1/2) to $^2D_{5/2}$ (m_j= -5/2) transition over longer pulse durations 0 μs $\leqslant \tau \leqslant$ 1300 μs can be seen in Figure 6.9. Repeating the fitting procedure that was used in Figure 6.8, the Rabi frequency was found to

be $\Gamma/2\pi = 2.95$ kHz with a decoherence rate of $\gamma/2\pi = 0.01$ Hz and mean motional quantum numbers $\bar{n}_r = 11(4)$ and $\bar{n}_z = 27(10)$. Note that between Figures 6.8 and 6.9, there is a lager 1σ error in the measurement of the mean motional quantum number from the latter. This is due to the presence of technical noise that could arise from a number of sources; such as electric-field noise, magnetic field noise, laser frequency fluctuations etc. The errorbars in the two figures only account for the binomial statistical error. To account for the error from technical noise, the standard deviation of many measurements made of ρ_{DD} for each pulse duration would need to be made. By comparing the measured error and the calculated value from equation 6.9, if the former is greater than the latter then the measurement is limited by technical noise. By doing repeated measurements, it was found that there is a severe limitation due to technical noise that arises sporadically. This will be discussed in more detail in the next section.

6.6 Noise-limited Coherence

Repeated measurements of the Rabi flopping on the carrier of $\Delta m_j = -2$ Zeeman component of the $^2S_{1/2}$ to the $^2D_{5/2}$ transition showed the presence of intermittent noise. Figures 6.10-6.12 show sequential scans of increasing pulse duration. Figure 6.10 was recorded a week prior to Figures 6.11 and 6.12. In each of the separate figures, the subplots show measurements that were taken on the same day and with the same experimental parameters applied. Figure 6.10 shows a series of Rabi flops taken at short pulse durations where $0\ \mu s \leqslant \tau \leqslant 10\ \mu s$. In Figure 6.10a there is little to no coherence evident, however by Figure 6.10b the system has recovered. In Figure 6.10b to e there is a gradual increase in the noise present.In comparison to Figure 6.10b, Figure 6.10e shows a substantial reduction in the coherence time and the plot appears to show the signature of a hot ion. Similar trends are also observed at longer pulse durations. For example, in Figure 6.11 with $0\ \mu s \leqslant \tau \leqslant 40\ \mu s$; 6.11a to d shows a gradual recovery of the coherence, but in Figure 6.11e there is a very sudden loss of coherence at $\tau > 10\mu s$. Figure 6.12 shows the technical noise present at even longer pulse durations of $0\ \mu s \leqslant \tau \leqslant 600\ \mu s$. Here there are some noise fluctuations present in Figure 6.12a and b, which gets worse in Figure 6.12c. However in Figure 6.12d and e it is evident that there little coherence present in the range $0\ \mu s \leqslant \tau \leqslant 300\ \mu s$, yet when the pulses with longer durations are being recorded the coherence begins to recover. These measurements show the noise is

not unique to a specific pulse duration range but applicable to the full range measured. Furthermore, they show how this noise arises intermittently on timescale that can be greater than an individual scan ($\sim$ 2min) but short enough that between sequential scans there is poor repeatability.

An investigation into the sources of the technical noise is still on going. It was suspected that some of the noise was due to a faulty amplifier injecting noise onto the RF electrodes. The noise appeared sporadically and on a timescale that was suspected to correlate to the sudden drastic losses of coherence (as in Figures 6.10a and 6.11e). Since the amplifier has been changed the drastic loss of coherence has not been observed, however the other noise effects are still present. Several potential sources of this noise were checked including the DC voltages to the trap, the magnetic field and the laser extinction of all the lasers used. However the prime suspect is the spectroscopy laser pump, which was measured by Guido Wilpers to have a fractional frequency instability of $\sim 10^{-13}$ at 1 s averaging, compared to the $\sim 10^{-15}$ result that had been previously measured. Furthermore the noise is erratic and seems to occur on a timescale that is consistent with the observed loss of coherence in Figures 6.10 to 6.12. The origin of this noise is thought to be due to the multi-mode operation of the pump laser. Uncontrolled mode competition can result in intensity noise on the pump laser. This in turn results in frequency noise on the Ti:Sapphire laser that is outside the bandwidth of the laser frequency stabilisation electronics. Therefore the experimental apparatus is currently being upgraded to include a replacement pump laser source with single-mode operation.

6.7 Towards Entanglement

Mølmer and Sørensen presented a method for entangling ions based on quantum mechanical destructive interference paths [58]. When two ions are confined in a string, the mutual Coulomb repulsion causes the ions to oscillate with a shared vibrational motion along the COM mode. It is the mediation of the vibrational state though the COM mode that allows for the entanglement between the ions.

Before the gate is initiated the ions need to be cooled such that they are confined to the Lamb-Dicke regime. The ions are then excited with bichromatic light detuned from the lower and upper sidebands, which leads to four interfering paths, and results in entanglement of the two ions' internal states. The frequencies of the bichromatic laser

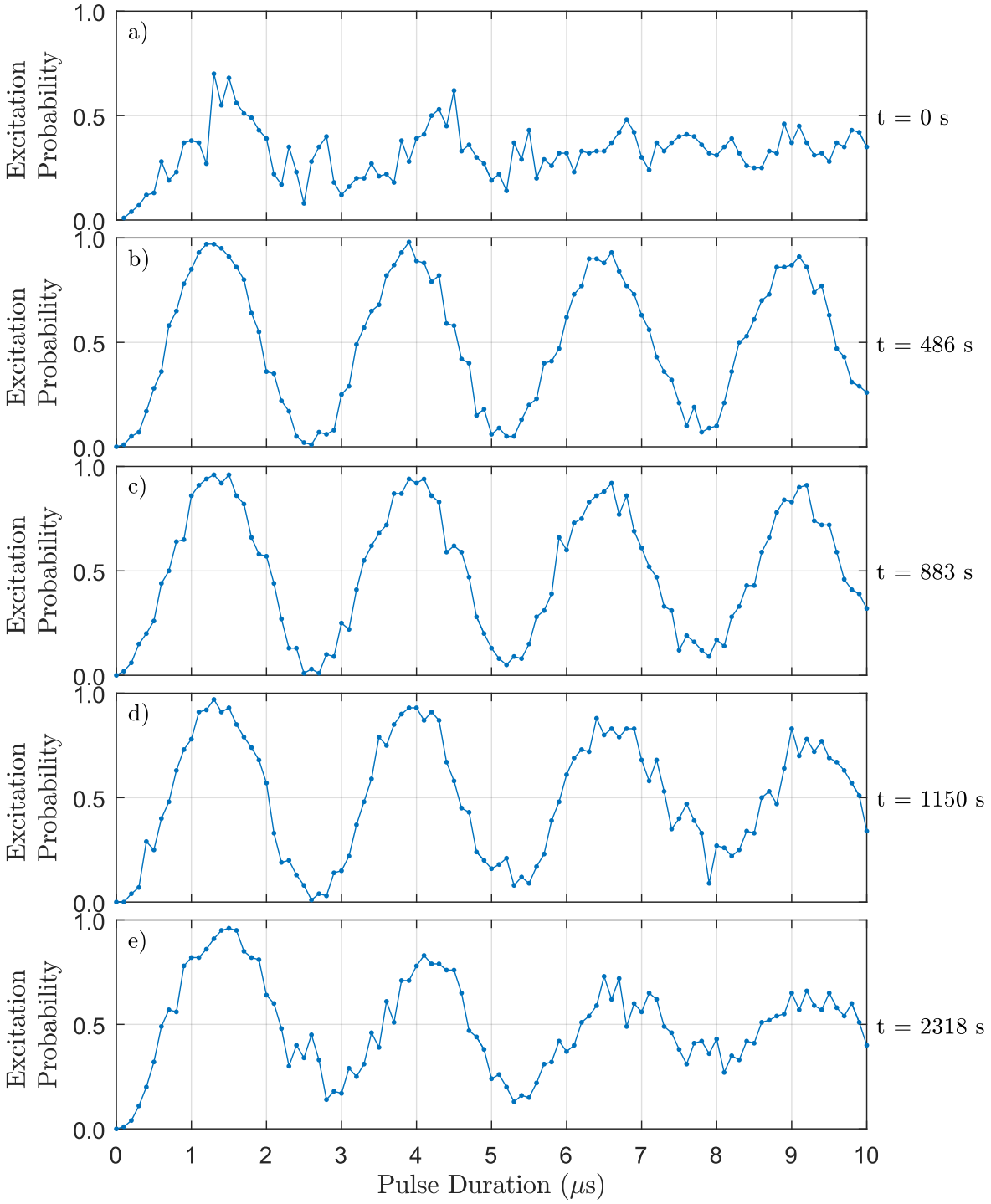

FIGURE 6.10: Rabi flopping on the carrier of the Δm_j= -2 transition in a 2.9 G bias field. The pulse duration was incremented in steps of 100 ns and the pulse power was set at 8.3 mW. Each data point is the result of 100 interrogations. The time taken for each of the scans is ∼2 min. The time t specifies the time of each of the scans relative to the start time of the scan presented in a.

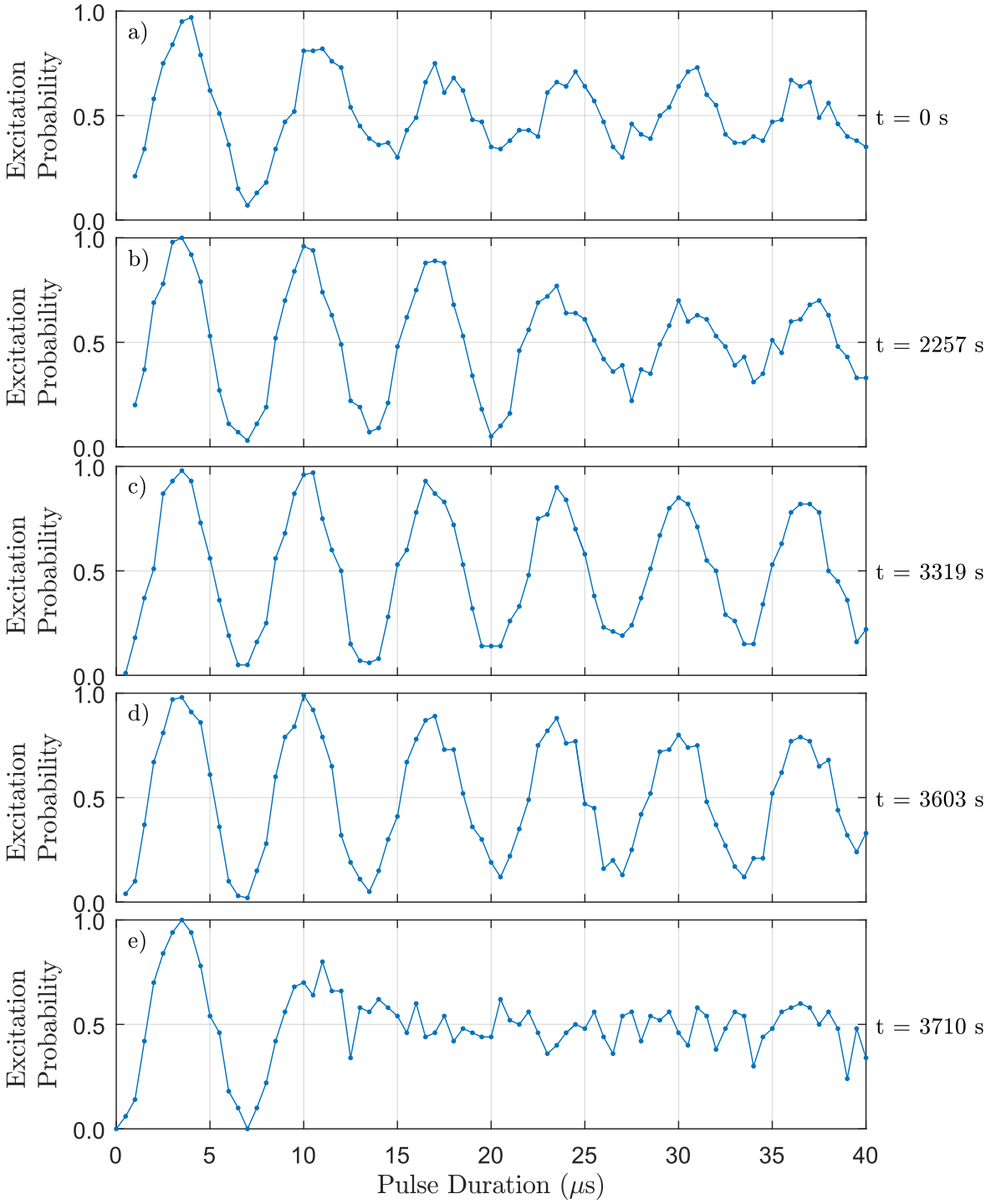

FIGURE 6.11: Rabi flopping on the carrier of the Δm_j= -2 transition in a 2.9 G bias field. The pulse duration was incremented in steps of 500 ns and the pulse power was set at 1.2 mW. Each data point is the result of 100 interrogations. The time taken for each of the scans is ∼2 min. The time t specifies the time of each of the scans relative to the start time of the scan presented in a.

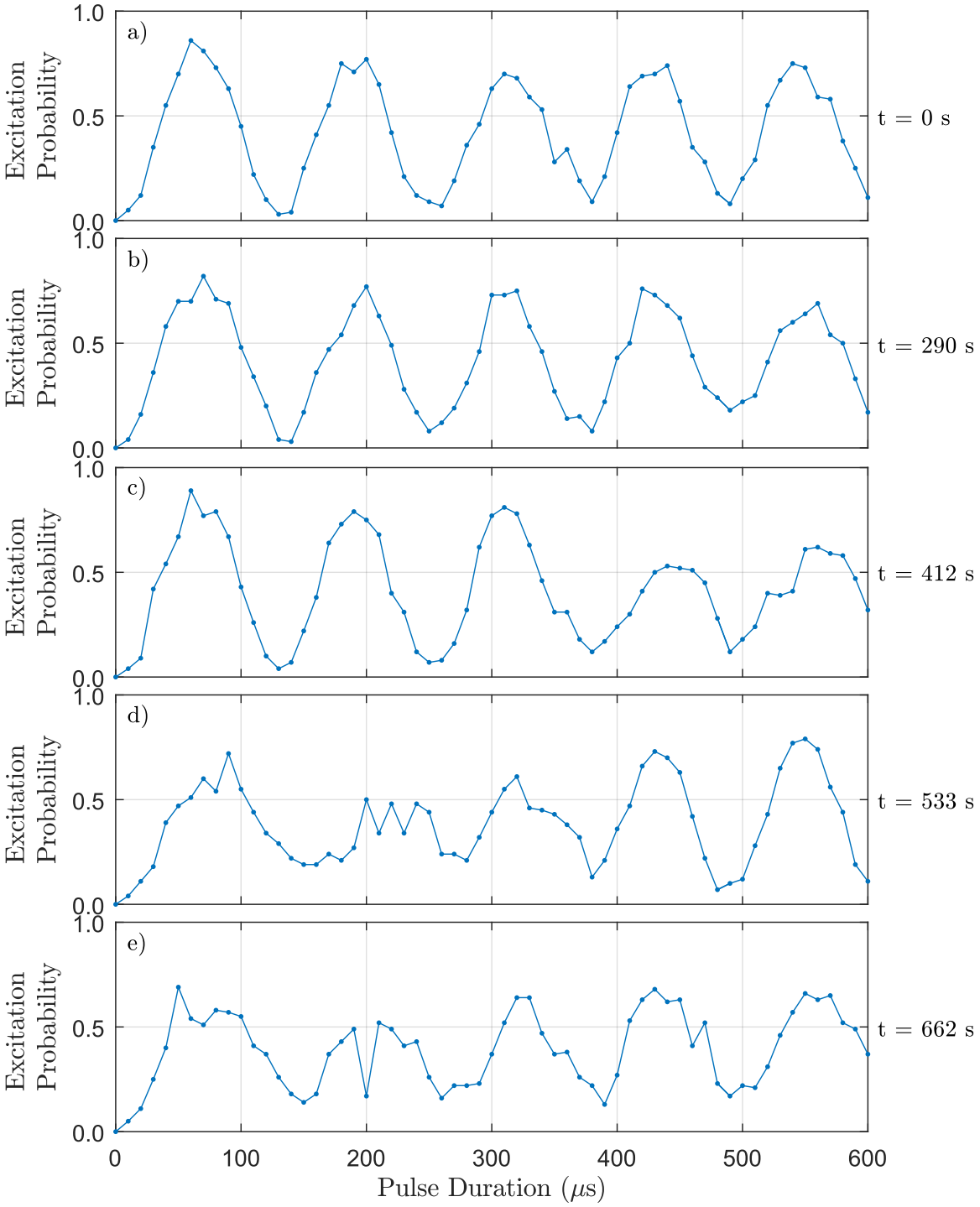

FIGURE 6.12: Rabi flopping on the carrier of the Δm_j= -2 transition in a 2.9 G bias field. The pulse duration was incremented in steps of 10 μs and the pulse power was set at 2.6 μW. Each data point is the result of 100 interrogations. The time taken for each of the scans is ∼2 min. The time t specifies the time of each of the scans relative to the start time of the scan presented in a.

are $\omega_{\pm} = \omega_0 \pm \delta$, where ω_0 is the transition frequency and δ is the detuning of the laser away from the blue and red sidebands as seen in Figure 6.13. The detuning of the laser is chosen to be far enough away from the sidebands such that these intermediate states are not populated and are effectively virtual states. For a string of ions in an ion trap, the interaction Hamiltonian in equation 1.16 can be generalised to

$$H_{int} = \sum_i \frac{\hbar\Omega_i}{2}(\sigma_{+i}e^{i[\eta(a+a^\dagger)-\omega_i t]} + H.c.), \tag{6.10}$$

where the subscript i denotes the parameters associated with the ith ion. Since the laser tuning is close to the vibration on the COM mode, the ions participate equally in the shared vibration, therefore the coupling of the recoil to the vibration should be identical for both ions [58] i.e. $\eta_1 = \eta_2 = \eta$. Furthermore, if the ions are equally illuminated it can be assumed that $\Omega_1 = \Omega_2 = \Omega$.

From the choice of detuning, the intermediate states are left unpopulated and the only transitions that conserve energy are between $|SS, n\rangle$ and $|DD, n\rangle$. Using second order perturbation theory and restricting the intermediate states to $|DS, n+1\rangle$ and $|DS, n-1\rangle$, the Rabi frequency for the transition between $|SS, n\rangle$ and $|DD, n\rangle$ via the intermediate states can then be written as [58]

$$\tilde{\Omega} = -\frac{(\Omega\eta)^2}{2\nu - \delta} \tag{6.11}$$

A remarkable feature about the Rabi frequency $\tilde{\Omega}$ is that it has no dependence on the vibrational number n. The n dependence cancels out due to the opposite detunings, which effectively describes the destructive interference present at the intermediate levels. This results in a gate operation that is insensitive to the vibrational state of the ions so long as they are confined to the Lamb-Dicke regime.

The evolution of the state populations can be used to identify the fidelity of the gate operation. The fidelity F is [36]

$$F = \langle\Psi_1|\rho^{exp}|\Psi_1\rangle = (\rho^{exp}_{SS,SS} + \rho^{exp}_{DD,DD})/2 + \mathrm{Im}\rho^{exp}_{DD,SS}, \tag{6.12}$$

with ρ^{exp} as the experimentally determined density matrix that is created by repeatedly

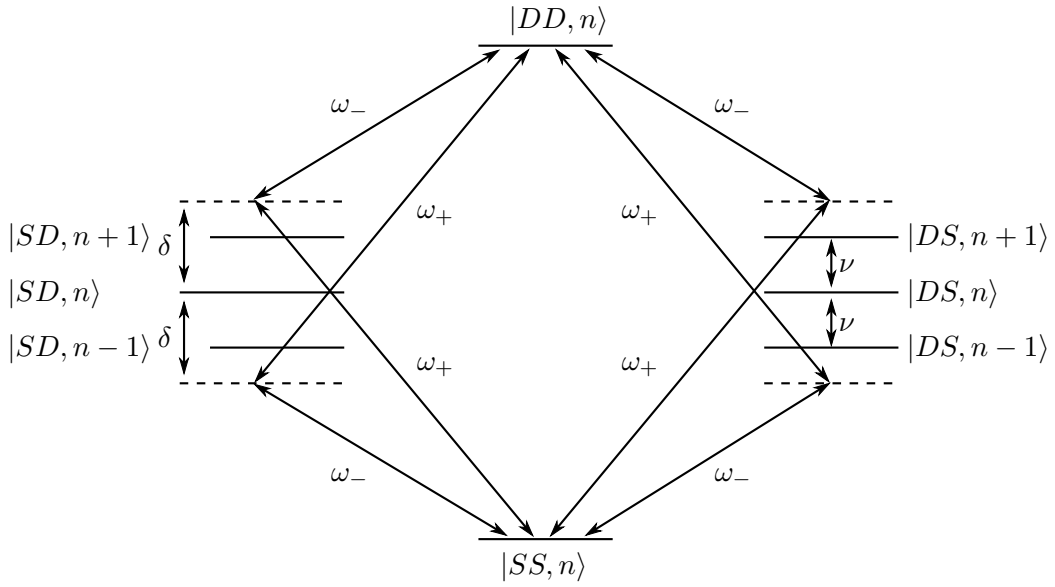

FIGURE 6.13: Schematic of the interference paths for the Mølmer- Sørenson gate. Laser frequencies ω_+ and ω_- are used to couple the states $|SS\rangle$ and $|DD\rangle$.

probing the states of the ions after the entanglement operation. Florescence measurements can be used to determine the states $\rho^{exp}_{SS,SS}$ and $\rho^{exp}_{DD,DD}$. For the off-diagonal term $\rho^{exp}_{DD,SS}$, the optical phase ϕ of an added $\pi/2$ bichromatic pulse is varied and the amplitude of the parity oscillations is measured. The measured amplitude of the parity oscillations A is is related to $\rho^{exp}_{DD,SS}$ using the following equation [36],

$$A = 2|\rho^{exp}_{DD,SS}|. \tag{6.13}$$

To implement the Mølmer-Sørenson gate a 2.9 G bias magnetic field was applied, the two-ion string was Doppler cooled and optically pumped so that both ions are initialised to the $^2S_{1/2}$ (m_j = -1/2) state. The ions are then illuminated with bichromatic light detuned by δ from ω_z of the $^2D_{5/2}$ (m_j = -5/2) transition and the states of the ions are read out. By repeating the measurement a number of times the probability of occupying the $|SS\rangle$ state after the entanglement operation can be determined. In order to generate the bichromatic light the spectroscopy laser is passed through a double pass AOM to set the amplitude and the phase, and then passed though another single pass AOM driven simultaneously by two RF frequencies. Phase coherence between the two exciting frequencies is maintained by phase locking the frequency sources to the same 10 MHz frequency reference. A measurement of the beat-note of the two frequencies of light showed that the intensities of each of the components were equal. To suppress

TABLE 6.2: Table of experimental parameters used in literature for the implementation of a Mølmer-Sørenson entanglement gate.

	[36]	[60]	[175]	[176]
Ion	Ca	Sr	Ca	Sr
Motional mode	ω_z	ω_s	ω_z	ω_s
Motional mode frequency (MHz)	1.23	1.697	1.232	1.679
Ion motional quantum number	0.05	0.05	20	
Rabi frequency (kHz)	110	200		
Lamb-Dicke parameter	0.044	0.04	0.044	0.03
Pulse rise time (μs)	2			
Entanglement gate time (μs)	50	130	50	130
Sideband detuning (kHz)	20	10.5	20	7.7
AC stark shift (kHz)	7		7.5	
Gate Fidelity (%)	99.3	98.5	97.4	98.1

off-resonant excitation, Blackman window-shaped laser pulses were used. For excitation on the axial COM mode ω_z it was found that a pulse rise time of 2.5 oscillation periods of the ω_z mode was sufficient to mitigate the effects of off-resonant excitation [36].

Several bichromatic routines have been established in order to optimise the parameters for entanglement. Set out in [60] is a procedure for optimising the parameters such as the gate-time and the detuning from the motional sidebands. By scanning the detuning for a fixed gate time, the detuning at which the excitation probability of two ions matches that of zero ions can be determined. By fixing the detuning that point, the gate time is then scanned to determine where there is a minimum in the probability of exciting a single ion. By iterating through these two scans the gate-time and sideband detuning should converge. As a starting point, published literature can give a good indication of the relative size of the required experimental parameters. Table 6.2 shows some of the experimental parameters that were used for optical qubits in ion traps.

The experimental procedures needed to implement the Mølmer-Sørenson gate have been developed. However the noise-limited coherence detailed in Section 6.6, presents an obstacle to the reliable implementation of the gate. Therefore these measurements remain a subject for future work.

6.8 Summary

Spectroscopic measurements on a single ion and a two ion string have been demonstrated. The motional frequencies in zero magnetic field as well as in a bias field have been recorded and were in line with expected values. Temporal control of the spectroscopy laser pulse was demonstrated by comparing a square-shaped pulse with a Blackman-shaped pulse. The Blackman-shaped pulse showed the suppression of Fourier components in the wings of the spectral line. Rabi flopping on the optical qubit transition has been shown over pulse durations $0\ \mu\text{s} \leqslant \tau \leqslant 1300\ \mu\text{s}$. However due to the presence of technical noise that is suspected to originate from the spectroscopy laser pump, the repeatability of the measurements is poor. The noise manifested itself with several characteristics, including a very sudden a dramatic loss of coherence and an intermittent decay or gradual recovery of the coherence at any point of the pulse duration scan. Furthermore, these characteristics were observed irrespective of the pulse duration range. A detailed investigation as to the source of the noise was conducted and it was found to be partly due to a faulty amplifier. However the dominant source of noise is expected to be from the spectroscopy laser pump. The investigation into replacing the laser pump is currently ongoing. When the system exhibits stable coherence measurements the next stages in the experiment is to implement a Mølmer Sørenson gate to entangle a two-ion string. The procedures need to implement the gate and explore the experimental parameter space have been constructed.

Chapter 7

Conclusion and Outlook

This work researched methods to reduce decoherence in the microfabricated ion traps. Decoherence from sources such as surface contamination, DC voltage noise and magnetic field instability were considered.

Hydrocarbon contamination on electrode surfaces is a possible source of electric field-noise that can cause motional heating of the ion and therefore decoherence. A theoretical framework was created which identified the plasma as a low frequency, high-pressure discharge with collisional and high-voltage sheaths. A capacitively-coupled RF microdischarge was generated *in situ* using He and He:N_2 gas mixtures. In order to measure the plasma parameters of interest, namely the electron density and the gas temperature, optical emission spectroscopy of the He I 667 nm and Hα 656 nm spectral lines was implemented. This enabled the calculation of the ion mean bombardment energies ϵ_{bom}. Testing with He microplasmas indicated 0.3 eV $\leqslant \epsilon_{bom} \leqslant$ 2.1 eV. It was found that with a He:N_2 gas mixture, higher ion energies in the range 1.2 eV $\leqslant \epsilon_{bom} \leqslant$ 4.1 eV can be achieved. However both these ranges are below the threshold for hydrocarbon removal (12 eV). Therefore the removal of surface contamination from the electrodes will be dependent on the high energy tail of the energy distribution. Surface processing times were estimated for the removal of two hydrocarbon monolayers. Cleaning times down to $\sim$40 min in microtrap type A and 60 s in trap type B and were calculated for a pure He microplasma. For He:N_2 mixtures, cleaning times down to 43 s were found for the same plasma coverage of the electrodes as in the pure He case. During the operation of the microplasma on these timescales, the effect on the Au electrode is expected to be negligible, which was confirmed by optical microscopy. The results suggest that the

microplasmas generated here are suited to selective removal of hydrocarbon contamination. The results of the microplasma testing was published in Journal of Physics B: Atomic, Molecular and Optical Physics, under the title 'Radio-frequency microplasmas with energies suited to *in situ* selective cleaning of surface adsorbates in ion microtraps' [177].

The effectiveness of the microplasma treatment can only be confirmed by a direct comparison of the ion heating rate measured before and after the processing. Earlier work has shown that hydrocarbon contamination can adsorb on to electrode surfaces during the vacuum bake-out process [90]. Therefore the surface processing has to occur after the bake-out, and the 10^{-11} mbar vacuum required for the ion trap to function effectively has to be recoverable post-processing. Therefore, the current experimental apparatus for vacuum bakeout will need to be updated to include bakeable gas lines that introduce gas of the highest purity. Furthermore, it is necessary that the gas does not react with elemental species in the vacuum, therefore the use of an inert gas such as He in this procedure is advantageous. Other techniques that remove surface contamination for reduced ion heating rate have reported varied results. Energetic Ar^+ (500 eV to 2000 eV) ion beam cleaning showed a factor of 10^2 reduction in ion heating [90]. Results with a less energetic Ar^+ bombardment (20 eV) showed a more modest reduction in the ion heating rate of a factor of 4 [93]. In the most recent generation of microtrap, Guido Wilpers conducted initial investigations that suggested the ion heating rate was $\sim$3(2) quanta/s. Therefore, if the microplasma technique presented here showed a reduction in the heating that was factor of 4, this would still result in a heating rate of $\leqslant$1 quanta/s in a microfabricated trap operated at room temperature. On the other hand, even if no reduction in ion heating rate is detected, the microplasma technique may still be useful in probing the origin of the electric-field noise affecting ion. Previous methods removed not only the surface adsobates, but also the electrode material. The microplasma method presented here operates at much lower bombardment energies, and so offers the prospect for selective removal of only the surface adsorbates. The technique could be useful for separating the effects of surface cleanliness from any due to electrode surface order [178].

If electrical noise present on the electrodes of the trap is resonant with the motion of the ion, ion motional heating can occur and result in a reduced ion coherence time. A system was created for versatile control of the DC potentials on the ion electrodes. A

termination board was designed to interface the 24 DC channels to any of the 42 DC line to the trap in a reconfigurable manner. Noise at the motional frequencies of the ion was attenuated by implementing a pair of interchangeable filter boards for purpose-specific operation. For heating rate measurements, a 2^{nd} order RC filter board was developed with an attenuation of 192 dB at 1 MHz and a cut-off frequency of 6 Hz. A second filter board was made for ion shuttling; a 3^{rd} order Butterworth filter with 59 dB attenuation at 1 MHz and a cut-off frequency of 100 kHz. The boards can be swapped without breaking vacuum. The filters on the DC potentials to the trap are tailored to result in a low-noise environment for the ion. However the RF potentials have no active stabilisation or purpose-built electrical filtering [82]. As explained in Section 6.6 noise on the RF electrodes resulting from a faulty amplifier was likely one source of measured decoherence. Therefore the experimental system in future would benefit from the active stabilisation and suppression of noise in the RF applied to the trap electrodes.

In this work, spectroscopy of the $^{88}Sr^{+}$ ions was performed using the $\Delta m_j = -2$ Zeeman component of the optical qubit transition. This transition is particularly beneficial since, given the geometry of the experimental apparatus used here, it allows for the highest coupling strengths relative to the other Zeeman transitions. The drawback with using the $\Delta m_j = -2$ transition is that it is more sensitive to magnetic field fluctuations than either the $\Delta m_j = 0$ or $\Delta m_j = \pm 1$ transitions. The separation of the ion's energy levels that need to be addressed is dependent on the magnetic field applied. Therefore instabilities in the magnetic field causes dampening of the phase relation between the states. A high-precision feedback system for the control of the magnetic field was implemented. Each of the magnetic field coil pairs were connected in series to a high precision source measure unit and a highly stable resistor with a low thermal coefficient. By by measuring the voltage over the resistor with a high resolution digital voltmeter the current was then calculated and used to feed back to the current source. A current stability can be derived from the voltage measured across the resistors over time, which then can be used to derive a magnetic field stability as generated by the coil pairs. From these calculations the magnetic field stability of 3×10^{-7} G over 1000 s was expected. However magnetic field measurements inside the mu-metal shielding showed a stability of 5×10^{-6} G in 1000 s; this was over a factor of 10 higher than anticipated. This was attributed to temperature drift resulting in magnetic field fluctuations from the ion pump magnet. By replacing the magnet (made from ferrite material) with a custom

one made of temperature compensated Sm-Co, the magnetic field drift is expected to decrease by a factor of 10^2. An investigation into implementing this solution is currently ongoing.

As atoms are evaporated towards the trap, the atomic flux can adsorb onto the electrode surfaces and, in a similar fashion to the hydrocarbon contamination, form sources of electric field-noise that can cause decoherence. In the new generation of microtrap design, a shield restricts the atomic flux to the loading zone which leaves the spatially separated experimental zones as low-noise environments for ion spectroscopy. By having well-controlled temperatures of the oven and hotplate the atoms can be generated more efficiently; minimising atom loss, maximising the lifetime of the devices and reducing the potential for electrode contamination. Automated control of the oven and hotplate was established such that the thermocouple of each of the devices was used to feedback to the DC source. This process applied well-defined limits on the temperatures of the hotplate and oven for efficient Sr atom generation and maximising the life span for both the devices. In addition, fluctuations in the magnetic field as a result of operating the hotplate were measured. It was found that large magnetic field perturbations were present during the operation of the hotplate and a settling time of $\sim$1000 s was needed for the magnetic field to get within 1.8×10^{-4} G of its final steady state (corresponding to $\sim$0.5 kHz shift in the $\Delta m_j = -2$ Zeeman component of the $^2S_{1/2}$ - $^2D_{5/2}$ transition). Furthermore, compared to before the hotplate operation the settled magnetic field had an offset that was measured to be as large as 3×10^{-3} G. Therefore in procedures where more ions are loaded into the trap, the state of the magnetic field will have to be checked after the field has had 1000 s to settle. The ion loading method here used resistive heating of the atomic source in order to generate the atomic flux. The presence of the high current needed and the large variations in temperature are a source of magnetic field instability. While these can be accounted for, there are other methods of loading that could potentially avoid this problem entirely. For example laser ablation of coated targets have been used to generate the atomic vapour [179]. Typically a pulse laser is focused onto the target that is in line of sight with the trapping aperture. A single pulse with the sufficient energy then ablates the surface; producing the atomic flux. This method could be used to generate the atoms on a millisecond timescale, avoiding the need for large currents and excessive heating.

Spectroscopy on a single- and two-ion string was conducted on trap type B (the newest

generation of ion trap design). The motional frequencies were measured in zero magnetic field as well as in the presence of a bias field. The measured motional frequency detuning was in line with expectations. To investigate the effect of pulse-shaping, measurements with square pulses and Blackman-shaped pulses were made. The excitation with Blackman-shaped pulses showed the suppression of Fourier components in the wings of the measured spectral line. The temporal control of the spectroscopy pulse is essential for minimising off-resonant excitation. Coherent control of a single ion was then further investigated with Rabi flopping on the carrier transition of the $\Delta m_j = -2$ Zeeman component. However the presence of intermittent noise detrimentally affecting the coherence of the ion was detected. Frequency fluctuations of the laser were measured and found to have a fractional frequency instability which was a factor of 10^2 higher that expected. This excess noise is suspected to arise due to mode competition from spectroscopy pump laser leading to intensity noise. Subsequently this intensity noise on the pump results in frequency noise on the Ti:Sapphire laser that the frequency stabilisation electronics cannot account for. This noise is a current limitation in the system. An investigation into installing a replacement single-mode laser pump is currently underway. Once the pump is replaced and the coherent control of the ion is deemed stable, the next stage is to implement two ion entanglement with a Mølmer-Sørenson gate. The experimental procedures needed to generate the bichromatic field has been implemented and the routines needed to optimise the experimental parameters (such as the pulse duration and sideband detuning) have been set-up. However due to the noise-limited coherence the optimisation of the parameters for entanglement remain a subject for future work. Beyond the experiments with two ions, an investigation of the trap performance when using larger ion strings still needs to be conducted. Due to the segmented structure of the ion microtraps, the devices have excellent prospects for the storage and manipulation of large numbers of ions. The ion storage capacity of the trap and the precise control of the applied DC potentials to reduced ion loss when loading larger ion strings remain subjects for future study.

Bibliography

[1] Gabriel Popkin. Quest for qubits. *Science (80-.).*, 354(6316):1090 LP – 1093, dec 2016.

[2] H. Häffner, C.F. Roos, and R. Blatt. Quantum computing with trapped ions. *Physics Reports*, 469(4):155–203, 2008. doi: 10.1016/j.physrep.2008.09.003.

[3] T. P. Harty, D. T. C. Allcock, C. J. Ballance, L. Guidoni, H. A. Janacek, N. M. Linke, D. N. Stacey, and D. M. Lucas. High-Fidelity Preparation, Gates, Memory, and Readout of a Trapped-Ion Quantum Bit. *Phys. Rev. Lett.*, 113(22):220501, nov 2014. doi: 10.1103/PhysRevLett.113.220501.

[4] Ye Wang, Mark Um, Junhua Zhang, Shuoming An, Ming Lyu, Jing-Ning Zhang, L.-M. Duan, Dahyun Yum, and Kihwan Kim. Single-qubit quantum memory exceeding ten-minute coherence time. *Nat. Photonics*, 11(10):646–650, oct 2017. doi: 10.1038/s41566-017-0007-1.

[5] Thomas Monz, Philipp Schindler, Julio T. Barreiro, Michael Chwalla, Daniel Nigg, William A. Coish, Maximilian Harlander, Wolfgang Hänsel, Markus Hennrich, and Rainer Blatt. 14-Qubit Entanglement: Creation and Coherence. *Phys. Rev. Lett.*, 106(13):130506, 2011. doi: 10.1103/PhysRevLett.106.130506.

[6] A H Cook. Quantum metrology-standards of measurement based on atomic and quantum phenomena. *Rep. Prog. Phys.*, 35:463, 1972.

[7] Thomas P. Heavner, Elizabeth A. Donley, Filippo Levi, Giovanni Costanzo, Thomas E. Parker, Jon H. Shirley, Neil Ashby, Stephan Barlow, and S. R. Jefferts. First accuracy evaluation of NIST-F2. *Metrologia*, 51(3):174–182, jun 2014. doi: 10.1088/0026-1394/51/3/174.

[8] Thomas E. Parker. Long-term comparison of caesium fountain primary frequency standards. *Metrologia*, 47(1):1–10, 2010. doi: 10.1088/0026-1394/47/1/001.

[9] Ruoxin Li, Kurt Gibble, and Krzysztof Szymaniec. Improved accuracy of the NPL-CsF2 primary frequency standard: evaluation of distributed cavity phase and microwave lensing frequency shifts. *Metrologia*, 48(5):283–289, oct 2011. doi: 10.1088/0026-1394/48/5/007.

[10] Krzysztof Szymaniec, Sang Eon Park, Giuseppe Marra, and Witold Chałupczak. First accuracy evaluation of the NPL-CsF2 primary frequency standard. *Metrologia*, 47(4):363–376, aug 2010. doi: 10.1088/0026-1394/47/4/003.

[11] H. S. Margolis. Optical frequency standards and clocks. *Contemp. Phys.*, 51(1): 37–58, jan 2010. doi: 10.1080/00107510903257616.

[12] N. Huntemann, C. Sanner, B. Lipphardt, Chr Tamm, and E. Peik. Single-Ion Atomic Clock with 3×10^{-18} Systematic Uncertainty. *Phys. Rev. Lett.*, 116(6): 063001, feb 2016. doi: 10.1103/PhysRevLett.116.063001.

[13] S. M. Brewer, J. S. Chen, A. M. Hankin, E. R. Clements, C. W. Chou, D. J. Wineland, D. B. Hume, and D. R. Leibrandt. An $^{27}Al^{+}$ quantum-logic clock with systematic uncertainty below 10^{-18}. *ArXiv*, feb 2019. URL http://arxiv.org/abs/1902.07694.

[14] R. Blatt and C. F. Roos. Quantum simulations with trapped ions. *Nat. Phys.*, 8 (4):277–284, 2012. doi: 10.1038/nphys2252.

[15] Michael Johanning, Andrés F. Varón, and Christof Wunderlich. Quantum simulations with cold trapped ions. *J. Phys. B At. Mol. Opt. Phys.*, 42(15):154009, aug 2009. doi: 10.1088/0953-4075/42/15/154009.

[16] Richard P. Feynman. Simulating physics with computers. *Int. J. Theor. Phys.*, 21 (6-7):467–488, jun 1982. doi: 10.1007/BF02650179.

[17] B. P. Lanyon, C. Hempel, D. Nigg, M. Muller, R. Gerritsma, F. Zahringer, P. Schindler, J. T. Barreiro, M. Rambach, G. Kirchmair, M. Hennrich, P. Zoller, R. Blatt, and C. F. Roos. Universal Digital Quantum Simulation with Trapped Ions. *Science (80-.).*, 334(6052):57–61, oct 2011. doi: 10.1126/science.1208001.

[18] K. Pyka, J. Keller, H. L. Partner, R. Nigmatullin, T. Burgermeister, D. M. Meier, K. Kuhlmann, A Retzker, M. B. Plenio, W. H. Zurek, A. del Campo, and T. E. Mehlstäubler. Topological defect formation and spontaneous symmetry breaking in ion Coulomb crystals. *Nat. Commun.*, 4:1–6, aug 2013. doi: 10.1038/ncomms3291.

[19] L. Lamata, J. León, T. Schätz, and E. Solano. Dirac Equation and Quantum Relativistic Effects in a Single Trapped Ion. *Phys. Rev. Lett.*, 98(25):253005, jun 2007. doi: 10.1103/PhysRevLett.98.253005.

[20] R. Gerritsma, G. Kirchmair, F. Zähringer, E. Solano, R. Blatt, and C. F. Roos. Quantum simulation of the Dirac equation. *Nature*, 463(7277):68–71, 2010. doi: 10.1038/nature08688.

[21] Paul M. Alsing, Jonathan P. Dowling, and G. J. Milburn. Ion Trap Simulations of Quantum Fields in an Expanding Universe. *Phys. Rev. Lett.*, 94(22):220401, jun 2005. doi: 10.1103/PhysRevLett.94.220401.

[22] Nicolas C. Menicucci, S Jay Olson, and Gerard J. Milburn. Simulating quantum effects of cosmological expansion using a static ion trap. *New J. Phys.*, 12(9): 095019, sep 2010. doi: 10.1088/1367-2630/12/9/095019.

[23] Ralf Schützhold, Michael Uhlmann, Lutz Petersen, Hector Schmitz, Axel Friedenauer, and Tobias Schätz. Analogue of Cosmological Particle Creation in an Ion Trap. *Phys. Rev. Lett.*, 99(20):201301, nov 2007. doi: 10.1103/PhysRevLett.99.201301.

[24] Anders W. Sandvik. Ground States of a Frustrated Quantum Spin Chain with Long-Range Interactions. *Phys. Rev. Lett.*, 104(13):137204, mar 2010. doi: 10.1103/PhysRevLett.104.137204.

[25] Patrik Henelius and Anders W. Sandvik. Sign problem in Monte Carlo simulations of frustrated quantum spin systems. *Phys. Rev. B*, 62(2):1102–1113, jul 2000. doi: 10.1103/PhysRevB.62.1102.

[26] A. Friedenauer, H. Schmitz, J. T. Glueckert, D. Porras, and T. Schaetz. Simulating a quantum magnet with trapped ions. *Nat. Phys.*, 4(10):757–761, oct 2008. doi: 10.1038/nphys1032.

[27] K. Kim, M. S. Chang, S. Korenblit, R. Islam, E. E. Edwards, J. K. Freericks, G. D. Lin, L. M. Duan, and C. Monroe. Quantum simulation of frustrated Ising spins with trapped ions. *Nature*, 465(7298):590–593, 2010. doi: 10.1038/nature09071.

[28] Jingfu Zhang, Man-Hong Yung, Raymond Laflamme, Alán Aspuru-Guzik, and Jonathan Baugh. Digital quantum simulation of the statistical mechanics of a frustrated magnet. *Nat. Commun.*, 3(1):880, jan 2012. doi: 10.1038/ncomms1860.

[29] A.M. Zagoskin. Analogue simulation with the use of artificial quantum coherent structures. *Rev. Phys.*, 3(November):1–14, nov 2017. doi: 10.1016/j.revip.2017.11.001.

[30] R Islam, C Senko, W C Campbell, S Korenblit, J Smith, A Lee, E E Edwards, C.-C. J. Wang, J K Freericks, and C Monroe. Emergence and Frustration of Magnetism with Variable-Range Interactions in a Quantum Simulator. *Science (80-.).*, 340(6132):583–587, may 2013. doi: 10.1126/science.1232296.

[31] Joseph W. Britton, Brian C. Sawyer, Adam C. Keith, C. C Joseph Wang, James K. Freericks, Hermann Uys, Michael J. Biercuk, and John J. Bollinger. Engineered two-dimensional Ising interactions in a trapped-ion quantum simulator with hundreds of spins. *Nature*, 484(7395):489–492, 2012. doi: 10.1038/nature10981.

[32] Julio T. Barreiro, Markus Müller, Philipp Schindler, Daniel Nigg, Thomas Monz, Michael Chwalla, Markus Hennrich, Christian F. Roos, Peter Zoller, and Rainer Blatt. An open-system quantum simulator with trapped ions. *Nature*, 470(7335):486–491, feb 2011. doi: 10.1038/nature09801.

[33] J. Cirac and P. Zoller. Quantum Computations with Cold Trapped Ionsl. *Physical Review Letters*, 74(20):4091–4094, 1995. doi: 10.1103/PhysRevLett.74.4091.

[34] T. D. Ladd, F. Jelezko, R. Laflamme, Y. Nakamura, C. Monroe, and J. L. O'Brien. Quantum computers. *Nature*, 464(7285):45–53, 2010. doi: 10.1038/nature08812.

[35] Lov K. Grover. Quantum Mechanics Helps in Searching for a Needle in a Haystack. *Phys. Rev. Lett.*, 79(2):325–328, jul 1997. doi: 10.1103/PhysRevLett.79.325.

[36] Jan Benhelm, Gerhard Kirchmair, Christian F. Roos, and Rainer Blatt. Towards fault-tolerant quantum computing with trapped ions. *Nature Physics*, 4(6):463–466, 2008. doi: 10.1038/nphys961.

[37] R. J. Epstein, S. Seidelin, D. Leibfried, J. H. Wesenberg, J. J. Bollinger, J. M. Amini, R. B. Blakestad, J. Britton, J. P. Home, W. M. Itano, J. D. Jost, E. Knill, C. Langer, R. Ozeri, N. Shiga, and D. J. Wineland. Simplified motional heating rate measurements of trapped ions. *Phys. Rev. A - At. Mol. Opt. Phys.*, 76(3): 2–6, 2007. doi: 10.1103/PhysRevA.76.033411.

[38] Philipp Schindler, Daniel Nigg, Thomas Monz, Julio T. Barreiro, Esteban Martinez, Shannon X. Wang, Stephan Quint, Matthias F. Brandl, Volckmar Nebendahl, Christian F. Roos, Michael Chwalla, Markus Hennrich, and Rainer Blatt. A quantum information processor with trapped ions. *New J. Phys.*, 15, 2013. doi: 10.1088/1367-2630/15/12/123012.

[39] Karan K. Mehta, Colin D. Bruzewicz, Robert McConnell, Rajeev J. Ram, Jeremy M. Sage, and John Chiaverini. Integrated optical addressing of an ion qubit. *Nat. Nanotechnol.*, 11(August):1–7, 2016. doi: 10.1038/nnano.2016.139.

[40] W. K. Hensinger, S. Olmschenk, D. Stick, D. Hucul, M. Yeo, M. Acton, L. Deslauriers, C. Monroe, and J. Rabchuk. T-junction ion trap array for two-dimensional ion shuttling, storage, and manipulation. *Appl. Phys. Lett.*, 88(3):1–3, 2006. doi: 10.1063/1.2164910.

[41] T. P. Harty, M. A. Sepiol, D. T. C. Allcock, C. J. Ballance, J. E. Tarlton, and D. M. Lucas. High-Fidelity Trapped-Ion Quantum Logic Using Near-Field Microwaves. *Phys. Rev. Lett.*, 117(14):140501, sep 2016. doi: 10.1103/PhysRevLett.117.140501.

[42] Ralph G. DeVoe and Christian Kurtsiefer. Experimental study of anomalous heating and trap instabilities in a microscopic ^{137}Ba ion trap. *Phys. Rev. A*, 65(6): 063407, jun 2002. doi: 10.1103/PhysRevA.65.063407.

[43] S Weidt, J Randall, S. C. Webster, K Lake, A. E. Webb, I Cohen, T Navickas, B Lekitsch, A Retzker, and W. K. Hensinger. Trapped-Ion Quantum Logic with Global Radiation Fields. *Phys. Rev. Lett.*, 117(22):220501, nov 2016. doi: 10.1103/PhysRevLett.117.220501.

[44] J. P. Gaebler, T. R. Tan, Y. Lin, Y. Wan, R. Bowler, A. C. Keith, S. Glancy, K. Coakley, E. Knill, D. Leibfried, and D. J. Wineland. High-Fidelity Universal Gate Set for $^{9}Be^{+}$ Ion Qubits. *Phys. Rev. Lett.*, 117(6):060505, aug 2016. doi: 10.1103/PhysRevLett.117.060505.

[45] K. R. Brown, A. C. Wilson, Y. Colombe, C. Ospelkaus, A. M. Meier, E. Knill, D. Leibfried, and D. J. Wineland. Single-qubit-gate error below 10^{-4} in a trapped ion. *Phys. Rev. A*, 84(3):030303, sep 2011. doi: 10.1103/PhysRevA.84.030303.

[46] David P. DiVincenzo. The Physical Implementation of Quantum Computation. *Fortschritte der Physik*, 48(9-11):771–783, 2000. doi: 10.1002/1521-3978(200009)48:9/11⟨771::AID-PROP771⟩3.0.CO;2-E.

[47] Nicolai Friis, Oliver Marty, Christine Maier, Cornelius Hempel, Milan Holzäpfel, Petar Jurcevic, Martin B Plenio, Marcus Huber, Christian Roos, Rainer Blatt, and Ben Lanyon. Observation of Entangled States of a Fully Controlled 20-Qubit System. *Phys. Rev. X*, 8(2):21012, 2018. doi: 10.1103/PhysRevX.8.021012.

[48] D Kielpinski, C Monroe, and D J Wineland. Architecture for a large-scale ion-trap quantum computer. *Nature*, 417(6890):709–711, 2002. doi: 10.1038/nature00784.

[49] Patrick See, Guido Wilpers, Patrick Gill, and Alastair G. Sinclair. Fabrication of a monolithic array of three dimensional si-based ion traps. *J. Microelectromechanical Syst.*, 22(5):1180–1189, 2013. doi: 10.1109/JMEMS.2013.2262573.

[50] A. Walther, U. Poschinger, K. Singer, and F. Schmidt-Kaler. Precision measurements in ion traps using slowly moving standing waves. *Appl. Phys. B Lasers Opt.*, 107(4):1061–1067, 2012. doi: 10.1007/s00340-011-4740-8.

[51] D. L. Moehring, C. Highstrete, D. Stick, K. M. Fortier, R. Haltli, C. Tigges, and M. G. Blain. Design, fabrication and experimental demonstration of junction surface ion traps. *New J. Phys.*, 13(7):075018, jul 2011. doi: 10.1088/1367-2630/13/7/075018.

[52] Amira M Eltony, Dorian Gangloff, Molu Shi, Alexei Bylinskii, Vladan Vuletić, and Isaac L Chuang. Technologies for trapped-ion quantum information systems. *Quantum Inf. Process.*, 15(12):5351–5383, dec 2016. doi: 10.1007/s11128-016-1298-8.

[53] C. Langer, R. Ozeri, J. Jost, J. Chiaverini, B. DeMarco, A. Ben-Kish, R. Blakestad, J. Britton, D. Hume, W. Itano, D. Leibfried, R. Reichle, T. Rosenband, T. Schaetz, P. Schmidt, and D. Wineland. Long-Lived Qubit Memory Using Atomic Ions. *Physical Review Letters*, 95(6):060502, 2005. doi: 10.1103/PhysRevLett.95.060502.

[54] F. Schmidt-Kaler, H. Häffner, S. Gulde, M. Riebe, G. P T Lancaster, T. Deuschle, C. Becher, W. Hänsel, J. Eschner, C. F. Roos, and R. Blatt. How to realize a universal quantum gate with trapped ions. *Applied Physics B: Lasers and Optics*, 77(8):789–796, 2003. doi: 10.1007/s00340-003-1346-9.

[55] D. Leibfried, B. DeMarco, V Meyer, D. Lucas, M Barrett, J Britton, W M Itano, B. Jelenković, C Langer, T Rosenband, and D J Wineland. Experimental demonstration of a robust, high-fidelity geometric two ion-qubit phase gate. *Nature*, 422 (6930):412–415, mar 2003. doi: 10.1038/nature01492.

[56] Tycho Sleator and Harald Weinfurter. Realizable universal quantum logic gates. *Physical Review Letters*, 74(20):4087–4090, 1995. doi: 10.1103/PhysRevLett.74.4087.

[57] Rainer Blatt and David Wineland. Entangled states of trapped atomic ions. *Nature*, 453(7198):1008–1015, 2008. doi: 10.1038/nature07125.

[58] Anders Sørensen and Klaus Mølmer. Quantum Computation with Ions in Thermal Motion. *Physical Review Letters*, 82(9):1971–1974, 1999. doi: 10.1103/PhysRevLett.82.1971.

[59] C. J. Ballance, T. P. Harty, N. M. Linke, M. A. Sepiol, and D. M. Lucas. High-Fidelity Quantum Logic Gates Using Trapped-Ion Hyperfine Qubits. *Phys. Rev. Lett.*, 117(6):060504, aug 2016. doi: 10.1103/PhysRevLett.117.060504.

[60] Nitzan Akerman, Nir Navon, Shlomi Kotler, Yinnon Glickman, and Roee Ozeri. Universal gate-set for trapped-ion qubits using a narrow linewidth diode laser. *New J. Phys.*, 17(11):113060, nov 2015. doi: 10.1088/1367-2630/17/11/113060.

[61] Hans G. Dehmelt. Monoion oscillator as potential ultimate laser frequency standard. *IEEE Trans. Instrum. Meas.*, IM-31(2):83–87, jun 1982. doi: 10.1109/TIM.1982.6312526.

[62] A. H. Myerson, D. J. Szwer, S. C. Webster, D. T.C. Allcock, M. J. Curtis, G. Imreh, J. A. Sherman, D. N. Stacey, A. M. Steane, and D. M. Lucas. High-fidelity readout of trapped-ion qubits. *Phys. Rev. Lett.*, 100(20):2–5, 2008. doi: 10.1103/PhysRevLett.100.200502.

[63] M. Acton, K. A. Brickman, P. C. Haljan, P. J. Lee, L. Deslauriers, and C. Monroe. Near-Perfect Simultaneous Measurement of a Qubit Register. *Quantum Info. Comput.*, 6(6):465—-482, 2006.

[64] A. H. Burrell, D. J. Szwer, S. C. Webster, and D. M. Lucas. Scalable simultaneous multiqubit readout with 99.99% single-shot fidelity. *Phys. Rev. A - At. Mol. Opt. Phys.*, 81(4):1–4, 2010. doi: 10.1103/PhysRevA.81.040302.

[65] P. Jurcevic, B. P. Lanyon, P. Hauke, C. Hempel, P. Zoller, R. Blatt, and C. F. Roos. Quasiparticle engineering and entanglement propagation in a quantum many-body system. *Nature*, 511(7508):202–205, 2014. doi: 10.1038/nature13461.

[66] J. I. Cirac, P. Zoller, H. J. Kimble, and H. Mabuchi. Quantum State Transfer and Entanglement Distribution among Distant Nodes in a Quantum Network. *Phys. Rev. Lett.*, 78(16):3221–3224, apr 1997. doi: 10.1103/PhysRevLett.78.3221.

[67] B. Vogell, B. Vermersch, T. E. Northup, B. P. Lanyon, and C. A. Muschik. Deterministic quantum state transfer between remote qubits in cavities. *Quantum Sci. Technol.*, 2(4):045003, dec 2017. doi: 10.1088/2058-9565/aa868b.

[68] Wolfgang Paul. Electromagnetic traps for charged and neutral particles. *Rev. Mod. Phys.*, 62(3):531–540, jul 1990. doi: 10.1103/RevModPhys.62.531.

[69] D. Leibfried, R. Blatt, C. Monroe, and D. Wineland. Quantum dynamics of single trapped ions. *Rev. Mod. Phys.*, 75(1):281–324, 2003. doi: 10.1103/RevModPhys.75.281.

[70] Jürgen Eschner, Giovanna Morigi, Ferdinand Schmidt-Kaler, and Rainer Blatt. Laser cooling of trapped ions. *J. Opt. Soc. Am. B*, 20(5):1003, may 2003. doi: 10.1364/JOSAB.20.001003.

[71] Valliappan Letchumanan. *Coherent Control and Ground State Cooling of a Single Sr + Ion*. PhD thesis, Imperial College London, 2004.

[72] H J Metcalf. Laser Cooling and Trapping of Atoms. *J. Opt. Soc. Am. B*, 6(11): 2020, nov 1989. doi: 10.1364/JOSAB.6.002020.

[73] R. Blatt, G. Lafyatis, W. D. Phillips, S. Stenholm, and D. J. Wineland. Cooling in Traps. *Phys. Scr.*, T22(T22):216–223, jan 1988. doi: 10.1088/0031-8949/1988/T22/032.

[74] C. E. Moore. *Atomic Energy Levels, vol. 2.* National Bureau of Standards, 1952.

[75] P A Barton, C J S Donald, D M Lucas, D A Stevens, A M Steane, and D N Stacey. Measurement of the lifetime of the $3d^2D_{5/2}$ state in $^{40}Ca^+$. *Phys. Rev. A*, 62(3): 032503, aug 2000. doi: 10.1103/PhysRevA.62.032503.

[76] D.J. Wineland, C. Monroe, W.M. Itano, D. Leibfried, B.E. King, and D.M. Meekhof. Experimental issues in coherent quantum-state manipulation of trapped atomic ions. *J. Res. Natl. Inst. Stand. Technol.*, 103(3):259, may 1998. doi: 10.6028/jres.103.019.

[77] Q A Turchette, David Kielpinski, Brian E King, D Leibfried, D M Meekhof, C J Myatt, M A Rowe, C A Sackett, C S Wood, Wayne M Itano, Christopher Monroe, and David J Wineland. Heating of trapped ions from the quantum ground state. *Physical Review A*, 61(6):063418, 2000. doi: 10.1103/PhysRevA.61.063418.

[78] D. J. Wineland and H. G. Dehmelt. Principles of the stored ion calorimeter. *J. Appl. Phys.*, 46(2):919–930, feb 1975. doi: 10.1063/1.321602.

[79] M Brownnutt, M Kumph, P Rabl, and R Blatt. Ion-trap measurements of electric-field noise near surfaces. *Rev. Mod. Phys.*, 87(4):1419–1482, dec 2015. doi: 10.1103/RevModPhys.87.1419.

[80] Jaroslaw Labaziewicz, Yufei Ge, Paul Antohi, David Leibrandt, Kenneth R. Brown, and Isaac L. Chuang. Suppression of heating rates in cryogenic surface-electrode ion traps. *Phys. Rev. Lett.*, 100(1):1–4, 2008. doi: 10.1103/PhysRevLett.100.013001.

[81] L. Deslauriers, S. Olmschenk, D. Stick, W. K. Hensinger, J. Sterk, and C. Monroe. Scaling and suppression of anomalous heating in ion traps. *Phys. Rev. Lett.*, 97 (10):1–4, 2006. doi: 10.1103/PhysRevLett.97.103007.

[82] K G Johnson, J. D. Wong-Campos, A Restelli, K A Landsman, B Neyenhuis, J Mizrahi, and C Monroe. Active stabilization of ion trap radiofrequency potentials. *Rev. Sci. Instrum.*, 87(5):053110, may 2016. doi: 10.1063/1.4948734.

[83] Marcus D. Hughes, Bjoern Lekitsch, Jiddu A. Broersma, and Winfried K. Hensinger. Microfabricated ion traps. *Contemporary Physics*, 52(6):505–529, nov 2011. doi: 10.1080/00107514.2011.601918.

[84] A. Safavi-Naini, P. Rabl, P. F. Weck, and H. R. Sadeghpour. Microscopic model of electric-field-noise heating in ion traps. *Physical Review A - Atomic, Molecular, and Optical Physics*, 84(2):1–7, 2011. doi: 10.1103/PhysRevA.84.023412.

[85] Ivan A. Boldin, Alexander Kraft, and Christof Wunderlich. Measuring anomalous heating in a planar ion trap with variable ion-surface separation. *ArXiv*, aug 2017.

[86] J. A. Sedlacek, A. Greene, J. Stuart, R. McConnell, C. D. Bruzewicz, J. M. Sage, and J. Chiaverini. Distance scaling of electric-field noise in a surface-electrode ion trap. *Phys. Rev. A*, 97(2):020302, feb 2018. doi: 10.1103/PhysRevA.97.020302.

[87] C W Chou, D B Hume, J C J Koelemeij, D J Wineland, and T Rosenband. Frequency Comparison of Two High-Accuracy Al+ Optical Clocks. *Phys. Rev. Lett.*, 104(February):070802, 2010. doi: 10.1103/PhysRevLett.104.070802.

[88] Amy Gardner, Kevin Sheridan, William Groom, Nicolas Seymour-Smith, and Matthias Keller. Precision spectroscopy technique for dipole-allowed transitions in laser-cooled ions. *Appl. Phys. B*, 117(2):755–762, nov 2014. doi: 10.1007/s00340-014-5891-1.

[89] J. Chiaverini and J. M. Sage. Insensitivity of the rate of ion motional heating to trap-electrode material over a large temperature range. *Physical Review A - Atomic, Molecular, and Optical Physics*, 89(1):1–6, 2014. doi: 10.1103/PhysRevA.89.012318.

[90] D. a. Hite, Y. Colombe, a. C. Wilson, K. R. Brown, U. Warring, R. Jördens, J. D. Jost, K. S. McKay, D. P. Pappas, D. Leibfried, and D. J. Wineland. 100-Fold Reduction of Electric-Field Noise in an Ion Trap Cleaned With Insitu Argon-Ion-Beam Bombardment. *Physical Review Letters*, 109(10):1–5, 2012. doi: 10.1103/PhysRevLett.109.103001.

[91] N Daniilidis, S Gerber, G Bolloten, M Ramm, A Ransford, E. Ulin-Avila, I Talukdar, and H. H??ffner. Surface noise analysis using a single-ion sensor. *Physical Review B - Condensed Matter and Materials Physics*, 89(24):1–7, 2014. doi: 10.1103/PhysRevB.89.245435.

[92] D Allcock, L Guidoni, T Harty, C J Ballance, M G Blain, A Lucas, M Steane, and D Lucas. Reduction of heating rate in a microfabricated ion trap by pulsed-laser cleaning. *New Journal of Physics*, 13(123023):11pp, 2001. doi: 10.1088/1367-2630/13/12/123023.

[93] Robert Mcconnell, Colin Bruzewicz, John Chiaverini, and Jeremy Sage. Reduction of trapped-ion anomalous heating by in situ surface plasma cleaning. *Physical Review A*, 92(020302(R)):1–5, 2015. doi: 10.1103/PhysRevA.92.020302.

[94] B. Merkel, K. Thirumalai, J. E. Tarlton, V. M. Schäfer, C. J. Ballance, T. P. Harty, and D. M. Lucas. Magnetic field stabilization system for atomic physics experiments. *arXiv*, pages 1–6, aug 2018.

[95] H. Rohde, S. T. Gulde, C. F. Roos, P. A. Barton, D. Leibfried, J. Eschner, F. Schmidt-Kaler, and R. Blatt. Sympathetic ground-state cooling and coherent manipulation with two-ion crystals. *J. Opt. B Quantum Semiclassical Opt.*, 3 (1):S34–S41, feb 2001. doi: 10.1088/1464-4266/3/1/357.

[96] T. Ruster, C. T. Schmiegelow, H. Kaufmann, C. Warschburger, F. Schmidt-Kaler, and U. G. Poschinger. A long-lived Zeeman trapped-ion qubit. *Appl. Phys. B*, 122 (10):254, oct 2016. doi: 10.1007/s00340-016-6527-4.

[97] M. F. Brandl, M. W. van Mourik, L. Postler, A. Nolf, K. Lakhmanskiy, R. R. Paiva, S. Möller, N. Daniilidis, H. Häffner, V. Kaushal, T. Ruster, C. Warschburger, H. Kaufmann, U. G. Poschinger, F. Schmidt-Kaler, P. Schindler, T. Monz, and R. Blatt. Cryogenic setup for trapped ion quantum computing. *Rev. Sci. Instrum.*, 87(11):113103, nov 2016. doi: 10.1063/1.4966970.

[98] E.L. Hahn. Spin Echoes. *Physical Review*, 80(4):580–594, 1950. doi: 10.1103/PhysRev.80.580.

[99] P. B. Antohi, D. Schuster, G. M. Akselrod, J. Labaziewicz, Y. Ge, Z. Lin, W. S. Bakr, and I. L. Chuang. Cryogenic ion trapping systems with surface-electrode traps. *Rev. Sci. Instrum.*, 80(1):013103, jan 2009. doi: 10.1063/1.3058605.

[100] Joseph Thom, Ben Yuen, Guido Wilpers, Erling Riis, and Alastair G Sinclair. Intensity stabilisation of optical pulse sequences for coherent control of laser-driven qubits. *Appl. Phys. B*, 124(5):90, may 2018. doi: 10.1007/s00340-018-6955-4.

[101] F.J. Harris. On the use of windows for harmonic analysis with the discrete Fourier transform. *Proc. IEEE*, 66(1):51–83, 1978. doi: 10.1109/PROC.1978.10837.

[102] H. Stoehr, F. Mensing, J. Helmcke, and U. Sterr. Diode laser with 1 Hz linewidth. *Opt. Lett.*, 31(6):736, mar 2006. doi: 10.1364/OL.31.000736.

[103] Miao Zhu and John L. Hall. Stabilization of optical phase/frequency of a laser system: application to a commercial dye laser with an external stabilizer. *J. Opt. Soc. Am. B*, 10(5):802, may 1993. doi: 10.1364/JOSAB.10.000802.

[104] Alan Gallagher. Oscillator Strengths of Ca II, Sr II, and Ba II. *Phys. Rev.*, 157 (1):24–30, may 1967. doi: 10.1103/PhysRev.157.24.

[105] V. Letchumanan, M. A. Wilson, P. Gill, and A. G. Sinclair. Lifetime measurement of the metastable $4d^2d_{5/2}$ state in $^{88}Sr^+$ using a single trapped ion. *Phys. Rev. A*, 72:012509, Jul 2005. doi: 10.1103/PhysRevA.72.012509.

[106] Guido Wilpers, Patrick See, Patrick Gill, and Alastair G. Sinclair. A compact UHV package for microfabricated ion-trap arrays with direct electronic air-side access. *Appl. Phys. B Lasers Opt.*, 111(1):21–28, 2013. doi: 10.1007/s00340-012-5302-4.

[107] M Brownnutt, G Wilpers, P Gill, R C Thompson, and A G Sinclair. Monolithic microfabricated ion trap chip design for scaleable quantum processors. *New Journal of Physics*, 8(10):232–232, 2006. doi: 10.1088/1367-2630/8/10/232.

[108] M. Brownnutt, V. Letchumanan, G. Wilpers, R. C. Thompson, P. Gill, and A. G. Sinclair. Controlled photoionization loading of88Sr+for precision ion-trap experiments. *Applied Physics B: Lasers and Optics*, 87(3):411–415, 2007. doi: 10.1007/s00340-007-2624-8.

[109] T W Hänsch and B Couillaud. Laser frequency stabilization by polarization spectroscopy of a reference cavity. *Optics Communications*, 35(3):441–444, 1980. doi: 10.1016/0030-4018(80)90069-3.

[110] Joseph Andrew Thom. *An agile and stable optical system for high-fidelity coherent control of a single p88ssrp+s ion.* PhD thesis, Strathclyde University, 2015.

[111] A. G. Sinclair, M. A. Wilson, and P. Gill. Improved three-dimensional control of a single strontium ion in an endcap trap. *Optics Communications*, 190(1-6): 193–203, 2001. doi: 10.1016/S0030-4018(01)01057-4.

[112] R W P Drever, J. L. Hall, F. V. Kowalski, J. Hough, G. M. Ford, A. J. Munley, and H. Ward. Laser phase and frequency stabilization using an optical resonator. *Applied Physics B*, 31(2):97–105, 1983. doi: 10.1007/BF00702605.

[113] Long-sheng Ma, Peter Jungner, Jun Ye, and John L Hall. Delivering the same optical frequency at two places : accurate cancellation of phase noise introduced by an optical fiber or other time-varying path. *Opt. Lett.*, 19(21):1777–1779, 1994.

[114] W McAlpine and R Schildknecht. Coaxial Resonators with Helical Inner Conductor. In *Proceedings of the IRE*, pages 2099–2105, 1959.

[115] Muir Kumph, Carsten Henkel, Peter Rabl, Michael Brownnutt, and Rainer Blatt. Electric-field noise above a thin dielectric layer on metal electrodes. *New J. Phys.*, 18(2):23020, 2016. doi: 10.1088/1367-2630/18/2/023020.

[116] Rainer Behrisch and Wolfgang Eckstein. *Sputtering by Particle Bombardment: Experiments and Computer Calculations from Theshold to MeV energies*, volume 110. Springer, 2007. doi: 10.1016/0030-3992(77)90116-5.

[117] C. García-Rosales, W Eckstein, and J Roth. Revised formulae for sputtering data. *Journal of Nuclear Materials*, 218(1):8–17, 1995. doi: 10.1016/0022-3115(94)00376-9.

[118] C. Hopf, A. Von Keudell, and W. Jacob. Chemical sputtering of hydrocarbon films. *Journal of Applied Physics*, 94(4):2373–2380, 2003. doi: 10.1063/1.1594273.

[119] W Jacob, C Hopf, and M Schlüter. Chemical sputtering of carbon materials due to combined bombardment by ions and atomic hydrogen. *Physica Scripta*, 2006 (T124):32, 2006. doi: 10.1088/0031-8949/2006/T124/007.

[120] Michael A. Lieberman and Allan J. Lichtenberg. *Principles of Plasma Discharges and Materials Processing.* Wiley-Interscience, 2 edition, 2005. doi: 10.1017/CBO9781107415324.004.

[121] Jurgen Meichsner, Martin Schmidt, Ralf Schneider, and Hans-Erich Wagner. *Nonthermal Plasma Chemistry and Physics.* CRC Press, 2012.

[122] Earle Kennard. *Kinetic Theory of Gases, with and Introduction to Statistical Mechanics.* McGraw-Hill Book Company, Inc., 1938.

[123] P. Mahadevan and G. D. Magnuson. Low-Energy (1- to 100-eV) Charge-Transfer Cross-Section Measurements for Noble-Gas-Ion Collisions with Gases. *Phys. Rev.*, 171(1):103–109, jul 1968. doi: 10.1103/PhysRev.171.103.

[124] Donald Rapp and W. E. Francis. Charge Exchange between Gaseous Ions and Atoms. *The Journal of Chemical Physics*, 37(11):2631–2645, dec 1962. doi: 10.1063/1.1733066.

[125] Harold F. Winters and Peter Sigmund. Sputtering of chemisorbed gas (nitrogen on tungsten) by low?energy ions. *J. Appl. Phys.*, 45(11):4760–4766, nov 1974. doi: 10.1063/1.1663131.

[126] R.S. Bauer. *Surfaces and Interfaces: Physics and Electronics*. Elsevier, 2012.

[127] E. Taglauer. Surface cleaning using sputtering. *Applied Physics A Solids and Surfaces*, 51(3):238–251, 9 1990. doi: 10.1007/BF00324008.

[128] A. Gras-Martí, H.M. Urbassek, N.R. Arista, and F Flores. *Interaction of Charged Particles with Solids and Surfaces*. Plenum Press, 1991.

[129] Vicanek and Urbassek. Reflection coefficient of low-energy light ions. *Phys. Rev. B. Condens. Matter*, 44(14):7234–7242, oct 1991.

[130] W. D. Wilson, L. G. Haggmark, and J. P. Biersack. Calculations of nuclear stopping, ranges, and straggling in the low-energy region. *Phys. Rev. B*, 15(5):2458–2468, mar 1977. doi: 10.1103/PhysRevB.15.2458.

[131] Ch. Steinbruchel. A simple formula for low-energy sputtering yields. *Appl. Phys. A Solids Surfaces*, 36(1):37–42, jan 1985. doi: 10.1007/BF00616458.

[132] W C Chen, X M Zhu, S Zhang, and Y K Pu. Reconstruction of ion energy distribution function in a capacitive rf discharge. *Applied Physics Letters*, 94 (211503):10–13, 2009. doi: 10.1063/1.3147216.

[133] Felipe Iza, Gon Jun Kim, Seung Min Lee, Jae Koo Lee, James L Walsh, Yuantao T Zhang, and Michael G Kong. Microplasmas : Sources , Particle Kinetics , and Biomedical Applications. *Plasma Processes and Ploymers*, 5:322–344, 2008. doi: 10.1002/ppap.200700162.

[134] Karl H. Schoenbach and Kurt Becker. 20 years of microplasma research: a status report. *The European Physical Journal D*, 70(2):29, 2016. doi: 10.1140/epjd/e2015-60618-1.

[135] S Hofmann, A F H van Gessel, T Verreycken, and Peter Bruggeman. Power dissipation, gas temperatures and electron densities of cold atmospheric pressure helium and argon RF plasma jets. *Plasma Sources Science and Technology*, 20(6): 065010, 2011. doi: 10.1088/0963-0252/20/6/065010.

[136] M. Moravej, X. Yang, G. R. Nowling, J. P. Chang, R. F. Hicks, and S. E. Babayan. Physics of high-pressure helium and argon radio-frequency plasmas. *Journal of Applied Physics*, 96(2004):7011–7017, 2004. doi: 10.1063/1.1815047.

[137] Liangliang Lin and Qi Wang. Microplasma: A New Generation of Technology for Functional Nanomaterial Synthesis. *Plasma Chemistry and Plasma Processing*, 35 (6):925–962, 2015. doi: 10.1007/s11090-015-9640-y.

[138] G J M Hagelaar, G M W Kroesen, and M H Klein. Energy distribution of ions and fast neutrals in microdischarges for display technology Energy distribution of ions and fast neutrals in microdischarges for display technology. *Journal of Applied Physics*, 88(5):2240–2245, 2000. doi: 10.1063/1.1287758.

[139] Filippo Mangolini, J. Brandon McClimon, Franck Rose, and Robert W. Carpick. Accounting for nanometer-thick adventitious carbon contamination in X-ray absorption spectra of carbon-based materials. *Anal. Chem.*, 86(24):12258–12265, 2014. doi: 10.1021/ac503409c.

[140] John Kotz, Paul Treichel, and Gabriela Weaver. *Chemistry and Chemical Reactivity, Enhanced Review Edition*. Thomson Books/Cole, 2006.

[141] J. D. Siverns, L. R. Simkins, S. Weidt, and W. K. Hensinger. On the application of radio frequency voltages to ion traps via helical resonators. *Applied Physics B: Lasers and Optics*, 107(4):921–934, 2012. doi: 10.1007/s00340-011-4837-0.

[142] Sergey G. Belostotskiy, Tola Ouk, Vincent M. Donnelly, Demetre J. Economou, and Nader Sadeghi. Gas temperature and electron density profiles in an argon dc microdischarge measured by optical emission spectroscopy. *Journal of Applied Physics*, 107(5):053305, 2010. doi: 10.1063/1.3318498.

[143] R Konjevic and N Konjevic. On the use of non-hydrogenic spectral line profiles for electron density diagnostics of inductively coupled plasmas. *Spectrochimica Acta Part B*, 52:2077–2084, 1997.

[144] Hye Sun Park, Sun Ja Kim, H. M. Joh, T. H. Chung, S. H. Bae, and S. H. Leem. Optical and electrical characterization of an atmospheric pressure microplasma jet with a capillary electrode. *Physics of Plasmas*, 17(3):033502, 2010. doi: 10.1063/1.3330507.

[145] R Konjevic and N Konjevic. On the use of non-hydrogenic spectral lines for low electron density and high pressure plasma diagnostics. *Plasma Sources Science and Technology*, 18(3):035011, 2009. doi: 10.1088/0963-0252/18/3/035011.

[146] Gordon W. F. Drake. *Springer Handbook of Atomic, Molecular, and Optical Physics*, volume 53. Springer, 2013. doi: 10.1017/CBO9781107415324.004.

[147] S. Namba, T. Yamasaki, Y. Hane, D. Fukuhara, K. Kozue, and K. Takiyama. Emission spectroscopy of a microhollow cathode discharge plasma in helium-water gas mixtures. *Journal of Applied Physics*, 110(7), 2011. doi: 10.1063/1.3646551.

[148] Hans R Griem. Spectral Line Broadening by Plasmas. *Pure and Applied Physics*, Volume 39:Pages 1–410, 1974.

[149] H. R. Griem, M. Baranger, A. C. Kolb, and G. Oertel. Stark Broadening of Neutral Helium Lines in a Plasma. *Phys. Rev.*, 125:177–195, 1962. doi: 10.1103/PhysRev.125.177.

[150] Atomic Spectra Database. https://www.nist.gov/pml/atomic-spectra-database, Created: 21-07-2009. Accessed: 30-06-2016.

[151] Lutz Baars-Hibbe, Christian Schrader, Philipp Sichler, Thorben Cordes, Karl-Heinz Gericke, Stephanus Büttgenbach, and Siegfried Draeger. Micro-structured electrode arrays:. *Vacuum*, 73(3-4):327–332, 2004. doi: 10.1016/j.vacuum.2003.12.107.

[152] P. Brandenburg, R; Wagner, H., Michel, P., Trunec, D., Stahel. Diffuse dielectric barrier discharges in nitrogen-containing gas mixtures. In *Int. Conf. Phenom. Ioniz. Gases [26th]*, page Volume 4, Greifswald,, 2003.

[153] R Tschiersch, M Bogaczyk, and H-E Wagner. Systematic investigation of the barrier discharge operation in helium, nitrogen, and mixtures: discharge development, formation and decay of surface charges. *J. Phys. D. Appl. Phys.*, 47(36):365204, 2014. doi: 10.1088/0022-3727/47/36/365204.

[154] N P Ferreira and P A Büger. Redeposition of Sputtered Material in a Glow-Discharge Lamp Measured by Means of an Ion Microprobe Mass Analyser. *Zeitschrift für Naturforsch. A*, 33(2):16–19, jan 1978. doi: 10.1515/zna-1978-0206.

[155] Vlasta Horvatic, Damir Veza, Cedomil Vadla, and Joachim Franzke. Atmospheric helium capillary dielectric barrier discharge for soft ionization : broadening of spectral lines , gas temperature and electron. *Journal of Analytic Atomic Spectrometry*, 29:498–505, 2014. doi: 10.1039/c3ja50343g.

[156] Tsuyohito Ito and Mark A Cappelli. Energetic neutral particle production in the cathode sheath of direct-current discharges. In *ISPC-18*, pages 4–7, Kyoto, Japan, 2007.

[157] Leanne C. Pitchford, Jianqi Wang, David Piscitelli, and Jean Pierre Boeuf. Ion and neutral energy distributions to the MgO surface and sputtering rates in plasma display panel cells. *IEEE Trans. Plasma Sci.*, 34(2 II):351–359, 2006. doi: 10.1109/TPS.2006.872426.

[158] Jang-Hsing Hsieh and Chuan Li. Calculation of Sputtering Rate during a Plasma-Assisted Process. *Jpn. J. Appl. Phys.*, 42(Part 1, No. 8):5295–5298, aug 2003. doi: 10.1143/JJAP.42.5295.

[159] R.S. Mason and M. Pichilingi. Sputtering in a glow discharge ion source - pressure dependence: Theory and experiment. *J. Phys. D. Appl. Phys.*, 27:2363, 1994.

[160] T. G. Ballance, Joseph F. Goodwin, Bethan Nichol, Laurent J. Stephenson, Christopher J. Ballance, and David M. Lucas. A short response time atomic source for trapped ion experiments. *Rev. Sci. Instrum.*, 89(5):053102, may 2018. doi: 10.1063/1.5025713.

[161] M. T. Baig, M. Johanning, A. Wiese, S. Heidbrink, M. Ziolkowski, and C. Wunderlich. A scalable, fast, and multichannel arbitrary waveform generator. In *Review of Scientific Instruments*, volume 84, 2013. doi: 10.1063/1.4832042.

[162] Wai-Kai Chen. *The Circuits and Filters Handbook*. CRC Press Inc., 1995.

[163] A. Walther, F. Ziesel, T. Ruster, S. T. Dawkins, K. Ott, M. Hettrich, K. Singer, F. Schmidt-Kaler, and U. Poschinger. Controlling fast transport of cold trapped ions. *Phys. Rev. Lett.*, 109(8):1–5, 2012. doi: 10.1103/PhysRevLett.109.080501.

[164] D Allen. Should the classical variance be used as a basic measure in standards metrology? *IEEE Trans. Instrum. Meas.*, 1(2):36, 1987.

[165] Edward P. Furlani. *Permanent Magnet and Electromechanical Devices*. Elsevier, 2001.

[166] K. Takasumi, P. Dent, J. Liu, M. Marinescu, and M. Walmer. New grade of temperature compensated samarium cobalt permanent magnets and design considerations. In *2009 IEEE Int. Vac. Electron. Conf.*, pages 565–566. IEEE, apr 2009. doi: 10.1109/IVELEC.2009.5193470.

[167] Kilian Singer, Ulrich Poschinger, Michael Murphy, Peter Ivanov, Frank Ziesel, Tommaso Calarco, and Ferdinand Schmidt-Kaler. Colloquium : Trapped ions as quantum bits: Essential numerical tools. *Rev. Mod. Phys.*, 82(3):2609–2632, sep 2010. doi: 10.1103/RevModPhys.82.2609.

[168] R. Bowler, J. Gaebler, Y. Lin, T. R. Tan, D. Hanneke, J. D. Jost, J. P. Home, D. Leibfried, and D. J. Wineland. Coherent diabatic ion transport and separation in a multizone trap array. *Phys. Rev. Lett.*, 109(8):1–4, 2012. doi: 10.1103/PhysRevLett.109.080502.

[169] Robin E. Bentley. *Handbook of Temperature Measurement Vol. 3*. Media, Springer Science & Business, 1998.

[170] D Leibfried. Toward Heisenberg-Limited Spectroscopy with Multiparticle Entangled States. *Science (80-.).*, 304(5676):1476–1478, jun 2004. doi: 10.1126/science.1097576.

[171] C F Roos, M Chwalla, K Kim, M Riebe, and R Blatt. Designer atoms ' for quantum metrology. *Nature*, 443(September):2–5, 2006. doi: 10.1038/nature05101.

[172] M.J. Madsen, W.K. Hensinger, D. Stick, J.A. Rabchuk, and C. Monroe. Planar ion trap geometry for microfabrication. *Appl. Phys. B Lasers Opt.*, 78(5):639–651, mar 2004. doi: 10.1007/s00340-004-1414-9.

[173] Stephan Gulde. *Experimental realization of quantum gates and the Deutsch-Josza algorithm with trapped 40Ca+-ions*. PhD thesis, Universität Innsbruck, 2003.

[174] W. M. Itano, J. C. Bergquist, J. J. Bollinger, J. M. Gilligan, D. J. Heinzen, F. L. Moore, M. G. Raizen, and D. J. Wineland. Quantum projection noise: Population fluctuations in two-level systems. *Phys. Rev. A*, 47(5):3554–3570, may 1993. doi: 10.1103/PhysRevA.47.3554.

[175] G Kirchmair, J Benhelm, F Zähringer, R Gerritsma, C F Roos, and R Blatt. Deterministic entanglement of ions in thermal states of motion. *New J. Phys.*, 11 (2):023002, feb 2009. doi: 10.1088/1367-2630/11/2/023002.

[176] Nir Navon, Nitzan Akerman, Shlomi Kotler, Yinnon Glickman, and Roee Ozeri. Quantum process tomography of a Mølmer-Sørensen interaction. *Phys. Rev. A*, 90(1):010103, jul 2014. doi: 10.1103/PhysRevA.90.010103.

[177] Mariam Akhtar, Guido Wilpers, Kaushal Choonee, Erling Riis, and Alastair G Sinclair. Radio-frequency microplasmas with energies suited to in situ selective cleaning of surface adsorbates in ion microtraps. *J. Phys. B At. Mol. Opt. Phys.*, 52(5):055001, mar 2019. doi: 10.1088/1361-6455/aaf704.

[178] D. A. Hite, K. S. McKay, S. Kotler, D. Leibfried, D. J. Wineland, and D. P. Pappas. Measurements of trapped-ion heating rates with exchangeable surfaces in close proximity. *MRS Adv.*, 2(41):2189–2197, jan 2017. doi: 10.1557/adv.2017.14.

[179] R. D. Knight. Storage of ions from laserproduced plasmas. *Appl. Phys. Lett.*, 38 (4):221–223, feb 1981. doi: 10.1063/1.92315.